Aero-acoustic response of an acoustic liner

Gijs Bouman

MSc thesis
July 2021

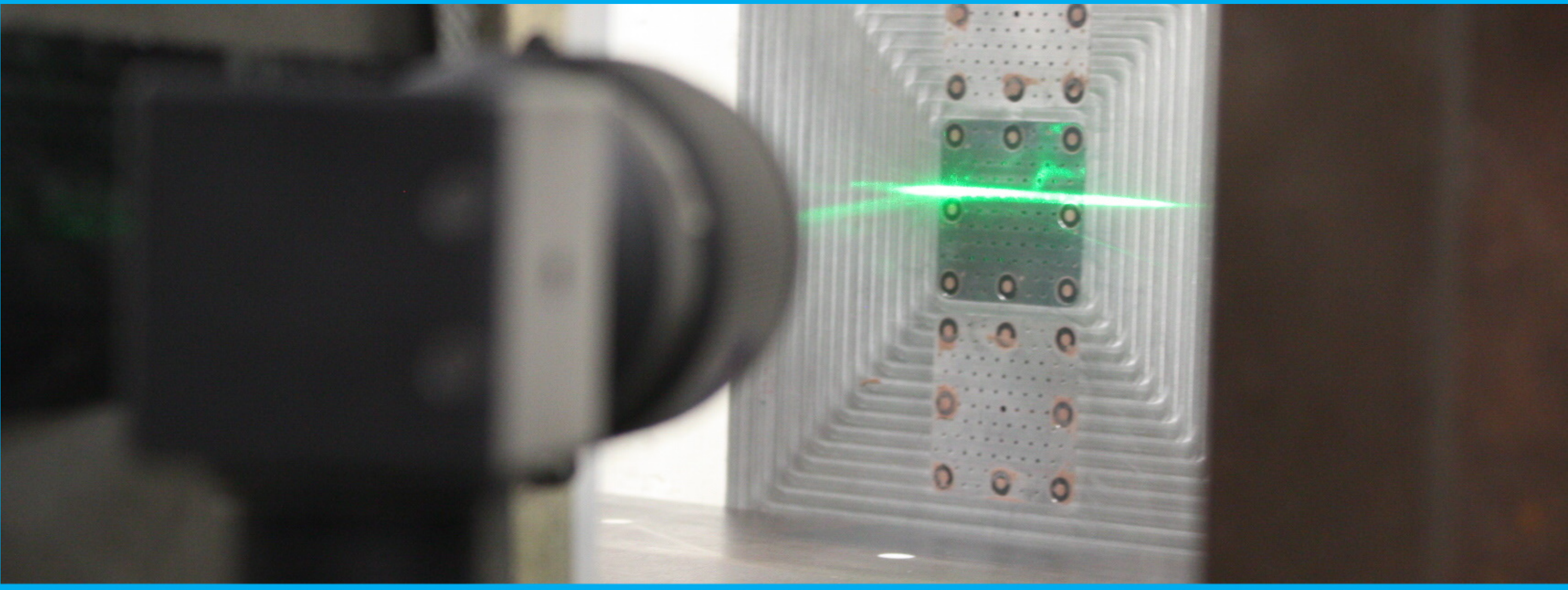

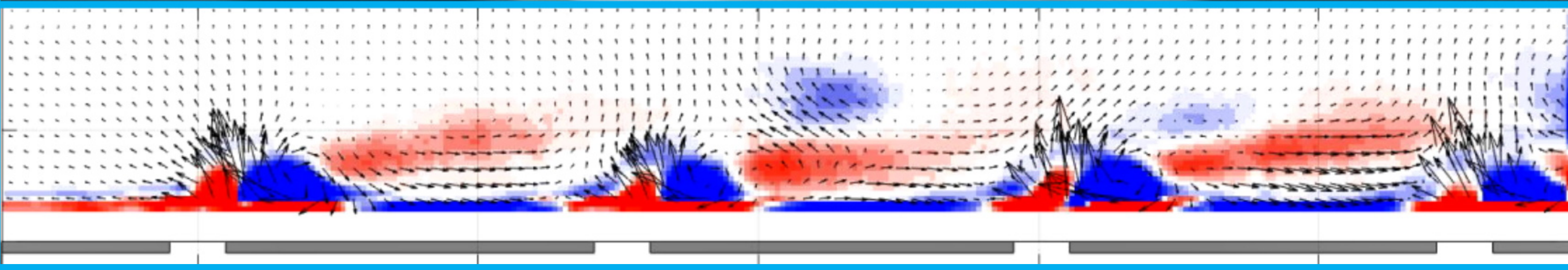

TU Delft

Aero-acoustic response of an acoustic liner

by

Gijs Bouman

to obtain the degree of Master of Science
at the Delft University of Technology,
to be defended publicly on Thursday July 15, 2021 at 10:00 AM.

Student number:	4227964		
Project duration:	August 17, 2020 – July 15, 2021		
Thesis committee:	Dr. D. Ragni	TU Delft	Committee chair
	Dr. F. Avallone	TU Delft	Supervisor
	Dr. M. Van der Meulen	NLR	Supervisor
	Dr. A. Sciacchitano	TU Delft	External examiner

An electronic version of this thesis is available at `http://repository.tudelft.nl/`.

Abstract

In this thesis, the resistance of a single degree of freedom liner is investigated experimentally. Semi-empirical resistance modelling fails at higher Mach numbers ($M_0 > 0.3$) and sound pressure levels ($SPL > 130dB$), and experimental work is missing in these conditions. An experiment combining in-situ impedance measurements and phase-locked particle image velocimetry is selected. This combined approach allows to evaluate the resistance, in-orifice velocity, friction velocity, vorticity and turbulence intensity.

The high grazing velocity and low acoustically induced velocity form a wide range of velocity scales that the PIV measurement must resolve. This sets a requirement for the dynamic velocity range that typical PIV with advanced interrogation techniques is not expected to achieve. A multi-frame approach is selected, which combines measurements with different pulse separation times. A second benefit of such a multi-δt approach is that information from different pulse separation times allows to decompose the PIV measurement noise from the turbulent fluctuations. Limits on the pulse separation time are seen in the freestream velocity, acoustic frequency, correlation strength and spatial filtering. The resulting timing ranges are evaluated before the experiment, and experimentally confirmed to be appropriate.

The decomposition between PIV measurement noise and turbulence is shown to be not applicable to the current data, as the measurement noise is correlated with the pulse separation time. This is caused by turbulence intensity and laser sheet reflections near the liner's face sheet. A DVR of 600 is achieved, and an improvement with respect to a grid refinement approach is seen. The difference between the multi-δt and grid refinement vanishes towards the wall, and the DVR itself is also seen to decrease, due to the increase in measurement noise towards the wall. It is shown that the DVR must exceed the expected range of velocity scales by approximately 25% to accurately resolve phase-dependent quantities.

Results for the friction velocity found from a momentum-integral method and from a log-law fit, modified for surface roughness, transpiration and inclusion of the outer layer, agree well with direct drag measurements. The boundary layer is seen to develop in a periodic manner over the orifices, and the influence of the aero-acoustic interaction at the liner on the local friction velocity can not be neglected. The in-orifice velocity fluctuation root-mean-square (RMS) is consistent between the in-situ impedance and PIV measurements. A lumped-element model suggested in literature is shown to accurately predict the in-orifice velocity scale, but it requires an accurate value for the orifice quality factor. The quality factor is associated to the reduction in effective open orifice area, known as a vena contracta. It is thereby inversely proportional to the friction velocity, and the in-orifice velocity scale. The current results on the quality factor agree qualitatively and quantitatively to statements and suggestions from literature. The resistance is confirmed to be a function of the friction velocity and the in-orifice velocity RMS, with both velocity scales associated to vena contracta. A velocity scale associated to the intensity of vortex shedding from the orifices is introduced by integrating the acoustically induced vorticity near the wall. The onset of non-linear resistance is confirmed at a ratio between the in-orifice and friction velocity scales of 2, and is clearly linked to the intensity of vortex shedding.

Preface

This thesis marks the end to an amazing time as a student, and to a challenging last year. Losing two of the most important people in my life has had a big impact, and it saddens me that I can not share this moment with them. At the same time, knowing how interested and most of all proud they would be has given me a lot of strength. I owe it to my wonderful family, friends and colleagues that I can look back in joy, both to this year as my entire time in Delft. They are too many to mention personally, but I will try and mention a few.

First of all, I must thank my (literally) daily supervisors, Mark-Jan and Francesco. Your support and incredibly constructive feedback has definitely raised the quality of this work. Working together with you has kept me motivated to keep pushing my work to the very end, but also helped me to see my achievements whenever I refused to. You even had the patience to put up with me every time I digressed in my enthusiasm. I feel very lucky having you both as my supervisors, your way of thinking and working has both impressed and inspired me.

I have to thank several study buddies for making it to a point where I could actually start my thesis. Reinier, Coert, Roger and Nick, the countless hours studying and many coffee breaks at the faculty would have been not as fun without you. I'm certain that without your company, I would have been distracted again by some project that seemed fun. Speaking of distractions, I am very happy I sidetracked at several points during my studies. My cycling friends from WTOS have been a constant source of joy and distraction throughout these years, and helped me realize that my second home is on a bike. There's not enough space to list everyone from my time with the Human Power Team, but you know who you are. I think we all agree that our year has been a roller-coaster. The friendships, lessons and memories will remain, let us never forget what happened at Badger Ranch Rd. Working in the D:DREAM Hall by extension for several years never felt as work, as I got to work with Mark, Salomon, Frans, Niels, and so many others. Starting at Kitepower was perhaps the least planned move of all, but equally enjoyable.

Restrictions and lockdowns aren't the best conditions for moving to a new city, surprisingly. I have to thank all my friends, too many to name here, for always being in for a chat or a video call. Extra credit goes out to Axel for always tolerating and even replying to my constant stream of messages. At NLR, the amazing group of people that make up the AVVA department made me feel at home very quickly, which is something that is not easy with me. I especially owe Arjan and Jaap, without whom my tests would not have been possible. Sorry again for breaking the horn and constantly bothering you with odd requests. At least the time that *someone* left the seeding generator on during lunch resulted in a fun story.

Finally, and most importantly, I thank my mom, my dad, and my brother and sister, who will understand this ridiculous font size. I find it difficult to find the right words to express what you mean to me. Mom and dad, it amazes me how you are always there for us, no matter what. I am glad that we are always there for each other, in both good and bad times. You inspire me.

Contents

Abstract iii

List of Figures ix

List of Tables xv

Nomenclature and notation xvii

I Problem background 1

1 Introduction 3
- 1.1 Acoustic liners 4
- 1.2 Impedance and resonance 5

2 Liner impedance modelling 9
- 2.1 Liner impedance prediction 9
- 2.2 Physics of non-linear resistance 17
- 2.3 Knowledge gap 31

3 Problem definition 33
- 3.1 Strategy 33
- 3.2 Experimental challenge 35
- 3.3 Research questions 38
- 3.4 Research objectives 39

II Methodology 41

4 Measurement techniques 43
- 4.1 Acoustic measurements: in-situ impedance evaluation 43
- 4.2 Aerodynamic measurements: high DVR PIV 44

5 Experimental set-up 53
- 5.1 Wind tunnel facility 53
- 5.2 Acoustic set-up 56
- 5.3 Optical set-up 57
- 5.4 Seeding 60

6 Data acquisition 65
- 6.1 Microphone recording parameters 65
- 6.2 PIV sample size 65
- 6.3 PIV Timing limits 67
- 6.4 Phase-locked PIV timing control 71
- 6.5 Test matrix 73

7 Data processing 75
- 7.1 In-situ processing 75
- 7.2 PIV image pre-processing 75
- 7.3 Vector field computation 81
- 7.4 Vector field post-processing 87
- 7.5 Validation of vector evaluation 87

III Results **91**

8 Assessment of multi-dt PIV **93**
8.1 Turbulence and measurement noise decomposition 93
8.2 Choice of datasets for PIV assessment 96
8.3 Measurement noise and DVR 96
8.4 Assessment of phase-dependent quantities 103
8.5 Combined: assessment and improvement of multi-dt PIV 109
8.6 Discussion on multi-dt and grid refinement PIV 112
8.7 Extension to arbitrary experiments 114

9 Results and discussion **117**
9.1 Friction velocity extraction 117
9.2 In-orifice velocity modelling 125
9.3 Non-linear resistance 128
9.4 Boundary layer development 132

10 Conclusions **137**
10.1 Multi-dt PIV 137
10.2 Aero-acoustic liner response 137
10.3 Main research question 138

Bibliography **139**

IV Appendices **143**

A Results summary **145**

B Multi-dt code **147**
B.1 Main: decomposeMultiDt2.m 148
B.2 shiftCorrelationMap.m 150
B.3 combinedScatterMap.m 150
B.4 fitScatteredPeak.m 151
B.5 turbNoisefit.m 153

List of Figures

1.1 Typical placement location of acoustic liners for fan noise suppression. Image taken from Mustafi [34], as adapted from Astley [2] 3
1.2 Schematic overview of (A) a single degree-of-freedom acoustic liner, built up from (B) a perforated face sheet, (C) a honeycomb structure and (D) a rigid backing plate. Image courtesy of Herbert and Copiello [12]. 4
1.3 Liner types, Figures 1.3a-1.3c are adapted from Motsinger and Kraft [33], Figure 1.3d is taken directly from Sugimoto et al. [45]. 5
1.4 Grazing and bias flow, using the SDOF liner of Figure 1.3a 5
1.5 Helmholtz resonator, image adapted from Anselmet and Mattei [1]. 6
1.6 Rectangular orifice spacing 7

2.1 Experimental impedance results from Jones et al. [20], SPL $= 130\ dB$. 11
2.2 Experimental impedance results from Jones et al. [20]. No grazing flow (normal impedance), SPL $= 120\ dB$. 12
2.3 Numerical impedance results of 2-D slit liners. 13
2.4 Impedance measurements of [5]. SPL $= 150 dB$. 13
2.5 Absorption coefficients of Heuwinkel et al. [13]. Note that M_b denotes a bias flow, M_g denotes a grazing flow. 14
2.6 Instantaneous streamline plots in the orifice, no grazing flow. 14
2.7 Numerical impedance results of 2-D slit liners. 15
2.8 Resistance, effects are a sum of the effects due to viscosity (green area), radiation (orange area), SPL (yellow area) and grazing flow (blue area). Modelling results of Guess [10] (lines), compared to experimental impedance results of Spillere et al. [43]: black diamonds and red circles denote experimental data from an upstream and downstream microphone, respectively. $M_0 = 0.25$, SPL $= 130\ dB$. 15
2.9 Impedance results of Jones et al. [20], with different backing depths. 16
2.10 Reactance, effects are summed from the backing effects (black line), the viscous and mass effects (green area) and the effects from radiation (orange area). Modelling results of Guess [10] (lines), compared to experimental impedance results of Spillere et al. [43]. $M_0 = 0.25$, SPL $= 130\ dB$. 16
2.11 Experimental results of Heuwinkel et al. [13]. laser Doppler velocimetry (LDV) measurements performed at 11 tones at $105\ dB$, particle image velocimetry (PIV) recorded with a tonal $f = 992\ Hz$ at $125\ dB$. $f_0 \approx 900\ Hz$. Grazing Mach number $M_0 = 0.1$. 18
2.12 Instantaneous vorticity contours, all at $f = 500\ Hz$ with $f_0 \approx 3\ kHz$. Images from Zhang and Bodony [58] 20
2.13 Outflow vorticity visualisations, SPL $= 160\ dB$, $M_0 = 0.5$ and $f = 3\ kHz$, slices at $x = 0$ and $z = 0$. Numerical results from Zhang and Bodony [60]. 20
2.14 Phase-averaged vertical velocity distributions in the centre-plane of the orifice, $0.07d$ above the orifice. Non-dimensionalized by the friction velocity, $132\ dB$, $M_0 = 0.048$. Experimental results of Léon et al. [27]. 21
2.15 Lid-driven cavity analogies from literature, which demonstrate that the grazing boundary layer is characterized by the wall shear stress, and hence the friction velocity. 22
2.16 $|\tilde{v}|_{rms}$ in the centre-plane of the orifice, $0.07d$ above the orifice. Excitation is multi-tonal, at an SPL per tone of $132\ dB$. Experimental results of Léon et al. [27]. 23
2.17 Classification schemes from literature for the distinction between non-linear cases where vortex shedding occurs, and linear cases where shedding is not observed. 24
2.18 In- and outflow average velocity distribution, with $M_0 = 0.5$, $f = 3\ kHz$, SPL$= 130\ dB$. Numerical results from Zhang and Bodony [60]. 25

2.19 Time-signals of in-orifice velocity in the centre (black curve), $0.36d$ upstream (red) and $0.36d$ downstream (blue) of the centre, with $M_0 = 0.5$, $f = 3\ kHz$ and SPL as labelled. Numerical results from Zhang and Bodony [60]. 25
2.20 Qualitative visualisation of effective open area reduction due to the 'vena contracta' effect, during inflow. 26
2.21 Quantification of vena contracta effects 27
2.22 Phase-averaged vorticity results, with $M_0 = 0.1$, $\Omega_f \approx 0.9$ and SPL as labeled. Experimental results of Van der Meulen [51]. 28
2.23 Vortex transport due to a $M_0 = 0.3$ grazing flow, instantaneous density field, image adapted from Tam et al. [47]. 28
2.24 Bounday layer profiles, axial velocity. The dashed grey lines denote the law of the wall ($U^+ = y^+$) and the log-law, with $\kappa = 0.42$ and $A = 5.4$). Experimental results of Léon et al. [27]. 29
2.25 Orifice interaction prerequisites: turbulence ejection and grazing flow. 30
2.26 Qualitative dependency of θ_{NL} on (M_0, SPL, Ω_f), via the process of vortex shedding. The red, dashed lines denote the orifice interaction mechanism. 31

3.1 Scope of current work: reduced version of Figure 2.26. 33
3.2 The Flow Duct Facility of Royal Netherlands Aerospace Centre. 34

4.1 Geometry of a liner cell instrumented for in-situ impedance measurements. 43
4.2 Working principle of pulse separation time switching: resolve low-speed regions with a large pulse separation time, and high-speed regions with a short pulse separation, such that the local particle image displacement is optimized. 45
4.3 multi-frame PIV (MF-PIV) ensemble correlation schemes. Arcs connecting two frames denote that cross correlation is performed between those two frames. 47
4.4 Particle image path reconstruction using 5 subsequent time-steps. Image adapted from Jeon et al. [16]. 47
4.5 Schematic overview of the selected MF-PIV implementation, including processing steps to the quadruple decomposition and dynamic velocity range (DVR) evaluation. 49

5.1 Depiction of experimental set-up in the Flow Duct Facility (FDF). 54
5.2 Comparison between experimental (PIV) and and log-law boundary layer profiles fitted to the log-law between $35 \leq u^+ \leq 350$. Results obtained with a smooth wall and no acoustic forcing. 55
5.3 Measured and fitted speed of sound versus wind-tunnel velocity 55
5.4 Dimensions of in-situ liner sample. 56
5.5 SPL measured at $f = 2kHz$ at the face sheet microphone. 56
5.6 Laser sheet optics, not to scale, and indicated distances are approximate. Top view, as in Figure 5.1. 57
5.7 Laser sheet height adjustment and orifice reflections. Laser intensity is kept constant throughout these tests, and is scaled 0-2000 counts in the PIV images. 58
5.8 Mach 0.3 laser intensity tests. $16x8mm^2$ domain centred over an orifice. $\delta t = 0.46\mu s$, standard processing over 100 samples, $1x48x48px^2$ first pass with a $1x16x16px^2$ final pass. Subfigures a-c show mean velocities, scaled $0 - 110ms^{-1}$. Subfigures d-f show the associated standard deviation fields, scaled $0 - 12ms^{-1}$. 59
5.9 Dewarped PIV calibration image. Dots are printed with a diameter of $0.5mm$, spaced $0.75mm$ apart. 60
5.10 Typical raw PIV image. Intensities are scaled $0 - 2000$ counts. 61
5.11 Evaluation of seeding density at tested Mach numbers. First phase, δt_0 taken of each datapoint. 62
5.12 Time-dependent seeding density. Running average over 20 samples, with a linear curve with gradient displayed. 63

6.1 Convergence of measurement error with sample size (number of image pairs). 66
6.2 Expected timing limits. 68
6.3 Feasible timing range of Figure 6.2, along with the resulting DVR. 68

6.4 sum of correlation (SOC) correlation value for the Mach 0.6 timing test, showing the spatial patterns due to laser sheet reflections. The domains shown are indicative and not exact, the color map is scaled approximately $0.5-0.9$. 69
6.5 SOC correlation value in the boundary layer. Solid lines are averaged with the area above the orifices excluded, the dashed lines are averaged in the domains above the orifices. 70
6.6 Overview of phase-locked timing control. 71
6.7 Measured phase, trigger delay and phase offset. 72
6.8 Face sheet microphone and laser trigger signals. The microphone signal is displayed in gray on the left y-axis. Laser triggers 1 and 2 are displayed in blue and red, respectively, on the right axis. 72

7.1 Scheme depicting the shift- and vibration correction. A reference image is prepended to the dataset, and all samples in the dataset are shifted to best match the reference. The reference image used in all cases is shown in Figure 7.2a. 76
7.2 Raw PIV images, showing the reference and domains used for the shift- and vibration correction. All intensities scaled $0-1000$ counts. Notice the vertical shift between subfigures (a) and (b). 76
7.3 Intensity over the face sheet reflection averaged in x. Intensity of Figure 7.2a (left) and fitted Gaussian peak (right). 77
7.4 Intensity over the face sheet reflection averaged in y. Intensity of Figure 7.2a (top) and fitted profile (bottom). 77
7.5 Installation error, raw and corrected. 78
7.6 Vibration standard deviation, raw and corrected. 79
7.7 Subsequent images of Figure 7.9 overlayed: all higher intensities of Figure 7.9a are coloured red, those of Figure 7.9b are coloured green. 79
7.8 Reflections due to laser sheet position. 80
7.9 Two subsequent images from a Mach 0.6 measurement, after pre-processing. All intensities scaled $0-200$. The red bands indicate regions outside of the original image, due to the shift and vibration correction. 80
7.10 Graphical representation showing data streams for multi-δt post-processing. This scheme shows in more detail how the processing steps in Figure 4.5 are performed. Two consecutive δt's are shown, dotted lines denote combining information from the entire δt range recorded. 82
7.11 Structure of data exports between Davis 8.4 and Matlab. 83
7.12 Visualisation of summing two multi-δt correlation maps. Correlation maps from a Mach 0.1 freestream, with $[\delta t_0, \delta t_1] = [1.37, 2.75]\mu s = [\delta t_0, 2\delta t_0]\delta t_0$. Note that the summed map has not been re-normalized after summation here. 85
7.13 δt_0 SOC correlation map within an orifice reflection, before and after reflection correction. Mach 0.6 timing test result, notice the decrease in correlation peak strength due to the reflection subtraction. 86
7.14 Effect of summing correlation values from the actual particle image displacement and from unsteady reflections. Both effects are represented by a Gaussian peak in one dimension. 87
7.15 No-flow vector field validation. Differences are evaluated per phase, after which the RMS is taken over all 12 phases. Differences in x- and y-velocity components are similar, and omitted for brevity. 89
7.16 Mach 0.1 vector field validation. Differences are evaluated per phase, after which the RMS is taken over all 12 phases. Differences in x- and y-velocity components are similar, and omitted for brevity. 89

8.1 Timing tests, multi-δt turbulence results. 93
8.2 Timing tests, multi-δt measurement noise results. 94
8.3 Timing tests, normalized multi-δt correlation peak height. 94
8.4 Mach 0.3 timing test, noise results, showing the domain where the measurement noise and DVR are evaluated. Image adapted from Figure 8.2a. 97

8.5 $\sigma_{\Delta x}$ results for the 2021 Mach sweep (left) and 2019 sound pressure level (SPL) measurements (right). Mach numbers and sound pressure levels as defined in Table 8.1. . . 98
8.6 DVR results, associated to Figure 8.5. The value for $R_I = 2568$ for the 2019 results at $108.8dB$ is not included for better and consistent visibility of all other points. 98
8.7 Variation of average correlation peak height with Mach number for the 2021 multi-δt data-sets. Peak height is evaluated in the same domain as the measurement noise. . . 99
8.8 Variation in measurement noise as a function of the timing range k_t (top), along with the associated DVR (bottom). 99
8.9 Variation of $\sigma_{\Delta x}/k_t$ with the correlation strength, 2021 multi-δt results. The re-processed Mach 0.4 sets with reduced timing range are also included. The $M_0 = 0.0$ result with $\sigma_{\Delta x} = 0.028$ is excluded for better visibility. 100
8.10 multi-δt SOC correlation strength for the 2021 Mach 0.4 set, for varying levels of k_t. . . 100
8.11 y-dependent measurement noise (left) and resulting DVR (right) for the Mach 0.4 cases with varying timing range k_t. The curves are moving averages with a sample size of 10. The single-δt results are also shown, denoted by its grid refinement factor $k_g = 2$. The three indicated regions are discussed in the text. 101
8.12 Variation of $\sigma_{\Delta x}/k_t$ with the correlation strength, based on the y-dependent quantities of Figure 8.11. 102
8.13 Incident acoustic vertical velocity, Mach 0.1, $144.3dB$. A flattened outflow is seen for phases $240 < \phi < 30^o$. 104
8.14 Instantaneous (phase-averaged) streamline field of the $M_0 = 0.0$, SPL= $138.7dB$ case, at phase $\phi = 180^o$. The domains in which the area flow rates are evaluated are indicated by the three boxes: upper (green), left (blue) and right (red). The outward-pointing normal vectors are also shown. 104
8.15 Area flow rates without grazing flow, for absolute velocity (left) and acoustic velocity (right). A reduction in outflow on the upper boundary is seen, similar to Figure 8.13. This reduction seems to be compensated by the side boundaries. 105
8.16 Instantaneous (phase-averaged) streamline field of the $M_0 = 0.0$, SPL= $138.7dB$ case, at phase $\phi = 180^o$. Main flow patterns are indicated: side inflow and top outflow (**A**), side inflow to outer orifices (**B**), recirculation between outer and inner orifices (**C**), and source-like (**D**) and sink-like (**E**) patterns. The definitions of the two 'inner' and two 'outer' orifices are also stated. Refer to Figure 8.14 for the streamline field without annotations. 105
8.17 Area flow rates for two well-resolved grazing cases. Results obtained using the acoustic velocity. 106
8.18 Streamlines of acoustic velocity with a grazing flow. Three sinks (**A**) are seen in small vortices near the face sheet. The large shedded vortices induce a downstream velocity, the most downstream vortex at (**B**) seems to force outflow through the downstream boundary (**C**) as a result. Effects are stronger at lower R_I, i.e. at stronger acoustic forcing. Background coloured with vorticity, calculated using the acoustic velocity (i.e. without mean velocity gradient). 107
8.19 Area outflow on the top boundary, as percentage of total inflow. Stronger acoustic forcing (higher Ω_v, lower R_I) results in a restricted outflow on the upper boundary. This is argued to indicate a flattened outflow phase, as seen in figures 8.17a and 8.13. Results computed using absolute velocities. 107
8.20 Test fits to incident acoustic velocity. 108
8.21 Evaluation of fitting functions to incident acoustic velocity. 109
8.22 Relative measurement error as function of R_I/DVR. The linear fit is given by $|\varepsilon_{v,inc}|_{RMS} = 0.03 + 0.2 * R_I/DVR$. 110
8.23 Contrast enhanced picture showing accumulated seeding on the liner sample. 112

9.1 Time-averaged $\bar{u}$ field for the Mach 0.1, $144.3dB$ case. The indicated domains are used in subsequent analyses: domain **0** is made up of the $2.5mm$ upstream of the first orifices, domains **1**-**3** all span from the upstream edge of an orifice to the upstream edge of the next. Note that the velocity scale does not go down to 0 for better visibility. 117
9.2 Velocity fits for Mach 0.1, $144.3dB$. Boundary layer averaged over domain '**3**' in Figure 9.1. 119
9.3 Weakly forced cases, with $R_I \geq 282$, should be fitted with a log-law without transpiration. 120

9.4 High-SPL Mach sweep wall friction results, shown as friction coefficient (left) and associated friction velocity (right). The ’smooth wall with sound’ PIV case is represented by domain **0** in Figure 9.1. 121
9.5 Working principle of the direct drag measurements. Internal (static) friction results in a damper during motion, or a constant friction force opposing the drag force in case of no motion. 122
9.6 Increase in friction coefficient due to the presence of an acoustic liner. These results are found by evaluating the difference between the ’liner with sound’ and ’smooth wall with sound’ curves in Figure 9.4. 122
9.7 Log-law fitting parameters fort the high-SPL Mach sweep results. The dashed lines in the ΔB graph denote the transitional roughness regime. The dashed line in the Π graph shows the flat-plate value $\Pi_{\beta=0} \approx 0.426$. Suction/blowing is disabled for $U_0 \geq 135 ms^{-1}$. 123
9.8 $|\widetilde{v}|_{RMS}$ over the orifices. 125
9.9 Variation of orifice quality factor with friction velocity. Results from the high-SPL Mach sweep. 126
9.10 Variation of orifice quality factor with in-orifice velocity RMS. No-flow SPL sweep results. 127
9.11 Difference between orifice velocity RMS found from PIV and impedance measurements. The labels indicate R_I values. 128
9.12 Vortex shedding intensity for the available grazed cases. 129
9.13 Acoustic resistance, normalized with the friction velocity (top) as a function of Ω_V . The dashed line indicates the fit from Equation 9.7. Also shown is the vorticity-related velocity scale v_ω from subsection 9.3.1 (bottom). 130
9.14 Instantaneous vorticity fields, calculated using the acoustic velocity fields. Phases selected to best show the ejection of vortices. Images rotated for compact presentation. . 131
9.15 Downstream development of the boundary layer over the liner at $M_0 = 0.1$, SPL= $144.3 dB$. The dashed red lines indicate regions of averaging per orifice. 133
9.16 Downstream development of the boundary layer over the liner at $M_0 = 0.1$, SPL= $144.3 dB$. 134
9.17 Downstream development of the boundary layer over the liner at $M_0 = 0.06$, SPL= $117.5 dB$, fitting with wall transpiration disabled. 134
9.18 Downstream development of the boundary layer over the liner at $M_0 = 0.06$, SPL= $117.5 dB$, fitting with wall transpiration enabled. 135

List of Tables

2.1 Expected results for the experiments of Van der Meulen [51], following the work of Léon et al. [27]. 28
2.2 Reviewed literature, reduced to studies including a grazing flow. References of Table 2.3 31
2.3 Characterisation of reviewed experimental work, restricted to acoustic liners **subjected to a grazing flow**. The numbers refer to the references in Table 2.2. 32

3.1 Quantities of interest 34
3.2 R_I estimation, as defined in Equation 3.4, with $|\widetilde{v}|_{rms}$ from Equation 6.2. Grey cells denote $R_I > 200$. 36
3.3 $\Omega_v \approx |\widetilde{v}_{or}|_{lumped}/u_\tau$, shaded by regions described by Léon et al. [27]: grey cells denote the transition region where $2 \leq \Omega_v \leq 5$, above which vortex shedding is observed. The red line denotes the limit $DVR = 200$, as observed in Table 3.2. Modelled with $\Omega_f = 1$ and $Q = 1$. Graphics taken from Léon et al. [27] (cf. Figure 2.17d). 37

4.1 Fundamental differences between grid refinement and pulse separation time switching. 46

5.1 Friction velocity results, as fitted to the profiles shown in Figure 5.2, compared to theoretical values of Equation 5.2. 54
5.2 Liner sample properties 56
5.3 Laser specifications [38]. 57
5.4 Seeding Stokes numbers, with particle response time $t_p = 2\mu s$. 61

6.1 Estimated uncertainty levels of Equation 6.1a, with $\sigma_x/U_0 = 10\%$ and $N = 1000$. 67
6.2 Estimated acoustic velocity RMS and orifice velocity RMS. 67
6.3 Timing test results for the displacement limit 70
6.4 Timing ranges, expressed as multitudes of δt_0. 71
6.5 Test matrix, with intended and achieved sound pressure levels. The associated freestream velocities and ranges of interest R_I are computed using c_0 from Equation 5.4, $p_0 = 101325Pa$ and $|\widetilde{v}_{inc}|_{RMS}$ from Equation 6.2. The actual SPL is the SPL at the face sheet microphone at $2kHz$. The velocity ratios Ω_v are computed with u_τ from Equation 2.13 and the orifice velocity from Equation 2.11b with $Q = 1$. 73

7.1 Overview of datasets used for vector validation 88

8.1 Overview of DVR assessment datasets 96

9.1 Limits imposed on log-law fitting coefficients 119
9.2 Comparison of $|\widetilde{v}_{or}|_{RMS}$, for high-SPL (top) and lower-SPL cases (bottom). 127
9.3 Values of $\Omega_V = |\widetilde{v}_{or}|_{RMS}/u_\tau$ at which the onset of non-linear resistance is observed. 130

A.1 Recording parameters 145
A.2 DVR and assessment 145
A.3 Impedance and quality factor results 146
A.4 Velocity scales 146

B.1 Relevant fields in the 'options' struct needed for decomposeMultiDt2.m. The 'Options' column lists possible values; default values are indicated in **bold**. For integer and float types, only the default value is displayed. 147

Nomenclature and notation

All standard and frequently used nomenclature can be found in the tables below. On several occasions in this document, a different or unique notation is used, which will be mentioned locally. Furthermore, several multiply defined symbols remain, and contextual definitions are stated when they apply. These can be easily recognized as they are preceded with a bracketed statement which notes the context. Numerous quantities are introduced in the context of PIV, which are all defined contextually below.

Greek symbols

Notation	Description	Units
α	Acoustic absorption coefficient	$-$
γ	Ratio of specific heats	$-$
Δ_{or}	Orifice pitch	m
Δ_{px}	Pixel size, on measurement plane	m
δ_{99}	Boundary layer thickness	m
δ^*	Boundary layer displacement thickness	m
δt	(PIV:) pulse separation	s
δ_z	(PIV:) laser sheet thickness	m
$\lvert\varepsilon_{v,inc}\rvert_{RMS}$	Relative error on incident acoustic velocity	$-$
ζ_n	Acoustic normalized impedance	$-$
θ	Resistance, $= Re(\zeta_n)$	$-$
λ	Acoustic wavelength	m
λ_{laser}	Laser wavelength	m
μ	(Property of air:) Dynamic viscosity	$Pa * s = kg * m^{-1} * s^{-1}$
μ	(In a statistical context:) Mean value	$-$
ν	Kinematic viscosity, $= \mu/\rho$	$m^2 * s^{-1}$
ρ	Air density	$kg * m^{-3}$
σ	(Liner property:) Liner porosity, fractional open area	$-$
σ	(In a statistical context:) Standard deviation	$-$
$\sigma_{\Delta x}$	PIV measurement noise, minimum resolvable scale	$pixel$
τ	(Liner property:) Facing sheet thickness	m
τ_w	(Flow property:) Wall shear stress	$Pa = kg * m^{-1} * s^{-2}$
ϕ	(In a phase-locked or temporal context:) Phase angle	rad
ϕ	(Property of acoustic forcing:) Acoustic wave angle of incidence	rad
χ	Reactance, $= Im(\zeta_n)$	$-$
ω	Angular frequency, $= 2\pi f$	$rad * s^{-1}$
ω_0	Angular resonance frequency	$rad * s^{-1}$
ω_z	Vorticity	s^{-1}
Ω_f	Relative frequency, $\Omega_f = f/f_0 = \omega/\omega_0$	$-$
Ω_v	Ratio between orifice and friction velocity, $\Omega_v = \lvert\tilde{v}_{or}\rvert_{RMS}/u_\tau$	$-$

Roman symbols

Notation	Description	Units
c_0	Speed of sound	$m * s^{-1}$
c_{II}	(PIV:) Correlation coefficient	$-$
C_D	Discharge coefficient	$-$
D	(For hexagonal liner cells:) Inscribed cell diameter	m
D	(For slit liners:) Cavity width	m
d	(For circular orifices:) Orifice diameter	m
d	(For slit liners:) slit width	m
d_{ap}	(PIV:) Aperture diameter	m
dB	Decibel	$-$
d_{diff}	(PIV:) Particle diffraction size	m
d_f	(PIV:) Focal length	m
D_h	Hydraulic diameter	m
d_i	(PIV:) Image distance	m
d_I	(PIV:) Interrogation window size	$pixel$
d_o	(PIV:) Object distance	m
d_p	(PIV:) Particle diameter	m
$d_{p,img}$	(PIV:) Particle image diameter	$pixel$
d_z	(PIV:) Focal depth	m
f	Frequency	$s^{-1} = Hz$
$f_{\#}$	(PIV:) Lens f-stop	$-$
f_0	Resonance frequency	$s^{-1} = Hz$
F_{mag}	(PIV:) Magnification factor	$-$
F_{OL}	(PIV:) Interrogation window overlap	$-$
k	Wave number, $= 2\pi/\lambda$	m^{-1}
k_g	(PIV:) Grid refinement DVR multiplier	$-$
k_t	(PIV:) Pulse separation DVR multiplier	$-$
L	Cell (backing) depth	m
M_b	Bulk Mach number	$-$
N_p	(PIV:) Particle image density	$pixel^{-1}$
p	Air pressure	$Pa = kg * m^{-1} * s^{-2}$
p_{ref}	Acoustic reference pressure, $= 20\mu Pa$	$Pa = kg * m^{-1} * s^{-2}$
R_I	Dynamic range of velocities of interest	$-$
Re	Reynolds number	$-$
Stk	Stokes number	$-$
Str	Strouhal number	$-$
TI	Turbulence intensity, $\lvert u' \rvert_{rms}/U_0$	$-$
t	Time	s
u, v, w	Velocity (3 components)	$m * s^{-1}$
U	Velocity magnitude	$m * s^{-1}$
U_τ	Friction velocity	$m * s^{-1}$
v_ω	Integrated vorticity	$m * s^{-1}$
Z_n	Acoustic impedance	$kg * m^{-2} * s^{-1}$

Notation, sub- and superscripts

Notation	**Description**
$\|x\|$	Amplitude
$\|x\|_{rms}$	Root-mean-square
$\hat{x}$	Fourier transform
$\hat{x}^*$	Fourier transform, conjugate
$\tilde{x}$	Fluctuation, acoustic
x'	Fluctuation, turbulent
x_0	Freestream/ambient property
x_{MP}	(PIV:) Multi-pass
x_{MF}	(PIV:) Multi-frame
x_{OL}	(PIV:) Overlap
x_n	Normal
x_{or}	In-orifice quantity
$\langle x \rangle_\phi$	Quantity averaged over phase ϕ
$\overline{x}$	Quantity averaged over time
$\mathbf{u} = [u, v]^T$	Vector notation for (2-D) velocity
$\mathbf{x} = [x, y]^T$	Vector notation for (2-D) coordinates

Acronyms

Notation	**Description**
2D2C	2-dimensional 2 component
DDOF	double degree of freedom
DEHS	di-ethylhexyl-sebacate
DNS	direct numerical simulation
DSR	dynamic spatial range
DVR	dynamic velocity range
FDF	Flow Duct Facility
FFT	fast Fourier transform
FOV	field of view
LDV	laser Doppler velocimetry
MF-PIV	multi-frame PIV
NLR	Royal Netherlands Aerospace Centre
PIV	particle image velocimetry
PTU	programmable timing unit
PTV	particle tracking velocimetry
RMS	root-mean-square
SDOF	single degree of freedom
SOC	sum of correlation
SPL	sound pressure level
TR-PIV	time-resolved PIV
UHBR	ultra-high bypass ratio

I

Problem background

1

Introduction

Noise mitigation is an important aspect in aircraft noise, and one of the main sources of noise is the turbofan engines. Without any treatment, the noise level generated by the fan, compressor, turbine and combustor would be higher than allowed by legislations [33]. Hence, noise suppression is required, and the forward-propagating fan noise is effectively mitigated by installing acoustic liners in the engine ducts [48], as shown in Figure 1.1 [34].

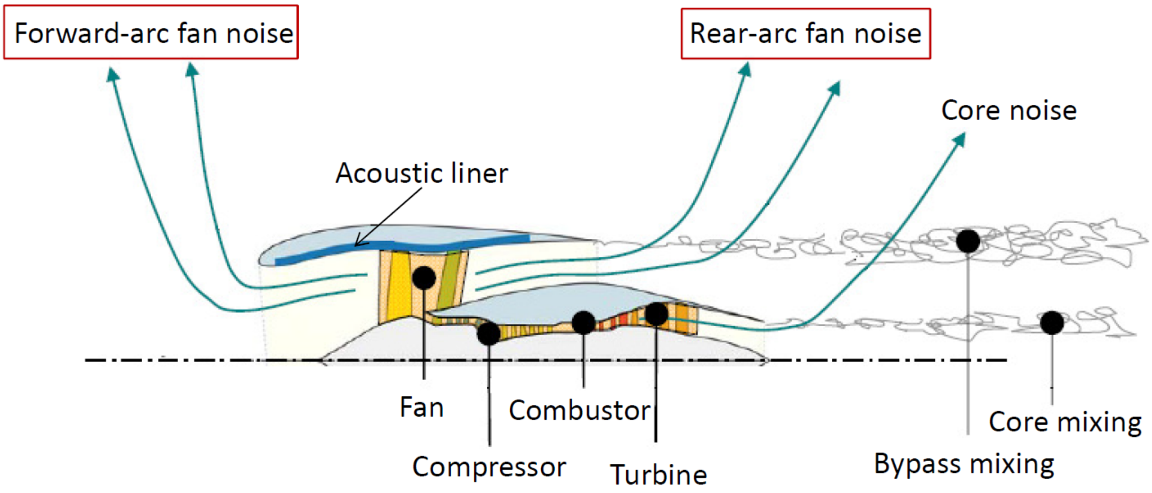

Figure 1.1: Typical placement location of acoustic liners for fan noise suppression. Image taken from Mustafi [34], as adapted from Astley [2]

.

Figure 1.2 shows the simplest and most common type of liner; a single degree of freedom (SDOF) liner, consisting of a perforated face sheet, backed with a honeycomb panel and a rigid backing plate, effectively making for a panel of Helmholtz resonators. Due to their simplicity in construction and light weight, this class of liners forms the industry standard [58]. The recent push for more efficient engines has led to the development of ultra-high bypass ratio (UHBR) turbine engines. Increasing the fan diameter for a fixed engine outer diameter reduces the depth available for liners, and reduces the duct length relative to the diameter, which leads to an overall reduction of space available for the installation of liners [4]. Furthermore, the noise spectrum is changed: the increase in fan diameter reduces the tonal fan noise, leading to a relative increase of the broadband turbomachinery noise [4]. Therefore, new liner designs are required to provide the required noise suppression in the reduced space.

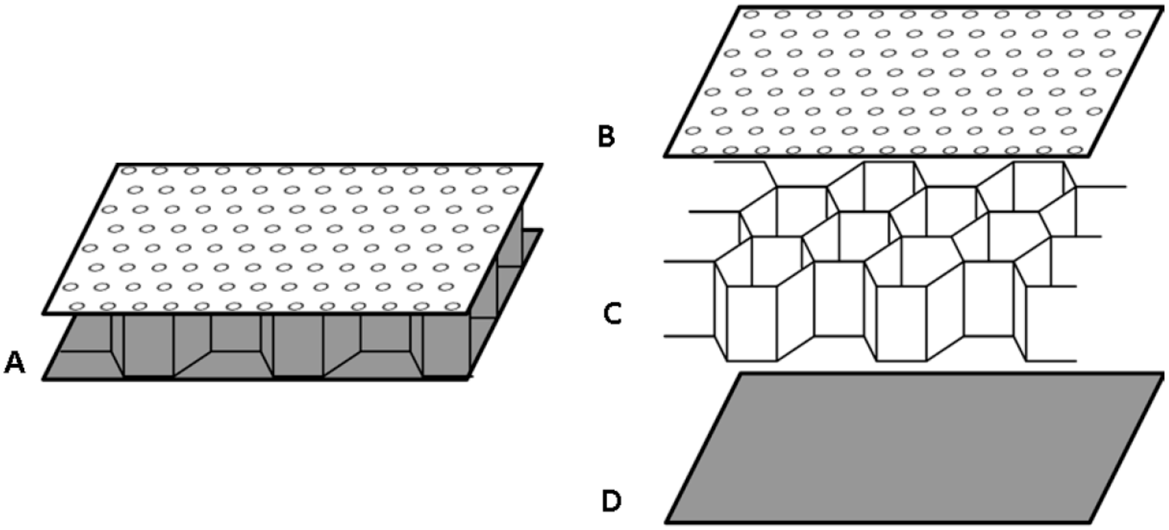

Figure 1.2: Schematic overview of (A) a single degree-of-freedom acoustic liner, built up from (B) a perforated face sheet, (C) a honeycomb structure and (D) a rigid backing plate. Image courtesy of Herbert and Copiello [12].

1.1. Acoustic liners

Motsinger and Kraft [33] describe the three more ’classic’ types of liners, depicted in Figure 1.3, and their main characteristics. The SDOF liner in Figure 1.3a is the simplest of the three, consisting of a perforated face sheet backed by a partitioning material, generally a honeycomb structure, and a solid backing plate. This construction resembles that of a Helmholtz resonator, with the orifices forming the necks and the backing cells acting as the cavity volume. Note that each cavity may be connected to multiple orifices in typical constructions. A slightly more advanced liner type is a double degree of freedom (DDOF) liner, shown in Figure 1.3b. This type may be seen as two layers of SDOF liners stacked on top of each other, with a single backing plate. Finally, bulk absorbers (Figure 1.3c) are made by using a layer of porous material instead of the cellular honeycomb. Note that Figure 1.3c shows a geometry with a face sheet, while bulk absorbers without one also exist [3]. Other, more advanced types of liners have been the result of more recent developments, Figure 1.3d shows as an example a ’folded cavity type’, as presented by Sugimoto et al. [45], consisting of L-shaped cavities.

The main acoustic characteristics of these liner types can quickly be derived from their structural properties. Due to their resemblance to Helmholtz resonators, SDOF liners give the strongest response, and thereby strongest sound attenuation, in a narrow frequency range near their resonant frequency. DDOF liners increase their effective frequency range by using the second layer of resonators. Finally, the bulk absorbers are effective over the widest bandwidth of the three. They are, however, often not suited, due to their difficult structural design and higher weight. Generally, SDOF liners are chosen over the DDOF type, due to the much simpler and lighter construction, and can be considered the industry standard. The folded cavity type can be seen as having two ’depths’, similar to a DDOF liner: the short, vertical channel helps to attenuate sound at high frequency, whereas larger wavelengths are absorbed in the longer, horizontal channel. As a result, a relatively thin liner can still absorb a broad range of frequencies, but this new type is currently still in development, as are other, more advanced concepts.

1.1.1. Grazing and bias flow

Two types of flow are related to liners. Shown with a blue arrow in Figure 1.4, a grazing flow is an external flow along the perforated liner sheet, which is usually a turbulent boundary layer. Liners installed in engine ducts are subjected to a grazing flow due to the flow through the engine, see Figure 1.1. A rigid backing sheet and closed backing cells do not allow for a net flow through the liner. The structure can be modified to force a net in- or outflow over the liner sheet, as shown by the red arrow in Figure 1.4. This is then called a bias flow, and can be used to include boundary layer suction- or blowing, cooling of the liner [61] or to tune the liner’s frequency response [17].

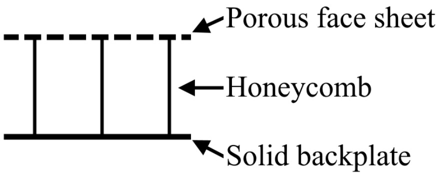
Porous face sheet
Honeycomb
Solid backplate

(a) Single degree of freedom (SDOF)

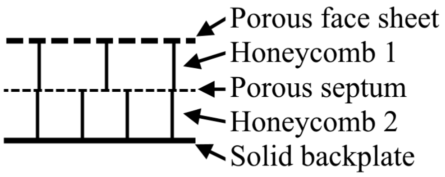
Porous face sheet
Honeycomb 1
Porous septum
Honeycomb 2
Solid backplate

(b) Two degree of freedom (2DOF)

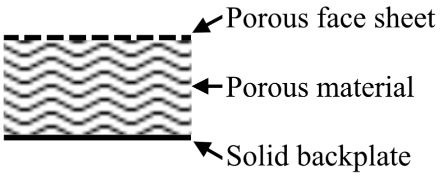
Porous face sheet
Porous material
Solid backplate

(c) Bulk absorber

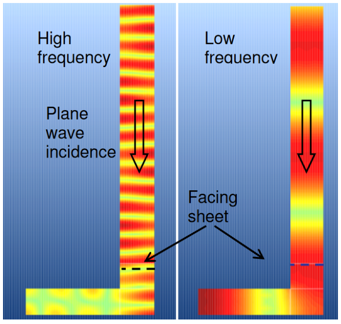
High frequency
Plane wave incidence
Low frequency
Facing sheet

(d) Folded cavity

Figure 1.3: Liner types, Figures 1.3a-1.3c are adapted from Motsinger and Kraft [33], Figure 1.3d is taken directly from Sugimoto et al. [45].

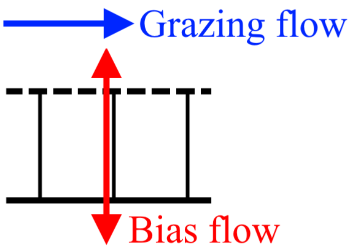
Grazing flow
Bias flow

Figure 1.4: Grazing and bias flow, using the SDOF liner of Figure 1.3a

1.1.2. Applications of acoustic liners

The main use of acoustic liners is to dampen the sound propagated in aero-engine ducts [10], which naturally means a reduction in the acoustic fluctuating pressure. Another use of this characteristic is to dampen pressure fluctuations originating from unsteady combustion phenomena in the combustion chambers of aero- and rocket engines, to improve the engine's stability [61]. In this case, bias flow is often applied to protect the liner structure from damage due to overheating. In the current work, the focus is on acoustic liners for fan noise attenuation in engine ducts. Therefore, bias flow is not required for protection from heat and is generally not used. Typical operating conditions for acoustic liners in the engine ducts, as seen in Figure 1.1, are a grazing flow Mach number $M_0 \approx 0.8$ and sound pressure levels (SPL) in the order of $\mathcal{O}(SPL) = 150\ dB$ [31, 56].

1.2. Impedance and resonance

A liner is characterized by its specific acoustic impedance Z_n, which is defined in the frequency domain as the ratio of the unsteady acoustic pressure and normal acoustic velocity on the liner surface [60]. This definition is shown in Equation 1.1a, where $\hat{p}$ and $\hat{v}_n$ denote the Fourier coefficients of the pressure and normal velocity. Dividing the acoustic impedance by the medium's characteristic impedance $\rho_0 c_0$ leads to the normalized specific acoustic impedance ζ_n, shown in Equation 1.1b. Its real part is called the resistance θ, and its imaginary part the reactance χ [10]. When impedance is discussed in this report, generally the normalized specific acoustic impedance is meant.

$$Z_n(\omega) = \frac{\hat{p}(\omega)}{\hat{v}_n(\omega)} \tag{1.1a}$$

$$\zeta_n(\omega) = \frac{Z_n(\omega)}{Z} = \frac{\hat{p}(\omega)}{\hat{v}_n(\omega)\rho_0 c_0} = \theta(\omega) + i\chi(\omega) \tag{1.1b}$$

The impedance and its resistive and reactive components are effective and simple metrics to express the liner's performance. The complex value for the impedance is therefore of crucial importance in the development and evaluation of new liners.

As the SDOF liner type can be seen as an array of Helmholtz resonators, it is informative to study this fundamental element in more detail to learn more about its acoustic characteristics. This is done in the following sections. Furthermore, the concept of acoustic impedance is explored by making use of an analogy to a mechanical system, and by discussing the absorption coefficient.

1.2.1. The Helmholtz resonator

The basic element of a SDOF liner is a Helmholtz resonator [10]. For such a resonator with neck area A, neck length τ and a cavity volume V, as shown in Figure 1.5, the natural frequency, called the resonance frequency can be determined analytically. Below, the derivation of this frequency, as explained by Anselmet and Mattei [1, Chapter 4], is presented.

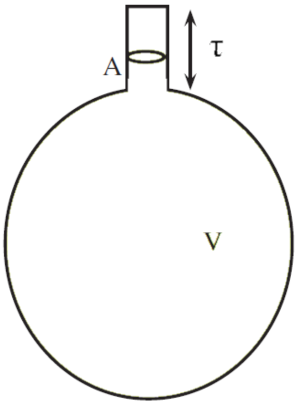

Figure 1.5: Helmholtz resonator, image adapted from Anselmet and Mattei [1].

The derivation for the resonance frequency involves applying Newton's second law to the volume of air in the orifice neck. In Figure 1.5, it can be seen that the mass contained in the neck equals $m = \rho_0 A\tau$. The volume displacement of the air in the neck is $dV = Ay$, with y being an arbitrary, small vertical displacement. Due to the small size of the domain and the short acoustic period, the displacement may be seen as adiabatic. For adiabatic processes, the pressure and volume are related, which allows to state the pressure differential and resulting force in Equation 1.2.

$$\begin{aligned} dp &= -\gamma p_0 \frac{dV}{V} \\ dF &= Adp = -\gamma p_0 A \frac{dV}{V} \end{aligned} \tag{1.2}$$

Next, Newton's second law is applied to the system, as shown below. Here, the statements for m, dV and dF as found above have directly been implemented:

$$\begin{gathered} dF = m\ddot{y} \\ -\gamma p_0 \frac{A^2 y}{V} = \rho_0 A \tau \ddot{y} \\ \downarrow \\ \rho_0 A \tau \ddot{y} + \frac{\gamma p_0 A^2}{V} y = 0 \end{gathered} \tag{1.3}$$

The result of Equation 1.3 may be seen as a mass-spring system, with mass $m = \rho_0 A \tau$ and spring stiffness $k = \gamma p_0 A^2/V$. This spring stiffness may be rewritten by using $c_0^2 = \gamma p_0/\rho_0$, resulting in $k = \rho_0 c_0^2 A^2/V$. Such a system is known to follow $\ddot{y} + w_0^2 y = 0$, with w_0 the natural frequency of the system. This allows to find the natural, or resonant frequency of the resonator from Equation 1.3, which is shown in Equation 1.4.

$$\omega_{0,HR} = c_0 \sqrt{\frac{A}{V\tau^*}} = c_0 \sqrt{\frac{A}{V(\tau + 2\Delta\tau)}} = c_0 \sqrt{\frac{d^2}{D^2 L(\tau + 0.8d)}} \tag{1.4}$$

For a resonator with a circular neck, the orifice area can be expressed as $A = \pi(d/2)^2$, with d the orifice diameter. The neck length is the face sheet thickness τ, but this requires a small correction. As air on both sides of the resonator neck is displaced, and the acoustic pressure field is scattered from the orifice [60], the length is corrected to $\tau^* = \tau + 2\Delta\tau$, with $\Delta\tau$ the correction factor. Anselmet and Mattei [1] mention several values for different resonator types, Zhang and Bodony [60] use a value of $\Delta\tau = 0.8\sqrt{A/\pi} = 0.4d$ for hexagonal resonators with a circular orifice. Finally, for straight hexagonal cells, the cavity volume V can be approximated as $V \approx \pi(D/2)^2 L$, in which D is the inscribed diameter of the hexagon, and L the backing cell depth. The resulting expression for the resonance frequency is shown in the last form of Equation 1.4.

When an acoustic liner has multiple orifices connected to a single cell, as is often the case, an effective diameter of $d^* = D\sqrt{\sigma}$ must be used. Here, σ is the open area ratio, or porosity. For a liner sheet of gridded orifices with streamwise and spanwise spacing Δx and Δy, and orifice diameter d, as shown in Figure 1.6, a porosity of $\sigma = \pi d^2/(4\Delta x \Delta y)$ can be found.

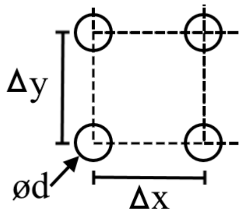

Figure 1.6: Rectangular orifice spacing

1.2.2. Structural analogy

In Equation 1.3, a mass-spring system was observed, with mass $m = \rho_0 A \tau$ and stiffness $k = \gamma p_0 A^2/V$, in the notation of Figure 1.5. While in the derivation of the Helmholtz resonant frequency there is zero damping, it is known that a forced Helmholtz resonator does dissipate acoustic energy. It is informative to view the impedance from the perspective of a *mechanical* mass-spring-damper system in order to better understand the concept of *acoustic* impedance. Mechanical impedance is defined as force over velocity [8]. Consider the classic mass-spring damper system of Equation 1.5, with mass m, damping coefficient c and stiffness k, where a dot denotes a time derivative. Its impedance is then $Z = F/\dot{y}$.

$$\begin{gathered} m\ddot{y} + c\dot{y} + ky = F_{ext} \\ \text{where: } \dot{y} = |\dot{y}| e^{i\omega t} \end{gathered} \tag{1.5}$$

By imposing a fluctuating velocity $\dot{y} = |\dot{y}|e^{i\omega t}$, and finding the reaction forces, the mechanical impedance of the three elements can be readily found. The reaction force for the mass is given by $F_m = m\ddot{y}$, yielding $F_m = i\omega m\dot{y}$ and thus $Z_m = F_m/\dot{y} = i\omega m$. Similarly, the spring force is given as $F_k = ky$, which gives $F_k = k\dot{y}/(i\omega)$, and thereby $Z_k = k/(i\omega) = -ik/\omega$. Finally, a damper is defined by $F_c = c\dot{y}$, resulting directly in $Z_c = c$. Collecting the terms, the mechanical impedance of a generic mass-spring-damper system is shown in Equation 1.6.

$$Z(\omega) = \frac{F}{\dot{y}} = \frac{F_m + F_k + F_c}{\dot{y}} = Z_m + Z_k + Z_c = c + i\left(\omega m - \frac{k}{\omega}\right) \tag{1.6}$$

Recall now the definition of the normalized acoustic impedance ζ_n in Equation 1.1b, and it can be seen that the resistance θ can be interpreted as the damping term in a mass-spring-damper analogy, while the reactance χ consists of a balance between spring and mass effects. Furthermore, combining equations 1.4, 1.6, and the mass and stiffness seen in Equation 1.3, it can be found that when $\omega = \omega_0$, i.e. at resonance, the mass and spring terms cancel each other out in a Helmholtz resonator. This concept is reversible, and allows to state that resonance occurs when $\chi = 0$. Other observations that follow directly are that at low frequencies, (far) below resonance, the system behaves spring-like, with the elasticity formed mostly by the cavity volume. Mass-effects due to the mass of air contained in the resonator neck dominate the reactance for $\omega > \omega_0$.

1.2.3. Absorption and reflection coefficients

The incoming acoustic energy is either absorbed or reflected at the face sheet. For normal incidence sound waves, the absorption and reflection coefficients α and R are related through Equation 1.7a [17]. Using the definition stated by Léon et al. [27], the reflection coefficient is expressed in terms of the normalized impedance in Equation 1.7b. Finally, Guess [10] presents a further worked-out result of Equation 1.7b, shown in Equation 1.7c.

$$\alpha(\omega) = 1 - \left|R(\omega)\right|^2 \tag{1.7a}$$

$$\alpha(\omega) = 1 - \left|\frac{1 - \zeta_n(\omega)}{1 + \zeta_n(\omega)}\right|^2 \tag{1.7b}$$

$$\alpha(\omega) = \frac{4\theta(\omega)}{\left(\theta(\omega) + 1\right)^2 + \chi(\omega)^2} \tag{1.7c}$$

Equation 1.7c shows that absorption is maximum when $\chi = 0$, i.e. at resonance. Here, the impedance is purely real, and equal to the resistance: $\zeta_n(\omega)|_{\chi=0} = \theta$. The maximum theoretical absorption is then $\alpha = 1$ for $\theta = 1$, which denotes complete absorption. The lower bound of $\alpha = 0$ is associated to complete reflection through Equation 1.7a. Note that the third component, of transmission, is not present in this framework. This is because the backplate of the liner is assumed to be a hard wall: acoustic waves within the cavity are completely reflected at the backing sheet [7, 10]. Therefore, waves that are transmitted trough the face sheet are either absorbed by the liner, or are reflected at the backplate and transmitted out of the liner. This latter effect is effectively reflection. As the absorption describes the noise attenuation, the impedance is of great interest when designing new liners. The next chapter presents a popular method to model the impedance of a liner, and identifies a knowledge gap regarding impedance modelling.

2

Liner impedance modelling

2.1. Liner impedance prediction

For grazed SDOF liners, numerous semi-empirical models have been developed to predict the acoustic impedance based on their geometric description, grazing flow Mach number, sound pressure level and acoustic frequency. Such an approach allows to quickly find the impedance for a given liner and environment, without evaluating the complicated aero-acoustic interaction at the liner. These models are therefore an important tool in liner development. Guess [10] presents an often-cited, semi-empirical model. Its popularity can be explained by its completeness: Guess [10] describes not only the impedance model but also the inverse problem, aimed at finding a liner geometry from a desired acoustic impedance in a given aero-acoustic environment. Effects from the a grazing flow and high sound pressure levels are included, which allows to use an aero-acoustic environment representative of engine ducts. Finally, the model takes insights from both analytical expressions and empirical function fits to model the liner directly in the frequency domain. This model is now discussed in more detail.

2.1.1. Model set-up and assumptions

The model concerns specifically SDOF liners with circular orifices. Several empirical curve-fits are used, based on numerous experiments on this type of liner. Therefore, the model's applicability to the development of more advanced concepts is limited. The backing plate is assumed to be hard wall, which reflects all incoming waves. The orifice diameter, backing cell diameter, face sheet thickness and orifice spacing are assumed small with respect to the incoming sound wavelength: $[d, D, \tau, \Delta x] \ll \lambda$. As a result, the face sheet is assumed thin, and with uniform properties. No assumption is made on the backing depth L. The assumption $D \ll \lambda$ results in a locally reacting liner, where sound waves can only travel along the height of the backing cells, and not transversely.

The model is not restricted to normal incidence, as an angle of incidence may be used. The forcing is assumed to be single-frequency. In a multi-tonal or broadband acoustic spectrum, Guess [10] suggests to use the dominant tonal frequency, or to use the RMS value of the multi-tonal environment. Using the RMS value of the forcing spectrum assumes that the liner responds to each frequency independently. This has recently been confirmed by Léon et al. [27], the relation they state is given in Equation 2.1, where the tonal contributions $|\tilde{v}_{or}|_{rms}(\omega_i)$ are modelled. In the current case, the liner is intended to dampen the dominant fan noise, and the tonal frequency approximation seems appropriate.

$$|\tilde{v}_{or}|_{rms} = \sqrt{\sum_{i=1}^{N} |\tilde{v}_{or}|_{rms}^{2}(\omega_i)} \tag{2.1}$$

2.1.2. Model overview

Guess [10] models the impedance assuming independent contributions from several effects: these are viscosity, mass, radiation, non-linear effects from the grazing flow and sound pressure level, and the backing cells. The combined formulation is shown in Equation 2.2, a detailed interpretation of each indicated term is presented in sections 2.1.3-2.1.6.

$$\zeta_n(\omega) = \zeta_v + \zeta_R + \theta_{NL} + i\chi_B = \theta + i\chi \tag{2.2}$$

The worked-out terms are shown in Equation 2.3. The third equation shown here is the equation given by Guess [10] for the in-orifice velocity amplitude, required for the non-linear resistance term and the radiation reactance.

$$\theta(\omega) = \underbrace{\frac{\sqrt{8\nu\omega}\tau^*}{\sigma c_0 d}}_{visc.,mass} + \underbrace{\frac{\pi^2}{2\sigma}\left(\frac{d}{\lambda}\right)^2}_{radiation} + \underbrace{\frac{1-\sigma^2}{\sigma}\frac{|\tilde{v}_{or}| + |u'|}{c_0}}_{non-lin.} \tag{2.3a}$$

$$\chi(\omega) = \underbrace{\left(\frac{\omega\tau}{\sigma c_0} + \frac{\sqrt{8\nu\omega}\tau^*}{\sigma c_0 d}\right)}_{visc.,mass} + \underbrace{\frac{\omega\delta}{\sigma c_0}}_{radiation} + \underbrace{- cot\left(\frac{\omega L}{c_0}\right)}_{backing} \tag{2.3b}$$

$$|\tilde{v}_{or}| = \frac{|\tilde{p}|}{\sigma\rho c_0\sqrt{(\theta)^2 + \chi^2}} \tag{2.3c}$$

Implementing the resonance condition $\chi = 0$ allows to find the resonant frequency from Equation 2.3b. Only using the backing and mass effects, the expression in Equation 2.4 is obtained. The associated sections below will demonstrate that finding the reactance using only the backing and mass terms is a valid approximation, as the viscous and radiation reactance are both negligible. It can be appreciated that this result is visually very similar to the analytical expression for the resonant frequency of a single resonator, which was shown in Equation 1.4. The expression found by Guess [10], however, now uses the porosity σ, in stead of the single-orifice expression d^2/D^2, which allows for multiple orifices per backing cell. Furthermore, the face sheet thickness correction term now not only depends on the diameter-based 'end correction', but also on the porosity (including orifice interaction), the sound pressure level and grazing flow velocity through the δ-term of Equation 2.3b.

$$\chi \approx \frac{\omega(\tau + \delta)}{\sigma c_0} - \frac{c_0}{\omega L} = 0 \quad \Rightarrow \quad \omega_{0,Guess} = 2\pi f_{0,Guess} = c_0\sqrt{\frac{\sigma}{L(\tau + \delta)}} \tag{2.4}$$

Next, a discussion is presented on each term in the model. The validity of each term is evaluated, and interpretations of the underlying physics are given when applicable. Furthermore, it is evaluated which terms dominate the resistance and reactance expressions.

2.1.3. Viscosity and mass

The impedance due to viscosity and mass is found by multiplying an analytical expression for the impedance Z_n of a single Helmholtz resonator by $(\sigma\rho_0 c_0)^{-1}$ and applying end corrections to the sheet thickness (see subsection 1.2.1). Guess [10] states two expressions for the impedance due to viscous and mass effects, dependent on the value of $(d/2)(\omega/\nu)^{1/2}$, with ω the angular frequency and ν the kinematic viscosity. The two limiting values shown in Equation 2.5 denote the Helmholtz and Poiseuille values for the impedance, respectively. Poiseuille flow denotes a pressure-driven flow through a tube [54], without a cavity as found in a Helmholtz resonator. Guess [10] states that in the intermediate region between the two limits, a (linear) combination of equations 2.5a and 2.5b can be used, but that Equation 2.5a usually applies for acoustic liners. This may be confirmed by a quick inspection of the criterion; for diameters in the order of a millimetre, an angular frequency in the kHz range, and a kinematic viscosity of $\mathcal{O}(1 \times 10^{-5}) m^2 s^{-1}$, a value of $(d/2)(\omega/\nu)^{1/2} = \mathcal{O}(10)$ results.

$$\zeta_v \approx \frac{\sqrt{8\nu\omega}\tau^*}{\sigma c_0 d} + i\left(\frac{\omega\tau}{\sigma c_0} + \frac{\sqrt{8\nu\omega}\tau^*}{\sigma c_0 d}\right) \qquad \text{for} \quad \frac{d}{2}\sqrt{\frac{\omega}{\nu}} > 10 \tag{2.5a}$$

$$\zeta_v \approx \frac{32\nu\tau^*}{\sigma c_0 d^2} + i\frac{4\omega\tau}{3\sigma c_0} \qquad \text{for} \quad \frac{d}{2}\sqrt{\frac{\omega}{\nu}} < 1 \tag{2.5b}$$

In the above equations, τ^* denotes the corrected Helmholtz neck length, as shown in Equation 1.4. In the separate terms, it can be seen that both the resistance and reactance due to viscous and mass effects increase with the forcing frequency and the face sheet thickness, while they decrease with increasing porosity and orifice diameter.

From the structural analogy made in subsection 1.2.2, the viscous (ν-related) term is expected to be resistive, and the (τ-related) mass term is expected to be reactive. This is confirmed in Equation 2.5, except that the viscous term also appears in the imaginary term in Equation 2.5a. No explanation for this appearance has been found in Guess [10], or in other literature. One possible explanation for this dependency could be that the friction in the orifice walls makes for an apparent mass term, as it slows down the velocity response of the mass of air in the orifice.

The scaling of resistance with porosity is confirmed in a parametric study performed by Jones et al. [20]. In Figure 2.1a, it can be seen that the resistance is a strong function of the porosity, especially at higher Mach numbers. The scaling of the impedance with face sheet thickness is weaker, which can be seen in Figure 2.1b. In fact, at the high end of the frequency spectrum, where mass effects should be more pronounced, the liner sample with lower thickness shows a higher resistance, which is not in line with Equation 2.5a. The thicker face sheets do show an increase in reactance at high frequency, which is modelled correctly. From these observations, it can be reasoned that viscous effects on the resistance are small with respect to the other terms. Tam and Kurbatskii [46] and Tam et al. [49] confirm that the dissipation due to viscous effects is dominated by the non-linear resistance term, which becomes 'active' at moderate sound pressure levels and in the presence of grazing flow. Only at very small forcing levels and in the absence of a grazing flow, the viscous resistance is expected to be visible. The mass term, however, does have a noticeable influence on the reactance.

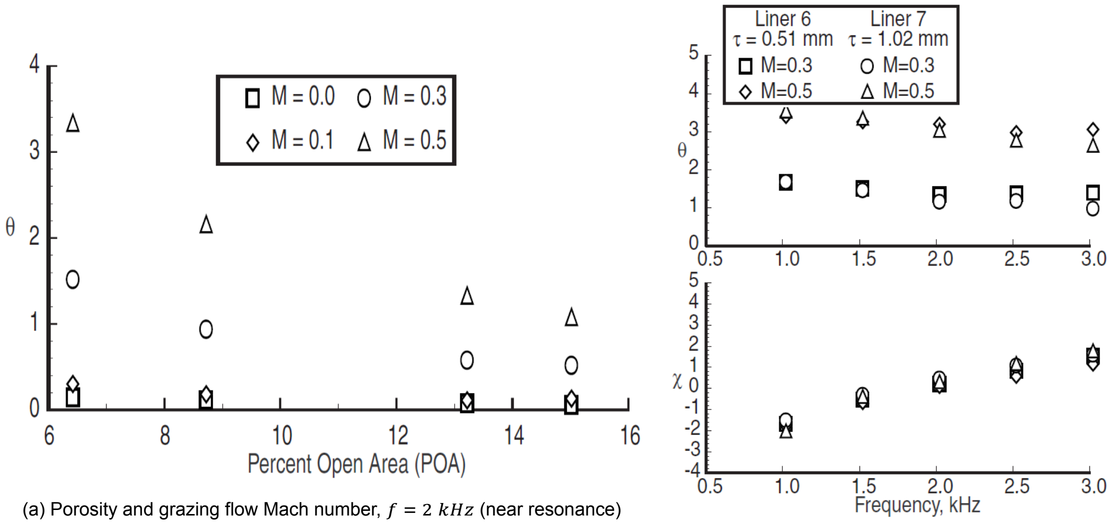

(a) Porosity and grazing flow Mach number, $f = 2\ kHz$ (near resonance)

(b) Face sheet thickness

Figure 2.1: Experimental impedance results from Jones et al. [20], SPL = $130\ dB$.

2.1.4. Radiation

The impedance due to radiation effects is found by modifying the theoretical expressions given by Morse and Ingard [32] to include end corrections, porosity, interaction between adjacent orifices, grazing flow and sound pressure levels. These modifications are curve fits based on experimental data, and the resulting expression is shown in Equation 2.6. Note that this is the equation valid for $\omega d/c_0 < 1/2$. This conditions originates from the fact that Equation 2.6 is a series expansion approximation for an analytical expression for the radiation of a single circular orifice. With forcing frequencies in the kHz range and orifice diameters of $\mathcal{O}(1mm)$, this conditions is generally satisfied for acoustic liners.

$$\begin{aligned} \zeta_R &= \frac{\pi^2}{2\sigma}\left(\frac{d}{\lambda}\right)^2 + i\frac{\omega\delta}{\sigma c_0} \\ \text{with:} \quad \delta &= \frac{8d(1-0.7\sqrt{\sigma})}{3\pi}\,\frac{1}{1+305M_0^3}\,\frac{1+5*10^3M_{or}^2}{1+10^4M_{or}^2} \end{aligned} \tag{2.6}$$

In this expression, $\lambda = c_0/f$ is the acoustic wavelength. The resistance due to radiation is seen to increase with orifice diameter and forcing frequency, while it diminishes with increasing porosity. The radiation resistance is generally very small, due to the $(d/\lambda)^2$ term, and can be neglected. This is also mentioned by Guess [10]. The radiation reactance is modified using the δ correction term, which is a curve-fit based on experimental data. Combined with the mass reactance, one finds $\omega(\tau + \delta)/(\sigma c_0)$, which shows that this radiation reactance acts as a tube end correction term. The $(1 - 0.7\sqrt{\sigma})$ term is meant to account for orifice interaction, and the last two fractions in the expression for δ in Equation 2.6 are to account for a grazing flow and sound pressure levels, respectively.

The reactance 'correction' for the porosity is confirmed qualitatively by Jones et al. [20], which is demonstrated using Figure 2.2. The liner samples with *lower* porosity show a slightly *higher* reactance; this agrees with the negative effect that the porosity σ has on the correction term δ in Equation 2.6. This effect is most pronounced at high frequencies, where the mass effects become more important (see subsection 1.2.2). With an increasing grazing flow Mach number, Jones et al. [20] show that the porosity effect on reactance diminishes. This agrees to the grazing flow correction in Equation 2.6, which sets δ to zero for high grazing flow Mach numbers.

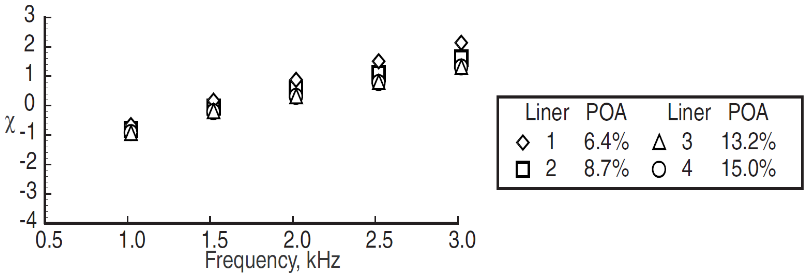

Figure 2.2: Experimental impedance results from Jones et al. [20]. No grazing flow (normal impedance), SPL = $120\ dB$.

The influence of the grazing flow in Equation 2.6 is studied next. Reactance results of Zhang and Bodony [58] are shown in Figure 2.3a. These reactance results seem similar to those of Jing et al. [18] in Figure 2.3b: the rise in reactance around $M_0 = 0.2$ may be just visible near the end of their Mach number range. Zhang and Bodony [58] show that for simulated 2-dimensional slit liners, a curve fit for the influence of grazing flow Mach number on the reactance can be made by $\chi/\sigma = A + B/(1 + CM_0^3)$. This is the same form as Equation 2.6. Zhang and Bodony [58] find a coefficient of $C = 1$, much lower than the $C = 305$ that Guess uses. This may be partially explained as Zhang and Bodony [58] simulate a slit liner, whereas Guess [10] addresses strictly perforated liners. The other coefficients A and B are demonstrated to be very sensitive to the forcing frequency. In the perspective of Guess [10], this can be explained as the B-coefficient represents the orifice interaction and sound pressure level terms in Equation 2.6, and the A-coefficient includes the reactance terms from viscosity, mass and backing in Equation 2.3b. The amount of cases run by Zhang and Bodony [58] is insufficient to conclude on the correctness of these other terms. The large discrepancy in the C-coefficient does show that this dependency deserves further analysis.

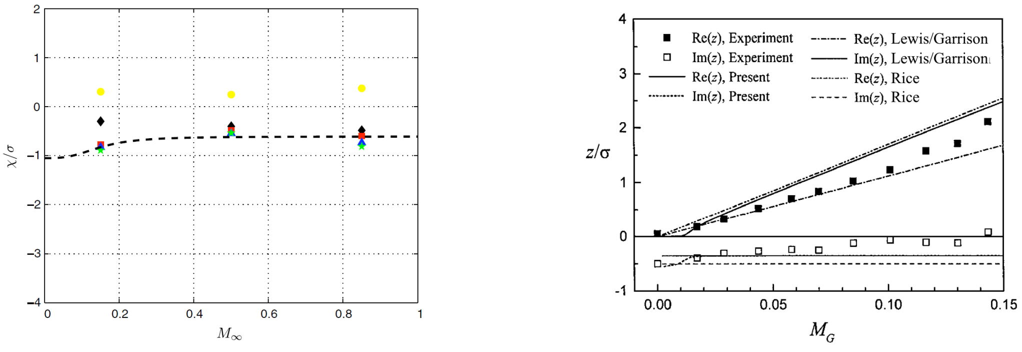

(a) Zhang and Bodony [58], $150\ dB$, $500\ Hz$.

(b) Jing et al. [18], $200\ Hz$, unknown SPL.

Figure 2.3: Numerical impedance results of 2-D slit liners.

For high grazing flow Mach numbers, the correction term δ approaches 0. Guess [10] suggests that this could be explained as the turbulent boundary layer could remove the end correction on the face sheet. The end correction on the inside of the liner would be washed out by turbulent fluctuations in the boundary layer, which enter the cavity. Another study by Zhang and Bodony [60] showed that a turbulent boundary layer indeed results in a much higher in- and outflow through a circular orifice than a laminar one. It also showed that the in-orifice flow becomes highly asymmetric due to the grazing flow. This last effect would make that the in-orifice flow no longer resembles a pipe flow, and that classic end corrections are therefore inappropriate. Both suggestions link to the δ term in Equation 2.6 through its similarity to an orifice end correction.

The inverse proportionality of ζ_R to the Mach number, i.e. $\chi_R \propto 1/(1+305M_0^3)$, in Equation 2.6 can also be observed. Brown and Jones [5] show that an increase in grazing flow Mach number flattens the reactance curve, shown in Figure 2.4. Following Equation 1.7c, a flatter reactance curve means that the liner operates near resonance over a broader frequency range, where $\chi \approx 0$. This is visible in the impedance measurements of Heuwinkel et al. [13] in Figure 2.5: the grazing flow case (red curve) shows a much broader dissipation (hence absorption) peak than the no-flow case (black curve).

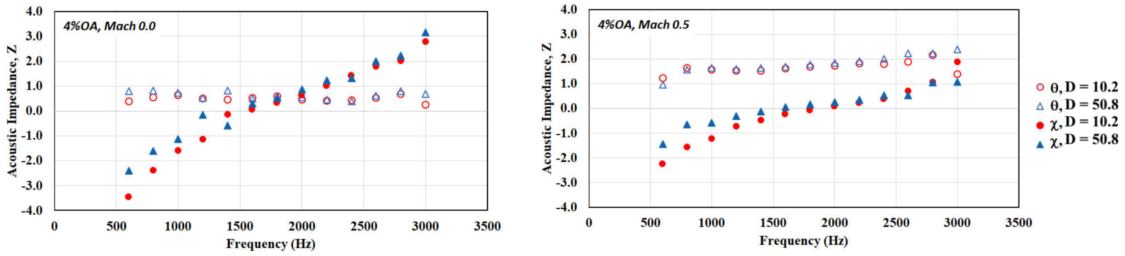

(a) $M_0\ = 0$

(b) $M_0\ = 0.5$

Figure 2.4: Impedance measurements of [5]. SPL = $150dB$.

The final term in Equation 2.6 involves the sound pressure level through the in-orifice Mach number M_{or}. This empirical fit approaches $1/2$ as M_{or} becomes high. Guess [10] postulates that this may be due to turbulent jets that form in the orifices at higher orifice flow rates. The turbulence at the orifice walls would then wash out the end correction term on one side only, hence the asymptotic value of $1/2$. Such turbulent orifice flows have been demonstrated by Tam and Kurbatskii [46] and Zhang and Bodony [59], among others, as is shown in Figure 2.6. At high sound pressure levels, turbulent boundary layers are formed at the orifice walls, which are not present at lower levels. While these observations confirm the hypothesis of Guess [10], no quantitative confirmation is given for the dependence of δ on M_{or}.

While the orifice interaction and grazing flow effects on the reactance are shown to be qualitatively correct in the model of Guess [10], it is concluded that the exact dependencies remain poorly addressed. Furthermore, no quantitative evaluation of the orifice Mach number correction term was found. This is further complicated as the orifice Mach number is not only dependent on the SPL, but also on the liner response, as Equation 2.3c suggests.

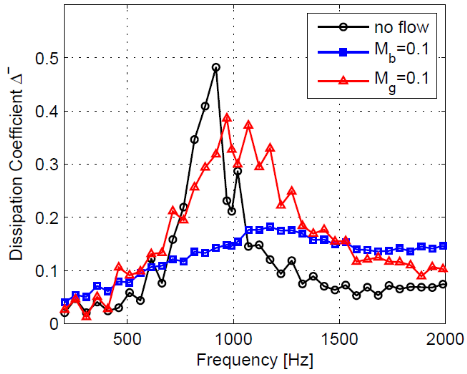

Figure 2.5: Absorption coefficients of Heuwinkel et al. [13]. Note that M_b denotes a bias flow, M_g denotes a grazing flow.

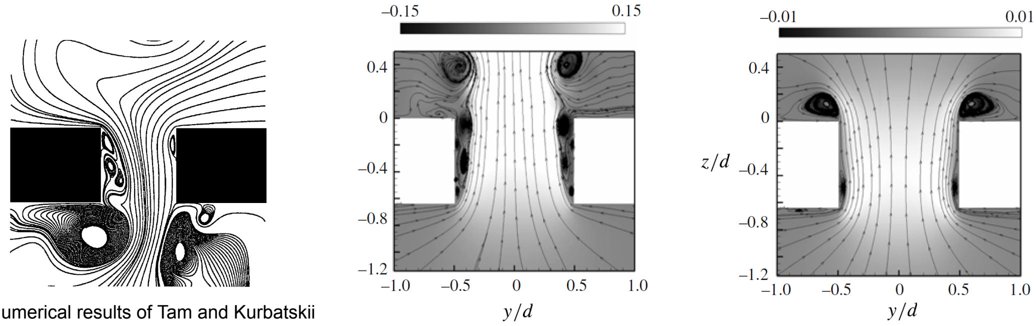

(a) Numerical results of Tam and Kurbatskii [46], $150\ dB$, $3\ kHz$

(b) Numerical results of Zhang and Bodony [59], $160\ dB$, $3\ kHz$

(c) Numerical results of Zhang and Bodony [59], $130\ dB$, $3\ kHz$

Figure 2.6: Instantaneous streamline plots in the orifice, no grazing flow.

2.1.5. Non-linear terms: sound pressure level and grazing flow

The non-linear effects on the resistance are approximated using Equation 2.7, and are based on curve-fits on the amplitudes of the vertical, in-orifice velocity amplitude $|\widetilde{v}_{or}|$ and the amplitude of the turbulent, tangential velocity fluctuations $|u'|$.

$$\theta_{NL} = \frac{1-\sigma^2}{\sigma}\frac{|\widetilde{v}_{or}| + |u'|}{c_0} \tag{2.7}$$

The $1-\sigma^2$ term is similar to the orifice interaction seen in the radiation reactance. While not explicitly stated by Guess, this may thus be seen as an empirical fit for the effect of interaction between adjacent orifices on the resistance. $|\widetilde{v}_{or}|$ is associated to two effects. The boundary layers that form on the orifice walls due to the in-orifice flow causes a reduction in effective open area, clearly visible between figures Figure 2.6b and Figure 2.6c. This reduction is called a vena contracta [27, 60]. In the viscous resistance term (cf. Equation 2.3a) it can be seen that a reduction in open area increases the resistance. The in-orifice velocity is also linked to vortex shedding from the orifice at high SPL: vortices are shedded into the grazing boundary layer, converting acoustic energy into kinetic energy, which can be dissipated in the boundary layer [49]. $|u'|/c_0$ 'captures' the effect of the grazing flow: Guess [10] postulates that turbulent fluctuations are transported into the orifice, increasing the in-orifice velocity and the associated turbulent dissipation through vortex shedding. Guess recommends $|u'|/c_0 \approx kM_0$, with $k = 0.3$ based on experimental data.

The resistance is modelled as directly proportional to the grazing flow Mach number. The function form is confirmed by Zhang and Bodony [58], who show that their results are accurately modelled using a function fit of $\theta/\sigma = aM_0 + b$, for $0 < M_0 < 1$. This can be seen in Figure 2.7a. This result is qualitatively very similar to that of Jing et al. [18] in Figure 2.7b (repeated from Figure 2.3b). In the function fit, the a coefficient in the two cases run is $a \approx 0.42$, which is close to the $|u'|/c_0 = 0.3M_0$ suggested by Guess [10]. The b coefficient changes strongly per case, as it contains the effects from the sound pressure level, viscosity and radiation. The experimental impedance results of Jones et al.

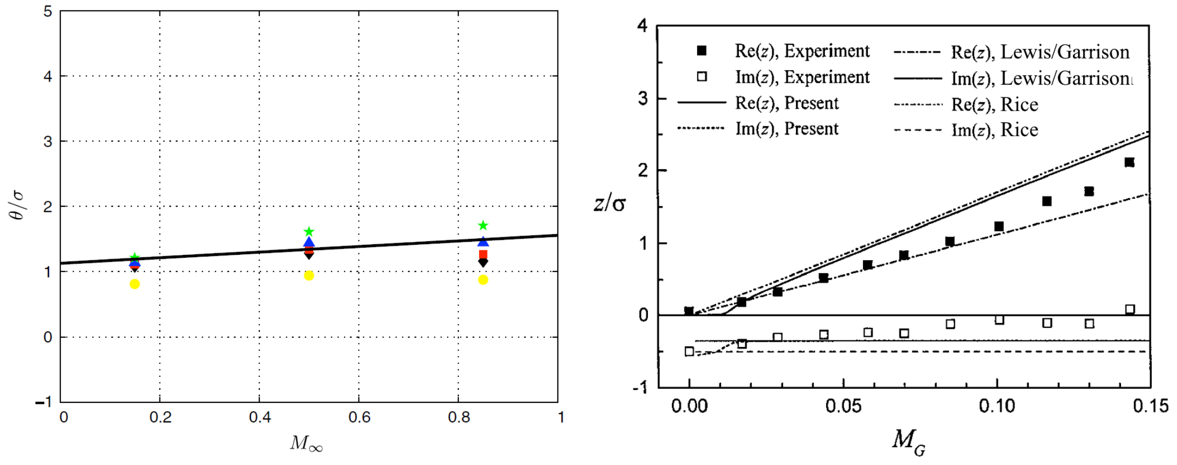

(a) Zhang and Bodony [58], 150 dB, 500 Hz.

(b) Jing et al. [18], 200 Hz, unknown SPL.

Figure 2.7: Numerical impedance results of 2-D slit liners.

[20] and Brown and Jones [5], shown in figures 2.1a and 2.4, also show a clear increase in resistance with grazing flow Mach number, although this does not seem fully linear, unlike the function forms of Guess [10] and Zhang and Bodony [58]. Spillere et al. [43] compares the model's results to experimental impedance results, shown in Figure 2.8. Two observations stand out from these results: that (1) the resistance is poorly modelled in the grazing conditions shown, and that (2) the effect from the grazing flow modelling terms is dominant. This leads to the conclusion that the effect due to the grazing flow is poorly modelled.

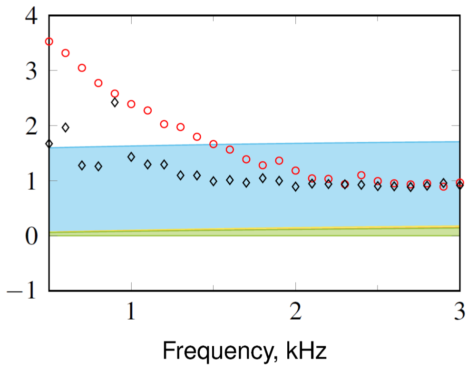

Figure 2.8: Resistance, effects are a sum of the effects due to viscosity (green area), radiation (orange area), SPL (yellow area) and grazing flow (blue area). Modelling results of Guess [10] (lines), compared to experimental impedance results of Spillere et al. [43]: black diamonds and red circles denote experimental data from an upstream and downstream microphone, respectively. $M_0 = 0.25$, SPL $= 130\ dB$.

The in-orifice velocity $|\tilde{v}_{or}|$ was shown in Equation 2.3c to be a function of the acoustic pressure amplitude and the impedance itself. While the results in Figure 2.8 suggest that the effect of the SPL is small, raising the SPL to more representative levels makes for a strong non-linear response in the liner's resistance. Early work by Tam et al. [49] has shown that at high sound pressure levels, the in-orifice velocity becomes high enough such that vortices are shedded from the orifice. This transfers acoustic energy into turbulent kinetic energy, which then becomes the dominant dissipation mechanism. Such vortex shedding is also seen in Figure 2.6b. Forcing at lower sound levels, as in Figure 2.6c, does not show vortex shedding. Léon et al. [27] have observed upper limits on the in-orifice velocity for an increasing SPL. Clearly, certain thresholds then exist, complicating the resistance term and the expression for $|\tilde{v}_{or}|$ itself. Furthermore, Zhang and Bodony [60] have shown that the in-orifice velocity is influenced by the grazing flow velocity and turbulence intensity. Guess's assumption that the grazing flow and SPL effects act independently of each other may therefore not be appropriate.

2.1.6. Backing

The backing impedance is purely reactive, which is explained by the analogy of subsection 1.2.2: the backing depth is associated to the elasticity of the resonator, hence the spring stiffness in the analogy. The backing impedance for a locally reacting liner with a rigid backing plate can be found analytically, using linear acoustics to model the wave motion in the backing cell [7]. Its approximation is shown in Equation 2.8a. In this equation L denotes the cell depth of the liner, which increases the reactance along with the forcing frequency. $\omega L/c_0$ is generally small, as the frequency is in the kHz range, and the backing depth in the order of centimetres. Therefore, a small angle, or in this case low-frequency assumption ($\omega L/c_0 \approx 0$) can be implemented, which yields the expression of Equation 2.8b.

$$\chi_B = -cot\left(\frac{\omega L}{c_0}\right) \tag{2.8a}$$

$$\chi_B \approx -\frac{c_0}{\omega L} \quad \text{for} \quad \frac{\omega L}{c_0} \approx 0 \tag{2.8b}$$

Theoretical limiting values are then $\chi_B = 0$ for $\omega L/c_0 = \pi/2 + n\pi$ and $\chi_B = \pm\infty$ for $\omega L/c_0 = n\pi$, both with n as an integer. The latter condition is called anti-resonance, and makes for a zero absorption, thus full reflection [19]. Qualitatively, the results of Jones et al. [20] in Figure 2.9 show that the backing depth indeed has a large influence on the reactance, as a clear shift is visible. The deeper backing depth leads to a much lower resonance frequency. The first anti-resonant frequency is also visible for the deeper liner. Resistance is independent of the backing depth, except near resonance or anti-resonance. At these locations, the liner's velocity response is theoretically either increased (resonance), or decreased to zero (anti-resonance), following Equation 2.3c. This velocity response affects the resistance through its non-linear term. Jones and Watson [19] show, however, that instead of a zero resistance, an increased resistance is observed near anti-resonance. The velocity equation of Equation 2.3c is therefore not capable of modelling this condition. Nevertheless, anti-resonance is not a condition of interest, due to its zero attenuation, and this modelling limitation is not a large problem.

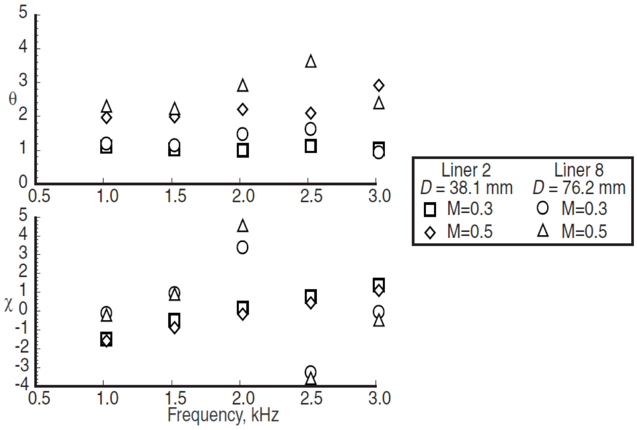

Figure 2.9: Impedance results of Jones et al. [20], with different backing depths.

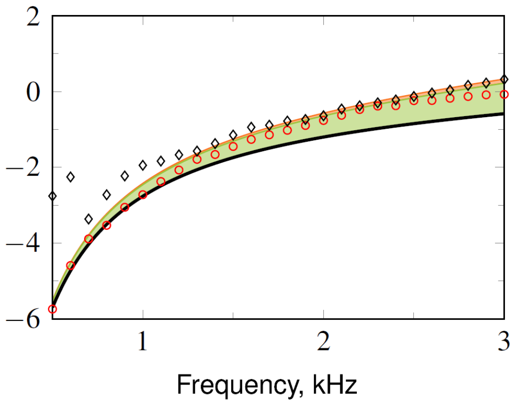

Figure 2.10: Reactance, effects are summed from the backing effects (black line), the viscous and mass effects (green area) and the effects from radiation (orange area). Modelling results of Guess [10] (lines), compared to experimental impedance results of Spillere et al. [43]. $M_0 = 0.25$, SPL = $130\ dB$.

Furthermore, Spillere et al. [43] compares the results from Guess's model to measured impedance data. The reactance results in Figure 2.10 show that the reactance is modelled closely by Guess's model, even in a grazing flow and moderate sound pressure levels. Furthermore, it can be seen that the backing effect dominates the reactance, especially in the low (spring-like) end of the frequency spectrum. At higher frequencies, the mass term also becomes evident and non-negligible.

2.1.7. Conclusions on impedance modelling for acoustic liners

Summarizing the above, it can be concluded that the non-linear resistance term fails to accurately model the impedance and the in-orifice velocity amplitude at higher grazing flow Mach numbers and sound pressure levels. Modelling is adequate at lower values, where $\theta_{NL} \approx 0$. This is called the linear regime. A typical bound for this region is an SPL of $130\ dB$ [31]. For the grazing flow Mach number, no clear bound is mentioned in literature. The rise in reactance around $M_0 = 0.2$, observed in Figure 2.3, might indicate the onset of non-linear behaviour due to grazing flow effects. The results in Figure 2.8 show that at $M_0 = 0.25$, a large discrepancy exists already. As typical conditions of interest are at high values for the sound level and flow velocity ($150\ dB$, $M_0 = 0.8$ [31, 56]), this popular model is then ill-suited for proper liner design at such conditions.

It was shown that similar points of concern exist for the radiation reactance. The grazing flow dependence was shown to be qualitatively correct, but doubts remained to its quantitative expression. Similarly, the effect of the sound pressure level lacks quantitative validation. As the radiation terms are dominated by the non-linear resistance and the mass and backing reactance terms, however, this poses no big problem for the accuracy of the impedance model.

A wrongly modelled resistance and associated in-orifice velocity amplitude leads to an erroneous absorption spectrum $\alpha(\omega)$. A second problem that arises from this concerns impedance eduction. Impedance eduction is an inverse technique, where the impedance is evaluated experimentally by taking measurements *around* the liner [44, 53]. The fundamental characteristic is that these liners can be described by their impedance, which acts as an effective boundary condition. This boundary condition can be used in numerical or theoretical models to model the flow through the test section with the liner installed. In liner eduction, it is attempted to then find a boundary condition ζ_n at the liner, which is able to represent the measurements taken well. It can easily be seen that this then directly depends on the model that is chosen to simulate the flow between the liner and the measurement locations, and thereby also on the impedance model. An inaccurate model will then lead to inaccurate impedance measurements.

It is clear then that further information is required regarding the non-linear resistance term. The effects are known to be due to the sound pressure level and grazing boundary layer. The details of these effects, however, and their quantitative effect on the impedance need further specification. This raises the following questions:

1. How are the sound pressure level, grazing flow Mach number, and grazing flow turbulence intensity related to:
    (a) the occurrence of vortex shedding from the orifices?
    (b) the in-orifice velocity amplitude $|\tilde{v}_{or}|$?
    (c) other aero-acoustic phenomena that might be affecting the non-linear resistance?
2. Which parameters then drive the non-linear acoustic resistance?
3. How can the relation between the impedance and these parameters be quantified?

2.2. Physics of non-linear resistance

Vortex shedding from circular orifices was observed as early as 1950 by Ingård and Labate [15], albeit at large orifice diameters. Melling [31] suggested in 1973 that this conversion of incident acoustic energy to turbulent kinetic energy was the dominant dissipation mechanism at high sound pressure levels. Since then, numerous experimental works have focussed on this phenomenon, Worraker and Halliwell [56] present an acoustic liner grazed by a high-speed ($M_0 = 0.5$) boundary layer. These studies, however, commonly used larger orifice diameters, due to restrictions in experimental measurement techniques. These larger orifices with $3.5 < d < 20\ mm$ may not scale all physics involved correctly, and thus yield a different balance between viscous and inertial effects [46].

Continuous improvements in numerical and experimental capabilities allowed to study the aero-acoustic interaction at the liner in more detail. Tam and Kurbatskii [46] and Tam et al. [49] showed in a combined numerical/experimental study in 2000-2001 that vortex shedding occurs at slit liners with a slit width of $1\ mm$ (cf. Figure 2.6a). Furthermore, it was demonstrated that the dissipation of acoustic energy increased drastically when vortex shedding was present. This occurred at high SPL, or at lower SPL near resonance. The work concerned a 2D slit liner due to computational restrictions, however, and no grazing flow was present, as the validation experiment used a normal impedance tube.

2.2.1. Relevant parameters

Heuwinkel et al. [13] showed experimentally that vortex shedding is present in perforated, SDOF liners subjected to a grazing flow. Selected vorticity results from LDV and PIV visualisations are displayed in Figure 2.11. Note that the vorticity can not be calculated as $\omega_z = \partial v/\partial x - \partial u/\partial y$ using the instantaneous velocity field (u, v), as LDV provides point-wise velocity measurements. Instead, the vorticity is calculated using the amplitude of the fluctuating velocity components, as shown in Equation 2.9a. For the LDV, these fluctuation components are extracted by calculating the cross-spectral density function between the velocity and loudspeaker signals. An in-depth explanation of this technique is also presented by Léon et al. [26]. For the PIV measurements, phase-locked measurements were taken and sinusoidal fluctuations were assumed. The fluctuations were then extracted by comparing two phases separated by a half period. The fluctuating velocity field associated to a phase ϕ (in radians) can then be expressed in vector form as in Equation 2.9b. A sinusoid was fitted to 18 phase angles, which allowed to extract the amplitude.

$$\omega_z = \frac{\partial|\tilde{v}|}{\partial x} - \frac{\partial|\tilde{u}|}{\partial y} \tag{2.9a}$$

$$\tilde{\mathbf{u}}(\mathbf{x}, \phi) = -\tilde{\mathbf{u}}(\mathbf{x}, \phi + \pi) = \frac{1}{2}\big(\langle \mathbf{u}(\mathbf{x})\rangle_{\phi} - \langle \mathbf{u}(\mathbf{x})\rangle_{\phi+\pi}\big) \tag{2.9b}$$

The resulting visualisations in the absence and presence of a grazing flow are shown in Figure 2.11. From the acoustic measurements (cf. Figure 2.5), the grazing flow case showed a higher dissipation coefficient, both in the broadband excitation range of the LDV study and at the tonal $f = 992Hz$ used in the PIV measurements. This is confirmed in both aerodynamic studies, as the vorticity is much stronger, and the regions where a high vorticity is observed is much larger in the grazed case than in the no-flow case. Note that the LDV study was performed with 11 tones at $105\ dB$, whereas the PIV measurements were taken with a tonal $125\ dB$ due to differences in the experimental set-ups.

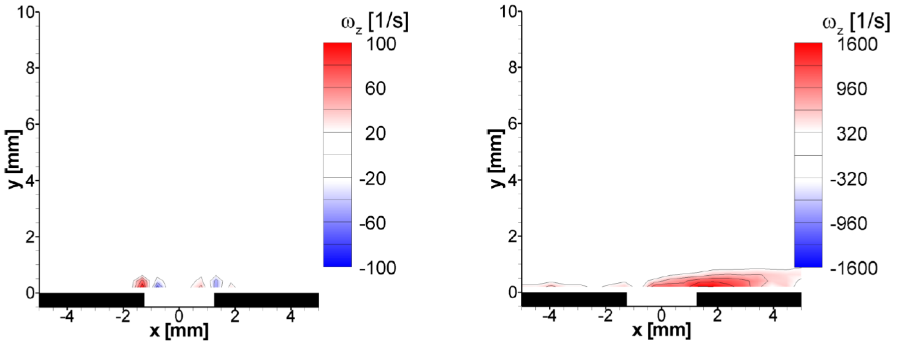

(a) LDV, no-flow

(b) LDV, grazing flow

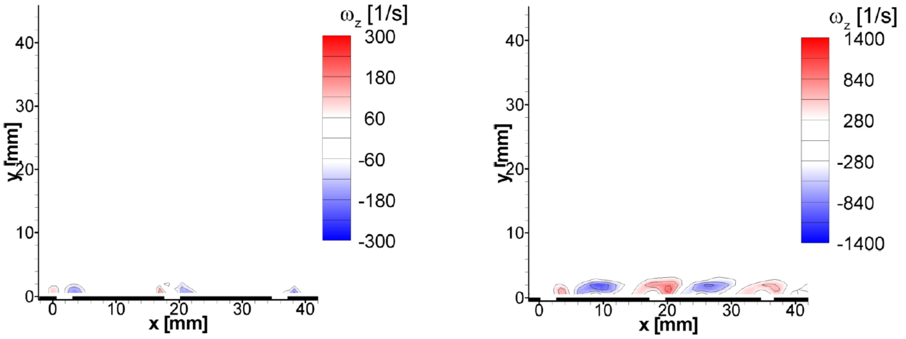

(c) PIV, no-flow

(d) PIV, grazing flow

Figure 2.11: Experimental results of Heuwinkel et al. [13]. LDV measurements performed at 11 tones at $105\ dB$, PIV recorded with a tonal $f = 992\ Hz$ at $125\ dB$. $f_0 \approx 900\ Hz$. Grazing Mach number $M_0 = 0.1$.

What can also be observed in Figure 2.11, however, is that the structures that are visible differ in size between the LDV and PIV measurements. The highest non-zero vorticity in the no-flow case is seen at $y \approx 0.6\ mm$ in the LDV results, but at $y \approx 2.1\ mm$ in the PIV measurements. Similarly, for the grazing flow, the 'height' of the vortical structures is $y \approx 0.9\ mm$ and $y \approx 3.5\ mm$ for LDV and PIV, respectively. The color scales used are very similar for the grazing flow results, whereas the scale used for the no-flow cases is larger for PIV. Clearly then, the regions of high vorticity are larger in the PIV measurements than in the LDV tests, for both flow cases. Several explanations for this observation can be looked for:

1. Firstly, as a general remark, both studies were performed in different facilities. Therefore, grazing flow conditions and errors from data acquisition may differ. Such systematic differences could result in a bias error between the two results, but this can not be evaluated here.
2. Heuwinkel et al. [13] suggest that the difference in SPL used in the LDV and PIV measurements could result in non-linearity. Maximum x and y velocities in the domains of Figure 2.11 are scaled with the excitation (far field) velocity, and compared by Heuwinkel et al. [13]. It is shown that differences up to a factor 10 remain between the scaled velocities resulting from LDV and PIV. As linear scaling does not account for the difference from the forcing levels, it can be argued that a non-linear liner response may be present. Maximum (scaled) velocities were higher in the LDV results, however, which would not explain the higher vorticity values in the PIV results. Furthermore, the dissipation coefficient did not change in any of the test cases when raising the SPL from 100 to $125\ dB$ at a tonal $f = 992\ Hz$ [13]. This therefore suggests a linear response of the liner.
3. The LDV measurements used a multi-tonal excitation, whereas the PIV measurements were excited with a tonal signal. While not stated explicitly, it is expected that the LDV's SPL of 105 is the sound level per tone. Therefore, following Equation 2.1, a higher effective sound pressure level is expected than the $105\ dB$ listed for the LDV tests. This would reduce the difference in vorticity caused by the higher SPL used in the PIV tests.
4. A sinusoidal fluctuating velocity component was assumed in the extraction of the acoustic fluctuation components in the PIV study. This was shown in Equation 2.9b. More recent studies have shown that this does not hold for higher sound pressure levels [27, 58, 60], or in the case of a turbulent grazing boundary layer [60]. This is demonstrated in more detail in subsection 2.2.3. Fitting a sinusoidal function and extracting the velocity fluctuating amplitude from this fit would then yield an erroneous velocity result. This problem could be circumvented by subtracting a time-averaged velocity field from a phase-averaged velocity field to find the velocity fluctuations associated to that phase [25].
5. Calculating the vorticity based on the fluctuating velocity components ignores any mean gradients present, which are clearly present in a turbulent boundary layer. This should not explain the differences between the LDV and PIV results, however, as all images in Figure 2.11 calculate the vorticity in the same way; only the methods of extracting the fluctuating component differ between the two measurement techniques.
6. Standard double-pulse PIV generally under-predicts the velocity magnitude in curved flows, as straight paths are assumed for the particle displacement. As a result, the vorticity derived from this velocity is also lower [39]. This can not explain the higher vorticity observed here, however.

From the above, no clear conclusion can be drawn. The differences in tonal or multi-tonal forcing, errors from the vorticity calculation and the bias of PIV towards lower vorticity values are not expected to explain the higher vorticity in the PIV results. The other explanations given, due to general differences between the two set-ups, the sound pressure level and the extraction of the velocity fluctuations in the PIV results are all deemed plausible. Of these three, the effect of the sound pressure level can be discussed in more depth.

The effect of the SPL is clearly demonstrated in the numerical study by Zhang and Bodony [58], of which selected results are shown in Figure 2.12. At the lowest grazing flow Mach number and SPL shown in Figure 2.12a, one counter-rotating vortex pair is seen ejected from the orifice. Increasing the SPL to $150\ dB$ in Figure 2.12b shows larger and more vortices that are ejected. Similarly, the resistance increased from $\theta/\sigma \approx 0.1$ to $\theta/\sigma \approx 1$. This large influence, both on the flow field and the normalized acoustic resistance could indicate how the PIV results of Heuwinkel et al. [13] were affected by the higher SPL.

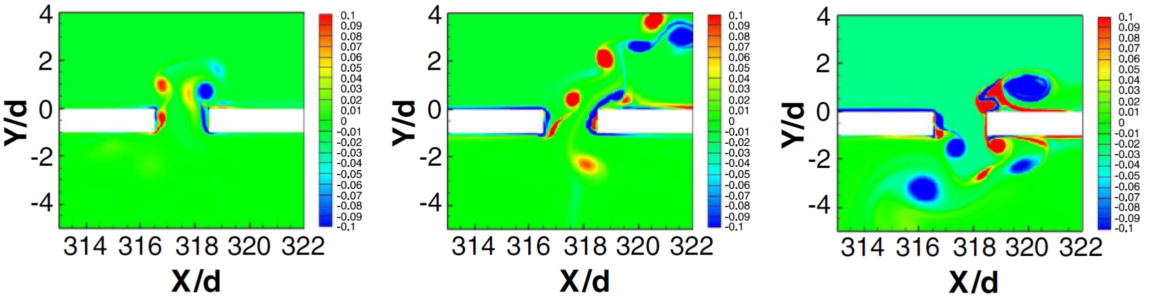

(a) $M_0 = 0.15,\ 130\ dB$ (b) $M_0 = 0.15,\ 150\ dB$ (c) $M_0 = 0.5,\ 150\ dB$

Figure 2.12: Instantaneous vorticity contours, all at $f = 500\ Hz$ with $f_0 \approx 3\ kHz$. Images from Zhang and Bodony [58]

The vortices from the downstream orifice edge, with $\omega_z < 0$, are seen to 'roll' over the edge in Figure 2.12b. As a result, non-circular structures are seen. Another downstream influence is seen in the thin layer of positive vorticity. The steady shear of a boundary layer would result in a constant, negative vorticity, which is also observed in the upstream part of the wall in Figure 2.12b. The downstream part, however, shows a clear disturbance with respect to this condition. This effect is further increased when moving to a higher grazing flow Mach number in Figure 2.12c. At $M_0 = 0.5$, the vortices from the upstream wall merge with those from the downstream wall, making for more complex flow structures that stay closer to the wall. The resistance is further increased between figures 2.12b and 2.12c, to $\theta/\sigma \approx 1.3$.

The numerical studies discussed so far all used a laminar boundary layer, while the liners in aero-engine ducts are subjected to a turbulent grazing boundary layer. Zhang and Bodony [60] present direct numerical simulation (DNS) results using both laminar and turbulent boundary layers to address the differences. In figures 2.13a and 2.13b, the differences can be qualitatively observed. Stronger vortex shedding is observed in the turbulent case. The increase in vorticity within the cavity is a result of increased in- and outflow through the orifice: in-orifice peak velocity is increased by a factor two when a turbulent boundary layer is considered in stead of a laminar one. In the laminar case, the different vortices can be distinguished more easily, whereas the vortices in the turbulent case merge at the downstream orifice edge and stay closer to the wall. In the laminar boundary layer, the ejected vorticity is strong enough to trip the boundary layer to turbulence at $160\ dB$: Figure 2.13c shows an x-z slice just above the liner face sheet, where a turbulent wedge with a half-angle of 9^o is visible.

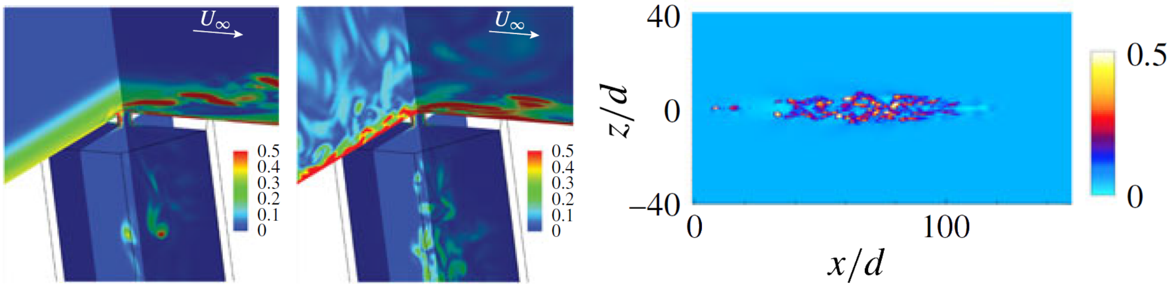

(a) Laminar boundary layer (b) Turbulent boundary layer (c) Laminar boundary layer, x-z plane at $y = 2d$ above the liner. Image has been cropped w.r.t. the original to only show the downstream part

Figure 2.13: Outflow vorticity visualisations, SPL = $160\ dB$, $M_0 = 0.5$ and $f = 3\ kHz$, slices at $x = 0$ and $z = 0$. Numerical results from Zhang and Bodony [60].

Acoustically, the state of the grazing boundary layer increases the resistance, from $\theta\sigma \approx 0.02$ to $\theta\sigma \approx 0.055$ at $130\ dB$. At $160\ dB$, however, this difference is almost completely absent. Nevertheless, all aerodynamic and acoustic observations made by Zhang and Bodony [60] show that turbulence in the grazing boundary layer must be considered, as it is capable of making for a large impact on the results.

A final parameter that influences the occurrence of vortex shedding is displayed by Léon et al. [27]. Figure 2.14a shows the absorption coefficient of Equation 1.7. The two lowest sound pressure levels of 110 and $120\ dB$ show a nearly identical absorption spectrum, which indicates that $\theta_{NL} \approx 0$ in Equation 2.3a. At the two higher sound pressure levels, the absorption coefficient is increased as the higher forcing levels result in vortex shedding, leading to $\theta_{NL} > 0$. This effect is strongest near resonance. Léon et al. [27] denote this by introducing a dimensionless frequency parameter $\Omega_f = f/f_0 = \omega/\omega_0$. Near resonance, $\Omega_f = 1$ and the absorption is highest. Moving to lower frequencies, away from $\Omega_f = 1$, the absorption coefficient is drastically reduced.

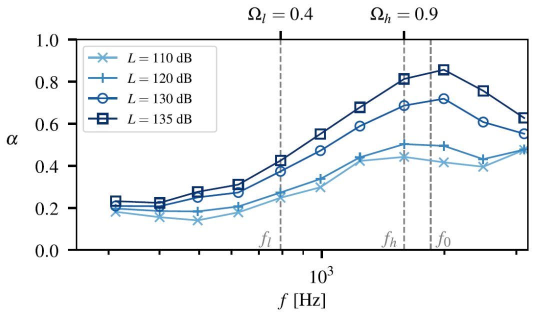

(a) Absorption coefficients and frequency identification

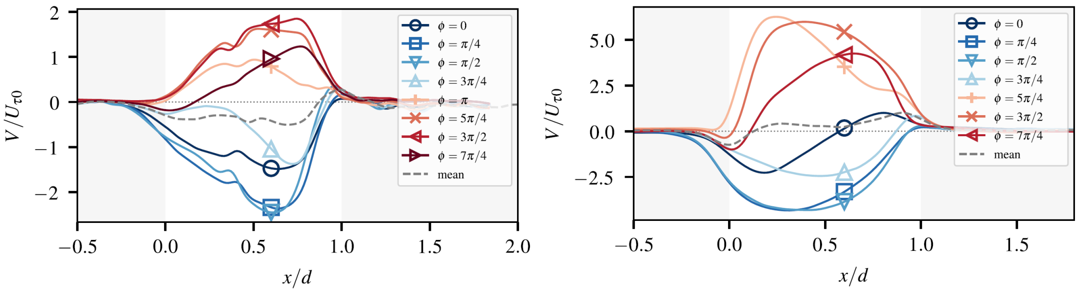

(b) $\Omega_f = 0.4$ (c) $\Omega_f = 0.9$

Figure 2.14: Phase-averaged vertical velocity distributions in the centre-plane of the orifice, $0.07d$ above the orifice. Non-dimensionalized by the friction velocity, $132\ dB$, $M_0 = 0.048$. Experimental results of Léon et al. [27].

This reduction in absorption can also be observed by looking at the in-orifice velocities in figures 2.14b and 2.14c. While these are result at the same sound pressure level and grazing flow Mach number, the in-orifice velocity amplitude at $\Omega_f = 0.9$ is approximately double that at $\Omega_f = 0.4$. Therefore, not only the sound pressure level, but also the forcing frequency has a large influence on the occurrence of vortex shedding, and thereby on the non-linear resistance term. Using the non-dimensional form of $\Omega_f = f/f_0$ allows to state that the resistance and absorption are highest for $\Omega_f \approx 1$, and lower when moving away from this value.

Concluding the above, it can be concluded that the parameters which influence the non-linear resistance term through vortex shedding are:

- The sound pressure level SPL
- The non-dimensional forcing frequency $\Omega_f = f/f_0 = \omega/\omega_0$.
- The grazing flow Mach number and associated level of turbulence, denoted by the amplitude of the turbulent velocity fluctuations in x: $|u'|$.

Qualitatively, these dependencies agree with the non-linear resistance term as modelled by Guess [10] (cf. Equation 2.7): the acoustic in-orifice velocity amplitude $|\widetilde{v}_{or}|$ is mainly dependent on the SPL and the forcing frequency, and the dependence on $|u'|$ is also directly visible. Next, a closer look is taken on function form for θ_{NL}, and on the modelling for the two terms $|\widetilde{v}_{or}|$ and $|u'|$.

2.2.2. Quantification of non-linearity

In the previous section, several observations can be made that suggest that occurrence and intensity of vortex shedding results from a combination of the in-orifice velocity amplitude $|\widetilde{v}_{or}|$ and the grazing flow velocity $U_0 = c_0 M_0$:

- In Figure 2.12, it was shown that the flow field around the orifice depends strongly on both the SPL and the grazing flow Mach number. At $M_0 = 0.15$ and $150\ dB$ (fig. 2.12b), vortices penetrated deep into the boundary layer. Reducing the SPL (fig. 2.12a) yields similar structures, but these dissipate much faster. Increasing the grazing flow Mach number (fig. 2.12c) results in larger vortices, which stay closer to the face sheet.
- Recall that Zhang and Bodony [60] stated that the influence of the grazing boundary layer was highest when the sound pressure was $130\ dB$, and lowest when an SPL of $160\ dB$ was used.
- In Figure 2.14, the higher velocities at $\Omega_f = 0.9$ also showed a more symmetric distribution in the orifice, whereas more asymmetric profiles are observed at $\Omega_f = 0.4$.

The velocity scale for the in-orifice flow is generally taken as the amplitude or RMS of the fluctuating velocity, i.e. $|\widetilde{v}_{or}|$ or $|\widetilde{v}_{or}|_{rms}$. For the grazing flow, Zhang and Bodony [60] and Kooi and Sarin [21] suggest that the flow in the orifice, near the facesheet is driven by the shear stress exerted by the grazing boundary layer. This is visualized in Figure 2.15a: at a low SPL of $130\ dB$ and grazing flow Mach number of $M_0 = 0.5$, the instantaneous streamline pattern shown resembles that of a lid-driven cavity. The driving force is then the shear stress over the orifice. The associated velocity scale is the friction velocity u_τ, defined in Equation 2.10.

$$u_\tau = \sqrt{\tau_w/\rho_0} \tag{2.10}$$

This shear stress is dominant when $u_\tau \gg |\widetilde{v}_{or}|_{rms}$. When the SPL is raised to $160\ dB$ in Figure 2.15b, the effects from the acoustic forcing dominate that of the grazing flow, i.e. $u_\tau \ll |\widetilde{v}_{or}|_{rms}$, and the lid-driven cavity analogy fails. Besides the phase-averaged flow fields, the time-averaged flow in the orifice at low SPL, shown in Figure 2.15c, also resembles that of a lid-driven cavity.

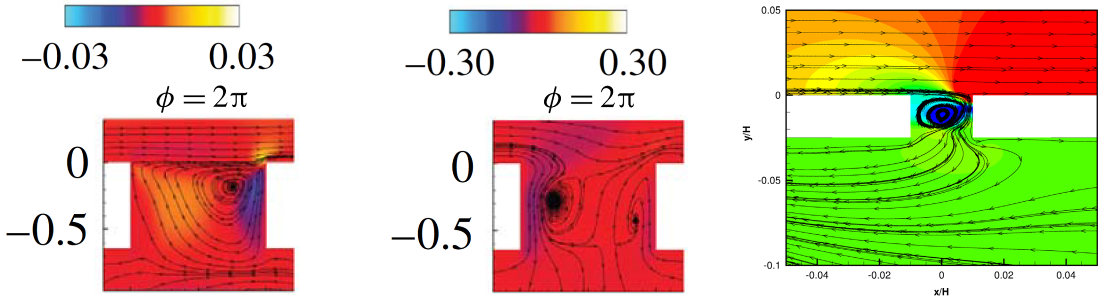

(a) Phase-averaged streamlines in the orifice at the beginning of the inflow cycle, $M_0 = 0.5$ (turbulent), $f = 3\ kHz$, SPL = $130\ dB$, $f_0 \approx 1.1\ kHz$. Numerical results from Zhang and Bodony [60].

(b) Phase-averaged streamlines in the orifice at the beginning of the inflow cycle, coloured by $\widetilde{v}/c_0$. $M_0 = 0.5$ (turbulent), $f = 3\ kHz$, SPL = $160\ dB$, $f_0 \approx 1.1\ kHz$. Numerical results from Zhang and Bodony [60].

(c) Time-averaged streamlines in the orifice, coloured by $\widetilde{v}/c_0$. $M_0 = 0.3$, $f = 1\ kHz$, SPL = $140\ dB$. Numerical results from Tam et al. [48].

Figure 2.15: Lid-driven cavity analogies from literature, which demonstrate that the grazing boundary layer is characterized by the wall shear stress, and hence the friction velocity.

These observations are continued upon by Léon et al. [27]: Figure 2.16 shows the velocity RMS profiles just above the orifice for different grazing flow Mach numbers. Note that the velocity is evaluated slightly above the orifice, hence it is denoted $\widetilde{v}$ in stead of $\widetilde{v}_{or}$, but it is expected that these should have similar values. In Figure 2.16a, it can be seen that an increase in M_0 makes for a slight increase in the velocity RMS. Also, a strong asymmetry is induced by the boundary layer. In Figure 2.16b, however, it can be seen that this increase in velocity grows only slowly with the grazing velocity, here characterized by the friction velocity. As a result, the relative strength of the forcing, characterized here by $|\widetilde{v}_{or}|_{rms}$, decreases with respect to the influence of the grazing flow, characterized by u_τ. Furthermore, it can be seen that the in-orifice flow is more symmetric when $|\widetilde{v}_{or}|_{rms}/u_\tau$ is high.

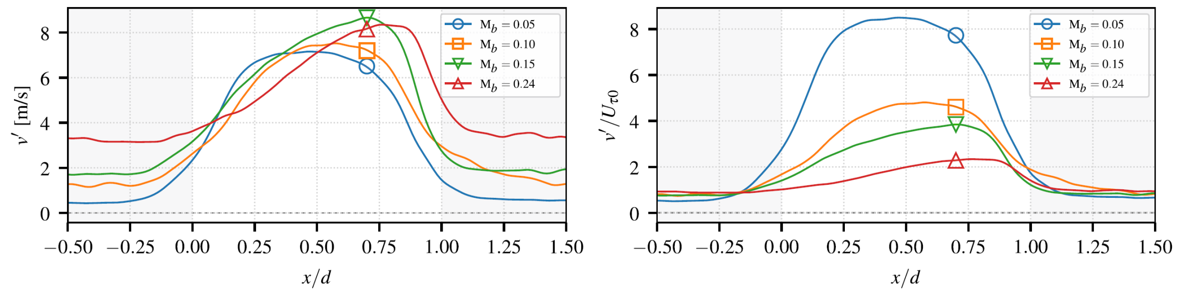

(a) Absolute: $|\widetilde{v}|_{rms}$

(b) Relative: $|\widetilde{v}|_{rms}/u_\tau$.

Figure 2.16: $|\widetilde{v}|_{rms}$ in the centre-plane of the orifice, $0.07d$ above the orifice. Excitation is multi-tonal, at an SPL per tone of $132\ dB$. Experimental results of Léon et al. [27].

The previous results then indicate that the occurrence of vortex shedding depends on the balance between the in-orifice and friction velocity scales. This concept has been demonstrated by previous sources in literature. Tam and Kurbatskii [46] and Zhang and Bodony [59] mention for all of their cases whether vortex shedding was observed. This allows for a distinction based on the forcing frequency and sound pressure level, shown in figures 2.17a and 2.17b. Note that both studies did not incorporate a grazing flow. It can be seen that vortex shedding can occur at sound pressure levels as low as $130\ dB$, provided that the forcing is near resonance, i.e. for $\Omega_f = f/f_0 \approx 1$. Away from resonance, shedding occurs only for higher sound pressure levels. It should be remembered here that the forcing frequency and SPL together make for an in-orifice velocity. An $SPL - f$ plot, in the absence of a grazing flow, can thus also be seen as a contour plot of $|\widetilde{v}_{or}|_{rms}$.

Alternatively, the vortex shedding itself can be characterized by the ratio between the in-orifice and friction velocities, $|\widetilde{v}_{or}|_{rms}/u_\tau$. This is demonstrated in an acoustic sense by Kooi and Sarin [21] and from an aerodynamic perspective by Léon et al. [27], in figures 2.17c and 2.17d, respectively. Kooi and Sarin [21] show that in their experiments, the non-linear resistance term θ_{NL} started to be apparent for $|\widetilde{v}_{or}|/u_\tau > 4$ (NB: amplitude), whereas they mention that Goldman [9] found a threshold at $|\widetilde{v}_{or}|/u_\tau = 3$. Below this value, the resistance is a constant, which is shown to be modelled well by the viscous term of Equation 2.3a. Furthermore, Figure 2.17c shows that for the low grazing Mach number $M_0 = 0.15$, a linear relation between θ_{NL} and $|\widetilde{v}_{or}|/u_\tau$ holds well for $|\widetilde{v}_{or}|/u_\tau > 4$. Tests were performed at higher Mach numbers, but these all remained below the threshold of non-linear behaviour and are therefore excluded here.

Alternatively, Léon et al. [27] look in flow field recordings whether vortex shedding was visually observed. They find a threshold at $|\widetilde{v}_{or}|_{rms} = 5$ (NB: RMS), higher than the other values reported [9, 21]. Nevertheless, it shows that $|\widetilde{v}_{or}|_{rms}/u_\tau$ makes for a non-dimensional metric whose value determines whether non-linear behaviour is present, and which quantitatively affects the non-linear resistance. While the amplitude can be used similarly, the RMS value is taken here, as it is a more intuitive metric for non-sinusoidal velocity fluctuations. The two velocities in the ratio depend on the aero-acoustic environment, defined by the forcing SPL and frequency, and the grazing flow Mach number. It remains to be determined how the individual terms, i.e. $|\widetilde{v}_{or}|_{rms}$ and u_τ, relate to the the SPL, frequency and grazing flow Mach number. This would then allow to determine the dependency of θ_{NL} on these input parameters. The next two sections will further look into these points.

2.2.3. In-orifice flow and velocity scales

In previous sections, the influence of the sound pressure level and non-dimensional forcing frequency Ω_f on the in-orifice velocity was visible. Further in-orifice flow details from literature are discussed below. Firstly, the in-orifice flow asymmetry is discussed. In figures 2.14, 2.15 and 2.16b, it could be seen that the presence of a grazing boundary layer makes for an asymmetric in-orifice flow velocity distribution. This is visualized in more detail by Zhang and Bodony [60] in Figure 2.18. In the no-flow case, an axially symmetrical velocity profile is observed in the orifice. In the two cases with a grazing boundary layer, this no longer holds: inflow is concentrated on the downstream part of the orifice, whereas the outflow is distributed more evenly over the orifice. This agrees to the results of Léon et al. [27] in Figure 2.16: for a high $|\widetilde{v}|_{rms}/u_\tau$, a nearly symmetrical distribution over the orifice is seen, whereas a low ratio results in the fluctuations being concentrated on the downstream part of the orifice.

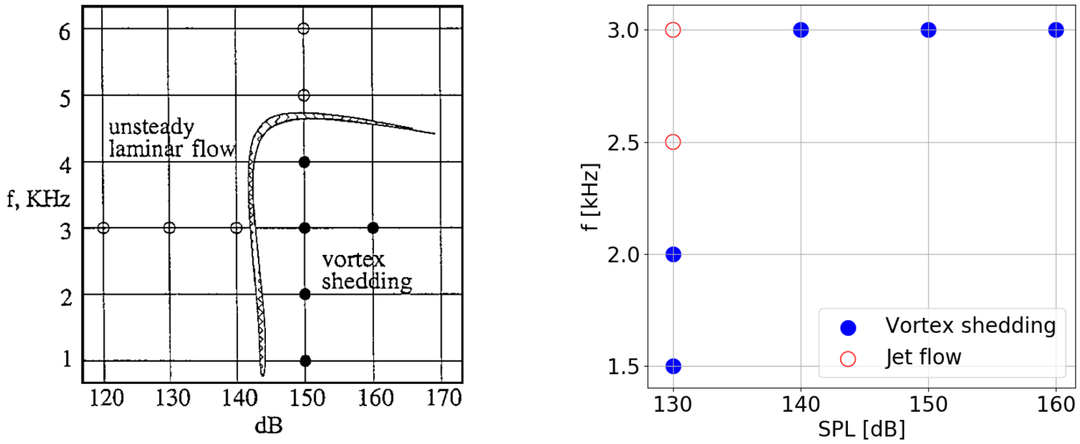

(a) Forcing frequency versus sound pressure level. Numerical results, image taken from Tam and Kurbatskii [46]. $f_0 \approx 3; kHz$ [46], although later experiments showed $f_0 \approx 1; khz$ [49].

(b) Forcing frequency versus sound pressure level. Numerical results from Zhang and Bodony [59]. $f_0 \approx 1.1; kHz$.

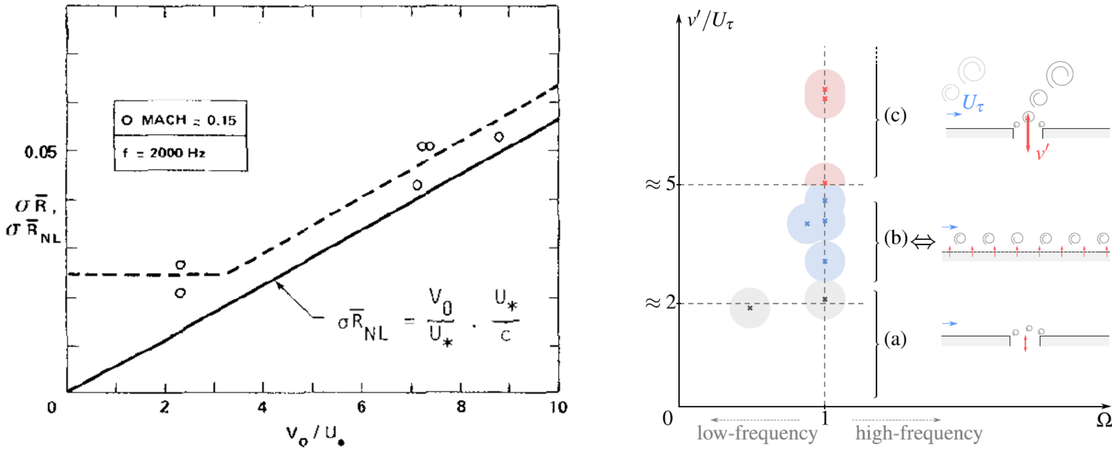

(c) Non-linear normalized acoustic resistance (with viscous term from Equation 2.3a subtracted) versus orifice-to-friction velocity ratio. Experimental results, image adapted from Kooi and Sarin [21]. $f_0 \approx 2.2\ kHz$.

(d) Orifice-to-friction velocity ratio versus non-dimensional forcing frequency. Experimental results, image taken from Léon et al. [27].

Figure 2.17: Classification schemes from literature for the distinction between non-linear cases where vortex shedding occurs, and linear cases where shedding is not observed.

This asymmetry is also visible in the time-dependent orifice velocity from Zhang and Bodony [60], shown in Figure 2.19. Without a grazing flow, the three probe locations show an identical, sinusoidal velocity over time. When a laminar grazing boundary layer is present, in Figure 2.19b, it can be seen that the downstream probe shows a larger amplitude, mostly due to the inflow phase. This observation holds in the turbulent case in Figure 2.19c, but the signal becomes less smooth, due to the strong influence of the turbulent fluctuations. When the SPL is increased from $130\ dB$ to $160\ dB$ in Figure 2.19d, a more periodic signal is observed, as the acoustic signal becomes stronger with respect to the effects from the grazing flow. Note, however, that the signal is still non-sinusoidal here for all three probes.

In figures 2.18 and 2.19 it can also be observed that the in-orifice velocity amplitude increases when a laminar grazing flow is present, with respect to a no-flow case. When the grazing flow is turbulent, another large increase in amplitude can be seen. The characteristic velocity associated to turbulence is the RMS of the turbulent, axial velocity fluctuations, $|u'|_{rms}$.

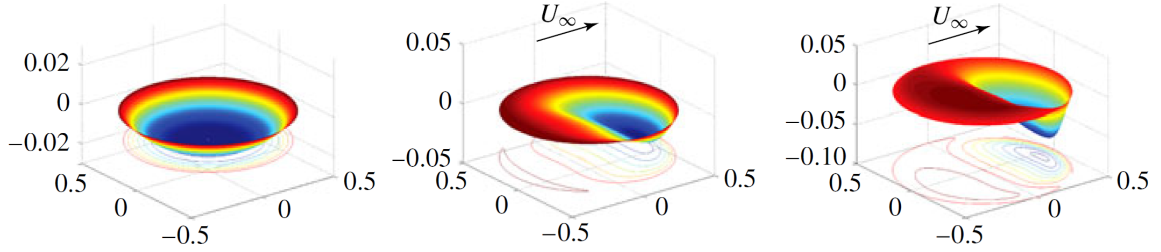

(a) No flow, in (b) Laminar boundary layer, in (c) Turbulent boundary layer, in

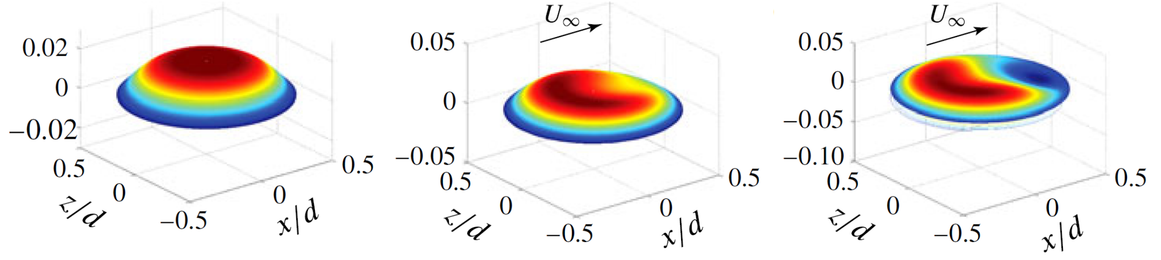

(d) No flow, out (e) Laminar boundary layer, out (f) Turbulent boundary layer, out

Figure 2.18: In- and outflow average velocity distribution, with $M_0 = 0.5$, $f = 3\ kHz$, SPL= $130\ dB$. Numerical results from Zhang and Bodony [60].

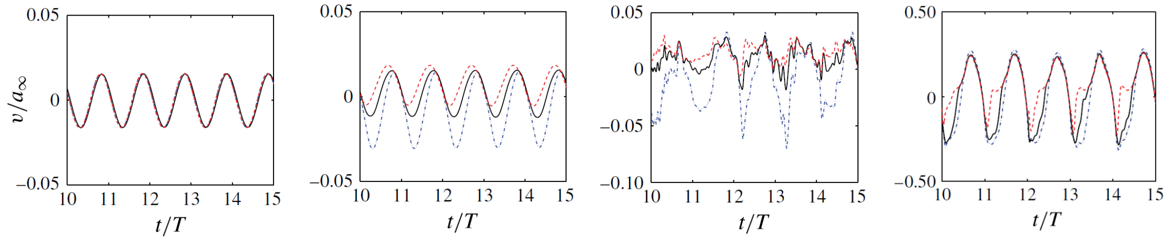

(a) No flow, $130\ dB$ (b) Laminar boundary layer, $130\ dB$ (c) Turbulent boundary layer, $130\ dB$ (d) Turbulent boundary layer, $160\ dB$

Figure 2.19: Time-signals of in-orifice velocity in the centre (black curve), $0.36d$ upstream (red) and $0.36d$ downstream (blue) of the centre, with $M_0 = 0.5$, $f = 3\ kHz$ and SPL as labelled. Numerical results from Zhang and Bodony [60].

Zhang and Bodony [60] show that in their simulations, the in-orifice velocity amplitude $|\widetilde{v}_{or}|$ can then be modelled well by superposition of three velocity scales: one scale for the liner response, modified by two terms that account for the turbulence level and friction velocity of the grazing boundary layer. This translates to a lumped velocity response for a Helmholtz resonator $|\widetilde{v}_{or}|_{lumped}$, the turbulent velocity scale $|u'|_{rms}$, and the friction velocity u_τ of Equation 2.10. This superposition is shown in Equation 2.11a, along with the curve-fitted coefficients found by Zhang and Bodony [60]. The lumped Helmholtz response is taken from Morse and Ingard [32], and is shown in Equation 2.11b. Here, the RMS of the incident pressure fluctuations can be found from the sound pressure level using Equation 2.11c [27], with p_{ref} an acoustic reference pressure of $20\mu Pa$. τ^* is the facesheet thickness, with end corrections as in subsection 1.2.1. The ω_0/ω terms can be recognised as the inverse of the dimensionless forcing frequency, i.e. $1/\Omega_f$. Finally, Q is the quality factor, with a typical value of $Q = 10$ [60]. Léon et al. [27] show that for a lumped-element model, the quality factor can be expressed as in Equation 2.11d.

$$|\tilde{v}_{or}|_{Zhang} = |\tilde{v}_{or}|_{lumped} + A|u'|_{rms} + Bu_\tau = |\tilde{v}_{or}|_{lumped} + |u'|_{rms} + 0.6u_\tau \tag{2.11a}$$

$$\text{with:} \quad |\tilde{v}_{or}|_{lumped} = \frac{|\tilde{p}|_{rms}}{\rho_0\omega\tau^*}\frac{1}{\sqrt{\left[\left(\frac{\omega_0}{\omega}\right)^2 - 1\right]^2 + \left[\frac{\omega_0}{\omega Q}\right]^2}} \tag{2.11b}$$

$$|\tilde{p}|_{rms} = p_{ref}10^{\mathrm{SPL}/20} \tag{2.11c}$$

$$Q_{lumped} = \frac{\omega_0\tau}{c_0\sigma\theta} \tag{2.11d}$$

Zhang and Bodony [60] use Equation 2.11b in a high-frequency approximation, where $\omega/\omega_0 = \Omega_f \gg 1$, and hence $|\tilde{v}_{or}|_{lumped} \approx |\tilde{p}|_{rms}/(\rho_0\omega\tau^*)$. In their case, however, $\Omega_f \approx 3$, and $|\tilde{v}_{or}|_{lumped} \approx 0.3|\tilde{p}|_{rms}/(\rho_0\omega\tau^*)$, using the typical value of $Q = 10$ they mention. The validity of this high-frequency assumption is therefore deemed questionable. Léon et al. [27] compare the predicted velocity amplitudes of equations 2.11a and 2.11b to experimentally measured amplitudes. They show that the scale suggested by Zhang and Bodony [60] drastically over-predicts the amplitude, and that the simple lumped response of Equation 2.11b is a much better approximation instead. Comparing the two works, several explanations may be posed for this difference:

Quality factor Q: a large quantitative difference is in how the two papers use Equation 2.11b. As mentioned, Zhang and Bodony [60] use the high-frequency approximation, and mention that typically $Q = 10$, whereas Léon et al. [27] use the full expression with a fixed $Q = 1$: they discuss how Q reduces from its typical value of $Q \approx 10$ to $Q \approx 1$ due to the presence of a grazing flow. This is due to the vena contracta effect, visualized in Figure 2.20: when the SPL and grazing flow velocity are low, no restriction is formed due to in-orifice flow effects, and the typical value of $Q \approx 10$ may be expected. When a strong grazing flow is present, flow separation occurs from the upstream orifice wall, as sketched in Figure 2.20b. As a result, the effective open area is reduced, which increases the resistance (see Section 2.1). Following Equation 2.11, a reduction in Q then results, followed by an increase in $|\tilde{v}_{or}|_{lumped}$. Léon et al. [27] mention that a high SPL may result in a similar phenomenon, sketched in Figure 2.20c: at high sound pressure levels, the in-orifice flow velocity is high enough such that recirculation is seen at both orifice walls. Note that these two effects seem to resemble the effects from $|u'|_{rms}$ and $|\tilde{v}_{or}|$ in the non-linear resistance θ_{NL} (cf. Equation 2.7).

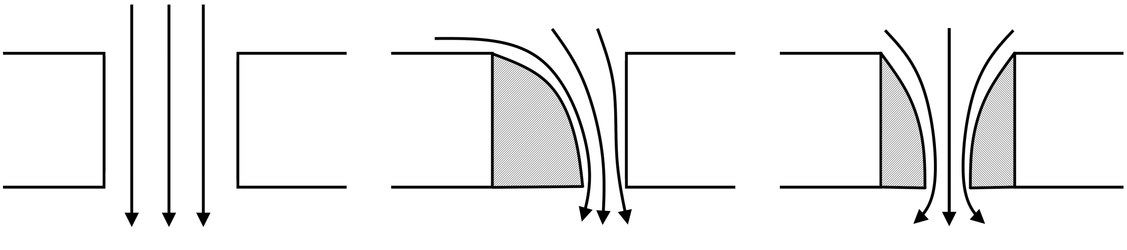

(a) Low SPL and no grazing flow: no restriction (cf. Figure 2.6c).

(b) High M_0: separation from upstream wall (cf. Figure 2.15c).

(c) High SPL: separation from both walls (cf. Figure 2.6b).

Figure 2.20: Qualitative visualisation of effective open area reduction due to the 'vena contracta' effect, during inflow.

Zhang and Bodony [59] relate this vena contracta effect quantitatively to the discharge coefficient C_D, defined in Equation 2.12. This coefficient shows the effect of the in-orifice boundary layers: when no boundary layer is present, the displacement thickness $\delta^* = 0$, and $C_D = 1$. When the boundary layers completely fill the orifice, $\delta^* = d/2$, and $C_D = 0$.

$$C_D \approx \left(1 - \frac{2\delta^*}{d}\right)^2 \tag{2.12}$$

Zhang and Bodony [59] show that without a grazing flow, the average discharge coefficient indeed reduces for an increasing SPL. This can also be seen in their more recent results in Figure 2.21a [60], and would confirm the effect sketched in Figure 2.20c. Furthermore, these results also showed that at a fixed SPL, the addition of a grazing flow strongly reduces the discharge coefficient, as is expected from Figure 2.20b. What can also be seen, however, is that increasing the SPL increases the discharge coefficient when a strong boundary layer is present. This may suggest that the symmetric vena contracta effect of Figure 2.20c could reduce the single-sided effect of Figure 2.20b. This again shows the balance between the effects from the grazing flow and the sound pressure level, indicated by $|\widetilde{v}_{or}|_{rms}/u_\tau$.

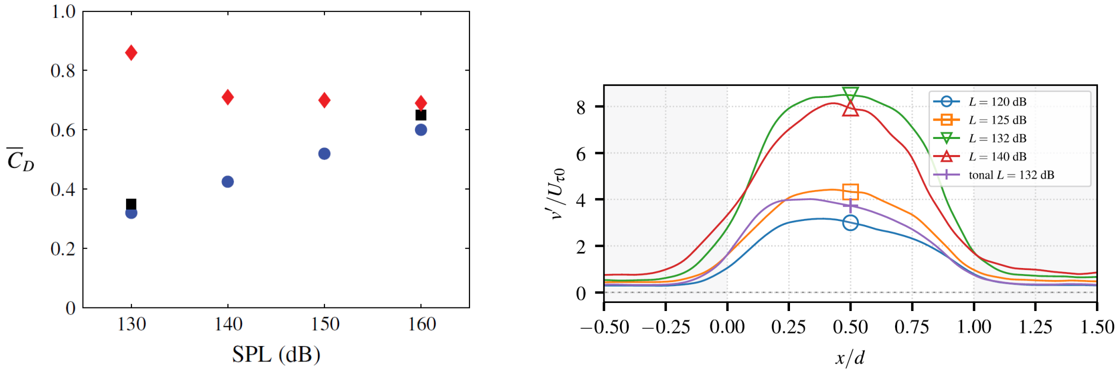

(a) Averaged discharge coefficient at $\Omega_f \approx 3$. Red diamonds: no grazing flow. Black squares: $M_0 = 0.5$ laminar boundary layer. Blue circles: $M_0 = 0.5$ turbulent boundary layer. Numerical results of Zhang and Bodony [60].

(b) $|\widetilde{v}|_{rms}$, $0.07d$ above the orifice, with $M_0 = 0/048$. Experimental results of Léon et al. [27].

Figure 2.21: Quantification of vena contracta effects

The omission of the second term in Equation 2.11b by Zhang and Bodony [60] may explain why this equation underpredicted the velocities in their numerical results, whereas Léon et al. [27] obtain decent results using the full expression with $Q = 1$. Following Equation 2.11 and the discussion above, a stronger vena contracta effect should increase the resistance, reduce Q and in turn increase the velocity scale $|\widetilde{v}_{or}|_{lumped}$. The results of Léon et al. [27] in Figure 2.21b seem to confirm this notion: these observed velocities are shown to be modelled moderately well with $Q = 1$, except that Equation 2.11b slightly under-predicted the vertical velocity RMS at low SPL, and over-predicted at high SPL. This suggests that Q should be increased for the low SPL case, and reduced at high SPL. Furthermore, a limit seems to be present between 132 and 140 dB. This may suggest that the vena contracta may reduce the effective area enough such that the orifice becomes 'choked', limiting the mass flow rate that can pass, and thereby reducing the aerodynamic influence of the resonator. In Figure 2.21a, the no-flow case also shows that the SPL$-C_D$ curve flattens at high SPL. These observations suggest that Equation 2.11b with a variable, possibly non-linear expression for Q could yield an accurate velocity scale prediction.

Preliminary analysis of tests performed by Van der Meulen [51] seems to qualitatively confirm that modelling the velocity scales with equation 2.11b is adequate at low grazing flow Mach numbers. Figure 2.22 shows several selected phase-averaged vorticity fields. It has been attempted to set the arbitrary phase $\phi = 0$ at the phase where vertical velocity, out of the orifice, is maximum. Large, separate vortical structures can be seen at 148 dB in Figure 2.22c, whereas only small near-orifice disturbances are seen at 130 dB in Figure 2.22a.

The friction velocity can be approximated using Prandtl's friction law for smooth ducts, discussed in more detail in subsection 2.2.4. Following equations 2.11b and 2.13, the modelled velocity scales for these measurements are listed in Table 2.1. The last column shows the expected phenomenon based on the distinction suggested by Léon et al. [27] in Figure 2.17d. Comparing Table 2.1 and Figure 2.22, qualitative agreement is observed. Further analysis is needed, however, to quantify the the actual velocities observed.

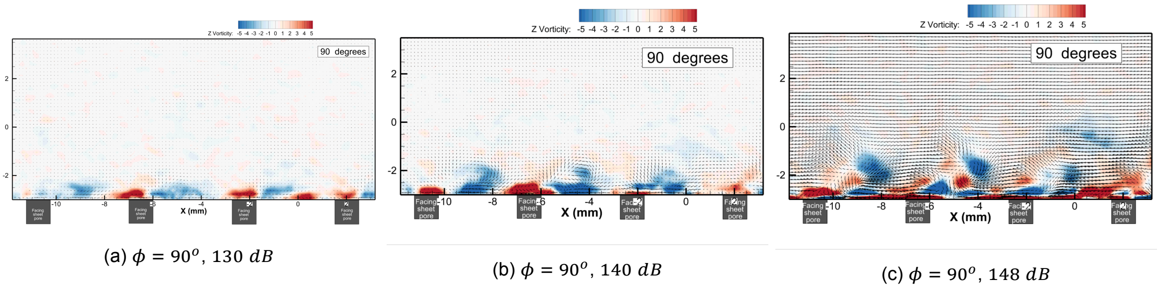

(a) $\phi = 90^o$, $130\ dB$ (b) $\phi = 90^o$, $140\ dB$ (c) $\phi = 90^o$, $148\ dB$

Figure 2.22: Phase-averaged vorticity results, with $M_0 = 0.1$, $\Omega_f \approx 0.9$ and SPL as labeled. Experimental results of Van der Meulen [51].

Table 2.1: Expected results for the experiments of Van der Meulen [51], following the work of Léon et al. [27].

SPL	$\|\widetilde{v}_{or}\|_{lumped}$	$\|\widetilde{v}_{or}\|_{lumped}/u_\tau$	Case (see Figure 2.17d)
130	1.67	1.23	a: localized effects
140	5.27	3.86	b: intermediate region
148	13.23	9.78	c: vortex shedding

Flow conditions tested: another big difference is found in the flow conditions tested by the studies of Zhang and Bodony [60] and Léon et al. [27]. The grazing flow Mach numbers tested by Léon et al. [27] are limited to $M_0 \leq 0.24$, whereas Zhang and Bodony [60] go up to $M_0 = 0.5$ conditions. Furthermore, impedance data is missing for the measurements of Léon et al. [27]. These limits hinder the evaluation of the sensitivity of the resistance to the grazing flow Mach number, and it is not known if the conclusions and suggestions made by Léon et al. [27] hold at high Mach numbers.

Velocity evaluation: Zhang and Bodony [60] are able to evaluate the velocity truly in the orifice. Here, the vena contracta effects of Figure 2.20 are expected to be strongest. Léon et al. [27] are restricted to evaluating the velocities just outside the orifice due to their use of PIV. Velocities might be lower here, due to the reduced influence of the vena contracta, and as the flow from the orifice is expanded into the much larger volume of the boundary layer. Further quantitative evaluation of numerical results could provide insight in how $|\widetilde{v}_{or}|_{rms}$ and $|\widetilde{v}|_{rms}$, just above the orifice, relate, and whether the assumption $|\widetilde{v}_{or}|_{rms} \approx |\widetilde{v}|_{rms}$ is valid.

Geometrical differences and friction velocity: finally, the geometries tested by both studies differ. Léon et al. [27] use a typical SDOF liner panel, whereas Zhang and Bodony [60] use a geometry reduced to a single resonator with a single orifice. This requires the assumption that the orifices respond independently. Tam et al. [47] note, however, that orifices may interact through the shedded vortices. This can be demonstrated with Figure 2.23: Tam et al. [48] show that the ejected vortices can remain in the grazing boundary layer for a long downstream distance. This could affect downstream orifices, as well as the boundary layer characteristics. As this is associated to the grazing flow, these interactions mechanisms are discussed in the next section which concerns the friction velocity.

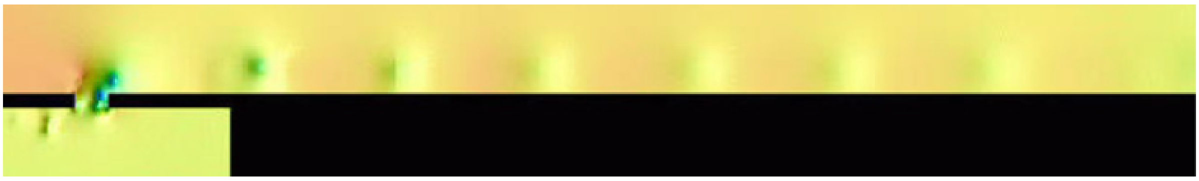

Figure 2.23: Vortex transport due to a $M_0 = 0.3$ grazing flow, instantaneous density field, image adapted from Tam et al. [47].

2.2.4. Friction velocity and interaction between orifices

The wall shear stress $\tau_w = \mu[\partial u/\partial y]_{y=0}$ can be extracted directly from DNS simulation results, as the mesh provides sufficient resolution up to the wall. This allows to evaluate the friction velocity directly. In experimental studies as performed by Léon et al. [27], the PIV resolution is too coarse to evaluate the shear stress, hence the friction velocity, directly. Léon et al. [27] find the global friction velocity using Prandtl's friction law for duct flow, shown in Equation 2.13. Here, Re_{D_h} is the Reynolds number based on the duct's hydraulic diameter.

$$\frac{U_0}{\sqrt{8}u_\tau} = 2 * log_{10}\left(Re_{D_h}\frac{\sqrt{8}u_\tau}{U_0}\right) - 0.8 \tag{2.13}$$

Two important limitations of this friction law must be considered. Firstly, its region of validity is $3.1\times10^3 < Re_{D_h} < 3.2\times10^6$ [30]. For the duct of Léon et al. [27], where $D_h = 50\ mm$, this corresponds to an upper limit of $M_0 = 2.7$, which is sufficient. More important in the current discussion, however, is the fact that the liner is not a smooth, closed wall. Léon et al. [27] validate the friction law in their case by comparing experimentally obtained boundary layer profiles above a smooth wall and above the installed liner. All profiles collapse in wall units: the boundary layers over the liner follow the law of the wall and log-law. Based on this, they conclude that the friction law of Equation 2.13 suffices to model the global friction velocity u_τ.

Léon et al. [27] also show, however, that the aero-acoustic interaction at the forced liner surface can seriously affect the boundary layer profiles, which is shown in Figure 2.24. They show in Figure 2.24a that at high M_0, but low $|\tilde{v}_{or}|/u_\tau$, the boundary layer can be modelled well with a log-law with uniform injection. The other case however, with a high $|\tilde{v}_{or}|/u_\tau$, shows large deviations from these theoretical profiles. This can be seen in Figure 2.24b. Furthermore, Léon et al. [27] show that a roughness analogy is incapable of accounting for these distortions. From these disturbances, it can be argued that the friction law in Equation 2.13 is insufficient to model the global friction velocity u_τ. Léon et al. [27] also mention explicitly that the aero-acoustic response of the liner is expected to to affect the friction velocity. They mention more sophisticated methods which fit a log-law to the experimental data, but it can be expected that these would also fail to extract the correct friction velocity, as the boundary layer no longer resembles a log-law.

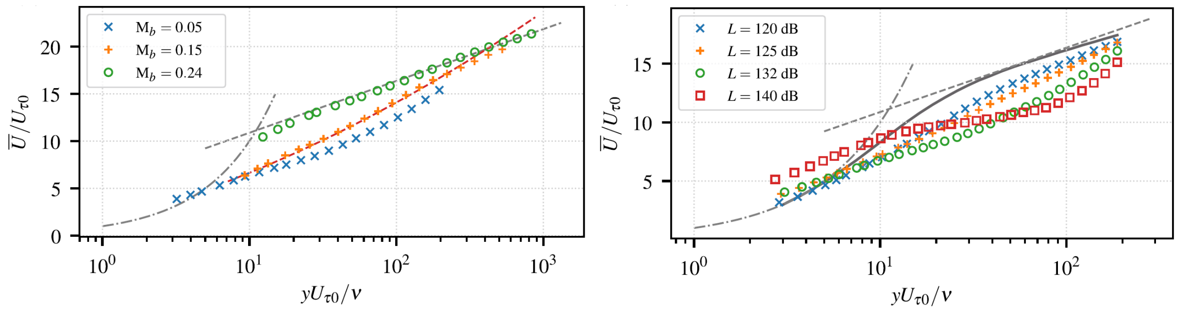

(a) With multi-tonal forcing, SPL = $132\ dB$. The dashed red line represents the log-law, modified for uniform injection.

(b) With multi-tonal forcing, $M_0 = 0.048$. The continuous line corresponds to the no-liner case.

Figure 2.24: Bounday layer profiles, axial velocity. The dashed grey lines denote the law of the wall ($U^+ = y^+$) and the log-law, with $\kappa = 0.42$ and $A = 5.4$). Experimental results of Léon et al. [27].

The effect of strong acoustic response in Figure 2.24b also introduces an interaction mechanism between downstream orifices: the first orifices of the liner experience a 'normal' turbulent boundary layer, whereas downstream orifices are subjected to the modified boundary layer. The turbulent kinetic energy is also increased by the vortex ejection from the orifices [49], which can be seen qualitatively in Figure 2.25a [59]. Recall now that Zhang and Bodony [60] showed that the in-orifice velocity amplitude is sensitive to the RMS of the turbulent velocity fluctuations $|u'|_{rms}$. Combining the above, it can be reasoned that the liner response modifies both the mean velocity profile (cf. Figure 2.24b) and the turbulent kinetic energy balance. As a result, both the in-orifice velocity and the friction velocity are affected, and the important ratio $|\tilde{v}_{or}|_{rms}/u_\tau$ changes accordingly.

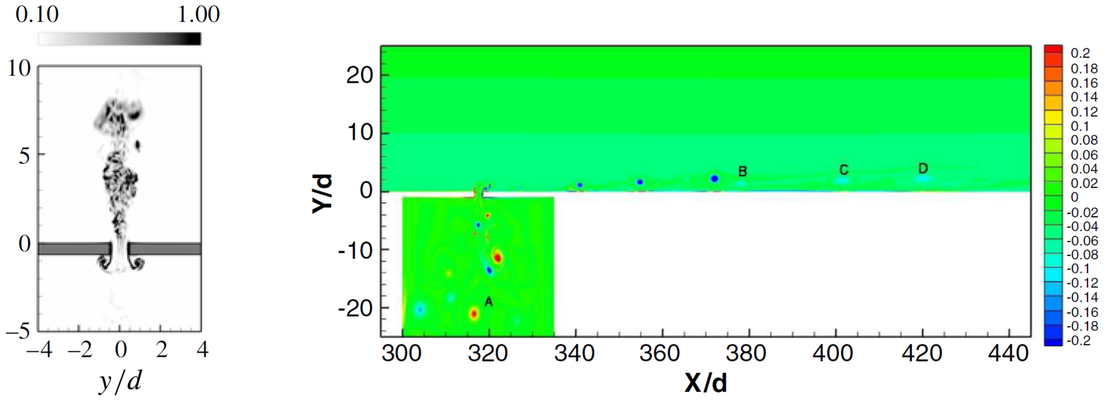

(a) Instantaneous vorticity contours at $\omega_z = 1s^{-1}$, coloured by the non-dimensionalised radial velocity u_r/c_0. $160; dB$, $\Omega_f \approx 2.7$. Zoomed-out variant of Figure 2.6b, numerical results of Zhang and Bodony [59].

(b) Instantaneous vorticity contours. SPL = $150\ dB, M_0 = 0.85, \Omega_f \approx 0.17$, numerical results of Zhang and Bodony [59].

Figure 2.25: Orifice interaction prerequisites: turbulence ejection and grazing flow.

The above discussion focusses on mean and fluctuation velocity profiles, and can thus be seen as a global effect. Instead, a more local interaction between orifices can also be expected. In Figure 2.23, Tam et al. [47] showed that ejected vortices can remain in the grazing boundary layer for a long downstream distance. A similar observation is made by Zhang and Bodony [58], as is shown in Figure 2.25b. What can be seen here, is that the vortex cores with $\omega_z < 0$ are sustained. This could be due to the steady shear force exerted by the turbulent boundary layer, promoting these vortices: in the near-wall region, $\partial u/\partial y > 0$ and $\partial v/\partial x \approx 0$, hence $\omega_z < 0$. If these vortices coincide with a downstream orifice at an inflow phase, this orifice experiences a local increase in turbulent kinetic energy. Thereby, the liner response may be modified more than the disturbed boundary layer of for example Figure 2.24b would suggest.

2.2.5. Combined: non-linear resistance dependence

An overview can now be made for the dependence of the non-linear resistance θ_{NL} on the grazing flow Mach number M_0, sound pressure level and forcing frequency $\Omega_f = f/f_0$. This aims to answer the questions posed at the end of subsection 2.1.7, and is visualized in Figure 2.26. It was shown that θ_{NL} is driven by the vortex shedding and by the vena contracta effect. The vortex shedding is characterized by the ratio of $|\widetilde{v}_{or}|_{rms}/u_\tau$. This velocity ratio is denoted Ω_v, as shown in Equation 2.14. The vena contracta effect of Figure 2.20 can be either due to the grazing flow, hence u_τ, or the in-orifice velocity itself, hence $|\widetilde{v}_{or}|_{rms}$.

$$\Omega_v = \frac{|\widetilde{v}_{or}|_{rms}}{u_\tau} \tag{2.14}$$

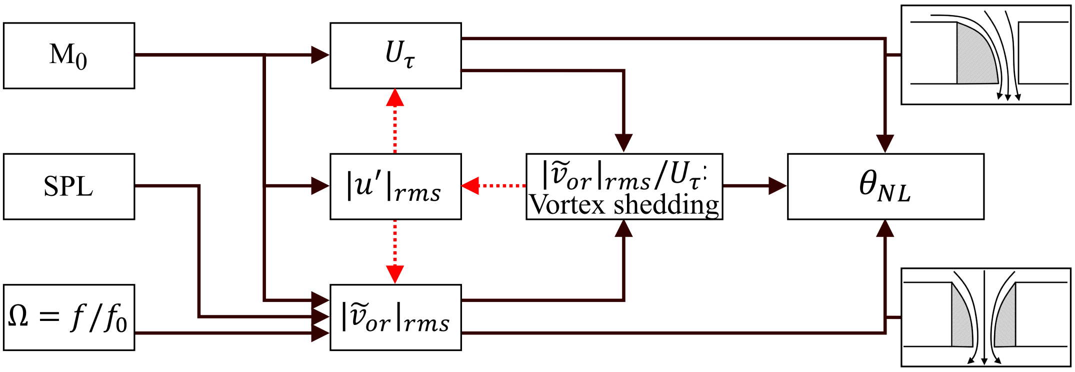

Figure 2.26: Qualitative dependency of θ_{NL} on (M_0, SPL, Ω_f), via the process of vortex shedding. The red, dashed lines denote the orifice interaction mechanism.

The friction velocity u_τ depends mainly on the grazing flow velocity, denoted indirectly by M_0. The previous section postulated, however, that it may be seriously affected by the level of turbulence, indicated by $|u'|_{rms}$, both in a local and a global sense. The RMS of the in-orifice velocity, $|\tilde{v}_{or}|_{rms}$, was shown to be a function of primarily the sound pressure level and non-dimensional forcing frequency Ω_f. The grazing flow velocity and turbulence level, however, can also affect the in-orifice velocity noticeably. Finally, the turbulence level is firstly a characteristic of the grazing flow, hence a function of M_0. Turbulent kinetic energy can be affected by the liner response through vortex shedding as well.

Looking back at Equation 2.7, the dependencies visualized in Figure 2.26 present a more complete overview than the direct linear dependencies on $|u'|$ and $|\tilde{v}_{or}|$ used by Guess [10]. Furthermore, it shows the current state-of-the-art regarding the understanding and modelling of θ_{NL}. Further improvements can be made, however, which is addressed in the next section.

2.3. Knowledge gap

From this chapter, a knowledge gap can be identified. The questions from subsection 2.1.7 have been partially answered in subsection 2.2.5, but all relations depicted in Figure 2.26 require further quantification, and the bounds for $|\tilde{v}_{or}|_{rms}/u_\tau$ that denote the onset of non-linear behaviour remain to be found. Furthermore, both Zhang and Bodony [60] and Léon et al. [27] mention explicitly that the turbulence driven orifice interaction mechanisms described in subsection 2.2.4 require further attention: in the case of Léon et al. [27], it is expected to influence the extracted friction velocity. For numerical studies such as performed by Zhang and Bodony [60], it needs to be evaluated whether interaction between orifices must be taken into account: the geometry of a single resonator with a single orifice currently does not allow for orifice interaction.

It is clear then that quantities of interest are the RMS of the in-orifice velocity scale $|\tilde{v}_{or}|_{rms}$, the friction velocity u_τ, the turbulent fluctuations RMS $|u'|_{rms}$ and the acoustic resistance θ. Phase-dependent vorticity and turbulence intensity fields over a liner could provide qualitative insights into the interaction between orifices, which require the associated velocity fields $\mathbf{u}(\mathbf{x}, \phi)$. To determine the approach, it is evaluated what has been studied already in the literature discussed in this document. To this end, all publications are filtered, to only consider those that concern acoustic liners with small orifices, with a grazing flow and without a bias flow, resulting in Table 2.2.

Table 2.2: Reviewed literature, reduced to studies including a grazing flow. References of Table 2.3

No.	Reference	Year	No.	Reference	Year
1	Melling [31]	1973	7	Tam et al. [48]	2014
2	Guess [10]	1975	8	Zhang and Bodony [60]	2016
3	Jing et al. [18]	2001	9	Brown and Jones [5]	2018
4	Jones et al. [20]	2002	10	Léon et al. [27]	2019
5	Heuwinkel et al. [13]	2010	11	Van der Meulen [51]	2019
6	Zhang and Bodony [58]	2011			

Next, these publications are categorized on the sound pressure levels and grazing flow Mach numbers that have been used. Low and high SPL and Mach numbers are distinguished, with the borders chosen at SPL$= 130\ dB$ and $M_0 = 0.3$. There are no formal definitions as to what is to be considered 'high' and 'low', but these values have been chosen based on the literature review: most documents show that below $130\ dB$, a linear response should be expected. This bound is also explicitly mentioned by Melling [31]. $M = 0.3$ is generally considered as the limit of fully incompressible flow, but is was also observed that most reviewed literature stayed below this value, so it is posed that above this value, difficulties arise from a high Mach number. Besides the flow and forcing conditions, it is checked whether the research addresses the acoustic or aerodynamic observations. Finally, a distinction is made between approaches: (empirical) modelling, numerical simulation or experiments. Following this categorization, Table 2.3 shows the classification of the selected literature in Table 2.2, with the numbers corresponding to those listed in the first column.

Table 2.3: Characterisation of reviewed experimental work, restricted to acoustic liners **subjected to a grazing flow**. The numbers refer to the references in Table 2.2.

		SPL			
		Low ($\leq 130dB$)		High ($> 130dB$)	
		Mach		**Mach**	
		Low (≤ 0.3)	High (> 0.3)	Low (≤ 0.3)	High (> 0.3)
Acoustic (impedance)	Modelled	1, 2, 3, 6	1, 2	1, 2, 6	1, 2, 6
	Numerical	3, 6	8	6, 7	6, 8
	Experimental	3, 4, 5	4	9	9
Aerodynamic	Modelled	6	8	6	6, 8
	Numerical	6	8	6, 7	6, 8
	Experimental	5, 10, 11		10, 11	

From Table 2.3, it is directly seen that experimental evaluation of the aerodynamic effects over the liner is lacking at high grazing flow Mach numbers. The works of Zhang and Bodony [58] and Zhang and Bodony [60] present two numerical studies at high M_0 that were found, but experimental validation is missing. An experimental approach seems best then to fill the knowledge gap that is described above. The next chapter presents the chosen methodology and defines the scope by setting the research questions and objectives.

3

Problem definition

Figure 2.26 showed the current understanding of qualitative links between the input parameters M_0, SPL and Ω_f on the one hand, and the non-linear resistance term θ_{NL} on the other. Section 2.3 discussed how all links shown required further quantification and understanding. Targeting all relations, is deemed too much to fit within the scope of a single thesis. Therefore, the scope is limited to the right side of Figure 2.26: before attempting to model the velocity scales, it should be confirmed whether the non-linear resistance is indeed dependent on the friction and in-orifice velocities. The resulting scope is then shown in Figure 3.1.

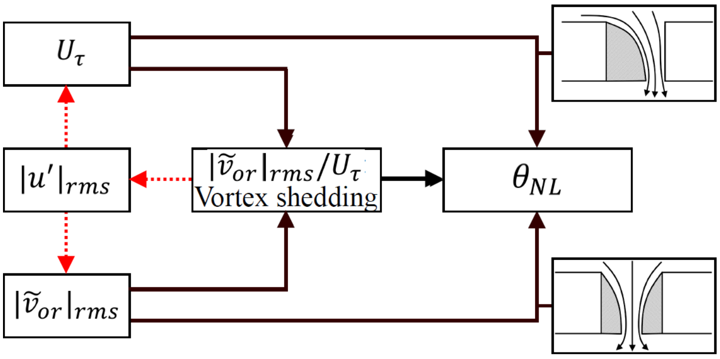

Figure 3.1: Scope of current work: reduced version of Figure 2.26.

3.1. Strategy

A general approach which can study the dependencies of the non-linear resistance is set up for the experimental work. This allows to define focused research questions. The type of liner is chosen, and the quantities of interest are defined. This in turn allows to choose appropriate measurement techniques. Finally, challenges associated to the specific research are identified and included in the research questions.

3.1.1. Liner type

A SDOF liner type is chosen for the investigation. This type is the industry standard, and most numerical and experimental evaluations have focussed on SDOF liners. This yields the largest possible database for validation of experimental results and the most lessons that can be learnt from earlier work. Chapter 2 showed that despite substantial earlier efforts, a lack of understanding regarding this simple type still remains. Finally, the SDOF type has a distinct resonant frequency. Combined with tonal excitation close to resonance, a strong response at a fixed frequency can be expected. It is argued that a strong, single-frequency behaviour can be studied more easily than a multi-tonal or broadband case.

3.1.2. Quantities of interest

Figure 3.1 shows the parameters associated to the aero-acoustic interaction. The acoustic resistance is required from the acoustic perspective. The aerodynamic behaviour is characterized by the friction and in-orifice velocity scales. Vortex shedding and its effect on local turbulence can be expressed by the vorticity and turbulence intensity. All parameters are summarized in Table 3.1. The third column lists the measurement techniques used for each quantity, these choices will be explained in subsection 3.1.3.

Table 3.1: Quantities of interest

Quantity	Symbol	Resolved by
Acoustic resistance	θ	In-situ impedance
Friction velocity	u_τ	Phase-locked PIV
In-orifice velocity RMS	$\lvert\widetilde{v}_{or}\rvert_{RMS}$	In-situ impedance and phase-locked PIV
Turbulent fluctuations RMS	$\lvert u'\rvert_{RMS}$	Phase-locked PIV
Vorticity	ω	Phase-locked PIV

The aero-acoustic environments of interest include both high- and low-speed grazing flows, with Mach numbers up to $M_0 = 0.8$, and both high and low sound pressure levels. Section 2.3 showed that experimental data is missing for all sound pressure levels in high-speed ($M_0 > 0.3$) grazing flows. The remainder of Chapter 2 showed that also at lower Mach numbers, the works of Heuwinkel et al. [13], Léon et al. [27] and Van der Meulen [51] required further validation.

3.1.3. Combined aero-acoustic experiments

The test facility is the FDF of Royal Netherlands Aerospace Centre (NLR), depicted in Figure 3.2. This is a closed-loop wind tunnel, capable of Mach numbers $0.06 \leq M_0 \leq 0.8$ with a test section of $150x300mm^2$. Acoustic measurements can be performed by means of insertion loss or in-situ impedance measurements. Available aerodynamic measurement techniques include PIV, hot-wire, and pitot probe measurements.

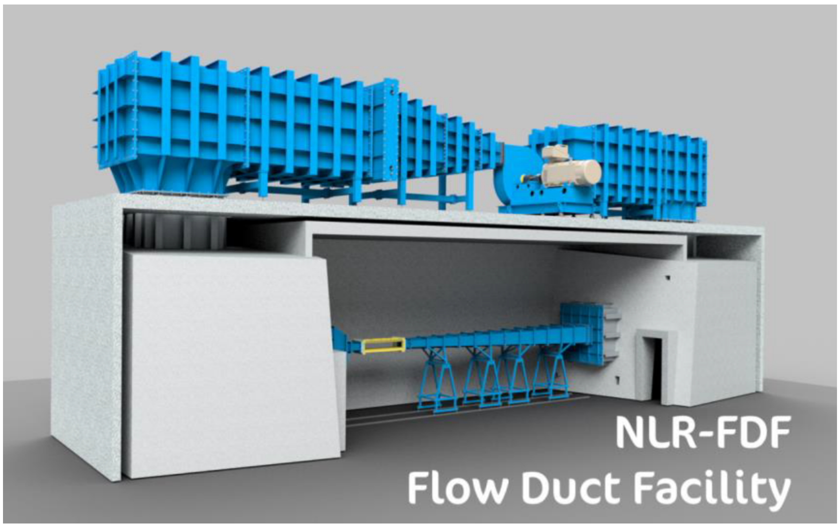

Figure 3.2: The Flow Duct Facility of Royal Netherlands Aerospace Centre.

The quantities of interest in Table 3.1 require a combined aero-acoustic approach, to evaluate both the impedance and the aerodynamic properties. For the acoustic measurements, in-situ measurements are selected; insertion loss measurements make use of impedance eduction. As discussed in subsection 2.1.7, these methods are deemed less accurate than in-situ measurements, as the propagation of sound waves is modelled. In-situ measurement uses a liner sample with two microphones, and allows to directly resolve the impedance through the Fourier components of the wall normal pressure and velocity signals. A horn is placed directly opposite of the liner sample, generating normal incidence acoustic waves.

For the aerodynamic measurements, phase-locked PIV is selected. In a plane perpendicular to the face sheet and through the orifice centers, out-of-plane velocity components are assumed negligible. Therefore, planar 2-dimensional 2 component (2D2C) PIV is chosen, as it reduces complexity with respect to stereo (2D3C) or tomographic (3D3C) PIV. This means the vorticity is calculated as a scalar field in the out-of-plane direction. The closed tunnel loop allows to seed the entire tunnel circuit. Being a whole field measurement, instantaneous vorticity fields can be evaluated, something that is not possible for hot-wire or pitot tube probe measurements. The friction velocity can be found from the PIV results through log-law fitting and momentum-integral measurements. These methods are discussed in greater detail when presenting the results in Section 9.1. Note that the in-orifice velocity can be found from both the impedance and the PIV measurements. Finally, phase-locking with a tonal acoustic signal allows to isolate effects associated to a certain relative phase. Assuming all phase-related flow effects are due to the acoustic forcing allows to isolate acoustically induced flow effects. This uses the concept of a triple decomposition, and is explained next.

Phase-locking: velocity decomposition

As explained by Lignarolo et al. [25], the spatio-temporal flow field $\mathbf{u}(\mathbf{x}, t)$ is seen as a combination of a time-averaged flow field $\overline{\mathbf{u}}(\mathbf{x})$, a flow related to the acoustic fluctuations $\widetilde{\mathbf{u}}(\mathbf{x}, t)$ and a term which collects all zero-mean fluctuations. These uncorrelated fluctuations are formed by both the turbulent fluctuation velocity field $\mathbf{u}'(\mathbf{x}, t)$ and a measurement noise term $\mathbf{b}(\mathbf{x})$ [26]. Equation 3.1 shows the decomposition into all four terms. Often, the turbulence and noise components can not be distinguished, and are grouped together.

$$\mathbf{u}(\mathbf{x}, t) = \overline{\mathbf{u}}(\mathbf{x}) + \widetilde{\mathbf{u}}(\mathbf{x}, t) + \mathbf{u}'(\mathbf{x}, t) + \mathbf{b}(\mathbf{x}) \tag{3.1}$$

In phase-locked PIV, images are recorded at certain relative phases with respect to the acoustic signal. Averaging Equation 3.1 over a phase cancels the zero-mean fluctuations out to $\langle \mathbf{u}'(\mathbf{x}, t)\rangle_\phi = \langle \mathbf{b}(\mathbf{x}, t)\rangle_\phi = \mathbf{0}$. Furthermore, phase-averaging the mean velocity field $\overline{\mathbf{u}}(\mathbf{x})$ yields the mean velocity field itself, as it is independent of time. Writing out these changes and rearranging yields Equation 3.2. The acoustic velocity field $\widetilde{\mathbf{u}}(\mathbf{x}, \phi)$, associated to the aero-acoustic interaction, is found by subtracting the time-averaged field from the phase-averaged field. Note that measurements can be at a low frequency with respect to the acoustic signal, as only the phase matters, and not the time.

$$\widetilde{\mathbf{u}}(\mathbf{x}, \phi) = \langle \mathbf{u}(\mathbf{x})\rangle_\phi - \overline{\mathbf{u}}(\mathbf{x}) \tag{3.2}$$

To stay consistent with the triple decomposition, the randomly fluctuating component $\mathbf{u}'$ must also be evaluated in a phase-locked perspective. From equations 3.1-3.2, it can be found that this is simply the standard deviation of the phase-locked velocity field, as shown in Equation 3.3. The global RMS over a full phase can be found similarly by finding the RMS of $|\mathbf{u}'|_{rms}(\mathbf{x}, \phi)$ over all phases.

$$|\mathbf{u}'|_{rms}(\mathbf{x}, \phi) = \sqrt{\frac{1}{N}\sum_{j=1}^{N}\left[\mathbf{u}_j(\mathbf{x}, \phi) - \langle \mathbf{u}(\mathbf{x})\rangle_\phi\right]^2} \tag{3.3}$$

3.2. Experimental challenge

In-situ measurements are routinely performed by NLR in the entire range of SPL and grazing flow Mach numbers, and no problems are expected here. For the PIV measurements, a challenge is observed in the range of velocity scales that needs to be resolved.

3.2.1. Expected range of scales

The largest velocity of interest is the free-stream flow velocity $U_0 = c_0 M_0$, whereas the smallest scale of interest is taken as the RMS of the incident acoustic velocity $|\widetilde{v}_{inc}|_{rms}$, still away from the liner surface. This is a conservative minimal scale, as the velocities above or in the orifice ($|\widetilde{v}_{or}|_{rms}$) are expected to be higher due to the response of the liner. The range of interest, denoted R_I, is then defined as in Equation 3.4.

$$R_I = \frac{u_{max}}{u_{min}} = \frac{c_0 M_0}{|\widetilde{v}_{inc}|_{rms}} \tag{3.4}$$

The incident velocity due to a wave of normal incidence can be found from the sound pressure level and ambient air properties, as shown in Equation 6.2 [27]. The incident pressure RMS amplitude is defined from the sound pressure level in Equation 2.11c.

$$|\widetilde{v}|_{rms} = \frac{c_0}{\gamma}\frac{|\widetilde{p}|_{rms}}{p_0} \tag{3.5}$$

Using equations 3.4, 6.2 and 2.11c, the range of scales that is to be resolved in the experiment can be estimated. The result for SPL-Mach number pairs is displayed in Table 3.2. The greyed cells denote a regions which is deemed unresolvable using current best practices, which is explained next.

Table 3.2: R_I estimation, as defined in Equation 3.4, with $|\widetilde{v}|_{rms}$ from Equation 6.2. Grey cells denote $R_I > 200$.

		SPL [dB]								
		120	125	130	135	140	145	150	155	160
Mach [-]	0.1	709	399	224	126	71	40	22	13	7
	0.2	1419	798	449	252	142	80	45	25	14
	0.3	2128	1197	673	378	213	120	67	38	21
	0.4	2837	1595	897	505	284	160	90	50	28
	0.5	3546	1994	1121	631	355	199	112	63	35
	0.6	4256	2393	1346	757	426	239	135	76	43
	0.7	4965	2792	1570	883	496	279	157	88	50
	0.8	5674	3191	1794	1009	567	319	179	101	57

3.2.2. Dynamic velocity range

The range of velocity scales that can be resolved by a PIV measurement is given by its dynamic velocity range, or DVR. The typical definition is stated in Equation 3.6a [39], where Δx_{max} and Δx_{min} denote the maximum and minimum displacements that can be resolved. The maximum displacement is one quarter of the interrogation window size, and is called the one-quarter rule [39]. This is denoted $\Delta x_{max} = d_I/4$, with d_I the size of the interrogation window. The minimum displacement that can be confidently resolved is dictated by the measurement noise $\sigma_{\Delta x}$. This noise is associated to several sources [39], the sources deemed most important are highlighted here. First, the camera sensor records pixel intensities with a certain measurement noise included. Another source of noise is a change in measurement conditions during a recording. Finally, in-plane velocity gradients and out-of-plane loss of particles create differences between the first and second frames of a double-frame pair. The peak location is estimated by fitting a Gaussian peak to 3 data-points in both dimensions. As a result, all noise sources introduce random fluctuations in the fitted peak location with respect to the actual displacement peak. Note that measurement noise corresponds to the noise term $\mathbf{b}(\mathbf{x})$ in Equation 3.1. A common estimate of $\sigma_{\Delta x}$ is $1/10^{th}$ of a pixel, through sub-pixel peak fitting [39].

$$\text{DVR} = \frac{\Delta x_{max}}{\Delta x_{min}} = \frac{d_I}{4\sigma_{\Delta x}} \tag{3.6a}$$

$$\text{DVR}_{GR} = \text{DVR}k_g = \frac{d_I}{4\sigma_{\Delta x}}k_g \tag{3.6b}$$

This leads to a basic DVR $= 80$ for an interrogation window size $d_I = 32px$. A common method of raising the DVR is using grid refinement schemes, as shown in Equation 3.6b [36]. Here, k_g denotes the window scaling factor, while d_I now denotes the *final* window size; refining from $64x64px^2$ to $32x32px^2$ through a grid refinement scheme gives $k_g = 2$, hence DVR$_{GR} = 160$. Values for the DVR vary in literature, ranging from numbers as 160 [36] up to 400 [26]. Judging from the estimation made here, an intermediate value of $DVR_{GR,max} \approx 200$, also stated by True and Crimaldi [50], seems appropriate for the maximum achievable DVR using advanced interrogation schemes.

3.2.3. Discussion on DVR and expected range of scales

The expected range of scales R_I can be seen as the requirement for the DVR. The greyed cells in Table 3.2 denote values of $R_I \geq 200$. It can be seen that the high Mach/high SPL cases should be resolvable using current methods. However, Section 2.3 highlighted that high Mach/low SPL is also of interest. Using the 'first' low SPL/high Mach case of $130\ dB, M_0 = 0.4$, as discriminated in Table 2.3, the range to be resolved is already as high as $R_I \approx 900$, which can not be resolved using current best practices.

Another approach to view the relation between R_I and the DVR is to check whether observable effects on the flow are expected. This is done following the approach of Léon et al. [27]. Using equations 2.11b, 2.11c, 2.13 with the liner and test-section properties, the discriminating velocity ratio can be approximated as $\Omega_v = |\tilde{v}_{or}|_{RMS}/u_\tau \approx |\tilde{v}_{or}|_{lumped}/u_\tau$. The results at resonance ($\Omega_f = 1$) and with a fixed value of $Q = 1$ are shown in Table 3.3. Greyed cells denote the transition region; to the left of this boundary, no serious effects are expected from Figure 2.17d, while clear vortex shedding is expected to the right. While this is only a crude estimation, these results reveal that all cases at low SPL ($\leq 130\ dB$) are expected to show no serious aerodynamic effects, even at $M_0 = 0.1$. But also at higher sound pressure levels, the transition region $2 \leq |\tilde{v}_{or}|/U_\tau \leq 5$ is reached quickly.

Table 3.3: $\Omega_v \approx |\tilde{v}_{or}|_{lumped}/u_\tau$, shaded by regions described by Léon et al. [27]: grey cells denote the transition region where $2 \leq \Omega_v \leq 5$, above which vortex shedding is observed. The red line denotes the limit $DVR = 200$, as observed in Table 3.2. Modelled with $\Omega_f = 1$ and $Q = 1$. Graphics taken from Léon et al. [27] (cf. Figure 2.17d).

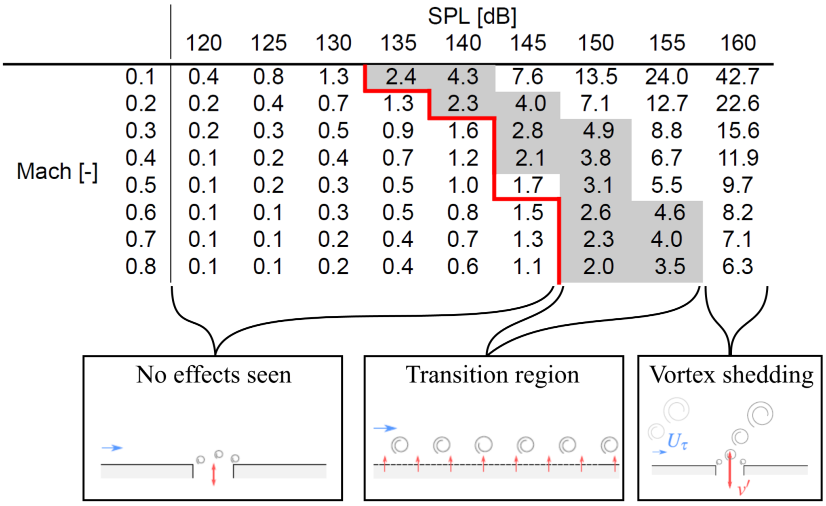

		SPL [dB]								
		120	125	130	135	140	145	150	155	160
Mach [-]	0.1	0.4	0.8	1.3	2.4	4.3	7.6	13.5	24.0	42.7
	0.2	0.2	0.4	0.7	1.3	2.3	4.0	7.1	12.7	22.6
	0.3	0.2	0.3	0.5	0.9	1.6	2.8	4.9	8.8	15.6
	0.4	0.1	0.2	0.4	0.7	1.2	2.1	3.8	6.7	11.9
	0.5	0.1	0.2	0.3	0.5	1.0	1.7	3.1	5.5	9.7
	0.6	0.1	0.1	0.3	0.5	0.8	1.5	2.6	4.6	8.2
	0.7	0.1	0.1	0.2	0.4	0.7	1.3	2.3	4.0	7.1
	0.8	0.1	0.1	0.2	0.4	0.6	1.1	2.0	3.5	6.3

No effects seen
Transition region
Vortex shedding
U_τ
v'

Comparing Tables 3.2 and 3.3 yields an important observation on the results of Léon et al. [27], and a challenge regarding PIV. The DVR limit of Table 3.2 is indicated by a red line in Table 3.3. The limit where no more vortex shedding is observed by Léon et al. [27] coincides near-perfectly with the DVR limit. This raises the question whether vortex shedding was not present, or could not be observed. It is argued that a higher DVR is needed to either confirm or reject the findings of Léon et al. [27]. Within the current work, a method must therefore be identified to raise the DVR of a phase-locked PIV measurement. Due to its importance, the DVR itself is also considered a quantity of interest. While this discussion may be insightful, three points must be taken into account:

- The DVR limit of 200 that is used in Table 3.2 is not a fixed value. The exact value depends on the exact execution of the experiment. Léon et al. [27] do not explicitly state the DVR of their measurements. Both Léon et al. [27] and Van der Meulen [51] use a typical PIV set-up with grid refinement, and therefore seem limited to the earlier stated DVR limit of 200.
- The velocity model of Equation 2.11b is only validated by Léon et al. [27] for use at low grazing flow Mach numbers, and is extrapolated in tables 3.2-3.3. Therefore, this model itself is not yet fully validated, and is here used to evaluate the work it is suggested in.
- Likewise, the friction law of Equation 2.13 to find u_τ was discussed in subsection 2.2.4: it was argued how this relation is not expected to hold for strong acoustic forcing. Furthermore, due to the FDF's larger duct diameter, the limit of validity at $Re_{D_h} = 3.2 \times 10^6$ is violated for $M_0 \gtrsim 0.45$. Therefore, also the accuracy of u_τ in Table 3.3 is approximate at best.

3.3. Research questions

The main question to be answered then concerns the resistance term itself:

> *How is the non-linear resistance θ_{NL} of a single degree of freedom acoustic liner a function of the in-orifice velocity scale $|\tilde{v}_{or}|_{rms}$, the friction velocity U_τ, and the ratio $|\tilde{v}_{or}|_{rms}/U_\tau$, for grazing flow Mach numbers $M_0 \leq 0.8$ and sound pressure levels $\leq 155\ dB$?*

3.3.1. Sub-questions

From Figure 3.1 and the lessons from chapter 2, multiple sub-questions can be identified. These questions concern understanding and quantification of the other relations visible in Figure 3.1, which build up the relation for the non-linear resistance term. This includes the vortex shedding, which is a combined effects from the friction and in-orifice velocity, and the interaction between orifices that is associated with vortex ejection. Furthermore, the discussions on the works of Kooi and Sarin [21], Zhang and Bodony [60] and Léon et al. [27] showed several points which require validation. The resulting questions are shown below, followed by a brief explanation of each item:

1. Can the PIV methodology be modified to provide the required DVR of 900?
    (a) What DVR is achieved in the PIV experiment?
    (b) Is an increase in DVR achieved with respect to a grid refinement approach?
2. What are the bounds for the orifice-to-friction velocity ratio Ω_v to classify the types of aerodynamic effects over the liner?
    (a) Can a formal, quantitative criterion be formed to classify the type of effect?
    (b) Can it be proven that for low values of the velocity ratio, indeed no vortex shedding occurs?
    (c) Can non-linear behaviour be confirmed consistently from both the aerodynamic (cf. [27]) and acoustic (cf. [21]) perspective, as was suggested by Heuwinkel et al. [13] and Léon et al. [27]?
3. Can a formulation be found to extract the friction velocity U_τ of the grazing boundary layer disturbed by strong acoustic forcing?
4. Can the interaction between orifices be observed?
    (a) After how many orifices is the liner response acoustically and aerodynamically independent of the downstream distance?
    (b) Can a local increase in turbulent kinetic energy be observed in the boundary layer near ejected vortices?
    (c) Can the influence of the liner response on the grazing boundary layer, hence on the friction velocity, be neglected?
    (d) Can the influence of ejected vortices on downstream orifices be neglected, and is the single orifice geometry of [58–60] therefore appropriate?

Sub-question 1 concerns the DVR of the PIV measurements. This limit governs the feasibility of measurement points, and must be established first. Sub-questions 2-3 continue directly upon the publication of Léon et al. [27]. Sub-question 4 concerns the feedback mechanism, which is missing from both works: question 4(c) is formed from the perspective of Léon et al. [27], question 4(d) is aimed at numerical studies such as that of Zhang and Bodony [60].

3.3.2. Additional: validation of velocity models

Finally, one additional question is set up, regarding the modelling of the in-orifice velocity term. This question is regarded as optional, as it does not provide further insight into the mechanism sketched in Figure 3.1, but is part of the bigger scope of Figure 2.26 instead. Zhang and Bodony [60] and Léon et al. [27] clearly discuss this velocity scale, and propose two versions of their own. This provides a clear starting point for the modelling of this important velocity scale. In the current work, this velocity scale is to be resolved in any case, and could therefore also easily be compared to the suggested models. This helps add to the body of reference data and to further validate both works.

5. What is an appropriate scale for the in-orifice velocity amplitude $|\tilde{v}_{or}|$? Would this be...
    (a) ... the scale $|\tilde{v}_{or}|_{lumped}$, as proposed by Léon et al. [27]?
    (b) ... the scale $|\tilde{v}_{or}|_{Zhang}$, as proposed by Zhang and Bodony [60]?
    (c) ... a new scale?

3.4. Research objectives

The research objectives that are to be fulfilled in order to answer the research questions can then be identified. First, the main objective is set up below. Note that 'evaluating the response' is a broadly interpretable term. This is further specified by breaking down the main objective into the sub-objectives.

> *Evaluate the aero-acoustic response of a single degree of freedom acoustic liner by measuring* $|\widetilde{v}_{or}|_{rms}$, U_τ, θ_{NL} *and* $\mathbf{u}(\mathbf{x})$ *at grazing flow Mach numbers* $M_0 \leq 0.8$ *and sound pressure levels* $\leq 155\ dB$*, using phase-locked PIV and in-situ impedance measurements.*

3.4.1. Sub-objectives

Sub-objectives are set up that build up to achieving the main objective. Note that these objectives closely tie together with the research questions.

1. Select a PIV measurement and post-processing method appropriate for the expected case by concurrently...
   (a) ...modelling the expected aerodynamic effects using models from the literature review.
   (b) ...exploring the theoretical capabilities of current PIV techniques.
2. Find a method of finding the friction velocity in the disturbed boundary layer by performing a further, limited literature study.
3. Show for which values of $|\widetilde{v}_{or}|_{rms}/U_\tau$ a non-linear liner response occurs at high and low grazing flow Mach numbers, and high and low sound pressure levels, by evaluating both the acoustic (cf. Figure 2.17c) and aerodynamic response (cf. Figure 2.17d).
4. Learn how the non-linear resistance θ_{NL} is a function of the friction and in-orifice velocities U_τ and $|\widetilde{v}_{or}|_{rms}$, by taking combined impedance and PIV measurements and using the function forms suggested by [21] and Zhang and Bodony [58] as starting points.
5. Explore the orifice feedback mechanism by evaluating phase-locked velocity, vorticity and turbulence fields $\tilde{\mathbf{u}}(\mathbf{x},\phi)$, $\omega_z(\mathbf{x},\phi)$ and $|\mathbf{u}'|_{rms}(\mathbf{x},\phi)$.
6. Validate the velocity scales proposed by Zhang and Bodony [60] and Léon et al. [27] by comparing these models to the data of Van der Meulen [51] and newly obtained test-points.

II

Methodology

4

Measurement techniques

4.1. Acoustic measurements: in-situ impedance evaluation

In situ measurements are carried out using the approach of Dean [7], who proposed a 2-microphone method that found a lot of use in tests performed since. The original technique used one microphone installed in the backing plate of the liner, and a second microphone which was able to traverse in height. Commonly, this traversing microphone is modified to a flush mounted microphone on the face sheet [57].

The work by Dean [7] is followed to derive the surface impedance in this section. The method requires several assumptions: firstly, a locally reacting liner is assumed, which means that acoustic waves in the cavity can only travel in height, normal to the face sheet. Secondly, it is assumed that linear acoustics can model the wave motion within the cavity. The backing plate is assumed to totally reflect the incoming pressure waves. Finally, the velocity just above the face sheet is assumed to be equal to the velocity just below the sheet. Recall now the definition of the acoustic surface impedance of Equation 1.1b, repeated below for clarity:

$$\zeta_n = \frac{Z_n}{Z} = \frac{\tilde{p}}{\tilde{v}_n \rho_0 c_0} \tag{4.1}$$

The complex acoustic surface pressure $\tilde{p} = |p_s| e^{i\omega t_s}$ can directly be measured using the flush-mounted face sheet microphone; note the time-scale t_s, the subscript denotes a quantity on the face sheet. The fluctuating acoustic velocity at the face sheet, normal to the surface, $\tilde{v}_n$, must be calculated from both microphone measurements. For the derivation below, the notation as shown in Figure 4.1 will be used.

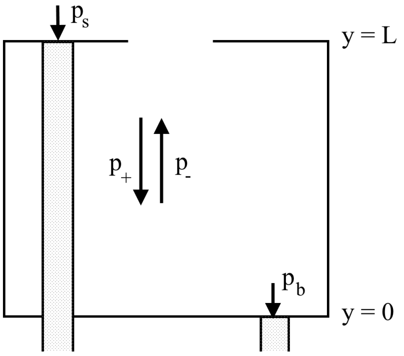

Figure 4.1: Geometry of a liner cell instrumented for in-situ impedance measurements.

The pressure p within the cavity is a sum of the incoming pressure wave p_+, which is completely reflected at the backing wall as p_-. The definition of the incoming pressure wave in Equation 4.2a then allows to find the reflected wave, and in turn the cavity pressure in Equation 4.2c. In these equations, k is the wavenumber $k = 2\pi/\lambda$, and the y-coordinate is as shown in Figure 4.1.

$$p_+ = |p_0|e^{i(\omega t - ky)} \tag{4.2a}$$

$$p_- = |p_0|e^{i(\omega t + ky)} \tag{4.2b}$$

$$p = p_+ + p_- = |p_0|e^{i\omega t}\left(e^{iky} + e^{-iky}\right) = 2|p_0|e^{i\omega t}cos(ky) \tag{4.2c}$$

Using the pressure in the cavity, the velocity in the cavity can by found, using the linearized momentum equation shown in Equation 4.3a: Equation 4.2c is differentiated with respect to y, after which the resulting expression is integrated with respect to the time t and multiplied by $1/\rho_0$ to yield the velocity expression in Equation 4.3c. Notice the appearance of the medium's characteristic impedance, $\rho_0 c_0$.

$$\rho_0 \frac{\partial v}{\partial t} = -\frac{\partial p}{\partial y} \tag{4.3a}$$

$$\frac{\partial p}{\partial y} = -2k|p_0|e^{i\omega t}sin(ky) \tag{4.3b}$$

$$v = \frac{2k|p_0|}{\rho_0 i\omega}e^{i\omega t}sin(ky) = -i\frac{2|p_0|}{\rho_0 c_0}e^{i\omega t}sin(ky) \tag{4.3c}$$

Note that the velocity v in Equation 4.3c is in the coordinate system of Figure 4.1, hence **positive upward**. The normal velocity $\widetilde{v}_n$ of Equation 4.1 is defined in the same direction as the normal pressure $\widetilde{p}$. Going back to Figure 4.1, the same direction as the surface pressure p_s must then be used, which is **positive downward**. Furthermore, the assumption is made that the velocity just above the face sheet is equal to that just below the face sheet, i.e. $-\widetilde{v}_n = v(y = L)$. Finally, from Equation 4.2c, it can be seen that the cavity backing sheet pressure, p_b occurs for $y = 0$, and thereby $2|p_0| = |p_b|$. Combining all, the expression for $\widetilde{v}_n$ can be found, as shown in Equation 4.4.

$$\widetilde{v}_n = -v(t, y = L) = i\frac{|p_b|}{\rho_0 c_0}e^{i\omega t}sin(kL) \tag{4.4}$$

Combined with the pressure signal from the face sheet microphone, the impedance ζ_n can be calculated, as shown in Equation 4.5a. Note that $e^{i\omega(t_s - t)} = e^{i\phi}$, with ϕ the phase angle between the surface and back pressure measurements. Furthermore, the ratio of pressure can also be expressed in the measured sound pressure levels, using Equation 2.11c. While the RMS is not the same as the amplitude, the scaling factor $\sqrt{2}$ between the two simply cancels out when moving to decibels. Expressing Equation 4.5a in terms of SPL and phase angle then results in Equation 4.5b.

$$\zeta_n = \frac{\widetilde{p}}{\widetilde{v}_n \rho_0 c_0} = -i\frac{|p_s|}{|p_b|}\frac{e^{i\omega t_s}}{e^{i\omega t}}\frac{1}{sin(kL)} = -i\frac{|p_s|}{|p_b|}e^{i\phi}\frac{1}{sin(kL)} \tag{4.5a}$$

$$\zeta_n = \left(10^{\frac{SPL_S - SPL_b}{20}}\right)\left(\frac{sin(\phi) - icos(\phi)}{sin(kL)}\right) \tag{4.5b}$$

4.2. Aerodynamic measurements: high DVR PIV

In subsection 3.2.3, it is shown that the DVR must be increased. As presented in Equation 3.6b, grid refinement increases the DVR by allowing a large maximum displacement. Typical grid-refinement factors of $k_g \leq 4$ are deemed insufficient to provide the desired dynamic velocity range. Alternatively, non-square interrogation windows can be used. A window that is stretched allows a larger displacement in its large dimension. This seems suited to the current problem, as a small displacement in y is expected for a large displacement in x. Due to the stretching, resolution is similarly decreased in x, and increased in y. This poses a problem, as local effects of the orifice are of interest. The orifices have a diameter $d = 1mm$, requiring a high spatial resolution in x. Window stretching is therefore deemed unsuited for the current problem.

Particle tracking velocimetry (PTV) is suggested to be capable of providing both a high DVR and a high dynamic spatial range (DSR). This is due to its fundamental difference with respect to PIV: the latter relies on a windowed, statistical approach to determine the particle image displacement. In PTV, particles are tracked exactly. The combination of a large range of velocity scales R_I and possible complex flow structures in the current case are expected to prove difficult for a PTV approach: finding a robust method of particle image matching may be difficult. Furthermore, staying with a PIV approach allows to build upon experience gained in a previous test [51].

Finally, MF-PIV is proposed as a possible solution. Here, measurements are conducted with varying pulse separation times. This aims to resolve large velocities using a short δt, and small velocities using a long δt. This allows to achieve optimal displacements for both scales, and increases the DVR. This concept is seen as most promising of the techniques discussed here. The capabilities and different implementations of multi-δt PIV are elaborated in the next section.

4.2.1. Multi-frame PIV methods

Hain and Kähler [11] explain how multi-frame PIV (MF-PIV) aims to overcome the challenges posed by the lower optical quality of typical time-resolved PIV set-ups. The combination of high repetition rate CMOS cameras and lasers results in larger pixels, higher noise and lower sensitivities with respect to CCD PIV systems. This yields in turn a reduction in DVR and DSR. Multi-frame techniques use information distributed in time to increase these dynamic ranges to acceptable levels. Since its introduction, several variants of multi-frame techniques have been developed, which can be categorized into three main branches: selecting an optimal pulse separation time, performing cross-correlation on an ensemble of image pairs from different pulse separation times, and using information in time to reconstruct the particle path. These three concepts are first explained below.

Pulse separation time switching

This first MF-PIV method is well explained by Hain and Kähler [11]. In pulse separation time switching, image pairs with a different pulse separation time are available. In time-resolved PIV (TR-PIV) measurements [11], two images from a continuous, high-frequency stream of single-frame images can be taken. In double-frame approaches [35, 36, 50], pulse separation times are defined in the experimental set-up and image acquisition scheme. The working principle in all cases is to locally optimize the particle image displacement dependent on the local flow velocity, and is visualized using Figure 4.2. The inhalant flow studied by True and Crimaldi [50] consists of two regions, shown in Figure 4.2a: a stagnant, infinite reservoir, and a high velocity region near the inhalant tube. The acquisition and correlation scheme in Figure 4.2b shows how a double-frame image pair is used to yield a short δt, whereas cross-correlating the first frames of two subsequent image pairs result in a very long δt. The short δt is used on the inhalant flow and the long δt is used in the reservoir. A long pulse separation time allows a near-zero flow velocity to give a large particle image displacement. This low velocity would not be detectable by the short δt, as a near-zero displacement would result, which can not be distinguished from the measurement noise $\sigma_{\Delta x}$. Combining the two, both flow regions can be resolved.

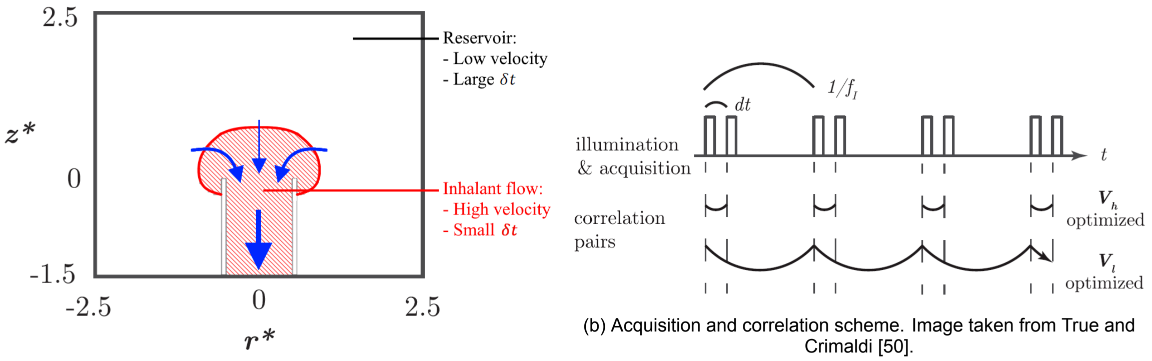

(b) Acquisition and correlation scheme. Image taken from True and Crimaldi [50].

(a) Conceptual overview of using MF-PIV to resolve both high- and low-speed regions. Image adapted from True and Crimaldi [50].

Figure 4.2: Working principle of pulse separation time switching: resolve low-speed regions with a large pulse separation time, and high-speed regions with a short pulse separation, such that the local particle image displacement is optimized.

A large improvement is obtained in the cases of Persoons and O'Donovan [36] and True and Crimaldi [50], which are characterized by distinct low-speed and high-speed regions. If the largest and smallest velocities are recorded with different pulse separation times, it can quickly be found that the DVR is further multiplied by $k_t = \delta t_{max}/\delta t_{min}$. The result of these improvements is shown in Equation 3.6b.

$$\text{DVR}_{GR,MPS} = k_g k_t \text{DVR} = k_g k_t \frac{d_I}{4\sigma_{\Delta x}} \tag{4.6}$$

It should be noted that these pulse separation switching schemes are similar to windows shifting processing techniques. For a fixed window size $d_I = 16px$, grid refinement allows to see a greater particle image displacement than $d_I/4 = 4px$, by increasing the initial window size. In pure multi-frame PIV (not combined with grid refinement), the window size remains constant, but the pulse separation time is varied: a longer δt allows to resolve smaller velocity scales. This also shows the fundamental difference between the two. Grid refinement increases the *maximum* velocity that can be seen, while pulse separation time switching makes a smaller *minimum* velocity detectable. Both directly affect the DVR, but from a different approach. These differences are quickly summarized in Table 4.1.

Table 4.1: Fundamental differences between grid refinement and pulse separation time switching.

Parameter	Grid refinement	δt switching
Pulse separation time δt	Fixed	Variable
Interrogation window size d_I	Variable	Fixed
DVR multiplication factor	$k_g = \frac{d_{I,max}}{d_{I,min}}$	$k_t = \frac{\delta t_{max}}{\delta t_{min}}$
DVR term which is affected	$\Delta x_{max} \propto \frac{1}{4} d_I k_g$	$\Delta x_{min} \propto \frac{\sigma_{\Delta x}}{k_t}$

Ensemble cross correlation

The pulse separation switching schemes base the cross-correlation on a single image pair. An improvement may be obtained when combining information from the different data sources. This is the concept of the ensemble cross correlation method. This method is introduced as a 'pyramid correlation' by Sciacchitano et al. [42].

Again, TR-PIV dataset is concerned, with individual images recorded at a fixed interval δt_0. From the continuous image sequence, a short subset is concerned. Figure 4.3a shows a subset of four images. Cross-correlation is performed between each subsequent image with $\delta t = \Delta t$, resulting in three correlation maps. Next, correlation maps are evaluated between each second image, with $\delta t = 2\delta t_0$, yielding two correlation maps. Finally, the correlation is taken between each third image, with $\delta t = 3\delta t_0$. This makes for a pyramid shape in the evaluated correlations in Figure 4.3a. Next, the correlation maps are averaged for each δt. After this, a homothetic transformation is performed, which means that correlation maps with $\delta t < 3\delta t_0$ are scaled up linearly by $3\delta t_0/\delta t$. This results in averaged correlation maps which are all associated to a pulse separation $\delta t = 3\delta t_0$. Assuming linear particle image paths allows to combine the averaged correlation maps into a single map, on which the correlation peak is fitted. This process is implemented as a moving filter over the entire image sequence. The pyramid width and height can be optimized locally, the details of which can be found in [42]. Correlation values must be normalized to be able to combine different maps.

The DVR gain is defined in Equation 3.6b. The added benefit of combining the information from different pulse separation times can best be explained by the transformation of the averaged correlation maps. The correlation maps which were evaluated on $\delta t = \Delta t$ provide a wide, but low correlation peak. Alternatively, the correlation maps from $\delta t = 3\Delta t$ (or longer) provide narrow and higher correlation peak after the transformation. Combining these two maps then provides a wide, smooth correlation peak with a distinct maximum value, on which a peak can be fitted with high accuracy [42]. The original scheme of Sciacchitano et al. [42] combines the maps of different δt's into the final correlation map using a standard (arithmetic) mean. It is mentioned, however, that weighed averages may be used instead.

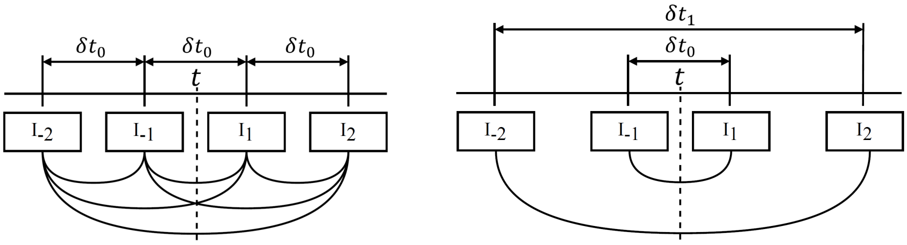

(a) Original scheme of Sciacchitano et al. [42]. (b) Double-frame, phase-locked adaptation.

Figure 4.3: MF-PIV ensemble correlation schemes. Arcs connecting two frames denote that cross correlation is performed between those two frames.

Lagrangian methods

The final branch of MF-PIV uses information in time to construct the particle path, visualized in Figure 4.4 [16]. This switches from a Eulerian to a Lagrangian perspective, and becomes similar to PTV. The first version described by Lynch and Scarano [29] reconstructs the particle path by fitting a polynomial function to the displacements using a least-squares regression. An improved version by Jeon et al. [16] views the correlation maps as probability density functions, and fits the polynomial particle path by maximizing the correlation value along the fluid trajectory. Resolving the particle path allows a more accurate evaluation of the velocity, as acceleration and flow curvature terms can be taken into account [6].

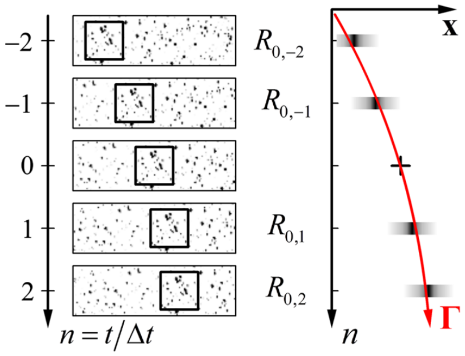

Figure 4.4: Particle image path reconstruction using 5 subsequent time-steps. Image adapted from Jeon et al. [16].

Chosen approach

The challenge in DVR in the current case exists between velocity components. Hence, no true low-speed regions exist, and pulse separation time switching is not an option. Ensemble cross correlation increases the DVR, while maintaining high- and low-speed (short and long δt) information. Particle path reconstruction aids mainly in improving the correlation, instead of raising the DVR. Of these three then, the ensemble cross correlation is expected to be able to provide the required increase in DVR. The original scheme of [42] is adapted for use in a single-camera, phase-locked set-up. In the next sections, the conceptual implementation is presented. Details on the measurement set-up and processing steps are provided in chapters 5-7.

4.2.2. Fluctuations decomposition

An additional possibility arises when information from different pulse separation times is available. Scharnowski [40] present a study into wind tunnel turbulence estimation in high-speed flows. Recordings at different pulse separations are used to decompose the random fluctuations term into a turbulence and noise component. Equation 4.7a shows the squared total fluctuating displacement (in pixels) in one dimension as a sum of the actual turbulence intensity and the measurement noise (cf. Equation 3.1). As before, the measurement noise $\sigma_{\Delta x}$ is associated to the positioning accuracy of the velocity vector. Assuming a fixed RMS value for this noise shows that its relative influence on the measured fluctuations decreases as the mean displacement increases.

$$\overline{\Delta x'^2}_{measured} = \overline{\Delta x'^2}_{turbulence} + \sigma_{\Delta x}^2 \tag{4.7a}$$

$$\frac{\overline{\Delta x'^2}_{measured}}{\overline{\Delta x^2}} = TI_x^2 + \frac{\sigma_{\Delta x}^2}{\overline{\Delta x^2}} \tag{4.7b}$$

Dividing Equation 4.7a by the mean squared displacement $\overline{\Delta x^2}$ results in Equation 4.7b. Here, the left-hand-side denotes the measured turbulence intensity. This is a function of a constant and a particle-shift-dependent term. The constant term is in fact the physical turbulence intensity, and the shift-dependent term is associated to the noise. Measurements at different pulse separations then provides multiple pairs of $\overline{\Delta x'^2}_{measured}/\overline{\Delta x^2}$ and $\overline{\Delta x^2}$. TI_x and $\sigma_{\Delta x}$ can then be found by performing a least-squares fit of Equation 4.7b to the experimental data.

4.2.3. Phase-locked, multi-dt PIV implementation

The original scheme of Sciacchitano et al. [42] combines TR-PIV data to obtain image pairs at different pulse separation times. This is not possible in a double-frame system aimed at applications with high flow velocities. Phase-locking allows to repeat a measurement, however. After performing a measurement at a certain pulse separation, the same relative phase can be re-evaluated, using a different pulse separation setting. This is similar to two-camera set-ups used by Persoons and O'Donovan [36] and True and Crimaldi [50], but the additional acquisition systems can be removed thanks to the phase-locking. A downside is that only corresponding double-frame image pairs can be evaluated. This is visualized in Figure 4.3b. In this figure, the measurement is performed at a short pulse separation δt_0. After taking the desired number of samples, the same phase is recorded, now at a longer pulse separation δt_1. This process can be repeated to yield a larger number of pulse separation times, which corresponds to the pyramid height of the pyramid correlation scheme. The process is visualized in the scheme of Figure 4.5, the different steps are categorized in several branches:

1. **Black branch** - measurements are taken at different pulse separation times. The shortest pulse separation, denoted δt_0, adheres to the one-quarter rule, and is processed using conventional methods. The information from this step informs the correlation process of the longer pulse separations. Therefore, the other pulse separation times can ignore the one-quarter rule. This is similar to grid refinement schemes, where only the first pass has to adhere to the one-quarter rule.
2. **Green branch** - the data can now be processed. Each phase-dependent displacement field serves as a first-pass estimator for the subsequent processing step, which has a longer δt: δt_0 informs the processing of δt_1, δt_1 in turn informs the processing of δt_2, and so on. Note that these first-pass displacement fields are the phase-averaged fields.
3. **Red branch** - the correlation maps are all scaled down linearly to the maps of δt_0; this is the homothetic transformation of Sciacchitano et al. [42]. The scaling factor for pulse separation i is then $\delta t_0/\delta t_i$. The correlation maps corresponding to δt_0 are unaltered. Care must be taken that correlation values are normalized. When this is done, an ensemble-average correlation map can be set up. Finding the correlation peak then yields the phase-averaged velocity field $\langle \mathbf{u}(\mathbf{x}) \rangle_\phi$. When all phases are processed, the time-averaged field $\overline{\mathbf{u}}(\mathbf{x})$ can be evaluated and the acoustic velocity field $\tilde{\mathbf{u}}(\mathbf{x}, \phi)$ can be found using Equation 3.2.
4. **Blue branch** - all individual correlation maps are also used to evaluate the fluctuation intensity fields for each pulse separation time. Next, the method of Scharnowski [40] is used to decompose these results in the noise term and turbulence intensity. The noise RMS is defined in pixel, and can be combined with the pulse separation time to give the 'noise velocity' $\mathbf{b}(\mathbf{x})$. The turbulence intensity can be multiplied with the phase-averaged velocity to give the turbulent fluctuation velocity $\mathbf{u}'(\mathbf{x}, \phi)$. Both quantities are often presented in their respective units of pixels and intensity in percents. Combined with the results of the red branch, this completes the quadruple decomposition of Equation 3.1.
5. **Purple branch** - as a last step, the DVR can be directly evaluated. This is owed to the fact that the measurement noise $\sigma_{\Delta x}$ is explicitly available.

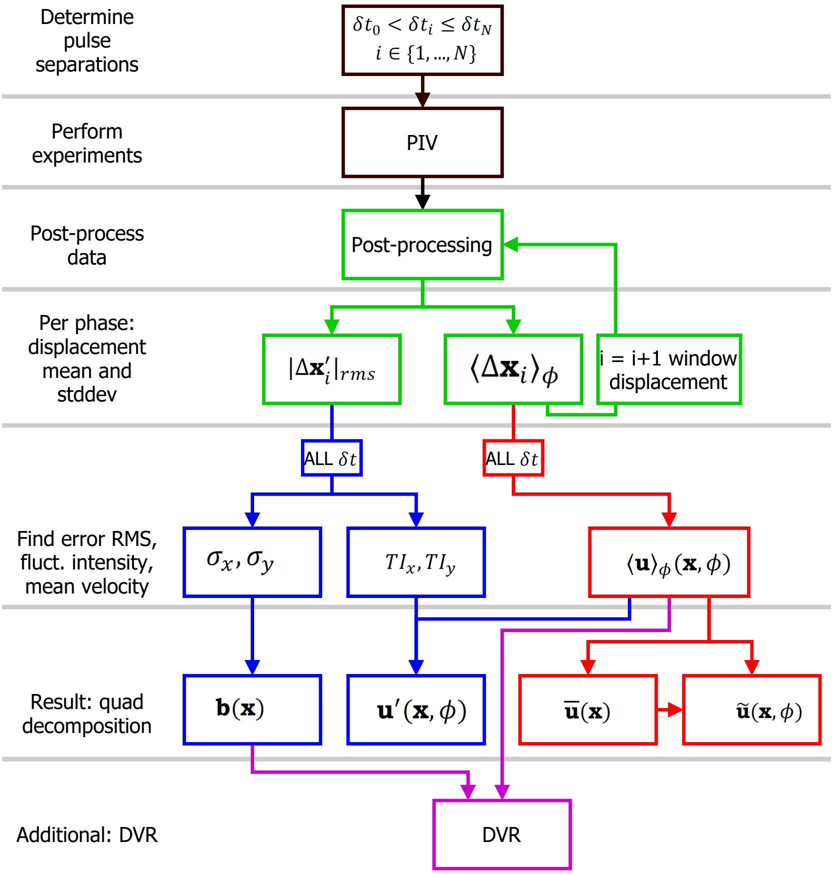
Determine pulse separations
$\delta t_0 < \delta t_i \leq \delta t_N$
$i \in \{1, \ldots, N\}$
Perform experiments
PIV
Post-process data
Post-processing
Per phase: displacement mean and stddev
$|\Delta \mathbf{x}_i'|_{rms}$
$\langle \Delta \mathbf{x}_i \rangle_\phi$
i = i+1 window displacement
ALL δt
ALL δt
Find error RMS, fluct. intensity, mean velocity
σ_x, σ_y
TI_x, TI_y
$\langle \mathbf{u} \rangle_\phi (\mathbf{x}, \phi)$
Result: quad decomposition
$\mathbf{b}(\mathbf{x})$
$\mathbf{u}'(\mathbf{x}, \phi)$
$\overline{\mathbf{u}}(\mathbf{x})$
$\tilde{\mathbf{u}}(\mathbf{x}, \phi)$
Additional: DVR
DVR

Figure 4.5: Schematic overview of the selected MF-PIV implementation, including processing steps to the quadruple decomposition and DVR evaluation.

4.2.4. Pulse separation times and timing limits

The turbulence and noise fitting through Equation 4.7b can be performed using as little as two data-points. Scharnowski [40] perform a regression using 9 points. To reduce recording and processing time, an intermediate number of 4 different pulse separation times is chosen. The pulse separation times are spaced logarithmically between the minimum and maximum value, as this best represents the inverse proportionality of the measured turbulence to the particle displacement (hence pulse separation time) in Equation 4.7b. The pulse separation times to be used are then fully defined by the shortest and longest pulse separation times. All limits considered are discussed below. Only one lower limit for δt_0 is identified, which is discussed first. All other limits mentioned concern the upper limit for δt_N.

Lower timing limit: freestream velocity

As discussed in subsection 4.2.3, the lowest pulse separation time δt_0 must conform to the one-quarter rule, stated in Equation 4.8. Here, d_I denotes the rectangular window size and Δ_{px} the pixel size on the measurement plane. Grid refinement can be used to raise δt_0, but the resulting DVR is the same: the changes in k_g and k_t in Equation 3.6b cancel each other out. It is deemed better to not use grid refinement processing, and set δt_0 to follow the one-quarter rule on the final window size. This allows to spread the pulse separation times as far as possible, which can be seen as maximizing k_t. A very short δt_0 results, which widens the correlation peak base of the pyramid correlation scheme. A large spread in δt will also allow to fit Equation 4.7b over a wider range of data-points, which is expected to improve the quality of the fit. As an added benefit, processing is made computationally less expensive.

$$\delta t_{lim,freestream} = \delta t_0 = \frac{d_I}{4} \frac{\Delta_{px}}{U_0} \tag{4.8}$$

Upper timing limit: relative acoustic phase

The correlation steps shown in Figure 4.3b assume that all samples evaluate the same relative phase. Furthermore, the homothetic transformation used in the ensemble correlation assumes that the displacement vector scales linearly with pulse separation time. To ensure locally linear conditions, all measurements must be performed within a sufficiently short pulse separation: extremely long pulse separation would mean that in fact the first and second images are taken in the preceding and following phase. This limit therefore also ensures that subsequent phase velocity fields are uncorrelated. The time limit can be expressed directly in time-domain and is fixed. The acoustic phase $T = 1/f$ is sampled using N_{phase} phases. A limit can be put on the relative phase, resulting in Equation 4.9. Here, lim_{phase} is defined as the fraction of a relative phase which is still deemed locally linear. For example, taking phase-locked samples at $f = 1000Hz$ in $N_{phases} = 10$ steps results in phases spaced $100\mu s$ apart. A limit of $lim_{phase} = 0.2$ then dictates that 20% of the phase step is deemed as the limit for local linearity, and a time limit of $\delta t_{lim,phase} = 20\mu s$ results.

$$\delta t_{lim,phase} = \frac{lim_{phase}}{N_{phases} f} \tag{4.9}$$

Upper timing limit: acceleration and curvature

Between all double-frames, tracer particles are assumed to follow straight paths at a constant velocity. If this assumption is violated, the velocity estimation is erroneous. Typically, the velocity is underestimated in such cases, as the straight path is the shortest possible [39]. Acoustic velocity results, with the time-averaged flow field subtracted, such as in Figure 2.22 show clear vortices. However, it should be remembered that the flow is dominated by the grazing boundary layer. The phase-averaged flow fields are expected to be nearly curvature-free, and streamline curvature ican be neglected.

Acceleration of particle images may be present, as tracer particles are ejected with a near-zero velocity from the orifices into the grazing boundary layer. Using the set-up described in Chapter 5, $16x16px^2$ interrogation windows and the friction velocity modelled by the Prandtl friction law (see subsection 5.1.1), the centre of the interrogation window closest to the face sheet is expected at a dimensionless wall distance of $7 < y^+ < 47$ for $0.1 < M_0 < 0.8$. This is already a substantial non-dimensional height into the boundary layer. Particles ejected from the orifices are therefore expected to have accelerated to their steady, phase-dependent velocity at this height. It is concluded that effects from acceleration and curvature can be neglected.

Upper timing limit: spatial filtering

Time-scales smaller than the pulse separation time can not be observed. This effectively low-pass filters the velocity fields [40]. Through the flow velocity, this corresponds to a certain spatial scale. The smallest spatial structures of interest are vortices from the orifice. Hence, the orifice radius $D/2$ is taken as the characteristic length scale. Dividing this by the local velocity gives the pulse separation limit associated to spatial filtering of the velocity field. As it is defined as a displacement limit, it is denoted as such in Equation 4.10.

$$\delta t_{lim,displacement} = \frac{D}{2|\mathbf{u}|} \tag{4.10}$$

Upper timing limit: out-of-plane motion and in-plane gradients

At long pulse-separations, particles may be lost due to out-of-plane motion. If particles are lost between both frames, the correlation signal strength is reduced [39]. The liner sample is installed directly in the wind-tunnel walls, and can hence be assumed to be perfectly aligned with the flow. Subsequently, the laser is aligned to a row of orifices. Therefore, out-of-plane motion due to laser sheet misalignment to the main flow is assumed negligible. Some cross-flow may be present, as the vortices from the orifices break down and mix. Sciacchitano et al. [42] mentions that an out-of-plane displacement of 40% of the laser sheet thickness is considered large. This corresponds to an out-of-plane angle of 22^o, assuming a laser sheet thickness and in-plane displacement of half the orifice diameter. Cross-flow components are expected to be much lower than this. Hence, the timing limit associated to out-of-plane loss of particles is dominated by the limit of Equation 4.10, and is not evaluated further.

In-plane gradients can deform the structures within an interrogation window, hindering cross- correlation between the two frames [39]. In-plane gradients of $0.5 pixels/pixel$ are considered large [42]. Note that this limit is mentioned for interrogation window deformation schemes. It is argued that this limit may still be used as an estimation; while window deformation is not used, the ensemble cross correlation improves the accuracy and correlation strength. The gradient limit of $0.5 pixels/pixel$ concerns the gradient between two images of a double-frame pair. As these are taken using a single pulse separation time, magnification factor and pixel size, this limit translates directly into the velocity gradient. The result is shown in Equation 4.11.

$$\delta t_{lim,gradient} = 0.5\left(\frac{\partial u}{\partial y}\right)^{-1} \tag{4.11}$$

Note that the definition of Equation 4.11 only serves as a general estimation. It might show that longer pulse separations can still yield satisfactory correlation strengths, or that correlation strength is reduced at lower pulse separation times. Therefore, the limit of $0.5 pixels/pixel$ is to be re-evaluated for the current purpose.

Combined timing limits and timing range

The discussed limits aim to ensure that all structures of interest can be resolved accurately in space and time, and that cross-correlation remains robust at the longer pulse separation times. The shortest pulse separation time δt_0 is found explicitly from the freestream velocity and the optical set-up. The longest pulse separation δt_N should be maximized until any of the three (four including the implicitly included out-of-plane loss) is violated. The combined statements are shown in Equation 4.12.

$$\delta t_0 = \frac{d_I}{4}\frac{\Delta_{px}}{U_0} \tag{4.12a}$$

$$\delta t_N = min \begin{cases} \delta t_{lim,phase} & = \frac{lim_{phase}}{N_{phases} f} \\ \delta t_{lim,displacement} & = \frac{D}{2|\mathbf{u}|} \\ \delta t_{lim,gradient} & = 0.5\left(\frac{\partial u}{\partial y}\right)^{-1} \end{cases} \tag{4.12b}$$

5

Experimental set-up

This chapter discusses details on the test set-up. Section 5.1 discusses the wind tunnel and its friction velocity and speed of sound. Section 5.2 presents details on the acoustic horn and the liner sample used. The optical set-up of the PIV measurement is discussed in Section 5.3. Finally, particle seeding for PIV is discussed in Section 5.4.

5.1. Wind tunnel facility

The Flow Duct Facility of NLR is a closed cycle wind tunnel, capable of Mach numbers up to $M_0 = 0.8$. The test set-up is shown in Figure 5.1. The channel cross-section is $300 \times 150mm^2$. The liner and horn are both installed on the $150mm$ sides, such that the distance between the face sheet and the opposite wall is $300mm$. The horn is installed in this opposite wall, generating normally incident waves. The laser sheet is introduced at an angle with respect to the liner. Instead of coating the liner with a black finish to absorb the laser light, the liner is machined to a smooth finish. This is done to result in a specular reflection: laser light is reflected to the upstream side of the horn, limiting the amount of diffuse reflections. Diffuse reflections may result in glare and thus locally over-expose the images.

5.1.1. Undisturbed friction velocity

PIV results of Van der Meulen [51] are used to evaluate the tunnel boundary layers. Standard turbulent boundary layers are often modelled closely by the log-law. Equation 5.1 shows the log-law, as discussed by Léon et al. [27]. Here, slightly different constants are used with respect to the classic log-law of White [54]: Léon et al. [27] use $\kappa = 0.42$ and $B = 5.4$.

$$\begin{aligned} u^+ = \frac{u}{u_\tau} &= \frac{1}{\kappa} ln(y^+) + B \\ \text{with: } y^+ &= \frac{u_\tau y}{\nu} \end{aligned} \tag{5.1}$$

The friction velocity u_τ can be found for measured velocity profiles $u(y)$, by finding a value for u_τ which fits Equation 5.1 best to the experimental data. This is done using a least-squares fit in the region $35 \leq y^+ \leq 350$, which is the region in which the log-law is valid [54]. The fitted boundary layer profiles are shown in Figure 5.2, where it can be seen that close matches between the measured profiles and theoretical log-law can be found. The corresponding friction velocities are listed in the second column of Table 5.1. These results are obtained with a magnification of $F_{mag} = 0.38$ and are processed with $16x16px^2$ windows with 50% overlap. This results in vectors spaced $0.14mm$ on the measurement plane. The first 2 points over the liner produced spurious results, and are hence excluded. This results in the first vector located $0.39mm$ above the liner surface; the corresponding y^+ value is often high, and can make that the friction velocity fit is performed on few data points.

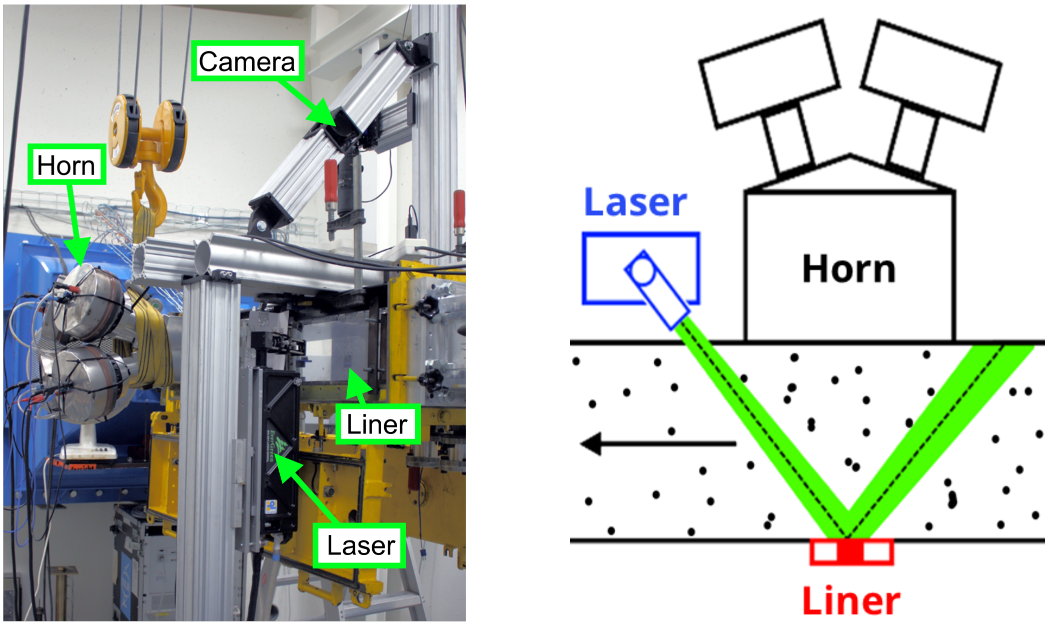

(a) Picture of the test section, looking in upstream direction. The liner sample is installed on the far vertical wall, opposite the horn.

(b) Schematic top view of the test section, from the perspective of the camera. drawing is not to scale. The in-situ liner sample (red, bottom) is installed opposite the horn (black, top). The laser (blue, top left) is installed such that the laser sheet is reflected to the other side of the horn.

Figure 5.1: Depiction of experimental set-up in the FDF.

Table 5.1: Friction velocity results, as fitted to the profiles shown in Figure 5.2, compared to theoretical values of Equation 5.2.

Mach number $[-]$	Fitted $[ms^{-1}]$	Prandtl $[ms^{-1}]$ (eq. 5.2)	Difference $[-]$
0.3	3.71	3.71	0.1%
0.4	4.76	4.83	1.1%
0.5	5.91	5.94	0.6%
0.6	6.98	7.02	0.6%
0.7	8.29	8.10	-2.2%

The friction velocity in smooth ducts is modelled by Prandtl's friction law for smooth pipes, shown in Equation 5.2 [37]. Re_{D_h} is the Reynolds number based on the duct's hydraulic diameter, which can be taken as the duct height [27]. Using the definition of the friction factor $f_D = 4C_f = 8(u_\tau/U_0)^2$ [27], an implicit expression is found for the friction velocity, based on the free-stream velocity U_0 and its associated Reynolds number. Pope [37] shows that Equation 5.2 holds well for $Re_{D_h} \geq 3 \times 10^3$.

$$\begin{aligned} \frac{1}{\sqrt{f_D}} &= 2.0log_{10}\left(R_{D_h}\sqrt{f_D}\right) - 0.8 \\ \frac{U_0}{\sqrt{8}u_\tau} &= 2.0log_{10}\left(R_{D_h}\sqrt{8}\frac{u_\tau}{U_0}\right) - 0.8 \end{aligned} \tag{5.2}$$

Modelled values using Equation 5.2 for the FDF are included in Table 5.1. It can quickly be observed that modelled and measured (fitted) values for the friction velocity agree very well. Results are within $\pm 2.2\%$ of each other. It is concluded that the friction velocity of the incoming boundary layer in the FDF is closely modelled by the friction law of Equation 5.2.

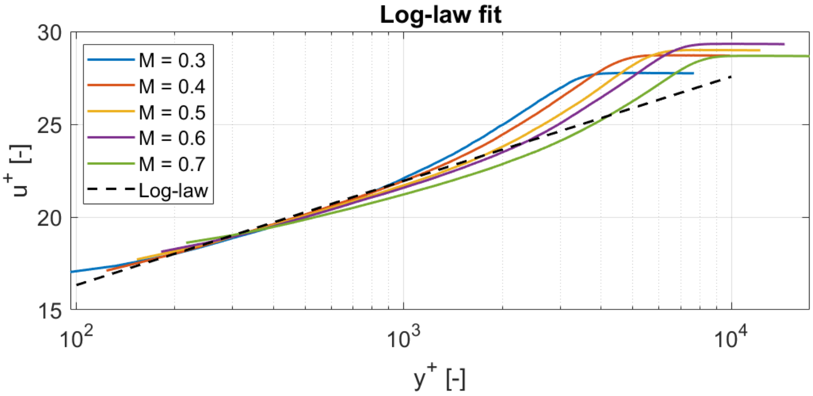

Figure 5.2: Comparison between experimental (PIV) and and log-law boundary layer profiles fitted to the log-law between $35 \leq u^{+} \leq 350$. Results obtained with a smooth wall and no acoustic forcing.

5.1.2. Speed of sound

At higher wind-tunnel velocities, the pressure in the test section decreases. Bernoulli's law states that $p + \frac{1}{2}\rho U_0^2 = p_0$, or $p \propto -U_0^2$. Using the definition for the speed of sound in an ideal gas $c_0 = \sqrt{\gamma p/\rho}$, it can be seen that a linear decrease in the speed of sound is expected as a result, i.e. $c_0 \propto -U_0$. In the FDF, the freestream Mach number and velocity is measured using the dynamic and total pressures q and p_0. Combining Bernoulli's law and the speed of sound, expressions for the Mach number and velocity can quickly be obtained, and are shown in Equation 5.3.

$$M_0 = \frac{U_0}{c_0} = \sqrt{\frac{2q}{\gamma p_0}} \tag{5.3a}$$

$$U_0 = \sqrt{\frac{2q}{\rho}} \tag{5.3b}$$

The conditions measured in the current test campaign are shown as scattered data in Figure 5.3. To simplify further analyses, a linear fit is performed to this data, and an upper limit to the standard speed of sound of $343ms^{-1}$ is imposed. The resulting fit is given in Equation 5.4, and is included as the solid line in Figure 5.3. Unless otherwise specified, this velocity-dependent speed of sound is used in all subsequent results.

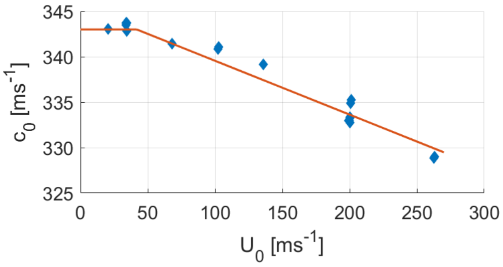

Figure 5.3: Measured and fitted speed of sound versus wind-tunnel velocity

$$c_0 = min\begin{cases}343\\345.47 - 0.0592.*U_0\end{cases} \tag{5.4}$$

5.2. Acoustic set-up

The acoustic set-up consists of two parts: the in-situ instrumented liner sample and the acoustic source. Both items are discussed briefly in this section.

5.2.1. Instrumented liner sample

The face sheet geometry of the instrumented liner sample is depicted in Figure 5.4, with all parameters listed in Table 5.2. Orifices are $1mm$ in diameter and organized in rows with a pitch of $4.259mm$. Each row is offset, so that equilateral triangles are formed. The liner is installed rotated 90^o by mistake, resulting in a pitch of $7.4mm$ instead. The face sheet thickness is $\tau = 0.5mm$, which leads to a corrected face sheet thickness of $\tau^* = 1.3mm$ (cf. subsection 1.2.1). For ease of microphone installation, the backing honeycomb is removed, showing a $29.7 \times 29.7mm^2$ cell instead. This is still small enough to result in a locally reacting liner, as $D \ll \lambda$. The backing depth is $L = 20mm$. Finally, from these parameters, a porosity of 5% can be found. In earlier broadband measurements, the resonant frequency without grazing flow is determined at $f_0 = 2250Hz$.

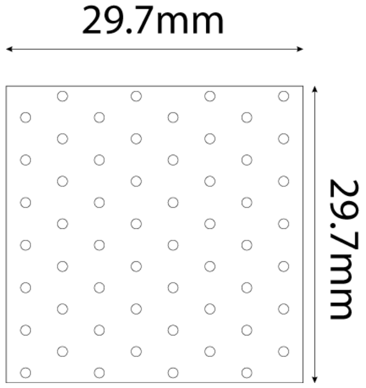

Figure 5.4: Dimensions of in-situ liner sample.

Table 5.2: Liner sample properties

Name	Symbol	Value	Units
Orifice diameter	d	1	mm
Orifice pitch	Δ_{or}	7.4	mm
Face sheet thickness	τ	0.5	mm
Corrected face sheet thickness	τ^*	1.3	mm
Backing cell size (square)	D	29.7×29.7	mm^2
Backing depth	L	20	mm
Porosity	σ	5	%
Resonant frequency	f_0	2250	Hz

5.2.2. Speakers and horn

Sound is introduced by the horn shown in Figure 5.1. The horn consists of four BMS 4590-8 2 inch coaxial drivers. The four drivers connect in a single channel, to which a BMS 2230 $90x55^o$ horn is mounted. The wide 90^o dispersion angle is in the horizontal plain, in which the liner is located as well. The maximum sound pressure level of this set-up at $2kHz$ is approximately $SPL_{max} = 148dB$, as measured at the face sheet of the in-situ liner sample.

5.2.3. Effective sound pressure level

A maximum value of $SPL = 148dB$ is intended in the current tests. At the beginning of the test, the horn input is calibrated to result in $148dB$ at a tonal sound at $2kHz$ on the face sheet. This level is kept constant during the test. As a result, the sound pressure level reduces at higher tunnel Mach numbers, as the acoustic field is convected downstream. The effective SPL reached in the high-SPL Mach sweep is shown in Figure 5.5. It can be seen that the sound pressure level is also low for the no-flow case. No clear explanation is found for this observation, it may be that reflections at the tunnel walls make for a complex acoustic field in the absence of a grazing flow.

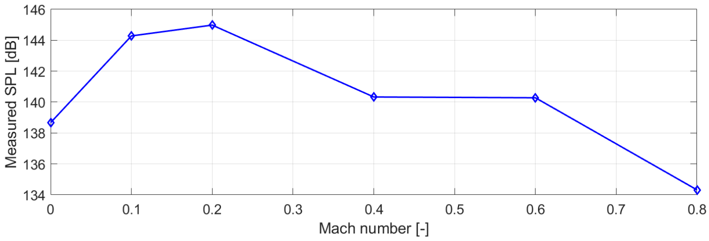

Figure 5.5: SPL measured at $f = 2kHz$ at the face sheet microphone.

Table 5.3: Laser specifications [38].

Name	Value	Units
Wavelength	532	nm
Pulse energy	$70 - 200$	mJ
Nominal beam diameter	6.35	mm
Repetition rate	15	Hz

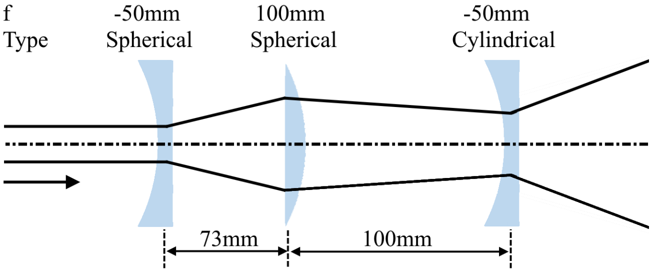

Figure 5.6: Laser sheet optics, not to scale, and indicated distances are approximate. Top view, as in Figure 5.1.

The dependency of the sound pressure level on the tunnel Mach number can be easily avoided. Instead in a no-flow condition, the calibration of the horn is conducted at the highest envisioned tunnel Mach number. At lower Mach numbers, the horn output is regulated such that the same sound pressure level is measured at the face sheet. This way, the maximum SPL is kept constant throughout the test.

5.3. Optical set-up

Next, the optical set-up is presented. This is comprised of the laser optics and the imaging system.

5.3.1. Laser sheet

Laser light is provided by a Quantel Evergreen Nd:YAG laser [38]. The laser head is attached directly to the test section, as seen in Figure 5.1. This laser emits double-pulses at a wavelength of $\lambda_{laser} = 532nm$ up to pulse energies of $200mJ$ and repetition rates of $15Hz$, as shown in Table 5.3.

Optics

The round laser beam is formed into a sheet using a set of two spherical and one cylindrical, as depicted in Figure 5.6. The distance between the last lens and the face sheet is approximately $450mm$. The first two lenses expand and focus the beam. The last, spherical lens expands the height of the laser beam, forming a sheet. Theoretically, a laser sheet with a thickness of $0.4mm$. In practice, however, the laser sheet is observed to be thicker. Laser sheet thickness is estimated to be approximately $0.7mm$.

Alignment

Laser alignment is adjusted using $0.3mm$ thick shims under the laser head. During alignment, it is observed that the set-up is very sensitive to the position of the laser sheet within the orifices. This is illustrated in Figure 5.7. At a baseline positioned, aligned through the orifice centres, severe reflections are seen in the PIV camera recordings. Raising the laser by one shim, the laser sheet is aligned slightly above the orifice centre, towards the camera. This reduces the severity of direct reflections. It is believed that the orifice edges make for strong reflections. In the configuration shown in figures 5.7c-5.7d, these reflections are on the edges on the camera. As the light is reflected away from the edges, this set-up ensure that light is reflected away from the lens.

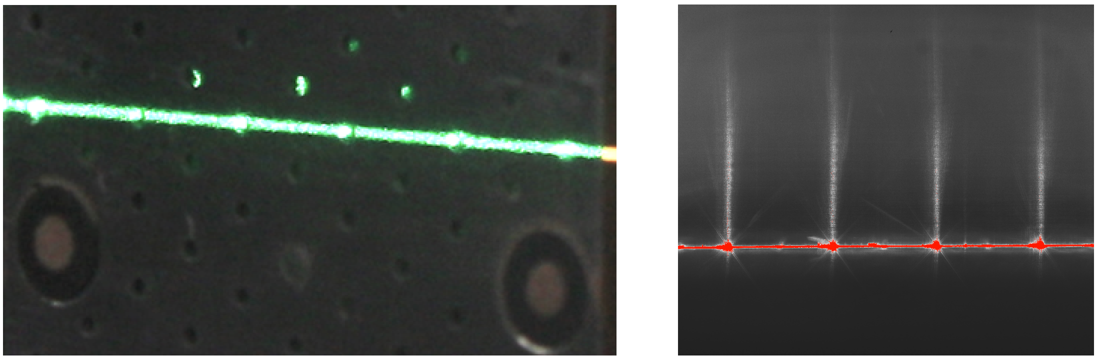

(a) Baseline position, aligned through orifice center.

(b) Corresponding image from PIV camera, mean of 100 samples without flow or seeding.

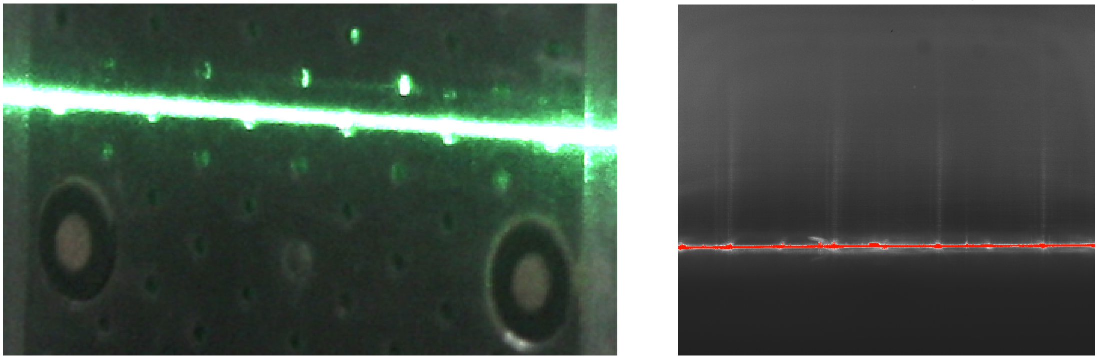

(c) Laser head raised by one shim of $0.3mm$. Laser sheet aligned slightly above the orifice centreline.

(d) Corresponding image from PIV camera, mean of 100 samples without flow or seeding.

Figure 5.7: Laser sheet height adjustment and orifice reflections. Laser intensity is kept constant throughout these tests, and is scaled 0-2000 counts in the PIV images.

Laser intensity

Another parameter influencing the severity of the reflections is the laser intensity. A sweep of small recordings with different pulse intensity settings is performed and processed using a standard multi-pass processing. The results are used to estimate an adequate laser intensity setting. Before each measurement, the first pulse intensity is set, after which the intensity of the second pulse is adjusted until overall particle intensity is visually matched. This step is performed as a large difference in intensity is seen between the two pulses, when set at an equal intensity setting. 100 samples are recorded at a Mach number $M_0 = 0$, with a pulse separation time of $\delta t = 0.46\mu s$. Processing is done in two passes, refining from $48x48px^2$ to $16x16px^2$ windows.

Figure 5.8 shows three selected results from this sweep. Consult the image caption for details on the measurement and processing parameters. At the lowest intensity setting of 44% and 39% for the first and second pulse, it is seen that laser intensity is too low: the standard deviation shows very high values throughout the boundary layer. This is attributed to measurement noise, as the particles are not illuminated bright enough. At the intermediate setting of $51/45\%$, this noise is seen to be reduced, and both the mean and standard deviation results look clean. At the highest setting shown of $82/76\%$, a clear reflection is seen over the orifice. As a result, displacement is locked, and a high standard deviation is seen, again attributed to measurement noise. Three more intensity pairs are tested between $51/45\%$ and $82/76\%$, but $51/45\%$ remains the highest possible laser intensity that does not show the reflection. This setting is used throughout all measurements.

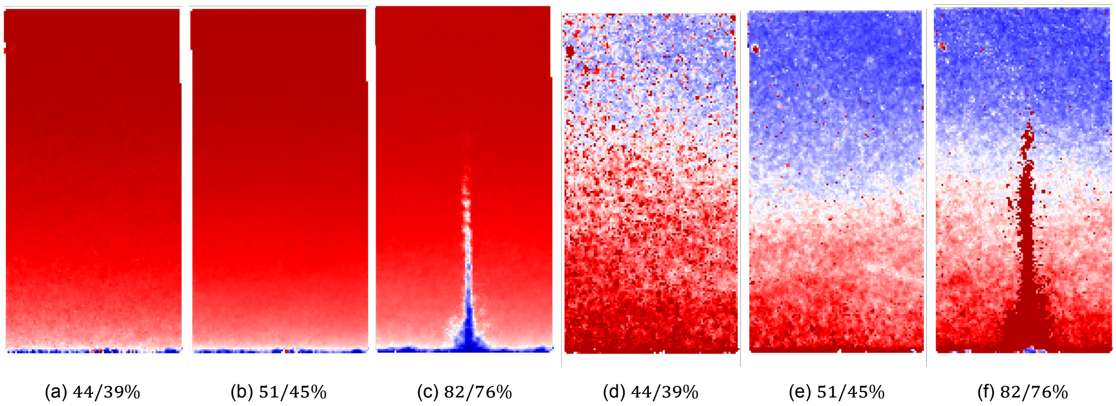
(a) 44/39% (b) 51/45% (c) 82/76% (d) 44/39% (e) 51/45% (f) 82/76%

Figure 5.8: Mach 0.3 laser intensity tests. $16x8mm^2$ domain centred over an orifice. $\delta t = 0.46\mu s$, standard processing over 100 samples, $1x48x48px^2$ first pass with a $1x16x16px^2$ final pass. Subfigures a-c show mean velocities, scaled $0 - 110ms^{-1}$. Subfigures d-f show the associated standard deviation fields, scaled $0 - 12ms^{-1}$.

5.3.2. Imaging system and calibration

Imaging is performed using a LaVision Images sCMOS camera [24], paired with a Nikon $200mm$ f/4 macro lens. A $20mm$ extension ring is used to allow an object distance smaller than the lens's minimal focusing distance of $500mm$. A magnification factor of $F_{mag} = 0.56$ is reached using this set-up, resulting in a field of view of $30x25mm^2$. The lens is set at an f-stop of $f/8$. The resulting depth of field is then calculated using Equation 5.5 [41]. A value of $\delta_z = 1.3mm$ is found. This is slightly larger than the estimated laser sheet thickness, and should allow to have all particles in focus.

$$\delta_z = 4.88\lambda_{laser}f_{\#}^2\left(\frac{F_{mag}+1}{F_{mag}}\right)^2 \tag{5.5}$$

The field of view (FOV) is set such that the entire active area of the liner, over the backing cell, is in view. With the orifice pitch of $7.4mm$ from Table 5.2, this results in 4 orifices in view. The camera is positioned with the bottom of the FOV slightly below the face sheet; this is done to capture less reflections from the face sheet. This is also clearly seen in the PIV images in Figure 5.7. The face sheet is $7.5mm$ above the bottom of the image, a usable height of $17.5mm$ above the liner. The positions of the face sheet and orifices are determined using a picture from the PIV camera using ambient lighting. All results are calibrated such that the origin is located in the centre of the most upstream orifice. This calibration also reveals that a small height over the face sheet is not visible due to a steady reflection. The first $0.6mm$ above the facing is obscured by this reflection, and is removed. Care should be taken not to find the face sheet location from a boundary layer velocity profile: within the reflection, displacement becomes locked to a displacement of $\Delta x = 0px$. As interrogation windows include more and more of the reflection towards the wall, the displacement slowly approaches 0 towards the wall. The resulting velocity profile resembles a boundary layer, which is resolved up to a near-zero velocity. The location at which the zero-velocity is estimated is $\approx 0.5mm$ above the actual face sheet position.

Due to the large magnification factors, the standard calibration plates are found to be unsuitable, as only several very large dots are in the field of view. Some local deformations in the bottom of the field of view are seen. These are attributed to the edges of the PMMA windows, which may be slightly stressed. A finer calibration plate is required to correct for these distortions. This is made by printing a custom field of dots at 1200 dots per inch. This sheet is then attached to a thick aluminium plate using thin double-side tape. The panel that shows the best print and calibration results uses dots with a $0.5mm$ diameter, and a pitch of $0.75mm$. The used calibration image is shown in Figure 5.9. Calibration in Davis 8.4 is done using a 3^{rd} order polynomial, which yields a fit RMS of 0.897 pixels and a mapping of $86.78px/mm$.

Focus is adjusted such that the dots in Figure 5.9 show the highest edge quality. The calibration plate is positioned slightly above the orifice centres, which should correspond to the location of the laser sheet. Image focus is very sensitive due to the low depth of field. Out-of-focus particles may be expected, in case the image focus is not perfect. The seeding and particle image quality is addressed in the next section.

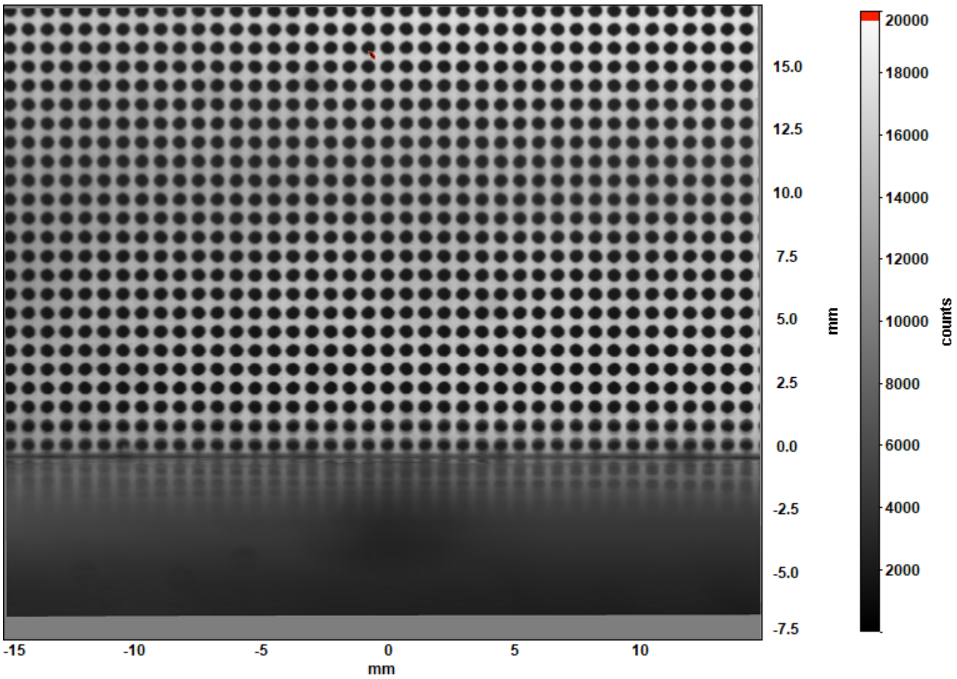

Figure 5.9: Dewarped PIV calibration image. Dots are printed with a diameter of $0.5mm$, spaced $0.75mm$ apart.

5.4. Seeding

The tunnel is seeded globally using di-ethylhexyl-sebacate (DEHS) particles. Seeing is introduced in the reverberation chamber after the test section. This section addresses the flow seeding for PIV. First, it is evaluated whether flow tracking and particle image size is deemed adequate. Next, qualitative observations made during testing are presented, followed finally by a quantitative evaluation of the seeding density.

5.4.1. Seeding particles Stokes number

An important metric regarding the seeding particle is the Stokes number. As explained by Raffel et al. [39], this metric indicates whether the seeding particles respond quickly to fluid accelerations. The Stokes number is defined as the ratio between characteristic timescales associated to the particle and the fluid, as shown in Equation 5.6. The seeding particle time-scale t_p depends on the particle diameter, density and viscosity.

$$Stk = \frac{t_p}{t_f} = \frac{2\mu s}{l_f/\Delta u} \tag{5.6}$$

A typical value for DEHS is $t_p \approx 2\mu s$ [39]. To evaluate the fluid response time, it is common to find a time-scale by dividing length- and velocity scales. Raffel et al. [39] suggest the boundary layer thickness and freestream velocity for turbulent flows, and the vortex diameter and swirling velocity for vortex flows. Both criteria are checked, as both phenomena are of interest. A third check is performed using the acoustic period as a timescale directly. The results are listed in Table 5.4. Note that for the vortex shedding case, the vortex radius is used with a velocity order of magnitude estimation of $1ms^{-1}$. This is done to estimate the Stokes number for this case on the conservative side. For $Stk < 0.1$, good fluid tracking is obtained [39]. It is quickly seen that all three criteria result in values $Stk \ll 0.1$, hence fluid tracking is adequate.

Table 5.4: Seeding Stokes numbers, with particle response time $t_p = 2\mu s$.

Situation	$l_f[mm]$	$\Delta v[ms^{-1}]$	$t_f[\mu s]$	$Stk[-]$
Boundary layer	$\delta_{99} = 14$	274	51.0	0.04
Vortex shedding	0.5	1	500	0.004
Acoustic period	N/A	N/A	$1/f = 500$	0.004

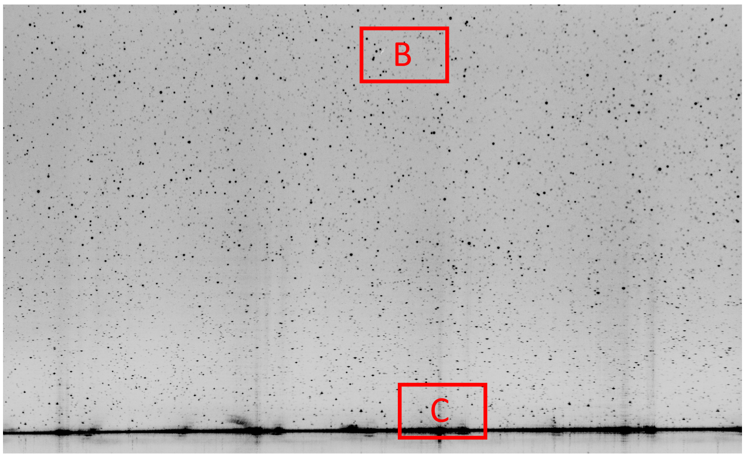

(a) Entire image, cropped to exclude the region below the face sheet.

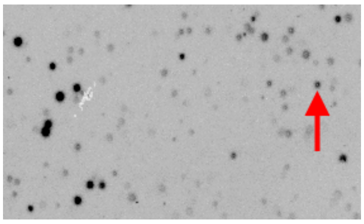

(b) Detail B.

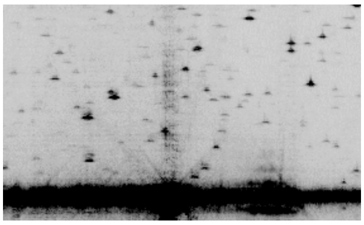

(c) Detail C.

Figure 5.10: Typical raw PIV image. Intensities are scaled $0 - 2000$ counts.

5.4.2. Particle image size

The DEHS particles have a modal diameter $d_p = 0.25\mu m$ [22]. The imaged particle size depends on the physical size $F_{mag}d_p$, but also on diffraction effects. Diffraction depends on the wavelength λ, the magnification factor and the f-stop $f_\#$. The combined statement for the imaged particle size is shown in Equation 5.7 [39]. Using the parameters in Section 5.3, an imaged particle size of $d_{p,img} = 16.2\mu m$ results. This corresponds to $2.5px$, well inside the optimal range of particle images sizes of $2 - 3px$ [39]. Observed particle size is discussed in the following section.

$$d_{p,img} = \sqrt{\left(F_{mag}d_p\right)^2 + d_{diff}^2} \qquad (5.7)$$
$$\text{with: } d_{diff} = 2.44\lambda f_\#\left(1 + F_{mag}\right)$$

5.4.3. Qualitative observations

Next, the quality of the seeding is addressed. This is started by evaluating PIV images qualitatively. Figure 8.23 shows a typical raw image, obtained at Mach 0.1. Several observations from testing are demonstrated using the two details, shown in subfigures b-c. First, the detailed section 'B' considered. In the left side of the figure, a damaged spot on the camera sensor can be seen; the sensor has been damaged during an earlier test. This spot is located approximately $15mm$ above the face sheet, just outside the boundary layer.

In Figure 5.10b, the largest particles are seen to be $\approx 10px$ in diameter, which is large. The bulk of the small particles seen throughout multiple measurement is at a size of $d_{p,img} \approx 4px$. In all recordings, however, a large amount of particles with $d_{p,img} \approx 10px$ remains visible. As the range $4 \leq d_{p,img} \leq 10px$ is much larger than the estimation from Equation 5.7, it is argued that the images are slightly out of focus. Several non-Gaussian particles are seen throughout the images, the most pronounced case in Figure 5.10b is indicated by the arrow. This is only seen when using the intensity scaling used in Figure 8.23. Using a slightly lower range reveals a higher seeding density, as there is a large amount of particles at an intensity below 1000 counts. Furthermore, these particles do not show the non-Gaussian nature. This further suggests that some particles are slightly out of focus.

The detail in Figure 5.10c shows several effects near the face sheet. First, it shows the steady reflection of the face sheet. Next, a weak reflection from the orifice is still seen, creating a vertical band. Finally, the deformation discussed in subsection 5.3.2 is seen: particles are clearly stretched in x-direction. The degree of stretching reduces with y, and is not visible from $6.5mm$ above the face sheet. The deformation is rather steady, and no direct influence on cross-correlation is observed.

5.4.4. Seeding density

With the large particle sizes and low seeding density found from the qualitative observations, the intended $16x16px^2$ windows may contain too few particles for a robust cross-correlation. Furthermore, test points at higher Mach numbers required frequent seeding. It is attempted to evaluate the seeding density using the 'particle seeding density' filter in LaVision Davis 10. First, a sliding average of 9 images is subtracted. Next, the seeding density filter is applied with a particle threshold at 90 counts, which is visually established to be well above the noise floor. For the final smoothing step, a filter length of 16 pixels is used. For each Mach number, the first relative phase ($\phi = 30^o$) is used, at the shortest $\delta t = \delta t_0$). As the tunnel is seeded before each of these measurements, these sets allow a fair comparison between cases. Seeding density is averaged over all 1000 samples per measurement, and over the entire field up to $1mm$ above the face sheet; this is done to not count within the steady face sheet reflection.

First, it is checked whether the cases with high Mach numbers can still be seeded properly. Figure 5.11a shows the seeding density as a function of Mach number. No clear dependency is seen. Instead, it is concluded that the seeding density depends on arbitrary factors such as time since seeding, and initial seeding amount.

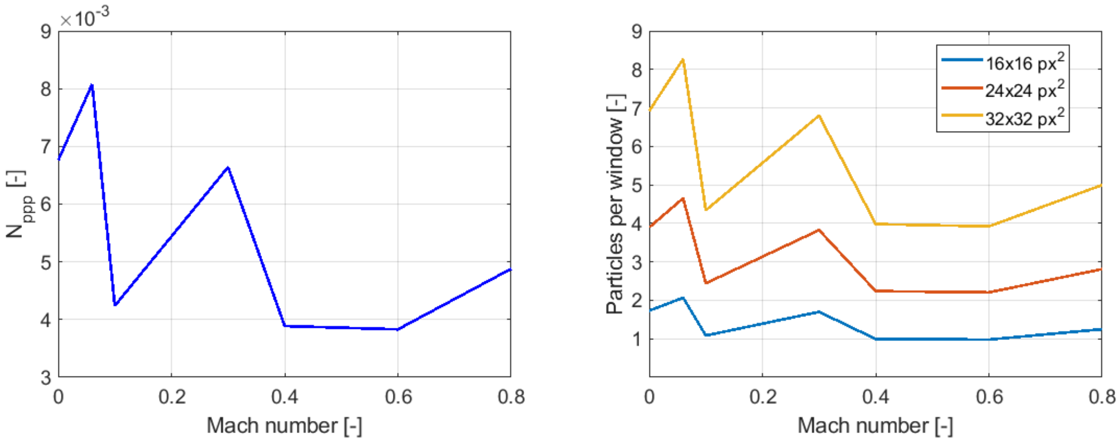

(a) Particles per pixel, N_{ppp}.

(b) Corresponding number of particles per interrogation window, for different window sizes.

Figure 5.11: Evaluation of seeding density at tested Mach numbers. First phase, δt_0 taken of each datapoint.

Next, the associated number of particles per window are shown in Figure 5.11b for three proposed final window sizes. It can be seen that $16x16px^2$ interrogation windows are estimated to result in ≈ 1 particle in each window. In test processing runs, it is also observed that high fluctuation intensities are obtained using such small windows. This is consistent with the estimation from Figure 5.11b. $32x32px^2$ interrogation windows are used in stead of the intended $16x16px^2$ windows to obtain a more robust cross-correlation with the low seeding density.

Finally, the decay in seeding density over time is evaluated. During testing, the tunnel is seeded at the start of each data-point. Seeding density is visually monitored during the test, and increased if the density is deemed to become low. The higher-Mach cases required frequent seeding, the Mach 0.8 measurement even required continuous seeding due to a rapid decay. Figure 5.12 shows results for one full measurement at Mach 0.4 and 0.6. Here the seeding density is only averaged spatially, and not in time over all samples. Both measurements show a comparable seeding density at the start. This is expected, as the tunnel is seeded at the start of each measurement. A decay is seen shortly after the start of each test, however. The seeding density in the Mach 0.4 test decays with 0.0007 particles per pixel per minute. The Mach 0.6 set shows a stronger slope of $\partial N_{ppp}/\partial t = -0.0011$ per minute. This shows that seeding density may vary per measurement, but also within each measurement. All measurements are conducted with the seeding density visually maintained at the same levels as those in figures 5.11-5.12. Therefore, no persistent problems are expected with regards to the seeding density.

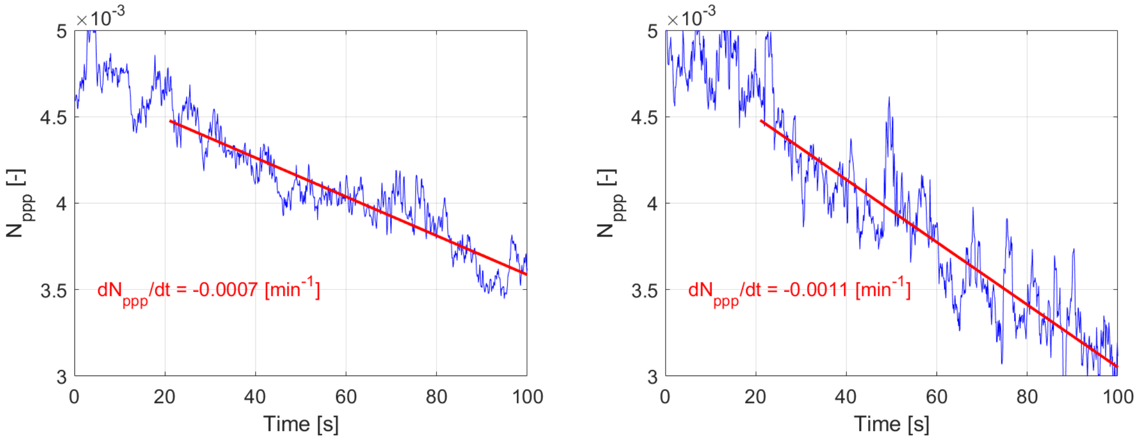

(a) $M_0 = 0.4$ (b) $M_0 = 0.6$

Figure 5.12: Time-dependent seeding density. Running average over 20 samples, with a linear curve with gradient displayed.

6

Data acquisition

In this chapter, data acquisition parameters are presented for both measurement techniques. Microphone recording parameters are shown in Section 6.1. The rest of the chapter focuses on the acquisition of PIV samples. Section 6.2 discusses the number of double-frame samples recorded. The timing range and chosen pulse separation times are an important factor introduced by the multi-δt method. Pulse separation times and timing control are presented in sections 6.3-6.4. Finally, Section 6.5 presents the test matrix of the experiment.

6.1. Microphone recording parameters

In-situ readings are sampled at a frequency of $f_s = 10.24kHz$. According to the Nyquist criterium, this allows to resolve a maximum frequency of $f_s/2 = 5120Hz$. This is more than twice the resonant frequency of the liner sample. A block size of $N_s = 4096$ samples is used in the Fourier transform for the impedance calculation, which allows a frequency resolution of $f_s/N_s = 2.5Hz$. Hanning windows with 50% overlap are used. Finally, the recording time is set at $T_s = 20s$. This allows to average impedance results over $f_s * T_s/N_s * (1/50\%) = 100$ processed measurements.

The NLR acoustic data acquisition software is linked directly to the wind tunnel monitoring system; each in-situ measurement is paired with a measurement of tunnel conditions. Before each measurement, the gains on the microphone amplifiers are automatically set.

6.2. PIV sample size

The sample size of the PIV measurement is directly related to the measurement uncertainty. This lays out the statistical framework of uncertainty, and determines the sample size used.

6.2.1. Uncertainty due to measurement noise

The measurement uncertainty is examined using previous test results of [51]. Turbulence measurements were carried out without acoustic forcing, at a tunnel Mach number of $M_0 = 0.1$ and pulse separation times $\delta t = [20, 40, 60, 80, 100]\mu s$. The multi-$\delta t$ information allows to resolve the measurement noise, as explained in subsection 4.2.2. The pulse separation times correspond to particle image displacements of $\overline{\Delta x} = [44, 89, 133, 178, 222]px$ in the freestream. A measurement was performed with $\delta t = 10\mu s$, but this gave erroneous results and is excluded from the analysis. The datasets are reduced to an $8mm$ wide area outside the boundary layer, between $16 \leq y \leq 25mm$ to reduce computational effort. These sets are then processed in 3 passes from $64x64px^2$ to $16x16px^2$ windows; the first pass is performed using a constant reference velocity of $34.3ms^{-1}$. The turbulence intensity is evaluated and averaged over the selected domain. The noise decomposition of subsection 4.2.2 is then applied, yielding a turbulence and noise term.

This processing is repeated for different sample sizes: the original recording contained 1000 image pairs, from which subsets with $N = [14, 20, 50, 100, 200, 500, 1000]$ samples are created. These subsets are evenly spaced over the entire recording to reduce measurement bias due to slow, physical changes during the measurement. The result of this evaluation is shown in Figure 6.1. Up to a sample size of 100 image pairs, seemingly random behaviour is observed. This can be explained as these bases are too small to allow for any meaningful statistical analysis. From 100 samples and higher, however, a clear convergence can be seen; the convergence rate between 10^2 and 10^3 samples is -0.48. This corresponds very well to the theoretical rate of $-1/2$, which is the convergence rate of Monte-Carlo methods, where random samples are drawn of a probability density function. The correlation peak positioning error at the highest pulse separation directly affects the DVR (cf. Equation 4.6). A sub-pixel accuracy of 0.1 is used in all estimations thus far. To comply to this value, 1000 image pairs are recorded for each measurement.

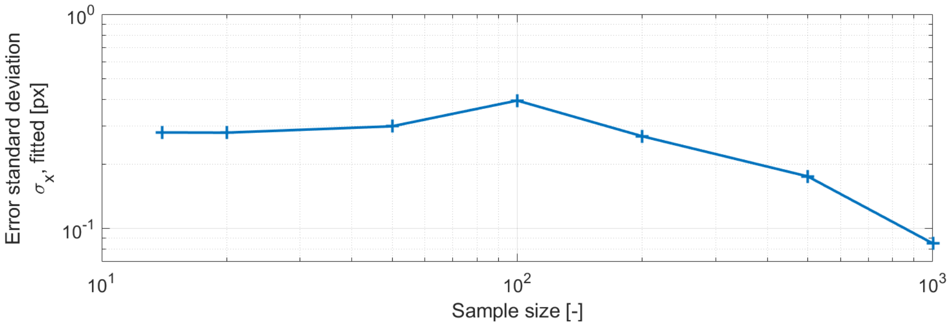

Figure 6.1: Convergence of measurement error with sample size (number of image pairs).

6.2.2. Uncertainty due to turbulence

The previous analysis concerned the measurement error. The turbulent fluctuations introduce another uncertainty. PIV measurement uncertainty is discussed by Wieneke [55]. It is assumed that samples are normally distributed, with a standard deviation σ_x. The uncertainty UC for the mean and fluctuating velocity components for N independent samples are shown in Equation 6.1. All samples in the current framework are uncorrelated, due to the low acquisition frequency. For time-resolved measurements, a further correction is needed to calculate the effective number of independent samples [55].

$$UC_{mean} = \frac{\sigma_x}{\sqrt{N}} \tag{6.1a}$$

$$UC_{\sigma_x} = \frac{\sigma_x}{\sqrt{2(N-1)}} \tag{6.1b}$$

The acoustic velocity in Equation 3.2 is a mean velocity. Away from the orifices, the acoustic velocity components are assumed in the order of magnitude as the incoming acoustic velocity. The incident velocity due to a wave of normal incidence can be found based on the sound pressure level and ambient air properties, as shown in Equation 6.2 [27]. The incident pressure RMS amplitude is defined from the sound pressure level in Equation 2.11c. Near the orifices, the liner response amplifies the velocities, and Equation 2.11b can be used to estimate its RMS value.

$$|\tilde{v}|_{rms} = \frac{c_0}{\gamma} \frac{|\tilde{p}|_{rms}}{p_0} \tag{6.2}$$

Next, the uncertainty is estimated and compared to the acoustic velocity scales of interest. The uncertainty is dominated by the standard deviation of the samples, hence by the turbulence level. A level of $TI = 10\%$ is used, typical for the turbulence level within a turbulent boundary layer [54]. Table 6.1 shows the estimated RMS values for the turbulent fluctuations, and the associated uncertainties, for different Mach numbers. Similarly, Table 6.2 shows the estimated velocity scales for different sound pressure levels.

Table 6.1: Estimated uncertainty levels of Equation 6.1a, with $\sigma_x/U_0 = 10\%$ and $N = 1000$.

Mach $[-]$	σ_x $[ms^{-1}]$	UC_{mean} $[ms^{-1}]$
0.1	3.43	0.08
0.2	6.86	0.15
0.3	10.29	0.23
0.4	13.72	0.31
0.5	17.15	0.38
0.6	20.58	0.46
0.7	24.01	0.54
0.8	27.44	0.87

Table 6.2: Estimated acoustic velocity RMS and orifice velocity RMS.

SPL $[dB]$	$\lvert\widetilde{v}_{inc}\rvert_{rms}$ (eq. 6.2) $[ms^{-1}]$	$\lvert\widetilde{v}_{or}\rvert_{rms}$ (eq. 2.11b) $[ms^{-1}]$
120	0.05	0.53
125	0.09	0.94
130	0.15	1.67
135	0.27	2.96
140	0.48	5.27
145	0.86	9.36
148	1.21	13.23

Tables 6.1-6.2 are now used to estimate whether the statistical (un)certainty is appropriate for the cases of interest. This is done by three regions of interest, listed below:

- **Far field**: the far field is the region outside of the boundary layer, where the incident acoustic velocity $|\widetilde{v}_{inc}|_{rms}$ is to be resolved. This velocity is in the same order of magnitude as the uncertainty level. In the far-field, however, the turbulence level is an order of magnitude lower[54]. As a result, the uncertainty also reduces by one order, and the acoustic velocity can be resolved in the far field.
- **Orifices**: near the orifices, the higher uncertainties of Table 6.1 do apply. In Table 6.2, it can be seen that the orifice velocity is typically one order higher than the uncertainty level, thanks to the amplification from the liner response. It is therefore expected that the orifice velocity can be resolved with sufficient accuracy.
- **Vortex shedding region**: the third region of interest concerns the lower portion of the boundary layer, where vortex shedding occurs (cf. Figure 2.22). Here, the acoustic velocity components are expected to be in the order of $|\widetilde{v}_{inc}|_{rms}$, and the uncertainty level as in Table 6.1. This quickly shows that for the higher-Mach cases, the acoustic velocity is in the same order of magnitude as the uncertainty level. Here, the acoustic velocity can not be resolved accurately. Moreover, the parameter of interest in this region is the vorticity. As this is a derived quantity, errors in the velocity results will be amplified in the vorticity.

Concluding, $N = 1000$ samples do not suffice to directly resolve the acoustically induced vorticity in the boundary layer. To achieve an uncertainty level of $0.15ms^{-1}$, which is the acoustic velocity at the low sound pressure level of $130dB$, $N = 35.000$ samples are required. Increasing the sample size is not a viable option, due to restrictions in data recording, storage and processing. Instead, assuming fully periodic behaviour allows to spatially average over multiple orifices. Furthermore, the acoustic velocities are obtained using multi-δt, sum-of-correlation processing. Peak-fitting on a summed correlation map is interpreted as a regression step. This helps rejecting fluctuations, and correctly finding the acoustic velocity.

6.3. PIV Timing limits

The timing limits of subsection 4.2.4 are estimated before the wind-tunnel test. The lowest pulse separation time is dictated by the freestream velocity and the one-quarter rule. Initially, $d_I = 16px$ windows were intended, yielding a freestream displacement of $4px$. The upper limits are constituted by the relative phase, displacement and correlation limits. The relative phase limit is defined directly in time, with $lim_{phase} = 0.3$ in Equation 4.9, resulting in an upper limit of $12.5\mu s$. The velocity input for the displacement and gradient limits of equations 4.10-4.11 are modelled using the log-law and Prandtl friction law of equations 5.1 and 2.13. The velocity gradient is evaluated at half the interrogation window height. Note that this is the used window size of $d_I = 32px$, as subsection 5.4.4 showed that the intended window size of $d_I = 16px$ results in too few particles in the window. The displacement limit is evaluated $1D = 1mm$ above the face sheet.

The results are shown in Figure 6.2. As can be seen, the gradient, displacement and freestream limits scale similarly with the freestream Mach number. At low Mach numbers, the upper limit is formed by the acoustic phase limit. At $M_0 \approx 0.2$, the displacement limit becomes the active limit. The gradient limit is not active in this modelling approach, although it is close in value to the displacement limit.

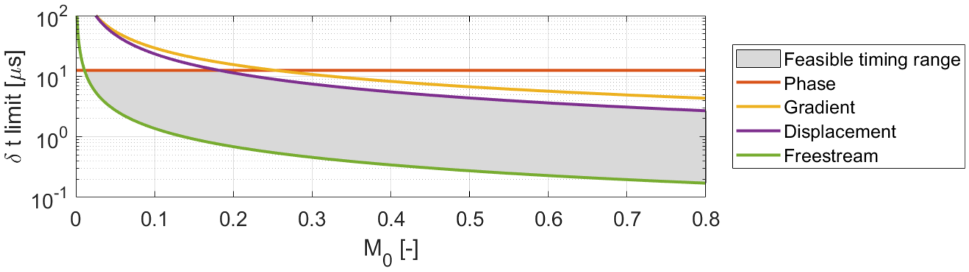

Figure 6.2: Expected timing limits.

The velocity-dependent limits can be seen to scale similarly with the freestream Mach number. Therefore, the feasible timing range $\delta t_N/\delta t_0 = k_t$ is nearly constant for higher Mach numbers. The same holds for the DVR, as the timing range and DVR are directly linked through Equation 3.6b. The timing range reduces when the acoustic phase limit is active, as it remains fixed in time. The timing range and DVR of Figure 6.2 is shown in Figure 6.3, with measurement noise estimated as $\sigma_{\Delta x} = 0.1px$. This assumption is based on the noise analysis of subsection 6.2.2. The timing range grows linearly up to the point at $M_0 \approx 0.2$ where the displacement limit is activated. From this point on, the range takes a nearly constant value of $k_t \approx 16$, with an estimated $DVR \approx 600$.

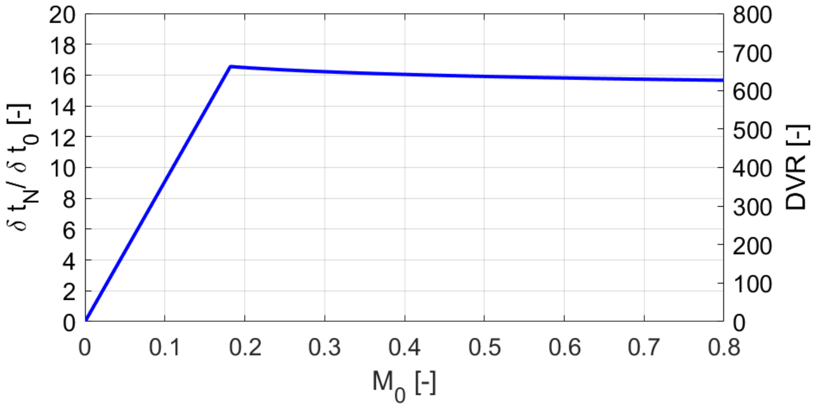

Figure 6.3: Feasible timing range of Figure 6.2, along with the resulting DVR.

Before the main test matrix, test points are performed and used to experimentally confirm the feasible timing range. These timing tests are performed at Mach 0.3 and 0.6. Both timing tests were performed with a δt_0 aimed at a freestream displacement of $4px$, with subsequent measurements at $[5, 10, 15, 20, 25] \times \delta t_0$. Only one phase with $\phi = 30^o$ is recorded, with 1000 samples per δt. This allows to confirm whether the timing range of Figure 6.3 is adequate, and whether the timing range indeed stays constant for higher Mach numbers. The acoustic phase limit of Equation 4.9 is defined directly in time and independent of flow characteristics. Therefore, only the displacement and correlation limits are discussed in further detail.

6.3.1. Gradient and out-of-plane-loss: correlation

For the correlation-related timing limit, the SOC correlation strength is evaluated. Before this is done, a division is required due to vibrations of the wind-tunnel at higher Mach numbers. For Mach numbers $M_0 > 0.3$, slight vibrations are introduced to the test section. This makes that the laser sheet also vibrates, leaving individual double-frames with a mis-aligned laser sheet with strong reflections as in Figure 5.7b. Sections 7.2-7.3 will discuss in more detail how these reflections are removed to the furthest extent possible. As these reflections are caused by vibrations, they are highly unsteady, and cannot be removed completely. As a result, vector evaluation is hindered above the orifices at higher Mach numbers.

Figure 6.4 shows the SOC correlation strength field for one of the Mach 0.6 timing tests. The reduction in correlation above the orifices is clearly seen. The diagonal bands are expected to be also caused by reflections; the laser sheet is generated from the downstream direction. These reflections are much less pronounced than the vertical reflections, however. In the following discussion, the correlation strength is presented in two domains: one outside of the vertical reflections and one within. The domain within the reflections is the combination of the four narrow domains with solid green borders in Figure 6.4. The domain outside of the reflections is the single large box with a dashed green border, with the reflection domains removed. Furthermore, the small domain with dashed black borders is removed; this is the are surrounding a damaged piece of the camera sensor.

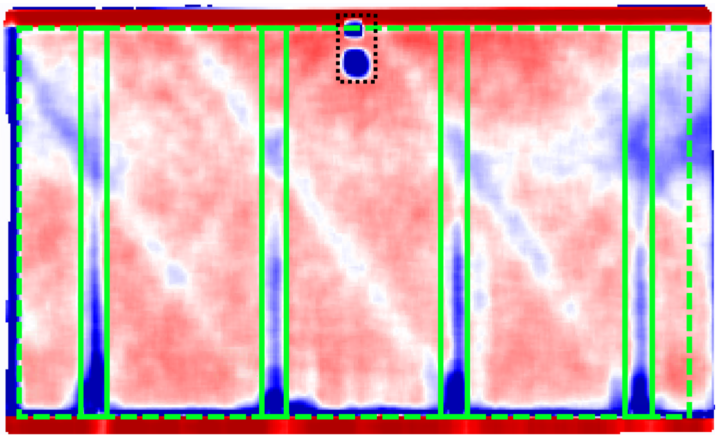

Figure 6.4: SOC correlation value for the Mach 0.6 timing test, showing the spatial patterns due to laser sheet reflections. The domains shown are indicative and not exact, the color map is scaled approximately $0.5 - 0.9$.

Figure 6.5 shows the correlation results for both timing tests. Correlation values are averaged in x-direction within the domains discussed above; solid lines indicate values from outside the reflections, dashed lines are taken in the domains above the orifices where reflections occur. First, the Mach 0.3 results in the left of Figure 6.5 are looked at. This measurement showed no vibrations, which is confirmed from the correlation perspective: correlation strength is the same for both domains. In the freestream, little to no variation in correlation strength is seen. Deeper into the boundary layer, correlation strength reduces. This shows the influence of turbulence, in-plane gradients and reflections near the wall. Turbulence and in-plane gradients make for deformations within the interrogation window, and turbulence may also lead to out-of-plane loss of particles. Reflections reduce the signal strength. The combined effects are more pronounced at larger timing ranges, suggesting that the timing range k_t amplifies any negative effects on the correlation strength. This is reasonable, as a larger overall displacement also results in larger deformations within the interrogation window.

The Mach 0.6 set shows a clear influence of the reflections. The correlation strength is reduced above the orifices. This reduction is not clearly dependent on the pulse separation time. Furthermore, the data from the 'clean' domain is influenced by the diagonal reflections which still remain in this domain. The decrease in correlation strength at $y = 15mm$ is attributed to the damaged pixels (cf. Figure 5.10b). Besides these impacts, the correlation strengths in the 'clean' domains are in the same order at both Mach numbers. This confirms the notion that the correlation limit indeed scales linearly with the Mach number, and that a constant timing range is appropriate for $M_0 >= 0.2$.

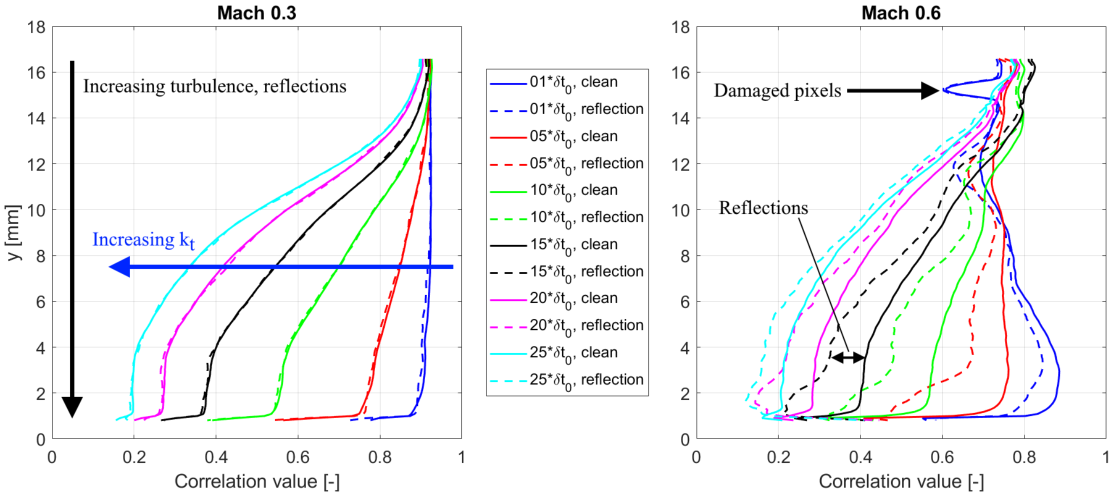

Figure 6.5: SOC correlation value in the boundary layer. Solid lines are averaged with the area above the orifices excluded, the dashed lines are averaged in the domains above the orifices.

A correlation strength of 0.3 is set as the lowest acceptable value. The correlation profile of $15 * \delta t_0$ is the highest pulse separation time in these measurements that stays above this limit in the clean domains. Note that this is very close to the limit at $\delta t_N / \delta t_0 = 16$, which is expected from the modelling. Within the reflection at Mach 0.6, the correlation strength is reduced, and falls below 0.3 at Mach 0.6. It is chosen to base the timing limit on the 'clean' domain, as basing it on the reflection domains leads to a much lower timing range and DVR accordingly. Data from higher δt's may be removed locally in these reflections. This allows to maintain a high DVR in the far field, and thus to resolve the incident acoustic velocity.

6.3.2. Displacement limit

The displacement limit is evaluated using multi-δt processing, using the data-sets up to $\delta t / \delta t_0 = 15$. This was chosen based on the correlation results discussed above. To evaluate the displacement limit, the displacement limit itself is not a problem: the evaluation requires the averaged velocity, while the limit concerns phase-dependent structures based on the acoustic velocity.

The boundary layer is averaged in x-direction, after which the velocity is evaluated at a height of $1mm$ above the face sheet. Dividing the orifice radius of $0.5mm$ by this velocity gives the upper timing limit, as defined in Equation 4.10. The results from the experimental timing tests are listed in Table 6.3. Both values for the limit timing range are deemed sufficiently close to $k_t = 16$ to confirm the modelled displacement of Figure 6.2.

Table 6.3: Timing test results for the displacement limit

$M_0[-]$	$\delta t_0 [\mu s]$	$u\|_{y=1mm} [ms^{-1}]$	$\delta t_{lim,displacement} [\mu s]$	$k_t[-]$
0.3	0.46	70.1	7.14	15.5
0.6	0.23	134.8	3.71	16.1

6.3.3. Timing range

Combining the above findings, $\delta t_N / \delta t_0 = k_t = 16$ is used as the timing range, with δt_0 chosen for a freestream particle image displacement of $4px$. This range is scaled down for Mach numbers $M_0 < 0.2$ to adhere to the acoustic phase limit. The pulse separation times chosen within the tested ranges are listed in Table 6.4. These times are generated logarithmically between δt and $16 \times \delta t$. A logarithmic spacing is chosen as it best suits the function form of the turbulence and noise decomposition in Equation 4.7b. Next, δt_2 is raised from $6.3 \times \delta t_0$ to $12.5 \delta t_0$. In case $16 \times \delta t_0$ proves too high, this allows for a back-up with a slightly lower δt.

Table 6.4: Timing ranges, expressed as multitudes of δt_0.

	Mach number		
Step	0.06	0.1	≥ 0.2
δt_0	1	1	1
δt_1	1.6	2	2.5
δt_2	3.6	7.2	12.5
δt_3	4.5	9	16

6.4. Phase-locked PIV timing control

To co-ordinate the PIV trigger timing and the acoustic phase, a Tabor WW1074 Waveform generator is used. Using arbitrary waveforms, the acoustic device is given a sine input, whereas the PIV trigger is defined using a square wave. The signals are monitored during the test using a multi-channel oscilloscope. Figure 6.6b shows a picture of the oscilloscope, on which the acoustic and trigger signals are clearly visible. The acoustic signal is sent to an amplifier which is in turn connected to the horn. The trigger signal is sent to a Lavision programmable timing unit (PTU), after which recordings can be taken using this external trigger signal. Further details on which settings are used are given next.

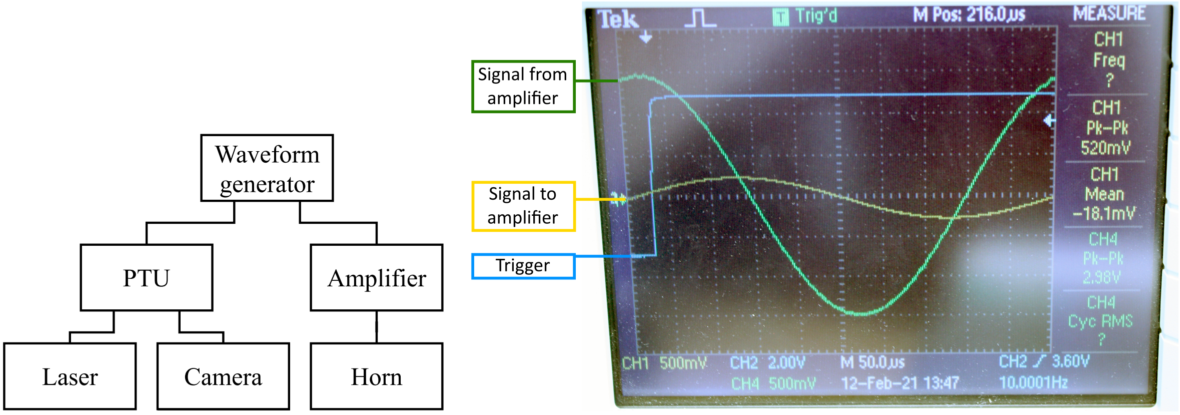
Waveform generator
PTU
Amplifier
Laser
Camera
Horn
Signal from amplifier
Signal to amplifier
Trigger
Tek
Trig'd
M Pos: 216.0μs
MEASURE
CH1 Freq ?
CH1 Pk–Pk 520mV
CH1 Mean −18.1mV
CH4 Pk–Pk 2.98V
CH4 Cyc RMS ?
CH1 500mV
CH2 2.00V
CH4 500mV
M 50.0μs
12-Feb-21 13:47
CH2 ∕ 3.60V
10.0001Hz

(a) Hardware and trigger lines schematic

(b) Picture of the oscilloscope tracking the phase-locked acoustic and trigger signals.

Figure 6.6: Overview of phase-locked timing control.

6.4.1. Sampling rate

The sampling clock has a fixed rate of 1×10^6 samples/second (1MS/s) [28]. Possible integer acoustic frequencies are therefore $[500, 1000, 1250, 2000, 2500, 3125, 5000, ...]$. The acoustic frequency of $2000Hz$ is closest to the resonant frequency of $2250Hz$, and gives $\Omega_f = f/f_0 = 0.89$. While $2500Hz$ is as close ($\Omega_f = 1.11$), the lower frequency is chosen as aerodynamic effects are expected to be stronger here. Similarly, the sampling frequency of the PIV system is reduced from its maximum of $15hz$ to $10Hz$. This is the highest frequency that allows phase-locked evaluation, while maintaining integer values. On the waveform generator, a sine wave made of 500 points is set to channel 1, while channel 2 outputs a square wave of 100.000 points.

6.4.2. Trigger offset and delay

The relative phase between the acoustic signal and PIV trigger is set by shifting the two signals on the waveform generator. To allow a central difference evaluation of the velocity at different pulse separations δt, double-frame samples are taken symmetrically around the relative phase of interest. This is also depicted in Figure 4.3b. The timing is shown in Figure 6.7. The phase shift on the waveform generator can be defined with a resolution of 0.1^o. At a frequency of $2000Hz$, this corresponds to a resolution of $0.14\mu s$. As this is the same order of magnitude as the shortest pulse separation times used, this is deemed insufficient. Instead, the trigger is given an offset of 10^o, corresponding to $13.9\mu s$. This offset is longer than half the longest pulse separation time expected. Next, a trigger delay is defined, on the DAVIS PIV control computer, which can be found by subtracting half the pulse separation time from the offset. Note that, as all phases are relative, the phase offset does not necessarily need to be explicitly defined on the waveform generator.

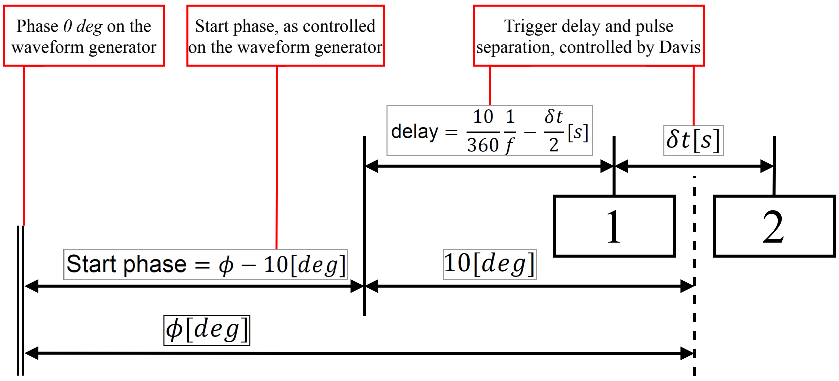
Phase *0 deg* on the waveform generator
Start phase, as controlled on the waveform generator
Trigger delay and pulse separation, controlled by Davis
delay = $\frac{10}{360}\frac{1}{f} - \frac{\delta t}{2}[s]$
$\delta t[s]$
1
2
Start phase = $\phi - 10[deg]$
$10[deg]$
$\phi[deg]$

Figure 6.7: Measured phase, trigger delay and phase offset.

One measurement is conducted at the system's maximum sampling frequency of $248kHz$, in which the laser triggers are also recorded. An acoustic frequency of $f = 2kHz$ was used, along with a trigger rate of $10Hz$, a start phase of 20^o, $\delta t = 200\mu s$ and a reference time of $10.000\mu s$. Figure 6.8 shows the results over two acoustic periods. The phase difference with respect to the acoustic positive zero-crossing is averaged over the recorded 10 triggers. Laser trigger 1 occurs at $\phi = 165^o$, trigger 2 at 309^o. Therefore, the actual phase evaluated is $\frac{165+309}{2} = 237^o$, and the system has an internal relative phase delay of $237 - 20 = 217^o$. Furthermore, the laser is clearly recorded in the microphone signal. For this reason, in-situ acoustics measurements are performed separate from the PIV recordings.

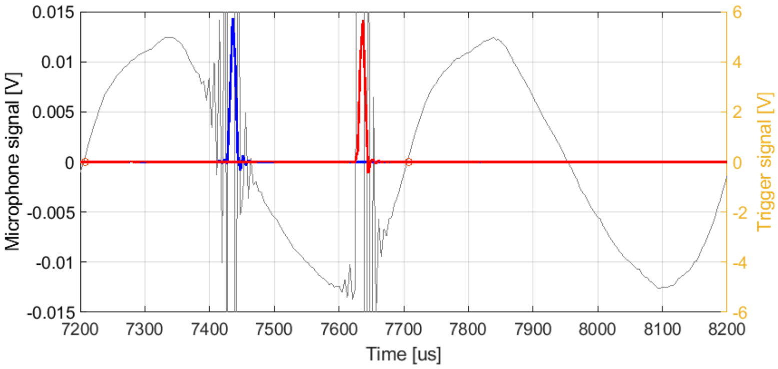

Figure 6.8: Face sheet microphone and laser trigger signals. The microphone signal is displayed in gray on the left y-axis. Laser triggers 1 and 2 are displayed in blue and red, respectively, on the right axis.

Before the experiment, internal trigger delays are adjusted to ensure that laser trigger timing is correct. The pulse separation is reduced down to its specified minimum of $0.12\mu s$ [24], and internal triggers are adjusted if laser pulses are recorded in the wrong frame. Pulses are recorded in the correct frame down to $\delta t = 0.13\mu s$, $0.12\mu s$ could not be measured correctly as the internal delays could not be set with sufficient significance. As the tested condition is only $0.01\mu s$ off from the specified limit of the camera, it is concluded that internal timing is accurate. The maximum acoustic sampling rate of $248khz$ yields a time-step of $4\mu s$, therefore the results of Figure 6.8 could not be used to further confirm the trigger timing.

6.4.3. Multi-dt recording logic

Image sets are recorded using Davis 10. This software version allows to create tables with multiple settings, called a 'table scan' [23, Section 10.4]. The pulse separation times and associated trigger delays depend on the tunnel velocity, the start phase is determined by the phase of interest. For each measurement, a recording table is made with the four pulse separation times $\delta t_0 ... \delta t_3$ and their associated trigger delays. After setting the start phase on the waveform generator, the four sets are then recorded in a single measurement. In Davis 10, these are stored as a multi-set. For evaluation in Davis 8.4, these multi-sets are split up into four standard stream sets.

6.5. Test matrix

This chapter concludes by showing the test matrix, and briefly explaining the reasoning for the chosen test-points. The test matrix as performed in the experiment is shown. Several additional, lower priority test-points have been defined, but not recorded due to time constraints. These points are also discussed, as they may be relevant for future experiments.

6.5.1. As-performed matrix

Table 6.5 shows the test matrix, in the order in which the measurements have been conducted. The sound pressure levels and resulting range of interest R_I are shown, as well as the expected velocity ratio Ω_v. All values are shown double. First, the values using the intended sound pressure levels are shown. As subsection 5.2.3 showed, the SPL that is reached during the experiment differs greatly from these intended values, as the horn input is not adjusted for a constant sound pressure level. The updated SPL, R_I and Ω_v values are included in Table 6.5.

Table 6.5: Test matrix, with intended and achieved sound pressure levels. The associated freestream velocities and ranges of interest R_I are computed using c_0 from Equation 5.4, $p_0 = 101325Pa$ and $|\tilde{v}_{inc}|_{RMS}$ from Equation 6.2. The actual SPL is the SPL at the face sheet microphone at $2kHz$. The velocity ratios Ω_v are computed with u_τ from Equation 2.13 and the orifice velocity from Equation 2.11b with $Q = 1$.

		Intended			Actual		
$M_0[-]$	$U_0[ms^{-1}]$	SPL $[dB]$	$R_I[-]$	$\Omega_v[-]$	SPL $[dB]$	$R_I[-]$	$\Omega_v[-]$
0.1	34.3	148	28	16.0	144.3	43	10.5
0.1	34.3	120	709	0.6	109.1	2491	0.2
0.06	20.6	132	107	4.0	117.5	568	0.8
0.2	68.3	148	56	8.6	145.0	80	6.0
0.4	135.0	148	111	4.6	140.3	269	1.9
0.6	200.2	148	165	3.2	140.3	401	1.3
0.8	263.8	148	217	2.5	134.3	1049	0.5
0.6	200.2	140	414	1.3	123.8	2685	0.2
0.6	200.2	135	736	0.7	116.0	6583	0.1
0	0	148	N/A	N/A	138.7	N/A	N/A

The first three points in Table 6.5 are intended as validation sets: the Mach 0.1 points correspond to measurements from Van der Meulen [51] while the Mach 0.06 case is presented by Léon et al. [27]. Unfortunately, the lower actual sound pressure level prevents any direct quantitative comparison. Next, a high-SPL Mach sweep is performed. This effectively makes for a range of R_I and Ω_v, which allows to evaluate the PIV measurement's performance, as well as the aerodynamic effects over the liner. Following this sweep are two cases at Mach 0.6 at lower SPL. These intend to explore and demonstrate the DVR limit: at least point that is not resolved is intended, such that the limit may be demonstrated clearly. Due to problems such as intense tunnel vibrations and seeding accumulation at Mach 0.8, these measurements are taken at a slightly lower Mach number of $M_0 = 0.6$. Finally, a no-flow case is seen. While not directly relevant for the research questions, it is argued that the inclusion of a no-flow case may be insightful when evaluating trends with Mach number.

6.5.2. Not-performed test points

Several test points have not been carried out, due to time limitations. These points and their relevance can be summarized in three testing blocks:

1. A second Mach sweep over Mach numbers 0.2, 0.4, 0.6 and 0.8 at an SPL of $140dB$. This presents more resolution wtihin the ranges for R_I and Ω_v.
2. An SPL sweep, at a Mach number 0.2. Adding a constant-Mach sweep allows to better separate effects from the friction velocity and in-orifice velocity.
3. A PIV-only measurement, on a larger, $10x10cm^2$ liner sample with an identical topology as the current sample. No impedance measurements would be taken, as this larger sample is not instrumented with microphones. A second camera would be added, and both cameras would be set at a lower magnification factor. This allows to view the entire sample at once. From observations during earlier tests, a Mach number and SPL are chosen; this would be the highest Mach number deemed possible to resolve. The longer sample would allow to better evaluate the downstream development of the boundary layer and liner response.

7

Data processing

Within the frameworks of the measurement techniques discussed in Chapter 4, there are still numerous choices regarding the exact implementation. These choices are explained here. First, impedance processing is discussed briefly in Section 7.1. Next, sections 7.2-7.4 present the details of the multi-δt PIV processing pipeline. As part of this pipeline is newly written, a validation of the methodology is presented in Section 7.5.

7.1. In-situ processing

Impedance is calculated using in-house NLR software. The fast Fourier transform (FFT) is computed on blocks of 4096 samples each with Hanning windows. The blocks are overlapped 50%. This combination of window type and overlap ensures all amplitudes are conserved. Results are averaged over all blocks. Taking the overlap into account, each current measurement consists of 100 blocks.

7.2. PIV image pre-processing

As seen in Figure 7.10, PIV processing is started in LaVision's Davis 8.4 software. The raw images must be pre-processed to allow for accurate cross-correlation [39]. Besides the more standard steps, vibrations introduced by the wind-tunnel are seen as a major concern in the current results. Image pre-processing also aims to correct for these vibrations. In this section, the specific steps implemented

7.2.1. Shift and vibration correction

Throughout the measurements, fixed shifts between measurements, and vibrations within measurements are observed. Both may be as large as $100px$ between two samples. Between measurements, the liner sample frequently requires to be cleaned. As the entire PIV set-up is attached to the wind-tunnel, it is possible that a small displacement is introduced between measurements. Due to the high magnification factor, this quickly leads to a large displacement of the images. A fixed offset of a dataset makes direct comparison to other datasets difficult. Secondly, wind-tunnel vibrations are noticeable for Mach numbers $M_0 \geq 0.4$, resulting in vibrations within a measurement. The unsteady vibrations must also be corrected, otherwise the correlation maps are associated to erroneous coordinates. These vibrations introduce two problems: a displacement of the images, and unsteady reflections. This section concerns the fixed and fluctuating displacements, the unsteady reflections are treated in subsection 7.2.3.

To correct for both the fixed and fluctuating shift, the 'shift and rotation' filter is used in Davis 8.4. The concept of the implementation is shown in Figure 7.1. A reference image is prepended to each dataset. In a second processing step, each individual image is shifted such that it best matches the reference image. After the correction, the reference image is removed again, making for a total of three processing steps. This yields the original data-set, but corrected for displacements.

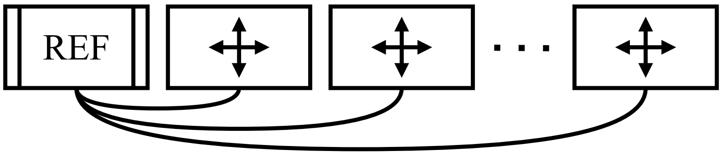

Figure 7.1: Scheme depicting the shift- and vibration correction. A reference image is prepended to the dataset, and all samples in the dataset are shifted to best match the reference. The reference image used in all cases is shown in Figure 7.2a.

Figure 7.2 shows the current implementation in more detail. A set of 10 images is recorded along with the final calibration, in absence of flow or seeding. Figure 7.2a shows the minimum image of this sequence: this is the image used as vibration/shift reference for all data-sets. The minimum filter ensures that only constant structures in the images remain. Using the same reference ensures that all images are corrected to the same base position, correcting both the fixed shift and instantaneous fluctuation in a single step. This allows direct comparison, as well as using identical masking operations in subsequent steps.

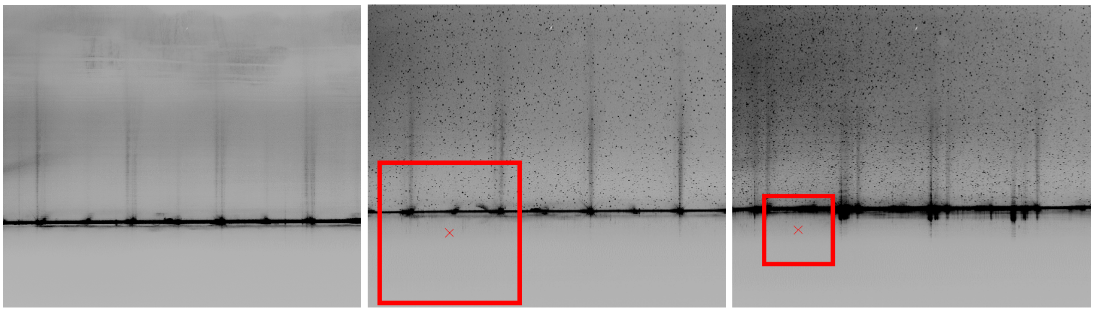

(a) Minimum of 10 no-flow images, associated to the final calibration. This image serves as the reference image for the vibration- and shift correction.

(b) $1024 \times 1024 px^2$ window, centred over the two downstream orifices. Used as default domain. Image from a Mach 0.1 dataset.

(c) $512 \times 512 px^2$ window, with the most downstream orifice in view. Used in case the correction fails with the larger window. Image from a Mach 0.8 dataset.

Figure 7.2: Raw PIV images, showing the reference and domains used for the shift- and vibration correction. All intensities scaled $0 - 1000$ counts. Notice the vertical shift between subfigures (a) and (b).

The shift for each individual image is based on cross-correlating a double-frame image pair with the reference image within a pre-defined window. The integer pixel shift for which the highest correlation is found is applied to the image pair. This is identical to PIV vector computation, but without sub-pixel interpolation. Figure 7.2a shows the visual patterns that persist throughout all measurements. The horizontal line presented by the face sheet reflection gives a clear signal on the y-position of the image. The vertical bands from the orifice reflections provide a consistent signal in x. The shift is computed using the second frame of each sample, as these reflections are seen to be slightly stronger than in the first frame. The same shift is applied to both frames of a smaple, such that the particle image displacement is not affected.

The default setting that is found to work most reliably is shown in Figure 7.2b. Here a 1024×1024 'interrogation window' is used, covering the face sheet and two orifices. The window is positioned as low as possible: including a larger part of the boundary layer reduces the correlation signal. This is caused by the seeding in the measurement images, which is not present in the reference image. After the correction, each dataset is inspected visually. Some cases are seen to be wrongly corrected, mainly in x-direction. It is thought that this is caused by droplets of seeding flowing over the face sheet. These cases show good results using the smaller window shown in Figure 7.2c, including only the most downstream orifice.

Validation of the correction

The shift- and vibration correction filter is validated, to ensure that this important step is performed correctly. To this end, the image position is tracked in Matlab throughout an entire measurement. Comparing raw and corrected positions allows to judge if the filter is effective in removing the fixed and fluctuating offsets. This evaluation is performed on the first measurement of each tested Mach number, to ensure all vibration intensities are corrected.

Image positions are tracked in Matlab using average intensity profiles. The profiles are computed in Davis 8.4, and exported for evaluation in Matlab. Figure 7.3 shows the reference image of Figure 7.2a, averaged in x-direction. The face sheet is seen to show a very clear signal. The y-coordinate of the face sheet is found by fitting a Gaussian peak to this signal, from which the peak position can be extracted.

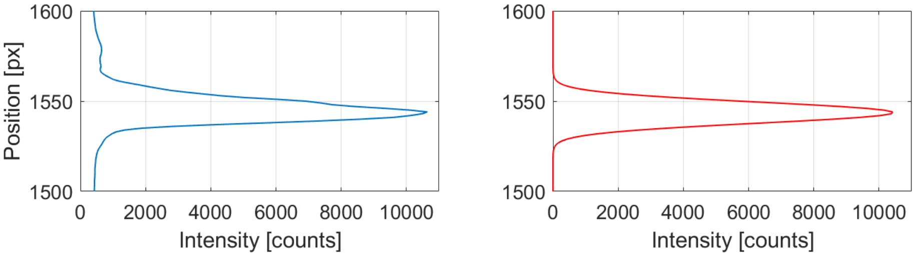

Figure 7.3: Intensity over the face sheet reflection averaged in x. Intensity of Figure 7.2a (left) and fitted Gaussian peak (right).

The profile in Figure 7.4 is an y-average over a band around the face sheet. It shows a less obvious peak than the face sheet in Figure 7.3. The equidistant spacing of the orifices makes for a spatially periodic signal, with each orifice typically showing two individual peaks. A test profile is set up on the reference image, using Matlab's built-in Fourier fit. This test profile is shown in the bottom graph of Figure 7.4. The displacement in x of an arbitrary image is found by fitting this profile to the image's y-averaged intensity. This fitting is performed using a least-squares approach, with the offset in x as a fitting coefficient. At higher Mach numbers, seeding accumulation on the face sheet strongly increase the overall intensity of the reflections. To account for this, two additional fitting parameters are introduced. These offset and scale the intensity levels. The build-up of seeing on the face sheet and seeding droplets moving over the surface can distort the profiles seen in Figure 7.4. Therefore, the tracked x-positions may included noise.

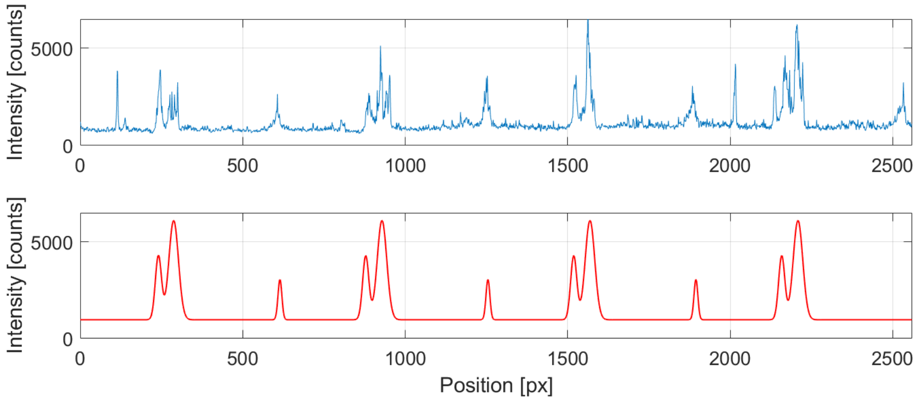

Figure 7.4: Intensity over the face sheet reflection averaged in y. Intensity of Figure 7.2a (top) and fitted profile (bottom).

Fixed shift (installation error)

First, the fixed shifts are evaluated. Figure 7.5 shows the original and corrected mean positions with respect to the reference image. The largest recorded fixed offset in x is seen to be approximately 30 pixels in x, and 100 pixels in y. The fixed shifts are found by averaging the position over all 1000 samples in a measurement, this mean is assumed to be statistically converged: noise from the tracking method is negligible here. The largest remaining offset in x of $2.84 px$ corresponds to $0.03 mm$. It is concluded that a good result is obtained for the correction of the fixed shifts, both in x and y directions.

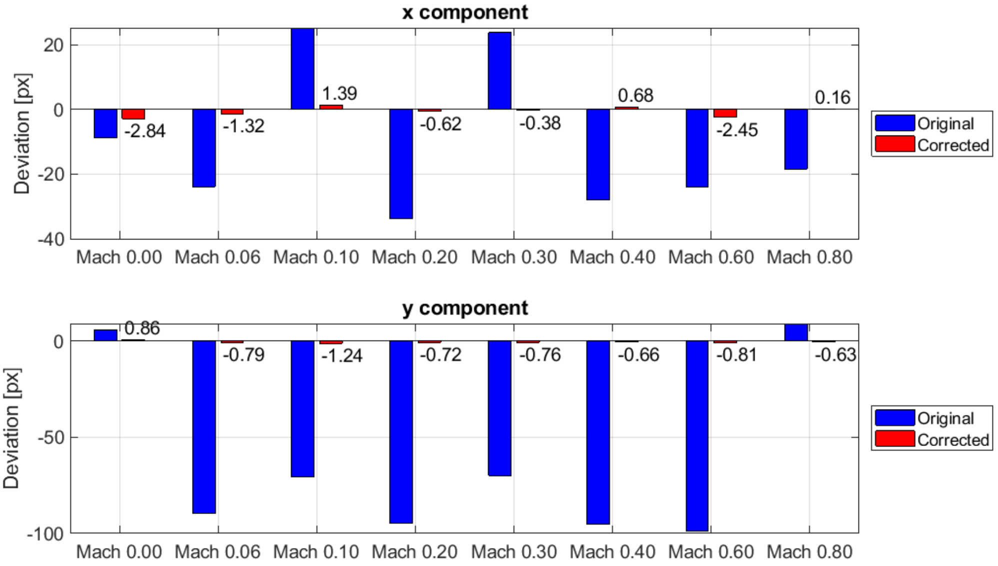

Figure 7.5: Installation error, raw and corrected.

Vibration

Next, the performance of correcting the individual samples is evaluated. Figure 7.6 shows the standard deviation of the tracked positions on the left y-axis, and the maximum-to-minimum distance on the right. Vibration intensity in x is seen to increase with the tunnel Mach number, although RMS values are small. The tracked fluctuations suggest that the vibration correction in x is ineffective. Both the corrected standard deviation and maximum difference show no clear dependence on the Mach number. It is argued that tracking the displacement in x in Matlab is indeed noisy. In the worst case, a standard deviation of $1px$ $0.01mm$ and a maximum difference of $10px$ $0.1mm$ as found here are deemed acceptable: the integer shift can not correct subpixel displacements. Furthermore, the correction as computed in Davis 8.4 is expected to be more accurate, as it is based on correlation in stead of fitting a pre-defined profile.

Tracking the y-position is much more accurate, due to the clear signal of the face sheet in all cases. Figure 7.6 shows clearly that wind-tunnel vibration start to become apparent at $M_0 \approx 0.3$, and increase nearly linearly with the Mach number. At Mach 0.8, a vibration RMS of $7.5px$ and maximum difference of $50px$ is seen in y-direction. The correction is seen to be effective in removing the vibration up to within a pixel. This is again within the accuracy of the correction, which applies an integer pixel shift. This is also seen in visual inspections of the corrected datasets.

Further confirmation is obtained by visually inspecting the datasets. Figure 7.7 shows two pre-processed images from a Mach 0.6 dataset, overlayed on each other. The individual images are shown in Figure 7.9. Here, the red bands indicate regions left blank, as the images are shifted to match the reference image in Figure 7.2a. The images are seen shifted downwards and to the right in the correction. An identical shift in x is seen, while the shift in y differs by 3 pixels. Going back to the overlay in Figure 7.7, it can be confirmed that the face sheet is located in the same position in both images, after the correction.

It is concluded that the shift and vibration correction is effective in correcting any fixed and fluctuating offset. As a result, all images have the liner at the same position as the reference image of Figure 7.2a after this first pre-processing step. All pre-processed sets are visually inspected to ensure the shift corrections has been successful. The datasets at Mach 0.2 and 0.4 show uncorrected or even amplified vibrations using the settings shown in Figure 7.2b. These sets are corrected using the smaller window of Figure 7.2c, which shows good performance again.

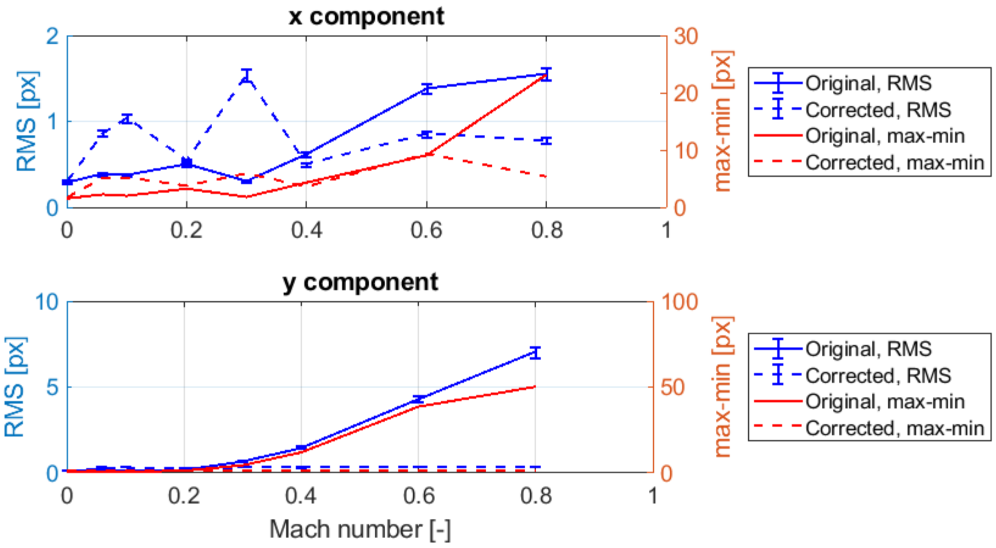

Figure 7.6: Vibration standard deviation, raw and corrected.

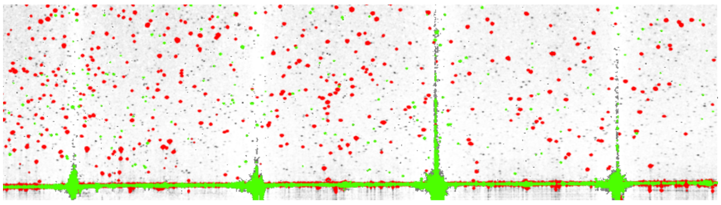

Figure 7.7: Subsequent images of Figure 7.9 overlayed: all higher intensities of Figure 7.9a are coloured red, those of Figure 7.9b are coloured green.

7.2.2. Geometric mask

The fourth step in the pre-processing is a masking operation. A fixed geometric mask is used, which excludes the region below the face sheet. From the top of the image, 74% of the height is included. The mask is identical for all datasets, as the shift- and vibration correction ensures that all images are calibrated to the same physical location. Removing the bottom part of the images alleviates computational effort in subsequent steps, as the data size is reduced by 25%.

7.2.3. Background removal

The final step in the image pre-processing is the removal of the background. This aims to obtain particle images of high contrast and high intensity. Typically, a sliding average image is subtracted from the instantaneous image pairs. Due to the variation in seeding between images, this removes any steady effects, while leaving the particle images at a high intensity. In the current case, this step is complicated by the vibrations.

From subsection 7.2.1, wind-tunnel vibration becomes apparent for Mach numbers $M_0 \geq 0.3$. As seen in Figure 5.1a, both the camera and laser head are attached directly to the wind-tunnel. As the laser head moves with respect to the tunnel during vibrations, the position of the laser sheet is no longer fixed at the face sheet. Figure 5.7 shows the sensitivity of the laser sheet alignment. The laser sheet is adjusted slightly above the orifice centers, such that the laser light reflects down, away from the camera lens. This desired situation is depicted in Figure 7.8a. As the laser sheet vibrates, it will be in the 'too low' position of Figure 7.8b at some moments.

From observations during testing, the frequency of the tunnel vibrations are deemed much larger than the PIV acquisition frequency of $10Hz$. This results in single samples in the image sequence which show a strong reflection from the orifice. Due to this unsteadiness, a sliding filter is not capable of filtering out the reflection completely. Both frames of a double-frame image pair are seen to have a similar reflection. This suggests that the period of the vibrations is much larger than the pulse separation time, which is in the order of $\mathcal{O}(1\mu s)$.

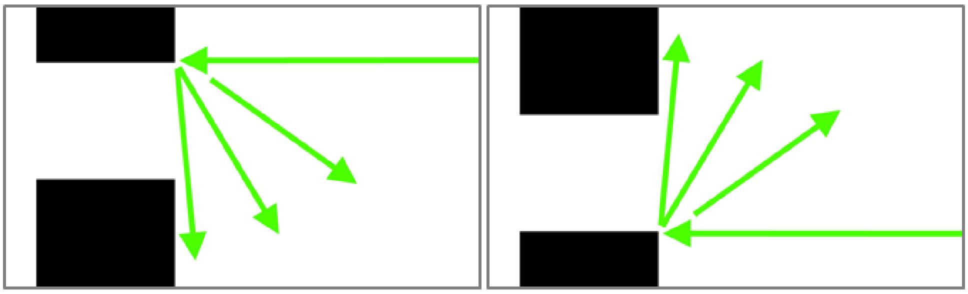

(a) Laser sheet above orifice center: reflection away from camera.

(b) Laser sheet too low: reflection towards the camera.

Figure 7.8: Reflections due to laser sheet position.

The method of removing the reflections that works best is found to be a combination of a sliding average subtraction, followed by a spatial averaging step. First, sliding average of 3 images is subtracted. This is the shortest filter length possible, and captures as much of the unsteady reflection as possible: longer filter lengths would include more images without a reflection, reducing the intensity that is subtracted. The short filter length does result in noticeable amounts of residual background noise. This uncorrelated measurement noise is confirmed to be $\mathcal{O}(1px)$. Recall from subsection 5.4.3 that the particle image size is much larger, at $4 \leq d_{p,img} \leq 10px$. A sliding spatial averaging is performed over 3 pixels: this smooths out the noise, while the much larger particle images are not affected much. This averaging is done independently in x and y directions. This is chosen over a true 2-dimensional approach, with regards to the skewed particles near the wall, visible in Figure 5.10c.

Figure 7.9 shows an example of pre-processed images with unsteady reflections. Two subsequent images are shown, both the second frame of their respective double-frame pairs. In the unprocessed images, a clear reflection is seen in the raw file of Figure 7.9b. In the processed images, the consequence of the unsteadiness is visible. The reflection is only reduced in intensity, but can not be fully removed. In Figure 7.9a, it is also seen that the noise is not fully removed, but reaches a steady value of several counts. In the area of the reflections, a zero background intensity is seen, as the background level is raised by the reflection in Figure 7.9b.

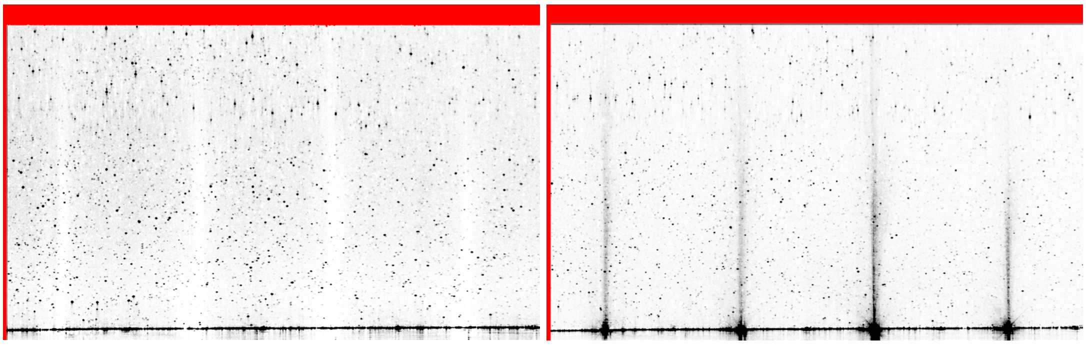

(a) Image pair without reflection

(b) Image pair with reflection

Figure 7.9: Two subsequent images from a Mach 0.6 measurement, after pre-processing. All intensities scaled $0-200$. The red bands indicate regions outside of the original image, due to the shift and vibration correction.

The background removal concludes the image pre-processing. In total, pre-processing requires six filter steps in Davis 8.4. Figure 7.9 shows that adequate results are obtained in terms of particle image contrast and intensity: the images shown are scaled to an intensity of $0-200$ counts, to visualize the reflection and noise residual more clearly. The brighter particle images are in the order $\mathcal{O}(2000)$ counts. Particles can also be distinguished well from the background. Unfortunately, the unsteady reflections from the orifices due to the tunnel vibrations can not be removed completely. The influence on the measurements is addressed in more detail in the assessment in Chapter 8.

7.3. Vector field computation

After image pre-processing, the vector fields can be computed. As shown in Figure 3.1, cross-correlation and computation of fluctuation vector fields are performed in Davis 8.4. The details on these two steps are discussed below.

While the current concept is similar to that of the pyramid scheme of Sciacchitano et al. [42], the recording and processing differs (cf. Figure 4.3). Hence, no 'standard' processing method is readily available. This section gives an overview of the PIV post-processing logic. Further detailed settings are based on the recordings itself, and are presented in Section 7.2.

Figure 7.10 shows how the recordings are processed in both Lavision's Davis 8.4 and Matlab software. Velocity field are evaluated using SOC processing in Davis 8.4. The reason for this is that the SOC process aids in rejecting turbulence, and thus in discriminating between the acoustic and turbulent velocity fluctuations, the ratio between which may be small. Secondly, exporting and externally processing 1000 (as recorded here) correlation maps is computationally very expensive. Using SOC processing, only one correlation map remains per δt, making processing in Matlab much more manageable. sum of correlation can not provide information on the turbulent fluctuations, therefore another 'standard' processing is used for this. In Figure 7.10, the ideal situation is depicted, in which the standard and SOC processing steps are made using the same correlation maps. In practice, however, storing the correlation maps in a standard processing step is not possible in Davis 8.4. Therefore, the pre-processed images are processed twice: first using sum of correlation followed by a standard processing step. The SOC velocity results are used within Davis 8.4 to provide a reference velocity field for the first-pass displacement for all $\delta t > \delta t_0$. It was found that the displacement field has to be multiplied by $(\delta t_{i+1}/\delta t_i)^2$ between two pulse separation times to provide the correct reference displacement field.

7.3.1. Sum-of-correlation evaluation

Processing starts at the shortest pulse separation time, δt_0. The sum-of-correlation field is computed in a single pass at $32x32px^2$ windows, with a circular window weighing. subsection 5.4.4 shows how the window size is determined by the seeding density. The perspective correction is applied in the correlation evaluation, and the 'high accuracy mode for final passes' is activated. The first pass is not given any initial window shift: the expected maximum displacement of 4 pixels is easily captured within the window size of 32 pixels.

The correlation is computed using the normalized correlation function. While this is computationally more expensive than the default approach, two advantages are seen. First, it is argued that the normalized scheme is affected less by the unsteady reflections than the standard option: the reflections are typically of high intensity. The normalized scheme is not biased towards higher intensities, while the standard scheme is. Secondly, the normalized correlation value is scaled from 0 to 1. Such a normalisation allows for better assessment on the measurements. Furthermore, it allows more freedom in the combination of the different multi-δt measurements. For example, it allows to weigh multi-δt correlation maps with their respective correlation values if needed.

A symmetric shift of the two frames of an image is applied. This ensures the evaluation is consistent with the symmetric timing shown in figures 4.3b and 6.7.

7.3.2. Post-processing for reference vector fields

Subsequent datasets with $\delta t > \delta t_0$ require an initial window shift, as they do not adhere to the one-quarter rule. Processing is one on progressively larger pulse separation times. Each dataset provides the initial window shift for the next, similar to grid refinement schemes. Even though sum of correlation is used here, vector validation is deemed necessary to provide robust displacement fields. This is implemented as vector post-processing, and the default settings for multi-pass validation are used. A vector is deleted if its peak ratio is less than 1.3. A $1\times$ universal outlier detection is applied on a filter region of 5×5 vectors. A vector is removed if the residual is greater than 2, and re-inserted if it is smaller than 3, with a minimum of 4 vectors in the window. Empty spaces are interpolated, and a 3×3 smoothing step is included.

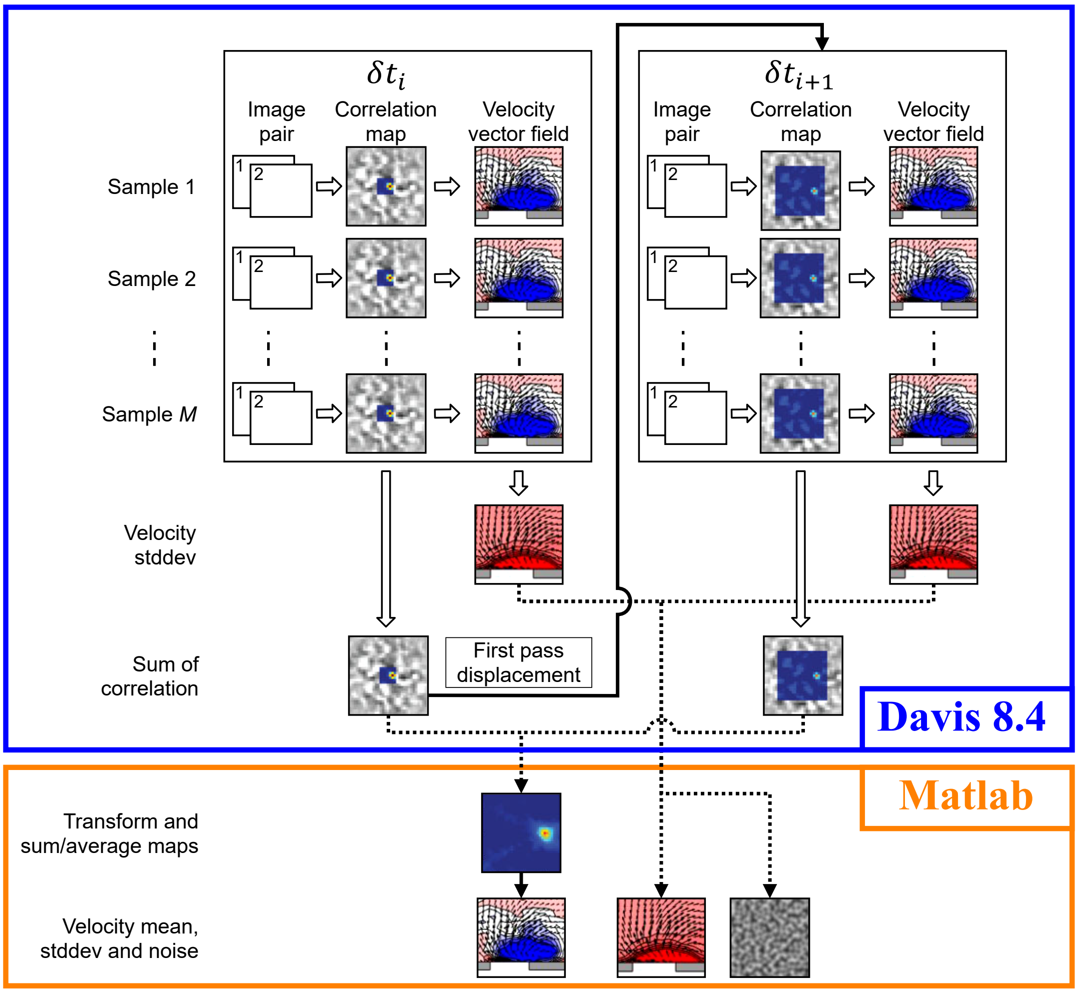
δt_i
Image pair
Correlation map
Velocity vector field
δt_{i+1}
Image pair
Correlation map
Velocity vector field
Sample 1
Sample 2
Sample *M*
Velocity stddev
Sum of correlation
First pass displacement
Davis 8.4
Matlab
Transform and sum/average maps
Velocity mean, stddev and noise

Figure 7.10: Graphical representation showing data streams for multi-δt post-processing. This scheme shows in more detail how the processing steps in Figure 4.5 are performed. Two consecutive δt's are shown, dotted lines denote combining information from the entire δt range recorded.

Finally, the vector field must be scaled to provide the initial window shift at a different pulse separation time. Consider using a vector field from a measurement with δt_i to provide a reference field for the next dataset with $\delta t_{i_+1} > \delta t_i$. It is found that the vector field must be multiplied with $(\delta t_{i+1}/\delta t_i)^2$. It is not known why the squared ratio is needed. It should be noted that these validation and scaling steps do not affect the final velocity fields. The multi-δt velocity fields are computed using the correlation maps.

7.3.3. Fluctuation evaluation

For the evaluation of the fluctuation vector fields, a standard processing is used. The same processing settings are used as for the SOC processing, described above. Vector post-processing is not applied. As with the SOC evaluation, the shortest δt is evaluated directly, without an initial window shift. Subsequent measurements with longer pulse separation times use their corresponding SOC vector field result to provide the window shift. As this is from the same δt, the unscaled vector field must be used. The fluctuation field is found by taking the standard deviation of the 1000 velocity fields from this processing step.

7.3.4. Multi-dt velocity vector evaluation

After processing the individual δt results in Davis 8.4, the results are exported for multi-δt evaluation in Matlab. For each multi-δt set, three categories of data are needed: the SOC velocity field and its corresponding velocity field, and the standard deviation vector field of the standard processing. The SOC results are used together for the velocity evaluation, the standard deviation fields are used for the turbulence and noise decomposition. Figure 7.11 shows how this data is organized for easy implementation into Matlab. Next, the logic of the Matlab processing pipeline is discussed, starting with the velocity evaluation. This discussion is presented within the scope of a single phase as depicted in Figure 7.11. The Matlab implementation of this section can be found in Appendix B.

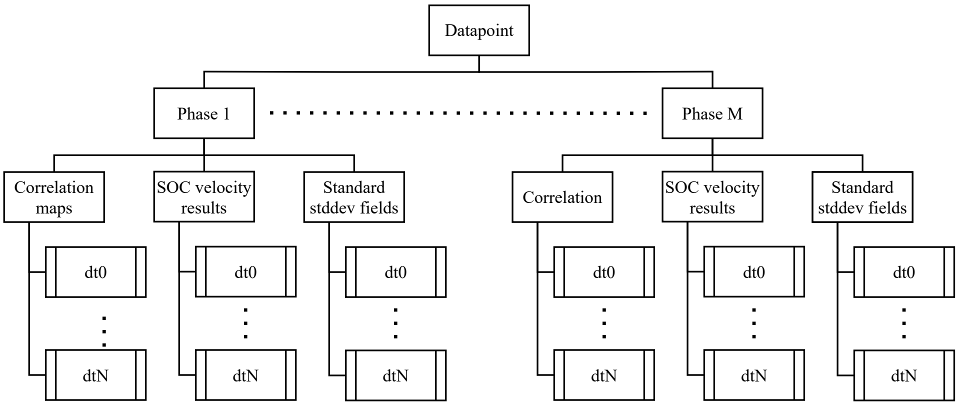

Figure 7.11: Structure of data exports between Davis 8.4 and Matlab.

Data import

Starting the data import, the pulse separation times are discovered. For each pulse separation time, the entire correlation map is read, along with the corresponding pixel coordinates. The pixel coordinates of all maps $\delta t > \delta t_0$ are corrected to implement the window shift and to scale all results down in pulse separation time to δt_0. Figures 7.12a-7.12b show an unaltered (δt_0) and transformed (δt_1) correlation map, overlaying these grids in Figure 7.12g clearly shows the shift and scaling of the δt_1 map. This transformation is shown in Equation 7.1a, the associated code is shown in Appendix B.2. In each interrogation window, the original coordinates $\mathbf{X}_i$ are corrected by a velocity term $\Delta\mathbf{X}_{vel}$. Scaling down to δt_0 is implemented by the $\delta t_0/\delta t_i$ and $\Delta\mathbf{X}_{scale}$ terms. Note that the subscripts denote δt steps, where $i = 0$ denotes the shortest pulse separation time.

$$\mathbf{X}_{i,corr} = \mathbf{X}_i + \Delta\mathbf{X}_{vel}\frac{\delta t_0}{\delta t_i} - \Delta\mathbf{X}_{scale}\left(1 - \frac{\delta t_0}{\delta t_i}\right) \tag{7.1a}$$

$$\Delta\mathbf{X}_{vel} = \mathbf{U}_{i-1}\frac{\delta t_i}{\Delta_{px}} \qquad \left(\begin{matrix}\text{Fixed within window,}\\ \text{variable through image}\end{matrix}\right) \tag{7.1b}$$

$$\Delta\mathbf{X}_{scale} = \begin{bmatrix} \left(-\frac{d_I-2}{2}, -\frac{d_I-2}{2}\right) & \cdots & \left(\frac{d_I}{2}, -\frac{d_I-2}{2}\right) \\ \vdots & \ddots & \vdots \\ \left(-\frac{d_I-2}{2}, \frac{d_I}{2}\right) & \cdots & \left(\frac{d_I}{2}, \frac{d_I}{2}\right) \end{bmatrix} \qquad \left(\begin{matrix}\text{Variable within window,}\\ \text{fixed through image}\end{matrix}\right) \tag{7.1c}$$

The velocity correction term shifts the interrogation window using the SOC velocity results from one pulse separation lower, $\mathbf{U}_{i-1}$. This is the velocity field used within Davis 8.4 for the window displacement. Using the current pulse separation time δt_i and the pixel size, the window displacement is found. To scale the interrogation window, a $d_I \times d_I$ matrix of grid points is set up with a grid spacing of 1. This matrix contains the relative positions in pixels to the centre pixel at $(d_I/2, d_I/2)$. Note that the y-axis is defined positive downward in the SOC correlation maps. Multiplying this matrix with $1 - \delta t_0/\delta t_i$ provides the correction for each point in the interrogation window, which must be subtracted from the original coordinates.

Combined, the transformation acts as a grid refinement of the correlation map, in the region near the correlation peak. This is visible in Figure 7.12g. After the transformation, the correlation values are normalized. SOC correlation values are summed in Davis 8.4. Dividing these values by the numbers of samples yields a correlation value ≤ 1, where a value of 1 indicates perfect correlation.

Multi-dt correlation map

Next, the information from multiple δt's is combined, the Matlab implementation can be found in Appendix B.3. Correlation maps can not be summed directly, due to the previously discussed transformation. The process used is visualized in Figure 7.12, using two correlation maps from an interrogation window in the freestream of a Mach 0.1 measurement, with $\delta t_1 = 2\delta t_0$. The SOC correlation map from δt_0 is shown in Figure 7.12a, Figure 7.12b shows the map from δt_1 after the previously discussed transformation of Equation 7.1. The overlap between both grids is found, and the coarse data is interpolated on the finer grid. The area outside the overlap is unaltered, shown in Figure 7.12c. This method is chosen over interpolating the entire map onto the finer grid, to reduce computational effort. The interpolated δt_0 and the δt_1 maps in 7.12d-7.12e can now be summed, as they are on the same grid. The result is the multi-grid map in Figure 7.12f. Note that the multi-δt data is now kept as scattered data, in stead of the single-δt gridded data.

Comparing figures Figure 7.12a and Figure 7.12f, it can be seen that the correlation peak is narrowed. While the pyramid scheme of Sciacchitano et al. [42] scales *up* to the higher pulse separation time, the result is the same: a low δt provides a wide base for the correlation map, whereas higher δt's add a narrow, high peak. As the velocity field of δt_0 is used to provide the window shift for the δt_1 evaluation, the higher-δt map is centered on the correlation peak of the lower.

In Figure 7.12, only two δt levels are shown. This process can be repeated for progressively finer correlation maps. To add information from a map at a certain δt_i, the map from one level down at δt_{i-1} is interpolated and summed. After summation, the correlation peak is divided by the number of levels used, to re-normalize the correlation value to ≤ 1. This step is not shown in Figure 7.12. The result is a scattered correlation map of $(\Delta x, \Delta y)$-coordinates and corresponding correlation values, on which the displacement peak is to be evaluated.

Vector evaluation

The fact that the data is now contained in scattered data-points adds a complication to the implementation of a 3-point peak estimator. In gridded data, the four points neighbouring the absolute peak can be extracted based on their indices. In the scattered data, the grid must be reconstructed. First the absolute maximum of the scattered map is found, and the distance from each point to this maximum is evaluated. The grid spacing Δ_g of the finest grid is found by finding the smallest distance to the maximum. The coordinates of four neighbour points, two in each dimension, are set up using the peak's coordinates and grid spacing. A scattered, linear interpolant is set up using the nearest 32 points, and evaluated at the constructed coordinates. This effectively picks the neighbours from the grid on which the peak is found, as there should be datapoints on these locations. Interpolation is only performed in case the peak exists on an edge between two correlation maps.

Using the absolute maximum and the constructed neighbours, a 3-point peak estimator is fitted. This is done in x- and y-dimensions separately, the process used will be explained in the x-direction next. A Gaussian peak is described by Equation 7.2a, where a, b and c denote the peak height, location and standard deviation, respectively. The x-coordinate of the absolute peak and the two constructed x-neighbours provide three datapoints (x_1, x_2, x_3) which allow to resolve these three unknowns. To this end, the Gaussian function is expanded in Equation 7.2b. This expansion allows to re-write the function into a linear system in Equation 7.2c, where the coordinates in $\mathbf{A}$ and the associated correlation values in $\mathbf{C}$ are known. Solving this linear system for $\mathbf{b}$ then allows to find the peak location and peak height. The peak heights found in the x- and y-peak fits are averaged to provide the fitted peak height.

The obtained peak coordinates $(\Delta x, \Delta y)$ give the particle image displacement in pixels. As the perspective correction is implemented in Davis 8.4 in the SOC evaluation, this displacement is simply multiplied by the pixel size from the calibration, and divided by δt_0 to find the associated velocity (u, v). The associated Matlab code of the vector evaluation can be found in Appendix B.4.

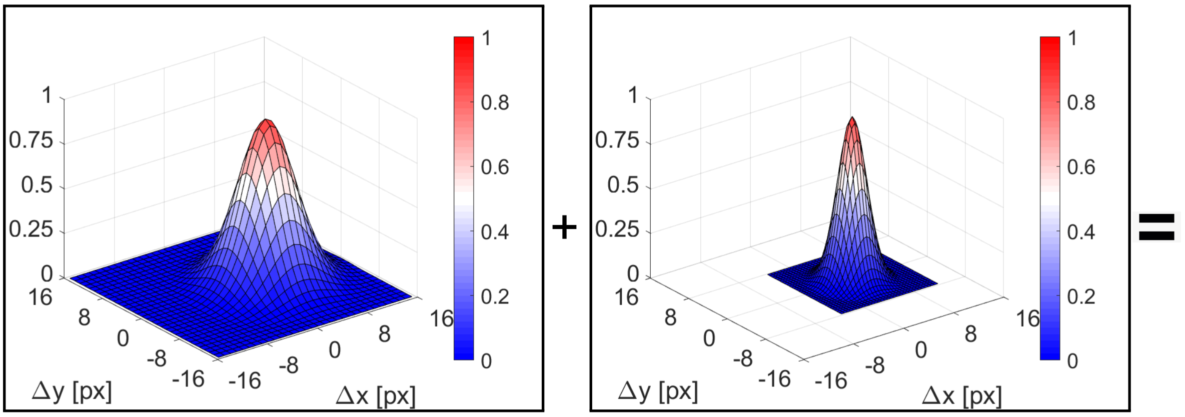

(a) δt_0 map

(b) δt_1 map, shifted and scaled down to δt_0

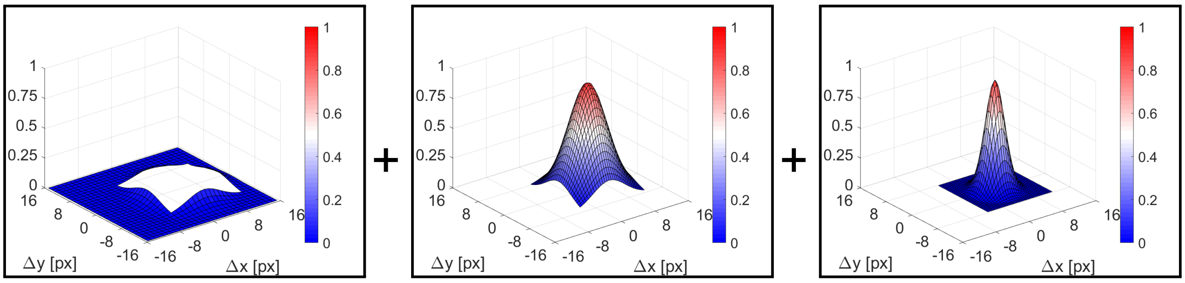

(c) δt_0 map, remainder after interpolation

(d) δt_0 map, interpolated on δt_1 grid

(e) δt_1 map

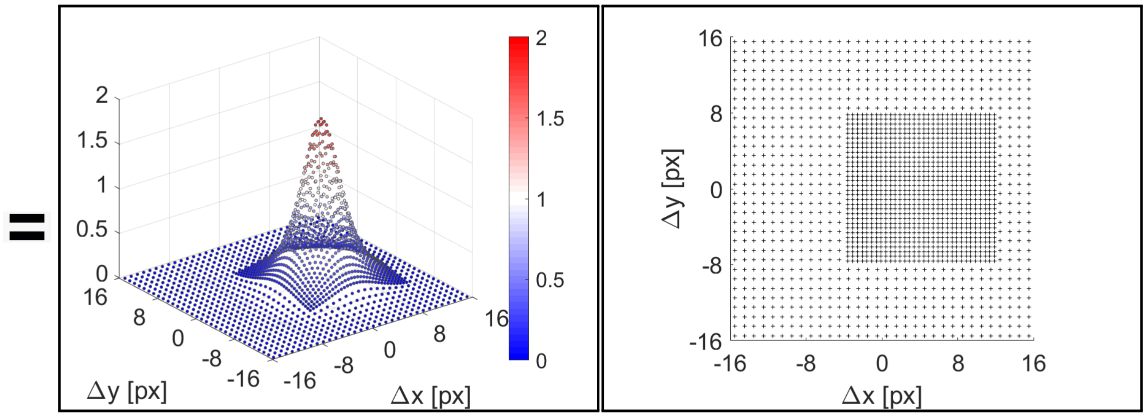

(f) Combined scatter map

(g) Combined scatter map coordinates, top view

Figure 7.12: Visualisation of summing two multi-δt correlation maps. Correlation maps from a Mach 0.1 freestream, with $[\delta t_0, \delta t_1] = [1.37, 2.75]\mu s = [\delta t_0, 2\delta t_0]\delta t_0$. Note that the summed map has not been re-normalized after summation here.

$$C(x) = a\exp\left\{-\frac{(x-b)^2}{2c^2}\right\} \tag{7.2a}$$

$$C(x) = \left[-\frac{1}{2c^2}\right]x^2 + \left[\frac{b}{c^2}\right]x + \left[log(a) - \frac{b^2}{2c^2}\right] \tag{7.2b}$$

$$\mathbf{C} = \mathbf{Ab} \tag{7.2c}$$

$$\begin{pmatrix} C(x_1) \\ C(x_2) \\ C(x_3) \end{pmatrix} = \begin{pmatrix} x_1^2 & x_1 & 1 \\ x_2^2 & x_2 & 1 \\ x_3^2 & x_3 & 1 \end{pmatrix} \begin{pmatrix} -1/(2c^2) \\ b/c^2 \\ log(a) - b^2/(2c^2) \end{pmatrix} \tag{7.2d}$$

Multi-dt turbulence/noise evaluation

Finally, the turbulence- and noise decomposition is performed. The 1-dimensional method of Equation 4.7 is easily extended into two dimensions, which is shown in Equation 7.3. The relative influence of the measurement noise diminishes with the actual particle image displacement $|\Delta x^2|$. To maintain consistency, the turbulence intensities in Equation 7.3 are therefore evaluated with respect to the local velocity magnitude. Numerical implementation of the decomposition is shown in Appendix B.5.

$$TI^2_{meas} = TI^2_{real} + \frac{\sigma^2_{\Delta x}}{|\Delta x^2|} \tag{7.3a}$$

$$\begin{pmatrix} TI^2_{meas,\delta t_0} \\ \dots \\ TI^2_{meas,\delta t_N} \end{pmatrix} = \begin{bmatrix} 1 & 1/|\Delta x|^2_0 \\ \dots & \dots \\ 1 & 1/|\Delta x|^2_N \end{bmatrix} \begin{pmatrix} TI^2_{real} \\ \sigma^2_{\Delta x} \end{pmatrix} \tag{7.3b}$$

A minimum of $N = 2$ is required to solve for the unknown turbulence intensity and measurement noise. When $N > 2$, the linear system in Equation 7.3 is overdetermined. Linear least-squares regression is used to efficiently fit a turbulence intensity that best fits the measurement data. After fitting, the turbulence intensity can be multiplied by $\sqrt{u^2 + v^2}/U_0$ to define the turbulence intensity on the freestream velocity instead of the local velocity magnitude.

The phase-averaged velocity fields are computed using the multi-δt SOC processing described above. Acoustic velocities are found using Equation 3.2. Here, the time-averaged velocity field $\bar{\mathbf{u}}(\mathbf{x})$ is the average of the 12 phase-averaged fields. Turbulence and measurement noise is decomposed using Equation 7.3. The measured turbulence intensity is found from the fluctuation vector fields, where $TI_{meas} = \sqrt{1/2(\sigma^2_u + \sigma^2_v)}/\sqrt{u^2 + v^2}$.

7.3.5. Reflection clean-up

At higher Mach numbers, the unsteady reflections produce a characteristic SOC correlation map. Such a map is shown in Figure 7.13a. Two structures can be seen. The peak in the center shows the signal from the particle image displacement. The vertical band shows the 'displacement' associated to a reflection. The reflections are consistent between double-frames, and do therefore not move in x. As they produce a vertical band of high, nearly constant intensity, the associated correlation map is a peak around $\Delta x = 0$, which is constant in y. As a result, the correlation value of the particle image displacement is increased around $\Delta x = 0$. The effect is demonstrated in Figure 7.14, where the two effects are modelled using simple 1-D Gaussian curves. Due to the addition of the 0-mean curve of the reflection, a lower displacement is found at the correlation peak. This causes the window displacement to fail in these cases, as a too low initial displacement is given.

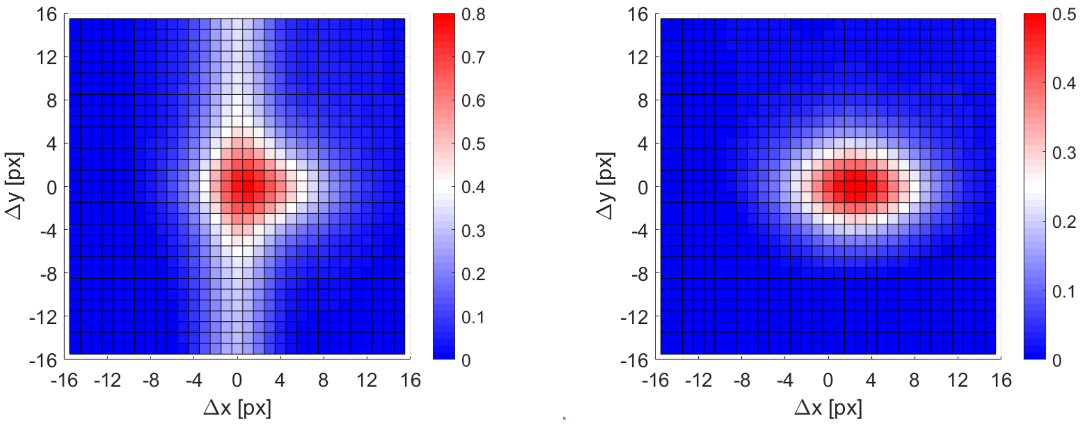

(a) Raw

(b) Cleaned up

Figure 7.13: δt_0 SOC correlation map within an orifice reflection, before and after reflection correction. Mach 0.6 timing test result, notice the decrease in correlation peak strength due to the reflection subtraction.

An attempt is made to alleviate the effect of the reflection in the multi-δt evaluation. The correlation associated to the reflection has a very consistent structure, which can be used. Before combining the individual correlation maps, the peak value is checked. If the peak correlation value is ≤ 0.35, it is assumed the signal is dominated by the reflection. In that case, only δt_0 and δt_1 are used: particle image displacements are still within these correlation windows, meaning they can be used even with a window shift that is reduced by the reflection.

Next, these two correlation maps are cleaned up. The correlation map structure of the reflection resembles a Gaussian curve in x, which is constant in y. The correlation map is averaged in y-direction in the top and bottom quarter of the interrogation window. The actual displacement peak is not expected in these regions, see Figure 7.13a. The average profile resembles the 'Reflection' curve in Figure 7.14. Subtracting this curve from each row in the interrogation window then yields a correlation map from which the reflection is removed.

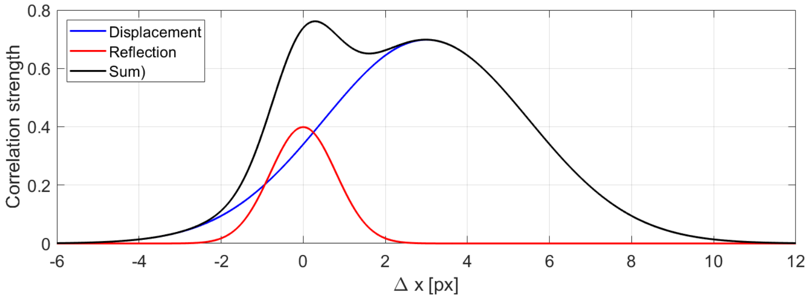

Figure 7.14: Effect of summing correlation values from the actual particle image displacement and from unsteady reflections. Both effects are represented by a Gaussian peak in one dimension.

Applying this correction to Figure 7.13a yields the correlation map in Figure 7.13b. While this method is far from perfect, a more round correlation peak is obtained. This allows to better find the actual displacement in the regions of reflections. The clean-up is implemented in the multi-δt correlation map code in Appendix B.3. This method is not implemented in the processing pipeline in Davis, as the velocity fields could not be written to a correct vector buffer file that Davis can read.

7.4. Vector field post-processing

For the evaluation of derived quantities, such as vorticity, the velocity fields are de-noised. This aims to reduce measurement noise, to which derived quantities are very sensitive [39]. At each vector coordinate, a polynomial of total order 2 is fitted to both velocity components in a $3x3$ range. The example for the polynomial fitted for u is shown in Equation 7.4. The 5 fitting coefficients c_i are found from a least-squares fit on the 9 values for u within the range. These denoised fields are only used when computing derived quantities. All other values are computed using the multi-δt vector fields without any further post-processing.

$$u(x, y) = c_0 + c_1 x^2 + c_2 x + c_3 y^2 + c_4 y + c_5 xy \tag{7.4}$$

7.5. Validation of vector evaluation

multi-δt vector evaluation is performed using a self-written script in Matlab. Before evaluating the results, it is validated whether the processing steps discussed above are implemented correctly. To this end, vector fields obtained from the Matlab code are compared to results obtained using LaVision Davis to validate the self-written code. Two cases are used for this, described in Table 7.1.

Table 7.1: Overview of datasets used for vector validation

	Lavision Davis		Matlab	
Case	δt's used	Processing details	δt's used	Processing details
No-flow	δt_0	Single pass, vector smoothing	δt_0	Single pass, vector smoothing
Mach 0.1	δt_1	Multi-pass, vector smoothing	δt_0, δt_1, δt_2, δt_3	Single-pass, multi-δt , no vector smoothing

For the no-flow case, only the first δt is evaluated. This allows to validate the peak fitting process apart from the window shifting and multi-δt correlation map combination. As single-δt sets are used as estimators for the next higher δt, vector smoothing (averaging) is included in the vector post-processing in Davis. As the no-flow set exhibits strong gradients in both directions, vector smoothing is applied in Matlab for the purpose of this comparison.

The aim of the comparison at Mach 0.1 is to validate window shifting and multi-δt evaluation in Matlab. Larger window displacements are used in this case than in the no-flow case, allowing to better validate these steps. The set is re-processed in Davis for the validation, using a multi-pass grid refinement scheme on the δt_1 dataset. As Matlab uses multi-δt processing, some differences are expected due to using different data-sets. These differences are expected to be negligible in the outer parts of the boundary layer, where the flow is steadiest. Vector smoothing was accidentally left active in Davis, which was not included in the Matlab vector post-processing. As the interest is on the outer part of the boundary layer, where velocity gradients are near zero, it was decided not to re-do this evaluation.

7.5.1. Single-dt vector validation

Differences between the velocity fields from Matlab and Davis are evaluated per phase, after which the RMS over all 12 phases is computed. Figure 7.15 shows these RMS differences over all phases for the absolute and relative velocity differences. Relative differences are evaluated relative to the velocity from Davis. Furthermore, differences are evaluated in velocities: for the $\delta t_0 = 5\mu s$, a difference of $0.1 px$ corresponds to $0.23 ms^{-1}$. In Figure 7.15a, it can be seen that the absolute difference is near-zero throughout the field of view. From this, it is concluded that no fixed shift is introduced by the peak fitting and vector evaluation.

Next, the RMS difference in relative velocity is looked at in Figure 7.15b. The time-averaged velocity field is displayed in Figure 7.15c, as the mean velocity is non-trivial. Relative errors rise to $\approx 10\%$ in regions of low velocity. This is attributed to the low velocity itself: a true zero velocity would yield an infinite error in relative velocity. In the regions where the velocity is higher, the relative error quickly reduces to zero. Based on these observations, it is concluded that vector computation is implemented correctly in the Matlab code.

7.5.2. Multi-dt: window shift validation

The Mach 0.1 is evaluated in similar fashion, the absolute and relative difference fields are shown in Figure 7.16. In the outer part of the boundary layer, both differences reduce to near-zero values. Near the wall, the differences grow to approximately 1%. Near the wall, turbulent fluctuations and gradients are stronger. It is expected that these differences in flow physics, combined with the difference in datasets and vector post-processing, are the cause for these differences. Any error in multi-δt processing would introduce more homogeneous errors through the field, in either an absolute or relative sense. As such an effect is not observed, it is concluded that the window shift and combination of multi-δt correlation maps is implemented correctly, completing the validation of the vector computation.

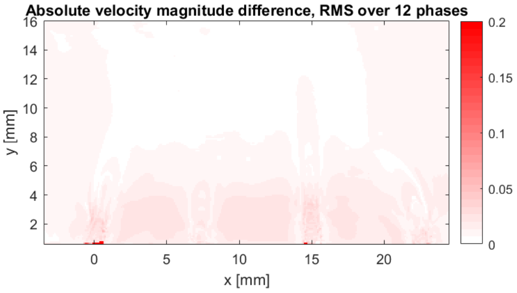

(a) Absolute difference in velocity magnitude.

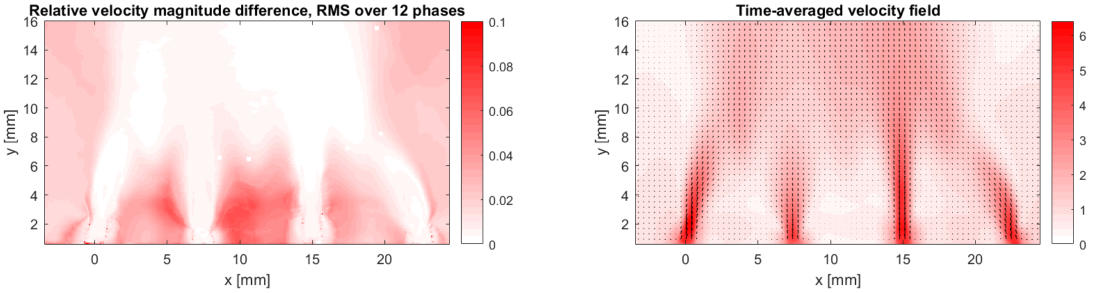

(b) Relative difference in velocity magnitude.

(c) Time-averaged flow field.

Figure 7.15: No-flow vector field validation. Differences are evaluated per phase, after which the RMS is taken over all 12 phases. Differences in x- and y-velocity components are similar, and omitted for brevity.

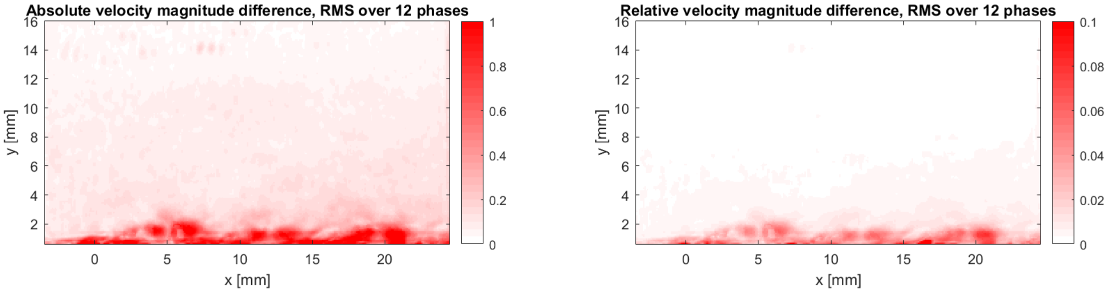

(a) Absolute difference in velocity magnitude.

(b) Relative difference in velocity magnitude.

Figure 7.16: Mach 0.1 vector field validation. Differences are evaluated per phase, after which the RMS is taken over all 12 phases. Differences in x- and y-velocity components are similar, and omitted for brevity.

III

Results

8

Assessment of multi-dt PIV

In this chapter, an assessment of the multi-δt PIV method is made. Before moving on to answering the research questions, the accuracy and validity of the method is addressed. Note that this is different from the validation in Section 7.5: whereas the previous section focussed on the correctness of the numerical implementation, the current chapter addresses the performance of the newly implemented PIV methodology.

8.1. Turbulence and measurement noise decomposition

First, preliminary results of the turbulence/noise decomposition of subsection 4.2.2 are evaluated. To this end, the multi-δt results of the timing tests are used, using the $\delta t = [1, 5, 10, 15] * \delta t_0$ sets. Recall from Chapter 4 that the decomposition is performed as shown in Equation 8.1. This decomposition assumes that the noise component $\sigma_{\Delta x}$ is independent of the global particle image displacement $|\Delta x|$.

$$TI_{meas}^2 = TI_{real}^2 + \frac{\sigma_{\Delta x}^2}{|\Delta x^2|} \tag{8.1}$$

8.1.1. Decomposition results

Figure 8.1 shows the turbulence intensity results from this decomposition for both sets. The results are deemed non-physical: while this is most obvious in the spikes and diagonal lines in the Mach 0.6 results, the Mach 0.3 results display diagonal lines, where turbulence intensity is reduced, as well. The global order of magnitude of the turbulence intensity seems physical: from near-zero in the freestream to $T_I \approx 10\%$ near the wall.

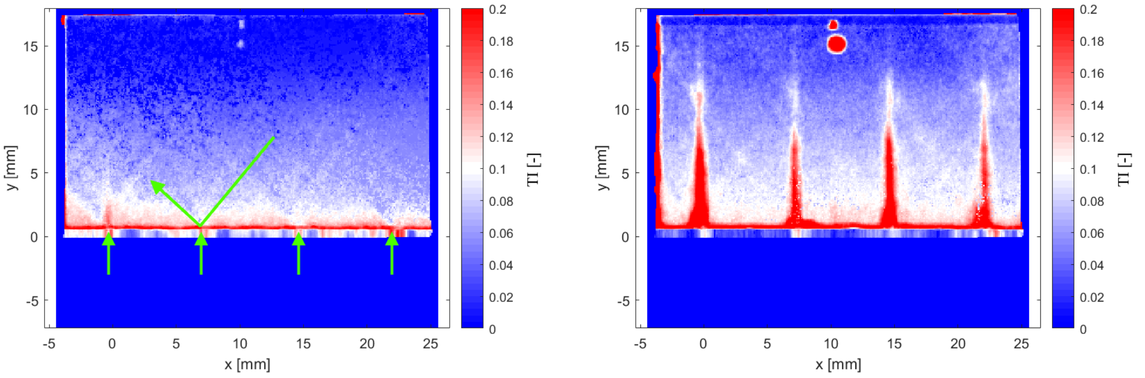

(a) Mach 0.3. Diagonal laser sheet reflections from the orifices are seen at the indicated positions. A reflection is indicated at the second orifice from the left.

(b) Mach 0.6. The diagonal reflections can still be seen, but are now dominated by the vertical reflections.

Figure 8.1: Timing tests, multi-δt turbulence results.

In the measurement noise results in Figure 8.2, the non-physical results are more pronounced: measurement noise in the order $\mathcal{O}(2px)$ is deemed erroneous: directly picking the correlation peak without further 3-point peak fitting should find the correlation peak within a pixel. Note that all turbulence fields are fully computed in Davis; only the decomposition is performed in Matlab, which is based on the velocity fields. As the patterns in figures 8.1-8.2 resemble the reflections from the laser sheet (cf. figures 5.7 and 6.4), it is expected that the errors in the decomposition are related to the current test set-up. This is further evaluated in the next section.

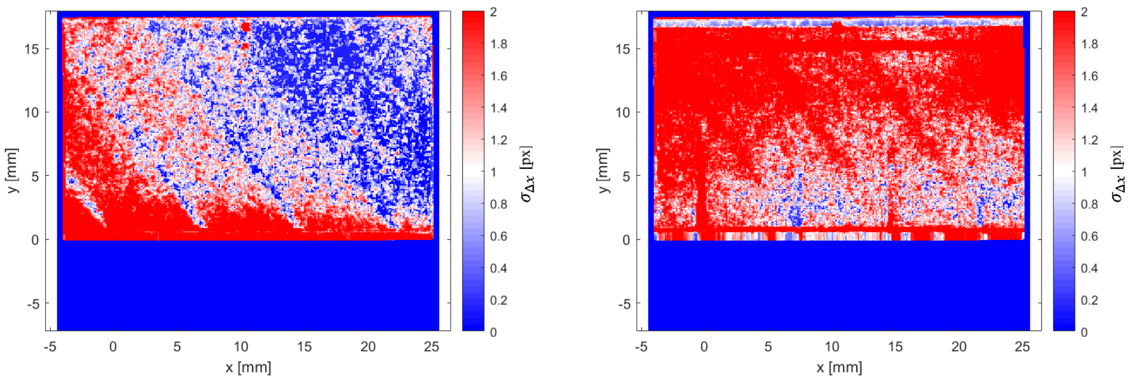

(a) Mach 0.3

(b) Mach 0.6

Figure 8.2: Timing tests, multi-δt measurement noise results.

8.1.2. Evaluation of turbulence/noise decomposition

Figure 8.3 shows the multi-δt SOC correlation peak height through the domains. Note that the turbulence fields are computed using a standard processing in Davis. The SOC correlation strength is expected to be different, but trends are expected to hold. Figure 8.3 shows similar information as the correlation profiles in Figure 6.5, but the full images show more clearly the link to the turbulence and noise results from the previous section. It is observed that the non-physical patterns in the decomposition results are closely related to the patterns seen in the correlation peak height fields.

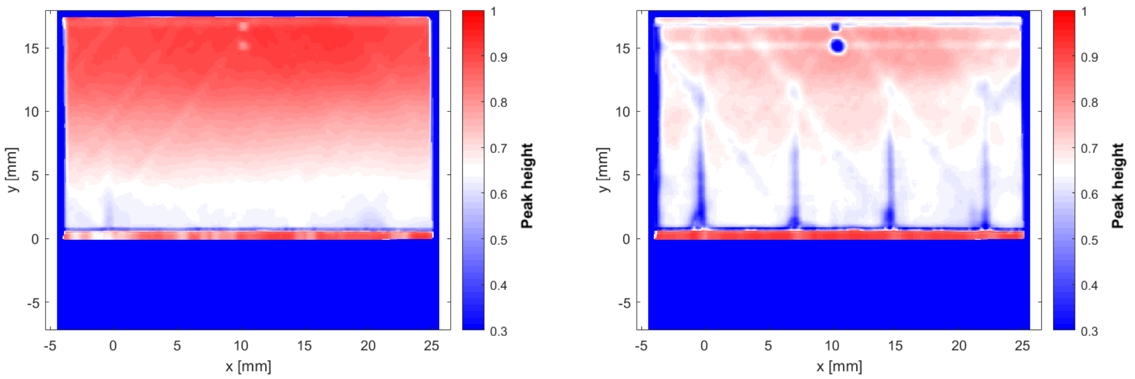

(a) Mach 0.3

(b) Mach 0.6

Figure 8.3: Timing tests, normalized multi-δt correlation peak height.

It can be argued that a reduction in average correlation peak height can indicate an increase in measurement noise: if correlation is lower, interrogation windows are matched between both frames with less certainty. In subsection 6.3.1, it is shown that correlation strength is reduced:

- Near the wall, due to turbulence, in-plane gradients and steady reflections.
- In unsteady reflections, as particles are less visible, and a distinct signal remains from the reflection itself.
- For increasing k_t, which is argued to amplify the effects from turbulence and gradients.

The results above, combined with subsection 6.3.1, shows that the measurement noise is not independent of the particle image displacement in the current work. The exact dependence of $\sigma_{\Delta x}$ on $|\Delta x|$, hence on δt and k_t, is unknown. For a thought experiment, a linear increase with the displacement is postulated, as shown in Equation 8.2a, with c an arbitrary constant. Substituting this expression into the original decomposition yields the expression in Equation 8.2b. In terms of the least-squares fitting process, two main changes can be seen. First, the constant term gets an addition of c^2. Secondly, a term proportional to $1/|\Delta x|$ is introduced. The term proportional to $1/|\Delta x^2|$ remains unchanged.

$$\text{Assume: } \sigma_{\Delta x} = \sigma_{\Delta x,true} + c * |\Delta x| \tag{8.2a}$$

$$TI^2_{meas} = \underbrace{TI^2_{real} + c^2}_{Constant} + \underbrace{\frac{\sigma^2_{\Delta x,true}}{|\Delta x^2|}}_{\propto|\Delta x^{-2}|} + \underbrace{\frac{2c\sigma_{\Delta x,true}}{|\Delta x|}}_{\propto|\Delta x^{-1}|} \tag{8.2b}$$

The main observation from Equation 8.2 is that violating the assumption of a fixed measurement noise RMS makes the decomposition of Scharnowski [40] inappropriate. A modification to the function form of Equation 8.1 is needed which captures the effects of turbulence intensity, in-plane gradients and reflections. Within the current work, only the qualitative dependencies discussed in subsection 6.3.1, repeated in the list above, could be made. These effects are all related to the measurement noise through the correlation peak height. Sections 8.3.2-8.3.3 present a further investigation into the measurement noise and its relation to the correlation strength, but no quantitative statement is found. Finally, it should be noted that any modification to Equation 8.1 should be a low-order model. In this thesis, 4 $|\Delta x|$ points are available for fitting, which allows to fit a maximum of 4 coefficients. 4 points already proved expensive in acquisition and processing effort.

It is concluded that the turbulence/noise decomposition is not applicable to the current investigation, due to a measurement noise which varies with the pulse separation time. The raw turbulence fields suffer similarly from the measurement noise, yielding results as in Figure 8.1, and are deemed unusable. Time did not allow to further look into these issues. All further evaluations into turbulence intensities are therefore dropped from the current research. Next, several suggestions are formed which could improve the decomposition and turbulence results.

8.1.3. Suggestions for future improvements

The original tests by Scharnowski [40] concern the evaluation of freestream turbulence of low intensity. As a next step, these test can be repeated using grid turbulence. This allows to evaluate the decomposition in more turbulent flows, without the influence of steady gradients and reflections near the wall. It can then be investigated if the measurement noise is indeed directly affected to the turbulence, through in-plane deformations and a lower correlation strength. If it is found to be so, a modified form of Equation 8.1 can be suggested for this effect. This modified form should then be better capable of performing the decomposition in flows where the measurement noise is not independent from the particle image displacement due to turbulence.

A step up from grid turbulence would be to perform the decomposition on a boundary layer over a smooth wall. This includes the steady near-wall gradients, but reduces the impact of reflections due to seeding accumulation and vibrations seen with the liner sample.

8.2. Choice of datasets for PIV assessment

Not all datasets that are recorded are used in the subsequent analysis. As shown and discussed in subsection 6.5.1, the sound pressure levels used in the experiment are lower than intended. The Mach numbers are reached properly. As a result, the range of interest R_I is increased with respect to the anticipated values. This means that the DVR is deemed insufficient to resolve all sets. The sets that are selected and their expected value for R_I are listed in Table 8.1. The first block, denoted ”2021, multi-δt ”, comprises the datasets selected for the current analysis. Two sets, listed as ”2021, single-δt”, are re-processed using a more standard grid-refinement scheme. Using the same raw data allows to evaluate differences that are caused by the methodology, such that any gain in DVR from the multi-δt method can be quantified. δt_1 is selected, as this results in a freestream displacement of $|\Delta x| \approx 10px$. These sets are chosen as one value for R_I is close to the estimated DVR limit of 200, while the other exceeds it. Finally, a Mach 0.1 SPL sweep is taken from the results of Van der Meulen [51], which effectively also makes for a sweep in R_I. These sets are shown in the last block in Table 8.1 as ”2019, single-δt ”.

Table 8.1: Overview of DVR assessment datasets

Name	px/mm	δt choice	Processing	$M_0[-]$	SPL $[dB]$	$R_I[-]$
2021, multi-δt	86.8	See subsection 6.3.3	multi-δt SOC, with $d_I = 32$ and $k_t \approx 16$	0.0	138.7	N/A
				0.06	117.5	568
				0.1	144.3	44
				0.2	145.0	82
				0.4	140.3	282
				0.6	140.3	420
				0.8	134.3	1169
2021, single-δt	86.8	δt_1 from subsection 6.3.3	single-δt SOC, with $d_I = 32$, $k_g = 2$, $75\%OL$	0.4	140.3	282
				0.6	140.3	420
2019, single-δt	55.4	Freestream displacement of $d_I k_g = 16px$	single-δt standard, with $d_I = 16$, $k_g = 4$, $50\%OL$	0.1	108.8	2568
				0.1	118.3	861
				0.1	128.3	271
				0.1	138.1	88
				0.1	145.7	36

8.3. Measurement noise and DVR

The definition of the DVR is re-stated in Equation 8.3. The original scheme in Figure 4.5 allowed to resolve this DVR directly from the turbulence/noise decomposition, but Section 8.1 discussed how this decomposition failed. Therefore, the DVR can not be found explicitly. This section describes how the DVR is estimated, and shows the results for the processed datasets.

One point of attentions is that for the 2021 datasets, formally the final interrogation window size is $d_I = 32px$ in Equation 8.3. In subsection 5.4.4, it is shown that $d_I = 32ox$ is required due to the seeding density. The measurements have been conducted aimed at a window size $d_I = 16px$, with a δt_0 leading to a freestream particle image displacement $\Delta x_0 = 4px$. Similarly, the ”2021, single-δt ” recordings are not optimized to adhere exactly to the one-quarter rule. For these reasons, it is better to evaluate the DVR in the second form in Equation 8.3. Theoretically, the 2021 cases could see a larger maximum velocity, as $\Delta x_0 < d_I k_g/4$. For the multi-δt approach, this does not matter in terms of DVR: increasing δt_0 to adhere to the one-quarter rule equally scales down k_t, as the upper time limits remain the same.

$$DVR = \frac{d_I/4}{\sigma_{\Delta x}} k_g k_t = \frac{\Delta x_0}{\sigma_{\Delta x}} k_t \tag{8.3}$$

To evaluate the measurement noise, the phase-averaged freestream velocity in x-direction is assumed steady. Next, it is postulated that all spatial variations in the freestream velocity are due to measurement noise. This allows to find the measurement noise as shown in Equation 8.4: the standard deviation of u with respect to the phase-averaged $\langle u\rangle_\phi$ is evaluated. After this, the RMS over all phases is taken. Multiplying by $\delta t_0/\Delta_{px}$ converts the standard deviation in units ms^{-1} to pixels. Finally, the scaling of the interrogation window needs to be accounted for: multiplying with k_t ensures the resulting noise $\sigma_{\Delta x}$ is for an unscaled interrogation window at δt_0.

$$\sigma_{\Delta x} = k_t \frac{\delta t_0}{\Delta_{px}} \sqrt{\frac{1}{N_\phi N_{vec}} \sum_{\phi=1}^{N_\phi} \sum_{i=1}^{N_{vec}} \left(u_{i\phi} - \langle u\rangle_\phi\right)^2} = k_t \frac{\delta t_0}{\Delta_{px}} \sigma_u \tag{8.4}$$

8.3.1. Global evaluation of measurement noise and DVR

To evaluate a global value for the measurement noise, a domain outside the boundary layer is chosen where Equation 8.4 is evaluated. The domain chosen for the 2021 data-sets is shown in Figure 8.4, spanning from $(x, y) = (12, 14)\ mm$ to $(x, y) = (22.5, 15.5)\ mm$. This is done to avoid the influence of the reflections as much as possible: the top-right suffers the least from the outgoing reflections of the laser sheet. The number of vectors is $N_{vec} = 1808$ within this domain. For the 2019 data-set, these locations are $(x, y) = (8, 14)\ mm$ to $(x, y) = (18.5, 15.5)\ mm$, for a total of $N_{vec} = 803$ vectors.

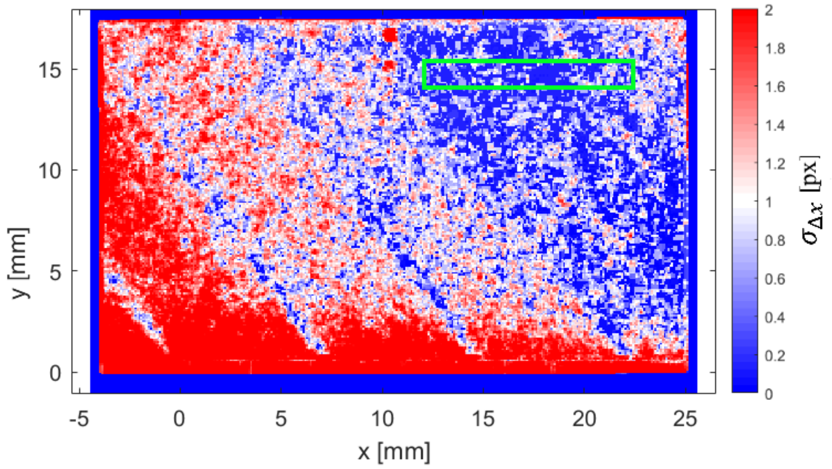

Figure 8.4: Mach 0.3 timing test, noise results, showing the domain where the measurement noise and DVR are evaluated. Image adapted from Figure 8.2a.

The resulting values for all data-sets are shown in Figure 8.5. For the 2021 multi-δt sets, the measurement noise grows in a non-smooth manner for an increasing grazing flow Mach number. The lowest value is reached at $M_0 = 0.06$, where $\sigma_{\Delta x} \approx 0.04px$. The highest value $\sigma_{\Delta x} \approx 0.13px$ is reached at the highest Mach number, $M_0 = 0.8$. The measurement noise for the single-δt results on the other hand are both much lower at $\sigma_{\Delta x} \approx 0.02px$, and vary much less for varying Mach numbers and SPL.

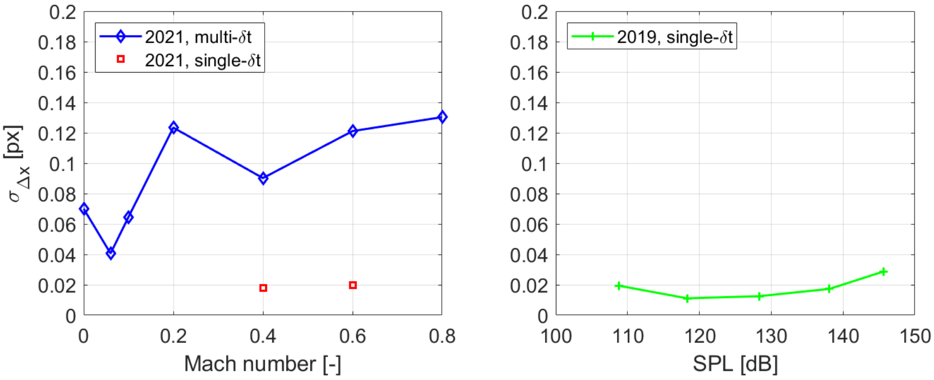

Figure 8.5: $\sigma_{\Delta x}$ results for the 2021 Mach sweep (left) and 2019 SPL measurements (right). Mach numbers and sound pressure levels as defined in Table 8.1.

Figure 8.6 shows the associated DVR results, which implement the noise results from Figure 8.5 in Equation 8.3. The dashed line indicates the DVR which is expected from the timing range at a constant $\sigma_{\Delta x} = 0.1px$. Deviations from this expectation are caused by the variation in the measurement noise. In the 2021 results, it can be seen that the multi-δt and single-δt methods perform similarly. Even though the single-δt sets show a much lower noise component, the multi-δt timing range $k_t = 16$ is much larger than the single-δt grid refinement factor $k_g = 2$. As a result, the final DVR is comparable. The 2019 results show a higher DVR, which can be explained similarly: the smaller magnification factor allows for a window size of $d_I = 16px$. Refining from $64x64px^2$ windows gives a factor $k_g = 4$, doubling the DVR.

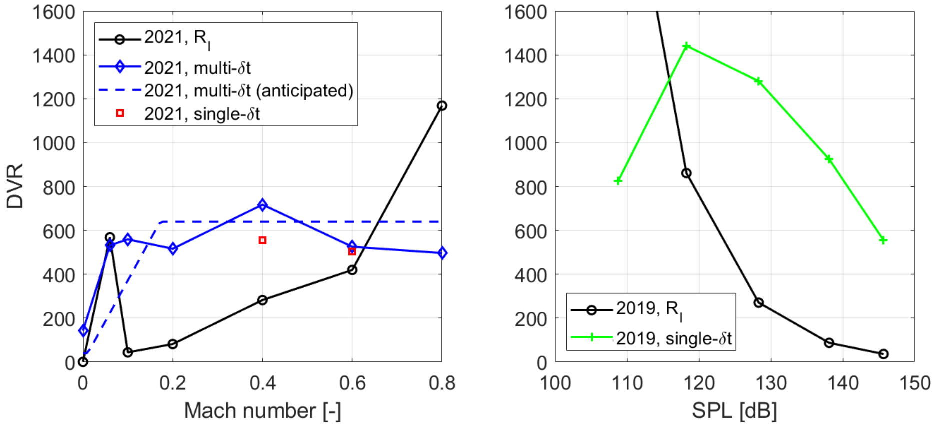

Figure 8.6: DVR results, associated to Figure 8.5. The value for $R_I = 2568$ for the 2019 results at $108.8dB$ is not included for better and consistent visibility of all other points.

From the above, it can be concluded that the multi-δt method performs as expected, while single-δt performs much better than anticipated. This is due to the much lower measurement noise, which has been assumed a priori to be fixed for all methods and pulse separation times at $\sigma_{\Delta x} = 0.1px$. These differences in measurement noise are now investigated further.

8.3.2. Dependencies of measurement noise

In subsection 8.1.2 it is shown that the variation of the measurement noise prevents a successful decomposition between fluctuation caused by turbulence and noise. As this shows that this variation is strong, its behaviour under varying the timing range deserves further attention. Figure 8.7 shows the average correlation peak height for the 2021 multi-δt sets of Figures 8.5-8.6. It can be seen that the point of the lowest $\sigma_{\Delta x}$ in Figure 8.5 corresponds to the peak correlation strength at Mach 0.06 in Figure 8.7. Furthermore, a near-mononotic and accelerating decrease in peak height with Mach number is seen. This is partly attributed to problems in seeding density and wind tunnel vibrations at higher Mach numbers. These problems are deemed negligible at Mach numbers $M_0 < 0.3$ based on observations during testing. Therefore, it is argued that the peak height steadily decreases with grazing flow velocity.

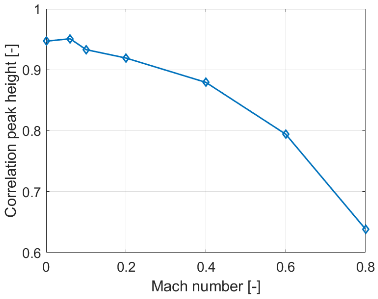

Figure 8.7: Variation of average correlation peak height with Mach number for the 2021 multi-δt data-sets. Peak height is evaluated in the same domain as the measurement noise.

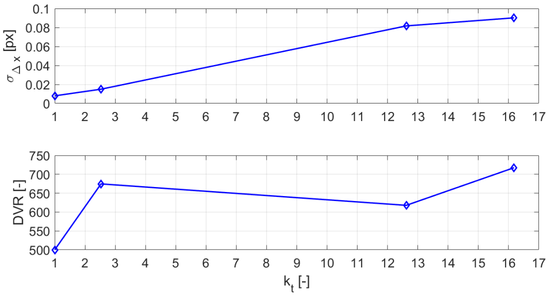

Figure 8.8: Variation in measurement noise as a function of the timing range k_t (top), along with the associated DVR (bottom).

To isolate the effect of the pulse separation time, the 2021 Mach 0.4 sets are processed again, with all four possible timing ranges $k_t \approx [1, 2.5, 12.5, 16]$. Note that, with the exception of the δt_0-only set, these are all still multi-δt results, as processing is continued up to a certain pulse separation time. Figure 8.8 shows the results for these four datasets. A clear monotonic increase in measurement noise can be seen for increasing the timing range. Note that at $k_t = 2.5$, the measurement noise $\sigma_{\Delta x} \approx 0.02$, which is similar to the corresponding 2021 single-δt result in Figure 8.5. This shows that the difference in measurement noise between the multi-δt and single-δt results is indeed due to the increase in timing range. Specifically, the longest δt used is the determining factor: in a grid refinement approach, the pulse separation time is increased with k_g. This is identical to how it is increased by k_t in a multi-δt approach. Furthermore, this result explains the lower $\sigma_{\Delta x}$ values at $M_0 < 0.2$ in Figure 8.5: here, the timing range is reduced to adhere to the acoustic phase limit $\delta t_{lim,phase}$. As a result, the measurement noise is reduced as well. Finally, a noise level of $\sigma_{\Delta x}$ is much lower than the more generally stated value of $0.1px$. This may be partly attributed to the very large particle image size, discussed in subsection 5.4.3.

In the bottom graph of Figure 8.8, it can be seen that the resulting DVR does not behave monotonically, as $\sigma_{\Delta x}$ is not linear in k_t. Instead, $\sigma_{\Delta x}$ shows a slight S-shape over the four points available. As a result, the highest DVR is reached for the highest timing range, although the steepest rise is seen between $1 < k_t < 2.5$.

Lastly, it is investigated whether a distinct relation exists between the correlation strength and the measurement noise. This is done by creating a scatter of the correlation peak height against $\sigma_{\Delta x}/k_t$ for the 2021 multi-δt sets, shown in Figure 8.9. Dividing the noise by the timing range yields the 'effective' measurement noise with the interrogation window scaling included. This quantity is inversely proportional to the DVR. In Figure 8.9, no distinct trend is observed.

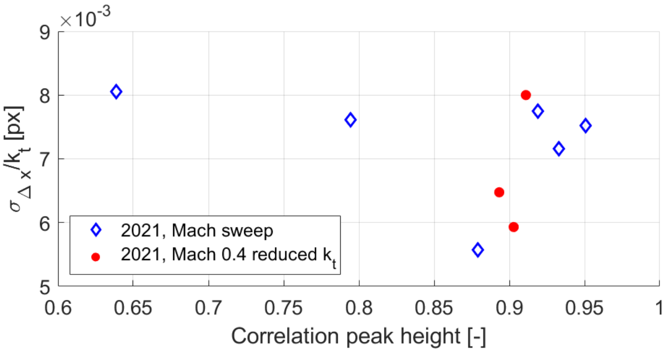

Figure 8.9: Variation of $\sigma_{\Delta x}/k_t$ with the correlation strength, 2021 multi-δt results. The re-processed Mach 0.4 sets with reduced timing range are also included. The $M_0 = 0.0$ result with $\sigma_{\Delta x} = 0.028$ is excluded for better visibility.

8.3.3. Local evaluation of measurement noise and DVR

So far, the evaluation has been limited to the evaluation of $\sigma_{\Delta x}$ in the freestream. In sections 6.3.1 and 8.1, it is shown that correlation strength is reduced strongly towards the face sheet. Therefore, it can be expected that the DVR decreases towards the wall. An attempt is made to evaluate the DVR as a function of the $y-$coordinate. Similar to the preceding discussion, this is also done for the Mach 0.4 multi-δt data-sets. As a first check, the multi-δt sum of correlation correlation strength is averaged in x-direction and over all 12 phases. The result is shown in Figure 8.10. The main patterns are similar to those discussed in sections 6.3.1 and 8.1: correlation reduces for increasing k_t and closer to the wall.

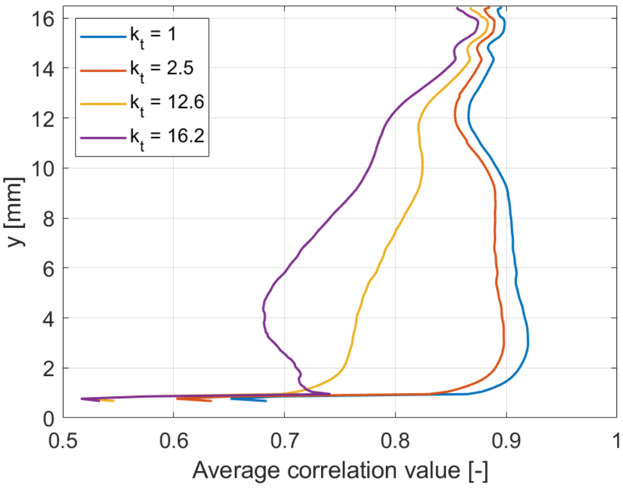

Figure 8.10: multi-δt SOC correlation strength for the 2021 Mach 0.4 set, for varying levels of k_t.

To evaluate the y-dependent measurement noise and associated DVR, Equation 8.4 is used. Instead of using the domain in the freestream for the global noise evaluation, each row of constant y-coordinate is taken as the domain, with $N_{vec} = 303$ vectors per row. To reduce the influence of phase-dependent structures in the boundary layer, the time-averaged $\bar{u}$ is used. Note that in this process, two assumptions are implicitly made:

- All turbulent fluctuations are statistically converged.
- There is no variation of $\bar{u}$ in x-direction.

These assumptions are not expected to be fully valid. The boundary layer and acoustic-flow interaction that are developing over the liner sample could violate the second assumption. At Mach 0.4 and $140.3dB$, aerodynamic effects of the acoustic forcing are expected to be low, indicated by the high value of $R_I = 282$. Furthermore, boundary layer development is expected to be similar for the different k_t cases considered. As it is a physical effect, visible in the mean $\bar{u}$ velocity component, it should be included similarly in the results at different k_t. Therefore, trends are expected to hold, but numerical results must be interpreted with some caution.

Measurement noise results

Figure 8.11 shows the measurement noise results, in a moving average of 10 samples. As with the global evaluation, the local measurement noise is nearly identical for the $k_t = 2.5$ and $k_g = 2$ cases. This further confirms that the measurement noise is influenced by the longest δt used, hence by k_t and k_g. In general, measurement noise increases only very slowly towards the wall in the upper parts of the boundary layer. Close to the wall, however, a sharp increase can be seen. This increase is attributed to laser sheet reflections, and partly to local changes in $\overline{u}$ near the orifices. Again, a direct link to the correlation strength in Figure 8.10 is seen. The noise for $k_t = 12.6$ and $k_t = 16.2$ can be seen to grow more steadily towards the wall, as the effects from turbulence and gradients are amplified by the longer pulse separation times (cf. subsection 6.3.1). These two curves show unexpected behaviour, as the lower $k_t = 12.6$ shows a higher measurement noise for $y >= 10$ and $y <= 2mm$. In Figure 8.10, the correlation value for $k_t = 16.2$ can be seen to decrease more rapidly in the region $2 < y < 10mm$, which can explain this difference. In contrast, the $k_t = 1$, $k_t = 2.5$ and $k_t = 16.2$ curves show a more constant growth in difference.

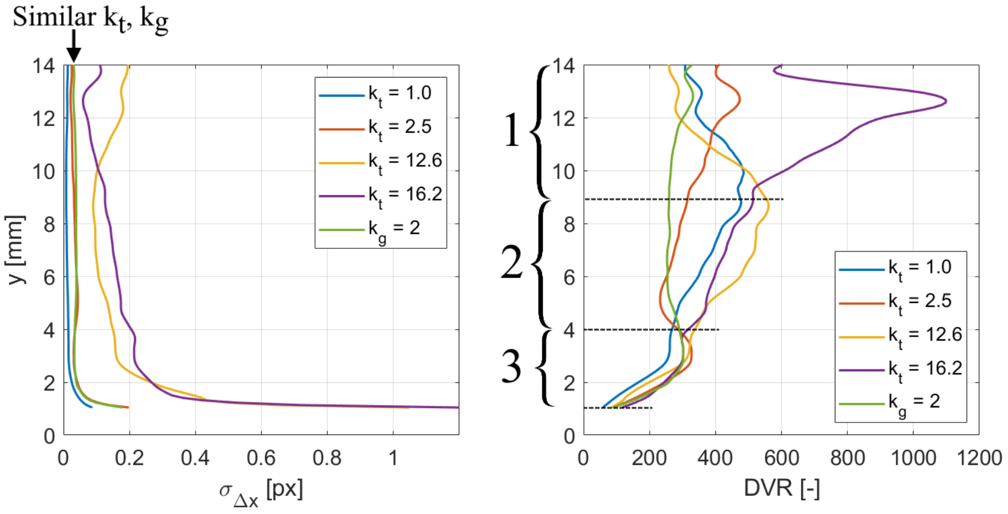

Figure 8.11: y-dependent measurement noise (left) and resulting DVR (right) for the Mach 0.4 cases with varying timing range k_t. The curves are moving averages with a sample size of 10. The single-δt results are also shown, denoted by its grid refinement factor $k_g = 2$. The three indicated regions are discussed in the text.

DVR results

Looking at the corresponding DVR in the right of Figure 8.11, several important observations can be made. First, the values in the top of the domain correspond roughly to those of the global evaluation, shown in Figure 8.8. Some discrepancy is allowed, as the domain of the global evaluation is not incorporated in the profiles of the local noise. This is to exclude the damaged section on the camera sensor (cf. Figure 5.10b). Next, three sections are identified, starting from the upper part of the boundary layer:

1. $y > 9mm$: all curves peak briefly around $y \approx 13mm$, to different degrees. At $y = 9mm$, the $k_t = 2.5$ and $k_g = 2$ cases show a DVR of ≈ 300, while the three others yield a DVR≈ 500. Throughout this range, the $k_t = 16$ case shows the highest DVR.
2. $4 \leq y \leq 9mm$: all multi-δt cases show a monotonic decrease in DVR towards the wall, the grid refinement case stays nearly constant. At $y = 4mm$, all cases are converged to a DVR of ≈ 300. In this range, the $k_t = 12.6$ performs best.
3. $y < 4mm$: all curves decrease similarly, approximately from a DVR of 300 at $y = 4mm$ to a low DVR of 100 at $y = 2.7mm$. This suggests that the DVR for all cases is dominated by measurement noise near the wall, due to laser sheet reflections near the wall. It is still possible that the noise level is raised due to local physical variations in $\overline{u}$ near the orifices.

A similar exercise as in Figure 8.9 is carried out by making a scatter plot of the effective noise $\sigma_{\Delta x}/k_t$ as a function of the correlation peak height. This time, data is taken from the profiles in y for the Mach 0.4 cases. The result is shown in Figure 8.12. As before, no clear trend is observed. All scatters show a sharp increase in effective noise, regardless of correlation value. This corresponds to the increase in noise near the wall.

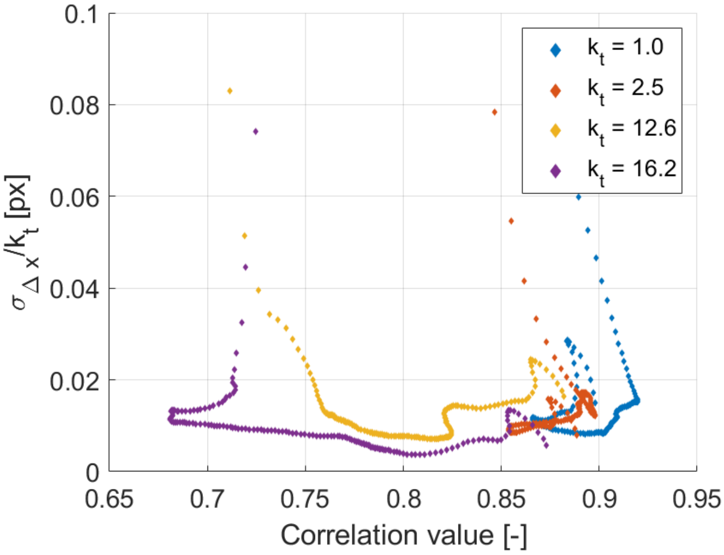

Figure 8.12: Variation of $\sigma_{\Delta x}/k_t$ with the correlation strength, based on the y-dependent quantities of Figure 8.11.

Interpretation and significance of local results

The local results demonstrate that using a single value for the DVR may be inappropriate in certain experiments. In the current case, the region of interest is near the orifices, in close proximity to the face sheet. Here, the DVR is seen to decrease dramatically. While a global DVR may suggest that a certain measurement condition (M_0, SPL) is fully resolved, the local DVR may prove insufficient. The gradient timing limit (cf. Equation 4.11) is established to avoid using a too long pulse separation time which would result in a loss of correlation strength. This is done to avoid failure in correlating double-frame image pairs. While the correlation strengths in Figure 8.10 are deemed sufficient to resolve the average vector field, the effect on the measurement noise is seen to be non-negligible. Therefore, another multi-δt time limit may exist, associated to the measurement noise and hence the DVR: pulse separation times that result in a lower DVR are to be avoided.

Figure 8.11 immediately shows a problem regarding this timing limit. While the measurement noise generally increases with an increasing timing range, the same can not be said for the DVR. The DVR curves are non-trivial, both in spatial (y-coordinate) and temporal (k_t) dimensions. Several suggestions are listed below to improve the understanding of this newly proposed timing limit. Note that the suggestions below are closely related to the suggestions regarding the decomposition between turbulence and noise. In both cases, the variation of the measurement noise with k_t and k_g needs to be determined for the methods to be improved.

- In this section, only one of the measurements is analysed in detail to investigate the local noise and DVR behaviour. The remaining data-sets could be processed similarly to provide a broader perspective. Care must be taken when interpreting the cases at low Mach numbers but with a high SPL. These cases are expected to show strong spatial fluctuations in $\overline{u}$ near the wall. In the current analysis, these fluctuations are interpreted as measurement noise.
- Further tests can be conducted, dedicated to learning about the timing limits. The current tests included both development of the multi-δt technique, as well as a physical analysis of the results. In dedicated tests, problems may be uncoupled. For example, grid turbulence test could be performed, to isolate the effect of turbulence intensity on the measurement noise and DVR, over a range of pulse separation times.
- It can be investigated if an accurate estimation of measurement noise can be made based on correlation strength. This would allow to switch or weigh multi-δt correlation maps aimed at optimizing the local DVR during processing.
- Statistical convergence is currently not evaluated. Recall from sections 6.2.2 and 8.3.3 that turbulent fluctuations are assumed to be statistically converged. Convergence can be checked as in subsection 6.2.1: smaller subsets can be extracted, which allows to evaluate convergence with sample size.

8.4. Assessment of phase-dependent quantities

While the DVR informs how well the set should be resolved, it does not provide insight into how well the velocity is in fact resolved. Therefore, it is informative to judge how well the velocity is resolved in time, before drawing conclusions on the DVR and resulting validity of the measurements. The most simple and robust quantity for this purpose is deemed to be the incident acoustic vertical velocity $\widetilde{v}_{inc}$. To evaluate the quality of the measurement in time, a function fit is made to the measured incident acoustic field, and the RMS difference between the fitted and measured curves is evaluated. This difference is then normalized by the RMS amplitude of the fitted incident acoustic velocity. The result can be seen as a relative RMS error in velocity, denoted $|\varepsilon_{v,inc}|_{RMS}$ and is shown in Equation 8.5.

$$|\varepsilon_{v,inc}|_{RMS} = \frac{1}{|\widetilde{v}_{inc}|_{RMS}} \sqrt{\frac{1}{N_\phi} \sum_{\phi=1}^{N_\phi} \left(\widetilde{v}_{\phi,meas} - \widetilde{v}_{\phi,fit}\right)^2} \tag{8.5}$$

Figure 8.13 shows $\widetilde{v}_{inc}$, averaged in the domain $(x, y) = (14, 15)\ mm$ to $(x, y) = (22.5, 15.5)\ mm$, for the Mach 0.1, $144.3dB$ set. For a tonal acoustic signal, a sinusoid is to be expected. The measured curve clearly is not sinusoidal, as a flattened outflow is present for phases $240 < \phi < 30^o$. For the downwards velocity, a more pronounced peak is seen. From the DVR results in Figure 8.6, it can be argued that this measurement should be easily resolved. The 1σ error bars in Figure 8.13 are also collapsed to a near-zero height. Velocity profiles from increasing Mach numbers show a similar flattening, which reduces until the incident signal resembles a sinusoid at Mach 0.4. This plateau may be caused by the influence of the liner and the small FOV: the height of $15mm$ at which this signal is evaluated is much smaller than the acoustic wavelength of $\lambda = c_0/f \approx 172mm$. Furthermore, an impermeable wall is present to the left and right of the FOV. The transition from a liner to a hard wall may create a discontinuity in aero-acoustic interaction. Therefore, it is first investigated whether this plateau in the phase-dependent velocity profile is physical. Knowing this, an appropriate function form for $\widetilde{v}_{\phi,fit}$ may be posed, which in turn allows to properly evaluate the relative error which expresses the quality of the measurement.

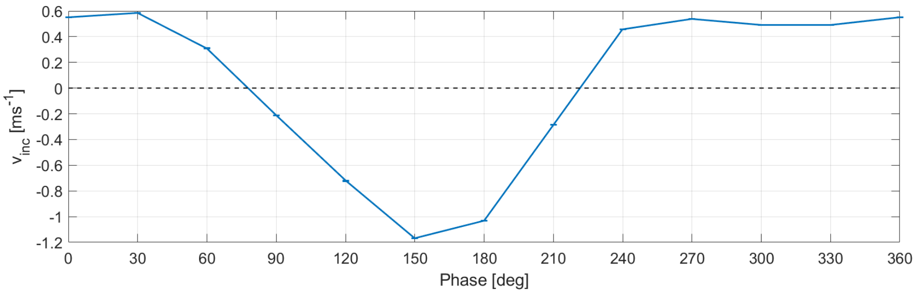

Figure 8.13: Incident acoustic vertical velocity, Mach 0.1, $144.3dB$. A flattened outflow is seen for phases $240 < \phi < 30^o$.

8.4.1. Flattening of outflow phase

Recall from Figure 7.15c that without grazing flow, a net outflow on the top boundary is seen, while net inflow occurs from the two sides. This phenomenon is investigated further by evaluating conservation of mass over the three open boundaries of the FOV. In a 2D2C vector field, continuity can not be evaluated formally, as this requires a volume and the out-of-plane velocity component. Integrating the normal velocity over the open boundaries in the current results yields an area flow rate per unit depth, with units m^2s^{-1}. Incompressible flow is assumed. The formal definition for the area flow rate is stated in Equation 8.6. Here, $\overline{n}$ is the outward-pointing normal vector, indicating that area flow rates are defines positive outward.

$$\dot{A} = \int_L \mathbf{u} \cdot \mathbf{n} dL \tag{8.6}$$

To evaluate the area flow rate per phase, the phase-averaged velocity fields $\langle\overline{u}\rangle_\phi$ are to be used. In the cases with a grazing flow, area flow rates are dominated by the boundary layer. Therefore, the analysis is made in two parts: first, the case without grazing flow is evaluated using the phase-averaged velocity $\langle\overline{u}\rangle_\phi$. Next, cases with a grazing flow are analysed using the acoustic velocity $\widetilde{u}$, with the time-averaged velocity subtracted. While this is not formally the area flow rate due to the missing mean component, this approach better allows to evaluate any phase-dependent interaction between the three boundaries. The boundaries are taken as $1mm$ thick, and the normal velocity is averaged over this thickness. Figure 8.14 shows these three domains and their normal vectors.

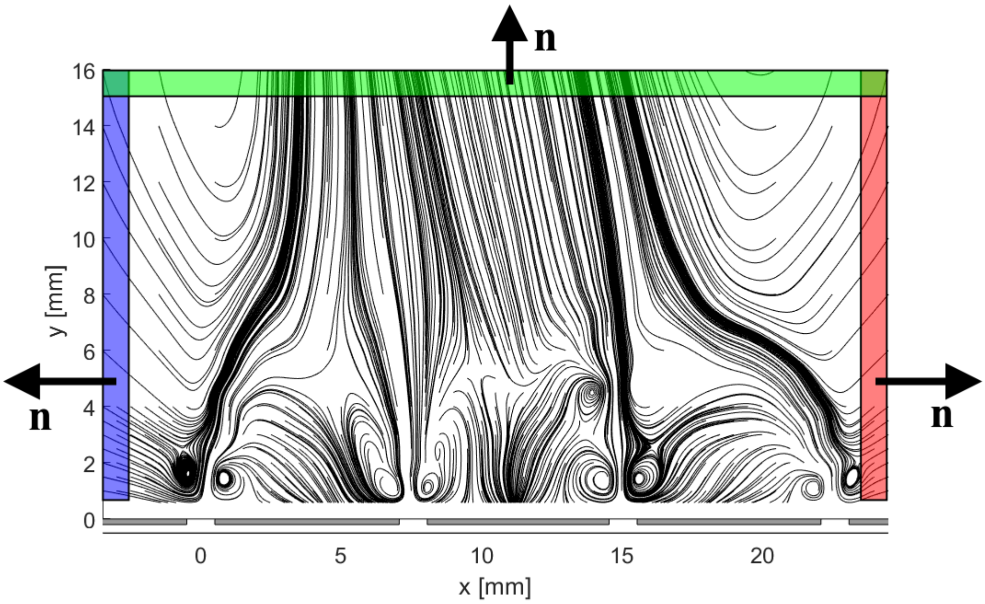

Figure 8.14: Instantaneous (phase-averaged) streamline field of the $M_0 = 0.0$, SPL= $138.7dB$ case, at phase $\phi = 180^o$. The domains in which the area flow rates are evaluated are indicated by the three boxes: upper (green), left (blue) and right (red). The outward-pointing normal vectors are also shown.

Area flow rates without grazing flow

Figure 8.15 shows the area flow rates for the case without grazing flow. In the absolute velocity, it is seen that outflow indeed occurs on the top boundary, while the side boundaries show a nearly symmetrical inflow. From the summed curve, it can be seen that a net outflow is seen on the domain. This inconsistency is treated first.

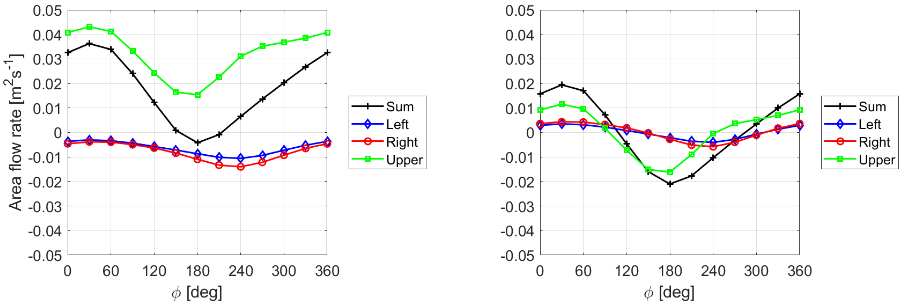

Figure 8.15: Area flow rates without grazing flow, for absolute velocity (left) and acoustic velocity (right). A reduction in outflow on the upper boundary is seen, similar to Figure 8.13. This reduction seems to be compensated by the side boundaries.

Figure 8.16 shows streamlines of the instantaneous flow field at phase $\phi = 180^o$, associated to Figure 8.15 (left). This phase most clearly demonstrates the effects seen. Overall, it is visually confirmed that inflow occurs on the side boundaries, while outflow is trough the upper boundary, indicated at positions **A**. Inflow into the orifices is seen in two stages. The two outermost orifices are fed directly through the sides (**B**). Note that some inflow may be missing here, due to the missing $0.6mm$ above the face sheet. The two inner orifices are fed by the outflow from the outer orifices (**C**). This creates a region of circulation between the orifices. Due to the absence of grazing flow, a similar interaction with the orifices in the out-of-plane direction is expected. This suggestion is further confirmed by the source-like structures at positions **D**: these sources may be caused by inflow from the out-of-plane orifices, which are positioned halfway between the in-plane orifices in x-direction (see Figure 5.4). This out-of-plane inflow and the missing side inflow below **B** can explain the net outflow seen in the domain. Finally, a sink-like structure is seen at position **E**, which seems to draw the outflow from the inner orifices. The out-of-plane area flow rate could be quantified by integrating the divergence of the velocity field over the field of view. For the current discussion, the qualitative observations made here are deemed sufficient to explain the net outflow seen on the domain.

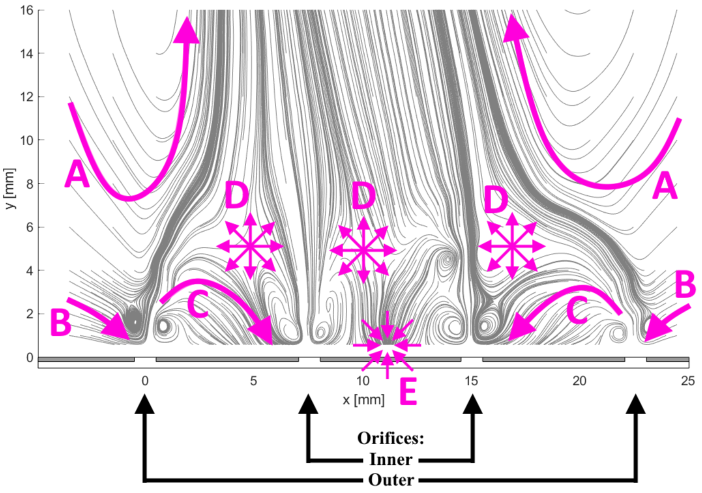

Figure 8.16: Instantaneous (phase-averaged) streamline field of the $M_0 = 0.0$, SPL= $138.7dB$ case, at phase $\phi = 180^o$. Main flow patterns are indicated: side inflow and top outflow (**A**), side inflow to outer orifices (**B**), recirculation between outer and inner orifices (**C**), and source-like (**D**) and sink-like (**E**) patterns. The definitions of the two 'inner' and two 'outer' orifices are also stated. Refer to Figure 8.14 for the streamline field without annotations.

The phase-dependent interaction between the top- and side boundaries is visible in both results in Figure 8.15. On the upper domain, a plateau is again seen for phases $240 <= \phi <= 30^o$, where the slope is flattened with respect to a sinusoid. The area flow rates on the left and right boundaries show a peak inflow at $\phi = 240^o$. After this, the inflow through the sides reduces, making for a relative inflow. Summing the area flow rates over the three boundaries shows a more sinusoidal signal, without a plateau. The plateau on the upper boundary's outflow seems to be compensated by a relative outflow on the sides of the FOV. The results also show that the effect is strongest on the outflow phase: at the peak inflow on the top boundary, the acoustic area flow rates on the side boundaries are near their average value, and no plateau on the upper boundary is seen here.

Area flow rates with a grazing flow

Next, the case with a grazing flow is considered. The Mach 0.1 and 0.2 results are used for this purpose. These cases are expected to be the better resolved measurements, based on the observations in Section 8.3. Figure 8.17 shows the area flow rates. Note that these are computed using the acoustic velocity, with the mean removed. In Figure 8.17a, a similar plateau on the upper boundary is observed as in the results without a grazing flow, for phases $240 <= \phi <= 30^o$. Outflow is complemented by outflow on the right boundary, and less so by the left boundary. In the Mach 0.2 case in Figure 8.17b, a slight flattening is observed at phases $0 <= \phi <= 60^o$, but to a lesser degree than in the non-grazed and Mach 0.1 results. The left boundary shows a small, nearly arbitrary fluctuation, and the right boundary mainly complements the outflow deficit on the plateau.

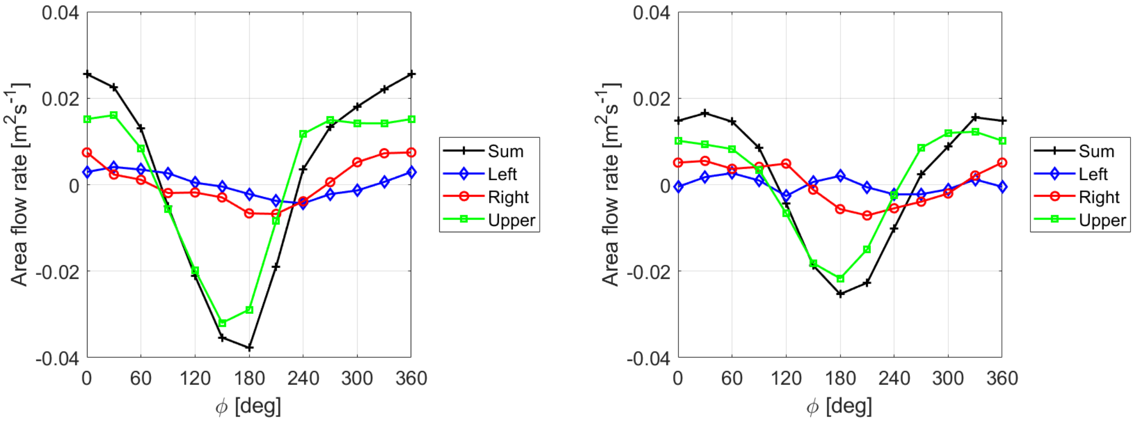

(a) Mach 0.1, $144.3dB$: outflow on upper boundary reduced between phases $240 \leq \phi \leq 30^o$. Outflow on mainly the right boundary is increased in these phases, compensating the restriction on the upper domain.

(b) Mach 0.2, $145dB$: less severe reduction in outflow on the upper boundary.

Figure 8.17: Area flow rates for two well-resolved grazing cases. Results obtained using the acoustic velocity.

In Figure 8.18a, the streamlines of the acoustic velocity are shown for phase $\phi = 300^o$ of the grazed case in Figure 8.17a. The associated vorticity is also displayed. At locations **A**, sink-like structures are seen again, now between all orifices, located in small vortices that roll over the face sheet. This can indicate that air flows out of the orifices, into these vortices, and leave the FOV in the out-of-plane direction. Larger, free vortices are seen to cause a velocity in the downstream direction. The most downstream vortex **B** causes flow to exit the FOV through the right boundary (**C**). Combined, the outflow at **A** and **C** can explain the reduction in outflow through the upper boundary, clearly visible in Figure 8.17a. Both effects can be linked to vortex shedding from the orifices.

This also explains the weaker flattening seen in the case at Mach 0.2 in Figure 8.17b: its higher value for R_I indicates that acoustic forcing is weaker with respect to the grazing flow. Therefore, weaker vortex shedding is expected. This is confirmed in Figure 8.18b, associated to Figure 8.17b. The phase $\phi = 30^o$ shows the largest deficit in outflow on the upper boundary with respect to the total area flow rate. Vorticity is seen to be much weaker here than in the case of Figure 8.18a, and no free vortices are seen in the boundary layer. Outflow is still seen on the right boundary, but the sink-like structures are absent.

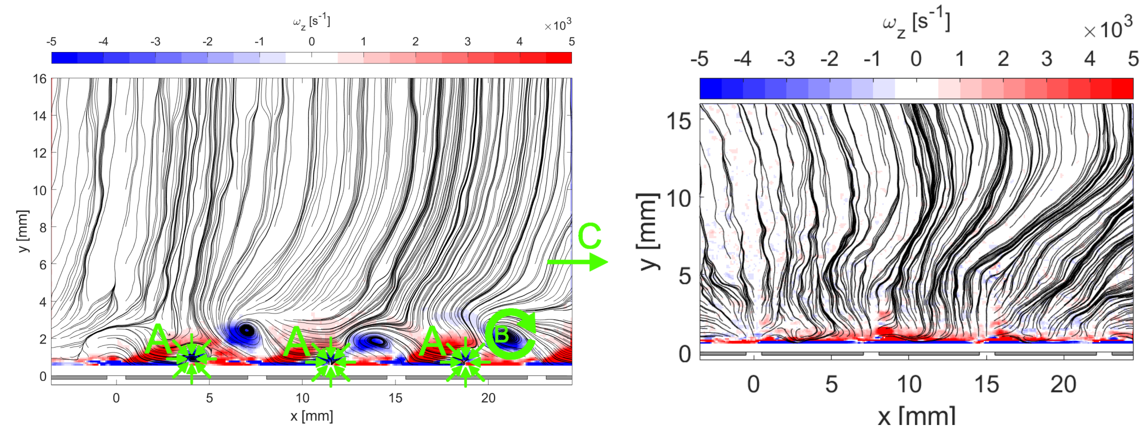

(a) Mach 0.1, $144.3dB$, phase $\phi = 300^o$ (Figure 8.17a). Expected range of scales $R_I = 44$.

(b) Mach 0.2, $145.0dB$, phase $\phi = 30^o$ (Figure 8.17b). Expected range of scales $R_I = 82$.

Figure 8.18: Streamlines of acoustic velocity with a grazing flow. Three sinks (**A**) are seen in small vortices near the face sheet. The large shedded vortices induce a downstream velocity, the most downstream vortex at (**B**) seems to force outflow through the downstream boundary (**C**) as a result. Effects are stronger at lower R_I, i.e. at stronger acoustic forcing. Background coloured with vorticity, calculated using the acoustic velocity (i.e. without mean velocity gradient).

Physics behind incident fluctuation flattening

From the observations above, it is postulated that the plateau in the incident acoustic velocity at low Mach numbers is indeed a physical effect from the interaction with the liner. The outflow through the upper boundary is restricted by out-of-plane outflow in vortices rolling over the face sheet, and by outflow on the right (downstream) boundary. Both effects seem to be driven by the vortex shedding from the orifices.

As a final check to this hypothesis, the net outflow on the top boundary is considered for the grazed cases in Table 8.1. Absolute area flow rates are again computed using the phase-averaged velocities without the mean removed. To evaluate the relative balance between the outflow on the top and on the downstream boundaries, the outflow on the top is given as percentage of the total inflow to the FOV. The result is shown in Figure 8.19. For all cases $0.06 <= M_0 <= 0.6$, a net outflow on the top boundary is seen. The results for Mach 0.8 are deemed unresolved, based on Section 8.3. The other cases follow the reasoning presented above: at strong acoustic forcing (low R_I), vortex shedding is stronger, and the outflow through the upper boundary is restricted. For weaker forced cases, with a higher value for R_I, these effects are reduced, and a higher percentage of the inflow exits through the upper boundary.

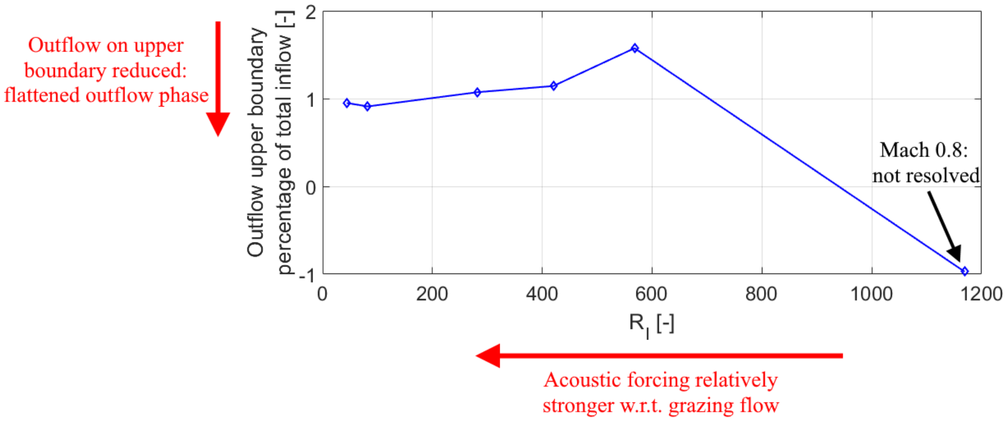

Figure 8.19: Area outflow on the top boundary, as percentage of total inflow. Stronger acoustic forcing (higher Ω_v, lower R_I) results in a restricted outflow on the upper boundary. This is argued to indicate a flattened outflow phase, as seen in figures 8.17a and 8.13. Results computed using absolute velocities.

8.4.2. Models for incident acoustic velocity

It is established that the plateau in the incident acoustic velocity is indeed a physical phenomenon. To asses how well time-resolved the measurements are, an appropriate model must then be fitted to the measurements, after which the relative error of deviations from this curve fit can be computed. It is important that the model is allowed to follow the physical signal, while rejecting noise.

Three models are considered for this purpose, shown in Equation 8.7. In all models, c_i denote arbitrary coefficients to be found from a least-squares fit to the measurements. The 'sine' model is simply a perfect sine, with a phase shift denoted by c_2. Next, a 'plateau' fit is suggested. Here, the cosine term with a fixed phase difference to the original sine wave dampens the upwards peak of the sine. Finally, an arbitrary Fourier fit is used using standard Matlab curve fitting. The frequency is fixed at the acoustic frequency $f = 2kHz$. The second degree Fourier fit used here allows a second mode at a double frequency. It must be checked whether this double frequency is still low enough to filter out random, higher-frequency measurement noise.

$$\text{Sine: } \tilde{v}_{inc}(\phi) = c_0 + c_1 sin(\phi - c_2) \tag{8.7a}$$

$$\text{Plateau: } \tilde{v}_{inc}(\phi) = c_0 + \left(c_1 + c_3 cos\left(\phi - c_2 + \frac{\pi}{2}\right)\right) sin(\phi - c_2) \tag{8.7b}$$

$$\text{Fourier2: } \tilde{v}_{inc}(\phi) = c_0 + c_1 cos(\phi) + c_2 sin(\phi) + c_3 cos(2\phi) + c_4 sin(2\phi) \tag{8.7c}$$

Figure 8.20 shows all three models applied to two measurements. The Mach 0.1 case should be well resolved, and has a high degree of flattening. It can be seen that the 'fourier2' fit follows the signal the best, followed closely by the 'plateau' fit. The 'sine' fit can be seen to yield a large modelling error. Next, the Mach 0.06 case is shown. Due to the lower SPL, this set is expected to be on the edge of being resolved, and the signal is expected to be sinusoidal. It can be seen that all three models yield a very similar fit, filtering out what seems to be random measurement noise. A slight difference is seen between the 'sine' fit, and the 'plateau' and 'fourier2' methods. Qualitatively, the 'plateau' and 'fourier2' functions fits seem to be most appropriate to fit the incident acoustic velocity. A further quantitative analysis on the models is presented in the next section, where a combination with Section 8.3 is made to evaluate the DVR along with the relative error. This allows to address the quality of the measurements.

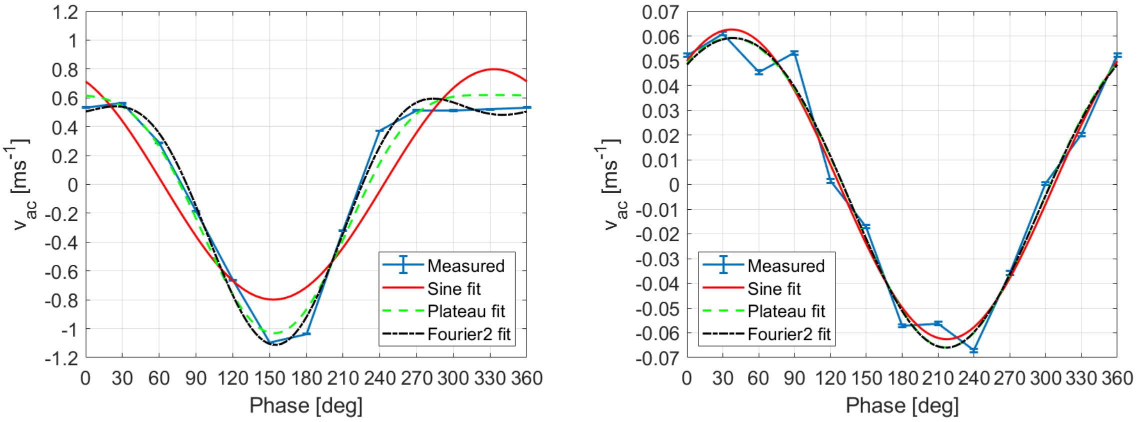

(a) Mach 0.1, $144dB$: modelling error in the velocity fit.

(b) Mach 0.06, $118dB$: error due to measurement noise.

Figure 8.20: Test fits to incident acoustic velocity.

8.5. Combined: assessment and improvement of multi-dt PIV

In this section, the results from sections 8.3-8.4 are combined to complete the assessment of the current multi-δt methodology, using the datasets of Table 8.1. The DVR is combined with the relative measurement error. First, another ratio, R_I/DVR is introduced as the ratio which dictates the theoretical accuracy of a measurement. R_I is a velocity-based ratio, computed using the freestream velocity, and an acoustic velocity scale which is found from the SPL at the face sheet. It can be seen as the requirement for the DVR. The ratio R_I/DVR then indicates the ratio between required and achieved DVR, as shown in Equation 8.8a. A further interpretation can be given by working out both terms. The statements in Equation 8.8b enforce the one-quarter rule and the method used to find the measurement noise. Substitution in Equation 8.8a yields Equation 8.8c. Note that this is an approximation.

$$\frac{R_I}{DVR} = \frac{DVR_{required}}{DVR_{resolved}} = \frac{\frac{u_0}{|\tilde{v}_{inc}|_{RMS,MIC}}}{\frac{d_I/4}{\sigma_{\Delta x}} k_t k_g} \tag{8.8a}$$

$$\text{Setting: } \frac{d_I}{4} k_g \approx u_0 \frac{\delta t_0}{\Delta_{px}} \quad \text{and using: } \sigma_{\Delta x} = k_t \frac{\delta t_0}{\Delta_{px}} \sigma_{u_0} \tag{8.8b}$$

$$\frac{R_I}{DVR} \approx \frac{\frac{u_0}{|\tilde{v}_{inc}|_{RMS,MIC}}}{\frac{u_0}{k_t \sigma_{u_0}} k_t k_g} = \frac{\sigma_{u_0}}{|\tilde{v}_{inc}|_{RMS,MIC}} \tag{8.8c}$$

The form of Equation 8.8c is similar to the relative measurement error of Equation 8.5. The difference between the two is that the ratio R_I/DVR predicts how well the measurement should be resolved, based on global velocity and spatial scales. The relative error $|\varepsilon_{v,inc}|_{RMS}$ indicates how well the measurement is resolved in time. A comparison between the two quantities allows to judge which value is required for R_I/DVR for a certain accuracy on phase-dependent behaviour.

8.5.1. Relative velocity error computation

The first step is to compare the different fitting models for the incident acoustic velocity. This analysis is done using the 2021 multi-δt datasets and the newly formed ratio R_I/DVR. The SPL is computed from the fitted acoustic velocity field, using equations 6.2 and 2.11c. Two methods of extracting $|\tilde{v}_{inc}|_{RMS}$ are tested: the first is to directly evaluate the RMS of the fitted signal. The second approach is to take the amplitude of the downwards velocity peak, after which division by $\sqrt{2}$ yields $|\tilde{v}_{inc}|_{RMS}$. This is done as subsection 8.4.1 showed that the upwards peak is damped by the interaction with the liner, while the downwards peak seem unaffected. The results from PIV are then compared to the SPL measured by the face sheet microphone, the absolute differences are shown in Figure 8.21a. All RMS-based approaches are seen to give similar results. In the range $R_I/DVR < 1$, the peak-based sound pressure levels found by the plateau and Fourier fits show the smallest error with respect to the microphone readings. This further confirms that the downwards peak is not damped.

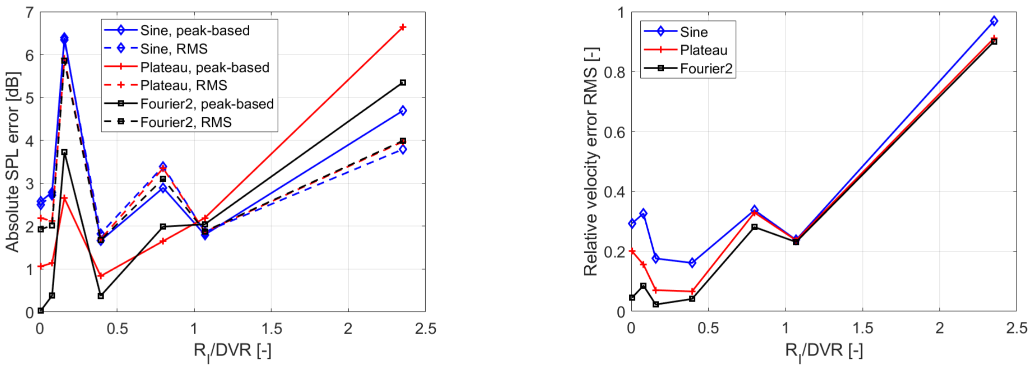

(a) Difference to microphone SPL

(b) Relative incident acoustic velocity error RMS

Figure 8.21: Evaluation of fitting functions to incident acoustic velocity.

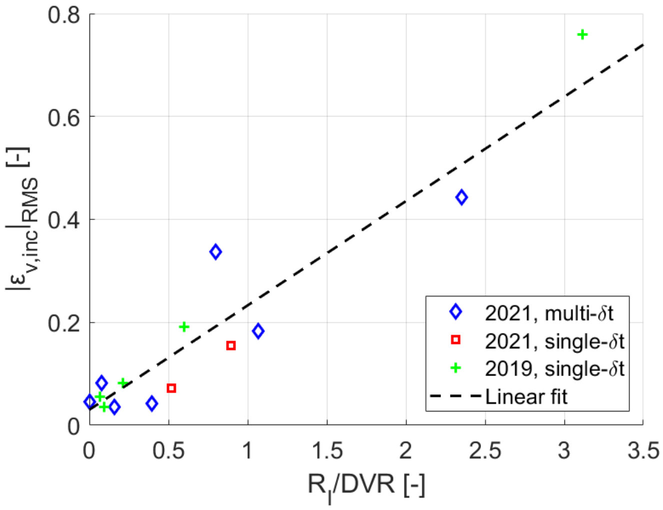

Figure 8.22: Relative measurement error as function of R_I/DVR. The linear fit is given by $|\varepsilon_{v,inc}|_{RMS} = 0.03 + 0.2 * R_I/DVR$.

Next, the relative difference between the velocity fits and the measurements are evaluated, again as a function of R_I/DVR. Due to their resemblance, shown in Equation 8.8c, $|\varepsilon_{v,inc}|_{RMS}$ is expected to increase monotonically with R_I/DVR in Figure 8.21b. For high values of R_I/DVR, the three methods can be seen to converge to the same error. A similar observation was made in Figure 8.20b. This confirms that all three models filter out the measurement noise in this region. Differences are seen for $R_I/DVR < 1$, however. This low region corresponds to the cases with low Mach number and high sound pressure levels, where the incident acoustic velocity is flattened the most. As the ratio R_I/DVR decreases towards 0, the differences between the three models grow. The sine fit produces the largest relative velocity error. As R_I/DVR is very low, and combined with the observation in the previous sections, this can be attributed to a modelling error, rather than an actual measurement error. Similarly, the plateau fit shows a slightly larger error than the Fourier fit in this region. Combining the above, it is concluded that the Fourier fit yields the smallest error from fitting, while still filtering out the higher-frequency noise. This fit is used to compute the relative velocity error $|\varepsilon_{v,inc}|_{RMS}$ in the remainder.

8.5.2. Combined assessment

Having established the methods for evaluating the measurement noise and relative measurement error, it can be evaluated which value of R_I/DVR is required for a certain error. Figure 8.22 shows all single- and multi-δt sets discussed. While some spread is present, a linear relation between $|\varepsilon_{v,inc}|_{RMS}$ and R_I/DVR can be seen in the scatter cloud. This confirms the similarity between the two quantities, despite being approached from different perspectives. The 2021, multi-δt point at $(R_I/DVR, |\varepsilon_{v,inc}|_{RMS} = (1.1, 0.18)$ corresponds to the datapoint for which Figure 8.20b shows the incident acoustic velocity track. This set is visually judged to be on the edge of being resolved: the random noise with respect to the fitted curve is noticeable, but still small enough to clearly show a sinusoidal signal. The sets with larger relative errors show a much more noisy signal, to which the relative phase can not be fitted properly. Therefore, $|\varepsilon_{v,inc}|_{RMS} = 0.2$ is taken as the upper limit.

The limit $|\varepsilon_{v,inc}|_{RMS} = 0.2$ corresponds to a ratio $R_I/DVR \approx 0.8$. A unity ratio theoretically indicates that the measurement accuracy is the same as the accuracy required. As the established limit occurs at a slightly lower value, a small buffer with respect to the theoretical unity value is required. From the scatter cloud in Figure 8.22, it can also be seen that a value of $R_I/DVR \leq 0.8$ does not guarantee a measurement error $|\varepsilon_{v,inc}|_{RMS} \leq 0.2$. This is due to the spread that is still present. An example is the 2021, multi-δt point at $(R_I/DVR, |\varepsilon_{v,inc}|_{RMS} = (0.8, 0.34)$: while its value for R_I/DVR suggests it should be well-resolved in time, it shows a high relative measurement error. Alternatively, the Mach 0.06 point at $(1.1, 0.18)$ is resolved better than the linear fit predicts.

The spread in the linear relation is argued to be due to errors from the test set-up. Closer inspection of Figure 8.22 shows that a larger spread seems to exist in the 2021 data-points than in the 2019 data-points. The 2021 data-points correspond to a high-SPL Mach sweep, whereas the 2019 points are from a low-Mach SPL sweep. Both effectively make for a DVR sweep. Throughout this report, it is observed that the Mach number has a great influence on the quality of the measurements, with the tunnel vibrations and resulting unsteady reflections having the largest impact. A constant-Mach SPL sweep would result in a lower variation in noise between measurements, causing the 2019 points in Figure 8.22 to be better aligned.

8.5.3. Validity of measurements

From the above, an assessment of the newly recorded measurements can be made. From Figure 8.22, combined with all other observations, it can quickly be concluded that the Mach sweep measurements up to and including $M_0 = 0.4$ are well resolved. The Mach 0.6 shows a high relative error, despite its lower value of R_I/DVR. It can be argued that this is due to the problems in the experimental set-up at higher Mach numbers. The Mach 0.8 is not resolved, shown by both its high relative error, and high R_I/DVR ratio.

Care must still be taken when evaluating properties close to the liner, as the local DVR may be too low to accurately resolve these (cf. Figure 8.11). The wind tunnel vibrations picked up at $M_0 = 0.3$, causing reflections which are strongest at the wall. Higher Mach numbers also showed increasing accumulation at the wall. The Mach 0.2 and 0.4 datasets may therefore produce erroneous data close to the wall, and must be considered with care.

8.5.4. Improvements on current test set-up

From the measurement noise results and observations during testing and processing, several improvement for the test set-up are identified. These are to be taken into account in case a follow-up of the current experiment is performed.

Steady reflections

Steady reflections makes it impossible to see in the lower $0.6mm$, and is seen to disturb the turbulence and noise decomposition. The face sheet of the liner is machined to a smooth finish, intended to result in a specular reflection (cf. Figure 5.1b). While most of the laser sheet intensity is indeed reflected in a specular manner, some diffuse reflection remains. Seeding accumulating on the face sheet further increases the reflection of the face sheet. Several possible improvements are identified, listed below:

- The surface may be anodized black. Unlike a coating, an anodized surface remains smooth and resistant to high flow velocities and laser intensities.
- Léon et al. [27] use a rhodamine coating combined with a band-pass filter. This eliminates any direct reflection from the liner. It is expected that high flow velocities may wear down the coating, however.
- Furthermore, Léon et al. [27] use a laser sheet parallel to the flow. This is more difficult in the FDF, which is a closed loop wind-tunnel. If this can be accomplished, for example by introducing the laser sheet through a mirror system, reflections are expected to be reduced.
- The lens axis is positioned slightly above the face sheet. Positioning the lens axis 'below' the face sheet reduces the impact of direct reflections. The cost is reduced light intake (thus a larger aperture required) and reduced FOV height.
- Observations during testing suggest that part of the laser reflections seen are not direct, but scattered by the PMMA wind-tunnel windows instead. Thoroughly polishing and cleaning the wall can aid in undisturbed light transmission.
- Surface treatments such as anodization and rhodomanine coating do not solve the reflections from accumulated seeding. Figure 8.23 clearly shows seeding build-up on the face sheet. It can be investigated whether a coating or surface treatment exists which prevents DEHS from accumulating on the surface.

As a final note, reflections from inside the liner are also seen. This is visible in figures 5.7a and 5.7c. This shows that laser light passes through the orifices, and reflects in a diffuse manner. No direct impact on the measurements is seen here.

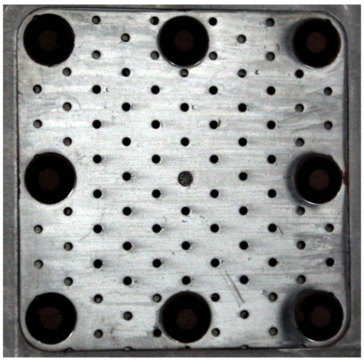

Figure 8.23: Contrast enhanced picture showing accumulated seeding on the liner sample.

Vibrations and unsteady reflections

From subsection 7.2.1, wind-tunnel vibration becomes apparent for Mach numbers $M_0 \geq 0.3$. As seen in Figure 5.1a, both the camera and laser head are attached directly to the wind-tunnel. As the laser head moves with respect to the tunnel during vibrations, the position of the laser sheet is no longer fixed at the face sheet. It is expected that detaching the laser head from the tunnel circuit can reduce the extent of the vibration. Currently, the arm with respect to the wind-tunnel and mass of the laser head could amplify the vibration introduced by the tunnel. By de-coupling both elements, only the tunnel vibration remains. This is expected to result in a less severe fluctuation of the laser sheet position on the face sheet.

Another improvement may be formed in image pre-processing. It can be argued that the images with strong reflections also show a large overall intensity over the entire image. A recording may be re-organized by sorting the sequence on the average image intensity. This average intensity can be computed either for the entire image, or within a selected domain. Another choice is whether one or both frames are used for the evaluation. The result would be an image sequence with a nearly monotonical in- or decrease in orifice reflection intensity, removing its unsteady nature. A sliding average subtraction with an intermediate sample size (e.g. 9 samples) can then be used: neighbouring images now should have similar orifice reflections, which the sliding average can capture well. No such filter is found to be implemented in Davis 8.4 or Davis 10.

Test points

A range of test points is set up here to result in a range of different R_I values. Here, a Mach sweep at near-constant SPL is performed. Most problems in the experimental set-up are associated to high tunnel velocities. Therefore, if purely an R_I range is desired, it is better to do an SPL sweep at a constant Mach number.

8.6. Discussion on multi-dt and grid refinement PIV

Summarizing the analyses made throughout sections 8.3-8.5, several conclusions can be drawn on the comparison between single- and multi-δt PIV. It is seen that for the same data-sets, multi-δt PIV can yield an increase in DVR, both in its global and local evaluation. The gain is smaller than anticipated, however, and diminishes in the current case towards the wall. This is caused by the measurement noise $\sigma_{\Delta x}$ which is seen to increase towards the wall, and for increasing k_t. The loss of DVR near the wall may be less severe than presented here, as local variations in the time-averaged velocity field are interpreted as noise. As δt scales similarly with k_g in a single-δt , grid-refinement approach, both methods suffer similarly from this increase. Nevertheless, several key differences remain between the two approaches, which are addressed below. Furthermore, several methods of improving upon the current test are identified and discussed.

8.6.1. Robustness

Multi-δt PIV as implemented here, and grid-refinement are very similar in their operation. However, a key difference exists between the working principle of the k_g and k_t multipliers. As visualized in Equation 8.8, the k_g multiplier acts on the largest scale that can be resolved, whereas the k_t multiplier is seen to be associated to the smallest scales. This can be explained from the fundamentals of both techniques. In grid-refinement, the largest velocity, typically the freestream velocity, is resolved using the largest, 'multiplied' interrogation window, with size $k_g d_I$. From here, refinement is applied until the final window size d_I is reached. In a multi-δt approach, the freestream is resolved in the first pass, at δ_0, hence at $k_t = 1$. The 'multiplied' interrogation windows, at $k_t > 1$, aim to resolve progressively smaller displacements. This shows that both methods work similarly, yet the implementation of the multiplier constant is reversed.

In the current work the measurement noise is seen to depend equally on either k_g or k_t, specifically through the pulse separation time. The different levels in a grid refinement processing still correspond to the same pulse separation time, fixed by the measurement. The different k_t levels in a multi-δt are linked to varying pulse separation times, therefore to different noise levels. This allows greater freedom during processing. As mentioned similarly by Sciacchitano et al. [42], the combination of the multi-δt correlation maps may be implemented as any form of weighted average. A simple form could be to locally reduce k_t near the wall, or to weigh the correlation maps with their correlation peak heights. Furthermore, k_t levels can be chosen freely, whereas k_g levels are powers of 2, owing to the Fourier-based evaluation of the correlation functions.

8.6.2. Experimental and computational effort

The increase freedom mentioned above is due to the additional data at different pulse separation times. The obvious cost of this advantage is the added effort in data acquisition and processing. Both increase roughly linear with k_t. The processing time required for the combination and evaluation of the multi-δt correlation maps in Matlab is much shorter than the computation of the sum of correlation maps in Davis. The effort in this part was seen to increase approximately linearly with the number of samples, hence with k_t. The longer acquisition times, over one hour for 12 phases with 4 pulse separation times each, may also pose challenges: heating of the loudspeaker voice coils was a concern in the current work. Furthermore, seeding accumulation over time required frequent breaks between phase recordings to clean the liner sample.

Similarly, data requirements may be very high for a multi-δt measurement, compared to a grid refinement approach. This is as k_t scales the number of samples recorded, whereas k_g does not. In the current work, one full measurement condition requires $N_{samples} N_{phases} k_t = 1000 * 12 * 4 = 48,000$ samples. This results in approximately $1TB$ of raw data for each data-point. For stereo- or tomographic PIV, this is further increased by the number of cameras involved. Therefore, the advantage of the increased robustness and freedom during processing must be seriously weighed against this cost.

8.6.3. Additional options

The different timestamps may be incorporated with trajectory reconstruction techniques. An example of such a technique is the four-frame PTV technique discussed by Cierpka et al. [6]. In a phase-locked PIV framework, no additional cameras are required, as the path of interrogation windows is reconstructed, in stead of instantaneous particles. Reconstructing the path presents another method of combining the information from multiple time-steps. Additionally, knowing path curvature could allow for more efficient window deformation. This could increase correlation strength in regions with high gradients, alleviating constraints on the timing limits.

Theoretically, the information contained in the temporal dimension of the measurements might still allow to perform the decomposition between fluctuations from turbulence and noise. It is deemed difficult, however, to resolve the problems discussed in Section 8.1. Unless an appropriate, low-order modification to the decomposition is found, the decomposition remains restricted to problems in which the measurement noise is independent from the pulse separation time.

8.7. Extension to arbitrary experiments

In this section, it is attempted to generalize some of the lessons from the current experiment into guidelines for arbitrary multi-δt experiments. Discussions are kept high-level, and details specific to the current test are not treated in depth.

8.7.1. Local quantities

The synthesis in subsection 8.5.2 is made for the globally evaluated DVR. Similarly, R_I and $|\varepsilon_{v,inc}|_{RMS}$ are evaluated on the incident acoustic velocity field, away from the wall. subsection 8.3.3 showed that these global conditions may differ from local behaviour. In the current work, the DVR is estimated to be much lower near the wall than in the freestream. Therefore, it is recommended to take local effects into account when preparing for an experiment. A challenge then exists in making adequate estimations for the local measurement noise and the local velocity scale of interest.

The local velocity of interest depends on the nature of an experiment. For the local measurement noise, no clear relations could be established in this work. In general, turbulence intensity and in-plane gradients are seen to reduce the correlation strength, and increase the measurement noise. These effects are amplified equally by either k_t or k_g. Unsteady reflections as in the current work should be avoided in all cases, as the correlation suffers severely in these regions.

8.7.2. Sizing experiments a priori

In the preparation of the current experiment, the feasibility and test matrix were determined by preliminarily sizing and estimating the experimental parameters. This section briefly summarizes these steps.

Timing limits and timing range

The shortest δt_0 follows directly from the largest expected velocity and the one-quarter rule. Generally, this velocity can be estimated well. The longest pulse separation time is less trivial. In the list below, the factors to be taken into account are listed, with a short explanation.

- Spatial filtering: the longest pulse separation time should not yield a physical particle displacement larger than the flow structure of interest. Log-law modelling, combined with the Prandtl friction law, proved to be effective in the current work to estimate the local velocity.
- Relative phase: in phase-locked studies, the pulse separation time should not exceed a certain relative phase. In the current work, this limit is set at 30% of a relative phase of 30^o. This limit is defined directly in time.
- Correlation: this limit concerns the ability to correlate two double-frame images successfully. Out-of-plane motion is not considered here, as it is deemed to be dominated by the spatial filtering limit. In cases where the spatial filtering limit is less strict or not present, the out-of-plane motion should be considered when evaluating timing limits. As for in-plane gradients, the limit of $0.5(\frac{\partial u}{\partial y})^{-1}$ with log-lag modelling using the Prandtl friction law proved accurate.
- DVR: a final limit may be imposed due to the local decrease in DVR discussed in subsection 8.3.3. At this time, no method of estimating this limit beforehand is seen.

Having established the timing range k_t, a choice remains on the pulse separation times between $\delta t = \delta t_0$ and $\delta t = k_t \delta t_0$. In the current work, 4 pulse separation times at quasi-logarithmic spacing were selected with regards to the turbulence- and noise decomposition. If such a decomposition is not to be attempted, 2 or 3 pulse separation times may suffice. It is recommended to include at least one pulse separation time slightly below $k_t \delta t_0$. Timing limits are only estimated beforehand, a back-up pulse separation time slightly below the envisioned highest value can prevent total loss of DVR in case a timing limit is exceeded. Finally, a linear spacing spacing of the pulse separation times may increase the gain from the added temporal information. A logarithmic spacing yields closely spaced pulse separation times at the low end, which are seen to behave very similarly.

Magnification factor and window size

A recommendation shared with Scharnowski [40] is that a high magnification factor is beneficial for multi-δt PIV. The timing range k_t is determined mainly by physical upper limits. Similarly, the measurement noise is seen to be dictated by the highest used value for the pulse separation time. Increasing the magnification factor decreases δt_0, but maintains δt_{max}. As a result, the timing range k_t is increased.

One side-note to this recommendation must be given with regards to the interrogation window size. In the current results, the seeding density necessitated the use of $d_I = 32px$ windows, in stead of the intended $d_I = 16px$. As the magnification factor is increased, the physical interrogation window size on the measurement plane is reduced, capturing fewer particles. The seeding particle size and density must be evaluated to determine the smallest physical interrogation window size.

8.7.3. Pre-tests

Test points before the main test conditions are deemed necessary to validate the points above at the start of a multi-δt wind-tunnel experiment. In the current work, time was dedicated in the test matrix to these tests, and a decision strategy was determined beforehand. This strategy dictated which parameters needed experimental validation, before finalizing the test matrix and experimental set-up.

9

Results and discussion

This chapter evaluates the multi-δt results and formulates answers to the research questions posed in Chapter 3. First, the friction velocity and orifice velocities are evaluated as separate quantities in sections 9.1 and 9.2. After these velocity scales are established, the dependence of the acoustic resistance on u_τ, $|\tilde{v}_{or}|_{RMS}$, and Ω_v is studied in Section 9.3. Finally, the downstream development of the boundary layer and liner response is evaluated in Section 9.4. A summary of the key results from this chapter can be found in Appendix A.

9.1. Friction velocity extraction

This section addresses the second sub-question of subsection 3.3.1. This question called for a method of evaluating the friction velocity of the grazing boundary layer, disturbed by the aero-acoustic interaction at the liner. Figure 9.1 shows the time-averaged $\bar{u}$ velocity field for the Mach 0.1 case (cf. Table 8.1). After each orifice, a clear velocity deficit is seen, due to the aero-acoustic interaction. Four domains are indicated. The **0** domain indicates an 'upstream' condition, before the first orifice. The other domains include an orifice and the downstream length up to the next orifice. Throughout this section, the boundary layer in the **0** domain is averaged to yield an 'upstream, undisturbed' condition. The boundary layer in the last domain, numbered **3**, is used as a 'downstream, disturbed' condition. Comparing the two conditions allows to see if a method can be set up to reliably find the friction velocity for both cases, thereby revealing the influence of the aero-acoustic interaction on the friction velocity. Several methods are attempted, which are explained below.

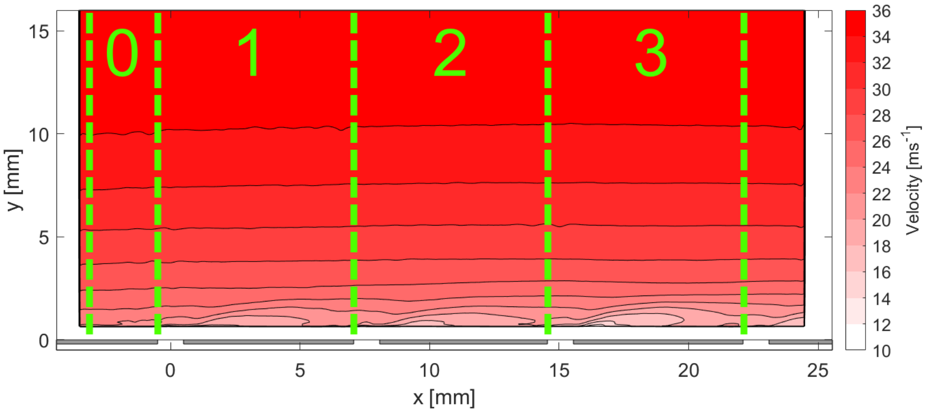

Figure 9.1: Time-averaged $\bar{u}$ field for the Mach 0.1, $144.3dB$ case. The indicated domains are used in subsequent analyses: domain **0** is made up of the $2.5mm$ upstream of the first orifices, domains **1**-**3** all span from the upstream edge of an orifice to the upstream edge of the next. Note that the velocity scale does not go down to 0 for better visibility.

9.1.1. Methodology

Three methods are used to evaluate the friction velocity. Léon et al. [27] suggested fitting a log-law to the boundary layer profile, modified with a wall transpiration term. Another method is to evaluate the change in momentum thickness in downstream direction, which is directly related to the wall friction coefficient. Finally, direct drag measurements from Van der Meulen [52] are included in the comparison. Before comparing and evaluating the results, the three methods are briefly explained in more detail below.

Log-law fitting for weak acoustic forcing (high R_I, low Ω_v)

In this method, the time-averaged boundary layer profile is fitted to the fundamental log-law. By converting the physical quantities $\bar{u}$ and y into inner variables $u^+ = \bar{u}/u_\tau$ and $y^+ = yu_\tau/\nu$, all boundary layers on smooth walls collapse to the same curve, in the near-wall region. In the current case, the wall is not smooth, and the boundary layer is further disturbed by the aero-acoustic interaction, as seen in Figure 9.1. Therefore, fitting is applied using the log-law in two modified forms: the first is intended for fitting the boundary layer in absence of strong acoustic forcing, with a further modification made to fit profile to the disturbed boundary layer. All statements below are based on White [54, Chapter 6].

The modified form of the log-law for weak acoustic forcing is shown in Equation 9.1a. The first two terms on the right-hand-side constitute the standard definition, with the Von Kármán constant $\kappa = 0.41$ and $B = 5.1$. The rightmost term incorporates Coles' law of the wake. In the current work, resolution at the wall is limited, and data availability is further limited as the final $0.6mm$ above the wall can not be seen. Using only the log-law reduces the available region to $30 \lessapprox y^+ \lessapprox 350$. In physical coordinates, this generally corresponds to $y/\delta_{99} \lessapprox 0.2$, leaving only $10 - 20$ points to fit the log-law to. Coles' law of the wake adds an S-shaped 'wake' to the outer part of the boundary layer, which depends on y/δ_{99}. This allows to fit a profile to the entire boundary layer, even when subjected to a (varying) pressure gradient. Coles' law is scaled by Coles' wake parameter Π.

The function form for the wake function $f(y/\delta_{99})$ is shown in Equation 9.1b. This function reduces to 0 for $y/\delta_{99} \ll 1$, leaving the original log-law near the wall. In the outer layer, the wake is added, until $f(y/\delta_{99}) = 1$ for $y/\delta_{99} = 1$. Coles' wake parameter Π is related to Clauser's equilibrium parameter $\beta = (\delta^*/\tau_w)\ \partial p_e/\partial x$. Constant-$\beta$ flows are in a turbulent equilibrium: even though the pressure varies, self-similar solutions can still be obtained. It can be seen that $\beta = 0$ denotes flat-plate flow, where $\partial p_e/\partial x = 0$. The empirical relation $\beta \approx -0.4 + 0.76\Pi + 0.42\Pi^2$ shows that this corresponds to $\Pi \approx 0.426$. As log-law fitting is performed with up to 4 coefficients, bounds are established to avoid non-physical fitting solutions using a combination of extreme values for the coefficients. From the relation between β and Π discussed in White [54], reasonal bounds for Coles' wake parameter are taken as $0 < \Pi < 20$.

$$u^+ = \frac{1}{\kappa} ln(y^+) + B - \Delta B + \frac{2\Pi}{\kappa} f\left(\frac{y}{\delta_{99}}\right) \tag{9.1a}$$

$$\text{with: } f\left(\frac{y}{\delta_{99}}\right) = sin^2\left(\frac{\pi}{2}\frac{y}{\delta_{99}}\right) \tag{9.1b}$$

$$\text{with transpiration: } u^+ = \frac{\left[\frac{v_w^+}{2}\left(\frac{1}{\kappa} ln(y^+) + B - \Delta B + \frac{2\Pi}{\kappa} f\left(\frac{y}{\delta_{99}}\right)\right) + 1\right]^2 - 1}{v_w^+} \tag{9.1c}$$

The second modification in Equation 9.1a is the surface roughness correction term ΔB. Wall surface roughness shifts the log-law profile downwards in inner variables. The value for ΔB depends on both the type and the size of the applied roughness. It can be quickly seen that $\Delta B = 0$ corresponds to a smooth wall. From sand-grain roughness studies presented in [54], with a roughness height in wall coordinates $k^+ = ku_\tau/\nu$, it is established that the flow is fully rough for $k^+ > 60$. For sand-grain roughness, a value $k^+ \approx 100$ corresponds to $\Delta B \approx 10$, a slightly larger $\Delta B = 15$ is imposed as an upper limit for this parameter.

Log-law fitting for strong acoustic forcing (low R_I, high Ω_v)

Léon et al. [27] suggest that the effect on the boundary layer due to strong acoustic forcing (Ω_V), can be expressed reasonably well using wall transpiration. With wall transpiration, the left-hand-side in Equation 9.1a is changed from u^+ into $(2/v_w^+)\left(\sqrt{1+v_w^+u^+}-1\right)$, re-writing results in Equation 9.1c. Here, $v_w^+ = v_w/u_\tau$ is the non-dimensional normal velocity at the wall, where $v_w^+ > 0$ denotes injection. White [54] mentions a typical range of $v_w^+ \pm 0.06$. Due to the strong disturbances observed by Léon et al. [27], bounds for fitting are established at a larger $v_w^+ \pm 0.1$. All log-law modifications discussed may be superimposed for a composite law [54]. The bounds for all coefficients are listed in Table 9.1.

Figure 9.2 shows the modification introduced by the transpiration for the case with the lowest R_I, i.e. strongest acoustic forcing. In Figure 9.2a, a clear error is seen in the near-wall region, as the log-law without transpiration is inadequate to model the effects of the acoustic forcing. In the outer layer, the introduced oscillation creates a further error. In Figure 9.2b, including wall transpiration is seen to make for a better fit, which is consistent with obervations made by Léon et al. [27]. The resulting friction velocity also varies between the two cases: without wall transpiration, a friction velocity of $u_\tau = 1.9ms^{-1}$ is found, whereas $u_\tau = 2.3ms^{-1}$ in the case with wall transpiration.

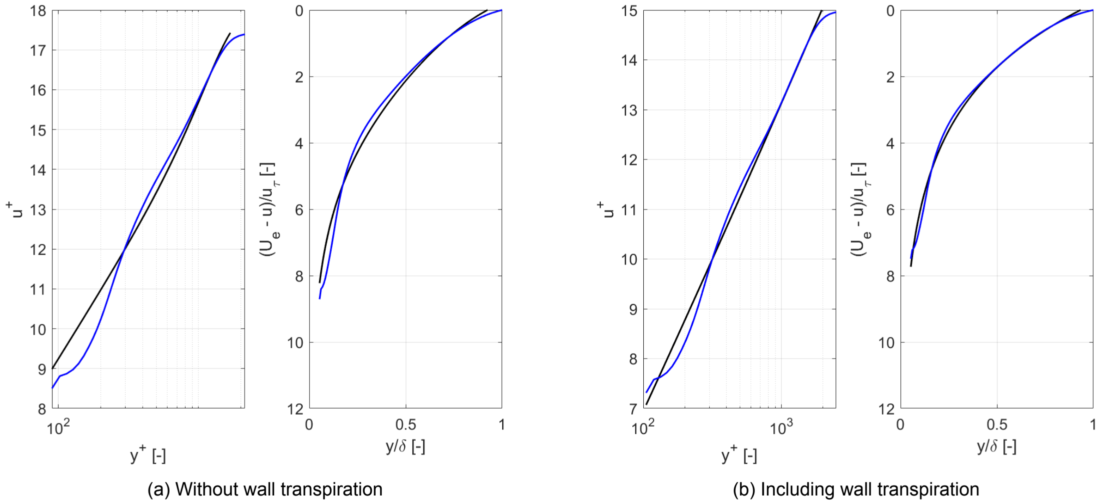

(a) Without wall transpiration

(b) Including wall transpiration

Figure 9.2: Velocity fits for Mach 0.1, $144.3dB$. Boundary layer averaged over domain '**3**' in Figure 9.1.

Table 9.1: Limits imposed on log-law fitting coefficients

Coefficient	Lower bound	Upper bound
Π	0	20
ΔB	0	15
v_w^+	-0.1	0.1

Figures 9.1-9.2 shows that the aero-acoustic interaction results in a lower velocity near the face sheet. This is further demonstrated in Figure 9.3a: the strongly forced case with $R_I = 44$ shows a clear deficit with respect to the case at Mach 0.4 where $R_I = 282$. As the latter shows a typical turbulent boundary layer profile, wall transpiration is expected to be near-zero here. This is confirmed in Figure 9.3b. It is also noticed that the friction velocity is very sensitive to wall transpiration: the small downstream growth in v_w^+ makes for a *decrease* in u_τ in downstream direction. This means that friction would be lower after the liner than it is in the upstream, undisturbed condition. It is thought that this decrease is not physical but a result of the sensitivity to the wall transpiration coefficient. The Mach 0.4 case is the one with the lowest R_I where such behaviour is seen. From the above, the choice is made to disable wall transpiration for $R_I \geq 282$.

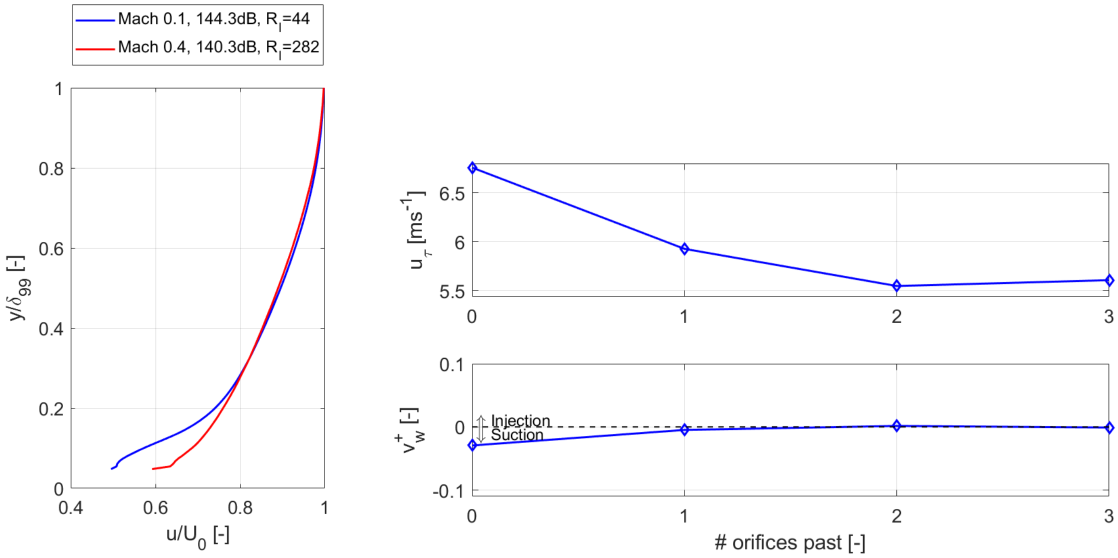

(a) Comparison of strongly and weakly forced boundary layer profiles $\bar{u} = \bar{u}(y)$ at the downstream location.

(b) Non-physical effects when including wall transpiration in a weakly forced case: friction velocity decreases downstream over the liner. The x-axis corresponds the domains in Figure 9.1.

Figure 9.3: Weakly forced cases, with $R_I \geq 282$, should be fitted with a log-law without transpiration.

Momentum thickness-based approach

An alternative approach is given using the momentum-integral relation, again presented by White [54]. By definition, the friction coefficient and friction velocity are related through $C_f \equiv 2(u_\tau/u_0)^2$. As it is observed in the current results that $\partial u_0/\partial x \approx 0$, the momentum-integral relation is used in its flat-plate form, shown in Equation 9.2. The momentum thickness θ is an integral quantity, and the entire boundary layer velocity profile can be used in this method. A point $(y, u) = (0, 0)$ is added to enforce a no-slip condition to the profiles.

$$C_f = 2\frac{\mathrm{d}\theta}{\mathrm{d}x} \tag{9.2a}$$

$$\theta = \int_0^\infty \frac{u}{u_0}\left(1 - \frac{u}{u_0}\right)dy \tag{9.2b}$$

Direct drag measurements

Finally, data from concurrent drag measurements by Van der Meulen [52] are included. In this study, drag is directly measured using a larger $10x10cm^2$ liner sample of identical topology shown in Figure 5.4. This 'drag sample' is oriented correctly, i.e. rotated 90 degrees with respect to the sample used in the PIV and impedance measurements. A smooth panel is also evaluated, installed in the same housing as the liner sample. These samples are suspended by springs, any displacement due to drag is measured using strain gauges. The samples are subjected to broadband sound, introduced using the same horn as shown in Section 5.2. Overall sound pressure level is similar at $OASPL \approx 145dB$. Installation drag, due to small gaps between the liner sample and wind-tunnel wall is assumed negligible. This allows to evaluate the wall shear stress based on the measured drag D, as shown in Equation 9.3. Two measurements are performed with each sample and averaged.

$$C_f = \frac{\tau_w}{\frac{1}{2}\rho u_0^2} = \frac{D}{\frac{1}{2}\rho u_0^2 S} = 2\left(\frac{u_\tau}{u_0}\right)^2 \tag{9.3}$$

9.1.2. Results

To compare the friction evaluated from the PIV measurements to the drag measurements, the domains **0** and **3** from Figure 9.1 are taken as 'undisturbed' and 'disturbed' conditions, as explained before. The log-law fits yield a friction velocity for each condition, whereas the momentum thickness-based approach results in a single value, based on the difference between the two locations. It should also be remembered that wall transpiration is disabled in the log-law fits for $R_I \geq 282$. Mach 0.8 is not included in the momentum thickness results, as it shows a negative change in momentum thickness, which is deemed non-physical. Sections 8.4-8.5 indicated that this data-set is indeed not resolved well. The log-law fits are performed for this test point, but should be evaluated with care.

Figure 9.4 shows the results from the three methods. Results are shown as a function of the freestream velocity and not the Mach number, to take into account the variable speed of sound (Equation 5.4). Firstly, it can be seen that the Prandtl friction law yields friction values much lower than all experimental results. The law considers smooth, circular ducts, which are expected to show a much lower friction than the aero-acoustic experiments. It is argued that the friction law underestimates the friction velocity, and is not suited to provide the friction velocity for subsequent analysis.

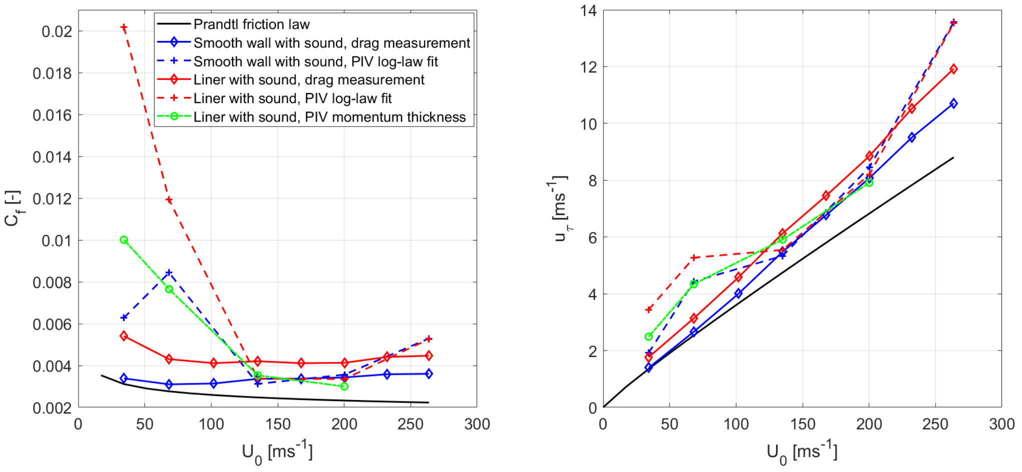

Figure 9.4: High-SPL Mach sweep wall friction results, shown as friction coefficient (left) and associated friction velocity (right). The 'smooth wall with sound' PIV case is represented by domain **0** in Figure 9.1.

The friction increases more sharply at low tunnel velocities in the PIV results than for the drag measurements. This is also clearly visible in Figure 9.6, where the difference between the 'disturbed' and 'undisturbed' conditions is shown. This sharp increase may be partly physical, and partly be attributed to a measurement error. Regarding the latter, Figure 9.2b still shows a log-law fitting error in a low-R_I case. However, the momentum-integral method also shows such a strong increase in friction at low tunnel velocities. As this method does not rely on fitting, it can work with any arbitrary boundary layer profile. The sharp increase in friction in these cases may therefore be physical, and the difference to the drag measurements may be explained differently: the total drag force is small at low tunnel velocities, approaching the measurement accuracy in these conditions [52]. As a result, the drag measurements may underestimate the friction velocity. This can be better explained by looking at the measurement technique, sketched in Figure 9.5: the displacement X due to a liner drag force F_{drag} is measured using strain gauges. If any static friction is present in the system, the mass m does not move for $F_{drag} \leq F_{friction}$. As a result, very small drag forces may not be measured. A large drag force F_{drag} can make internal friction negligible, effectively resulting in a perfect mass-spring system.

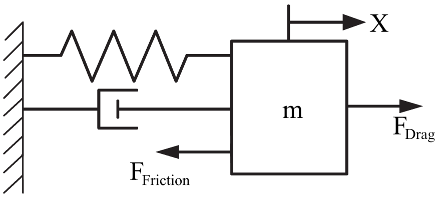

Figure 9.5: Working principle of the direct drag measurements. Internal (static) friction results in a damper during motion, or a constant friction force opposing the drag force in case of no motion.

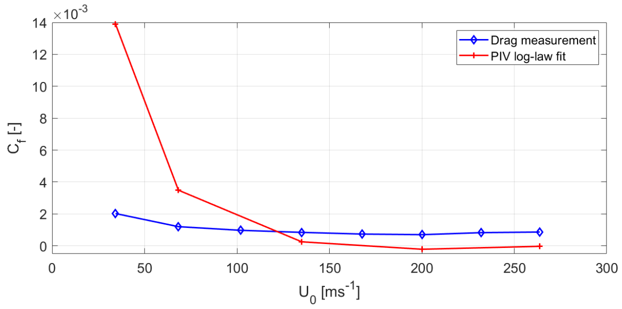

Figure 9.6: Increase in friction coefficient due to the presence of an acoustic liner. These results are found by evaluating the difference between the 'liner with sound' and 'smooth wall with sound' curves in Figure 9.4.

At high tunnel velocities, another sharp increase in friction is observed in the PIV results. Here, the PIV measurements are hindered strongly by the tunnel vibrations, reflections, and the missing $0.6mm$ at the wall. The last effect results in fewer sampling points within the overlap layer, as y^+ is increased by the higher friction velocity. Combined with earlier statements, it is argued that the highest-velocity case at $U_0 = 264ms^{-1}$ is not resolved well. Both drag- and PIV-based methods could then complement each other: the PIV methods seem more accurate at low tunnel velocities, while the drag measurements are deemed better suited for high velocities. Combining the two methods is not performed here, with regards to the different test set-ups used.

Finally, figures 9.4 and 9.6 show that friction is higher for the disturbed case than for the undisturbed condition. This difference is amplified for lower tunnel velocities, where R_I is lower. This is expected to correspond to stronger vortex shedding, hence a more pronounced effect on the friction velocity. For $U_0 \geq 135ms^{-1}$, all PIV-based results converge, whereas a difference remains in the drag measurements. Two possible reasons are postulated: firstly, at $R_I \geq 282$, the wall transpiration is disabled in the log-law fits. It could make for a discontinuity in the log-law curves. $R_I = 282$ is reached at $U_0 = 135ms^{-1}$ in the Mach-sweep of Figure 9.4. The momentum thickness results are seen to follow a similar trend to the 'smooth wall with sound' log-law fit, however: the values that both methods find are very similar at $135ms^{-1}$ and $200ms^{-1}$. Therefore, the switch in fitting settings is deemed adequate. As a second explanation, it is argued that the boundary layer on the small liner used in the PIV tests is still developing, and that the 'upstream' condition is taken too close to the liner. Boundary development is further studied in Section 9.4, but comparing a location further upstream with a fully developed boundary layer is expected to converge to a larger difference. A final explanation may be found in the installation of the drag measurement sample: small gaps remain between the sample and the housing body, which could result in a small installation drag.

9.1.3. Interpretation of log-law parameters

A deeper investigation can be performed into the log-law fitting method: besides the friction velocity, three coefficients, ΔB, Π and v_w^+, are fitted. To gain further insight into the aerodynamic effects of the aero-acoustic interaction, and to better judge the log-law fitting process, these coefficients are studied. Figure 9.7 shows the fitting parameters for the same conditions of Figures 9.4 and 9.6. The results are discussed below per parameter.

Surface roughness

In the top-right of Figure 9.7, it can be seen that all cases shown can be considered non-smooth. The two dashed lines approximate the 'transitional-roughness regime', based on the sand-grain roughness results in [54]. As all cases are above the lower limit, the assumption of a smooth wall is shown to be invalid. This further confirms the underestimation of the friction velocity when using the Prandtl friction law for smooth ducts.

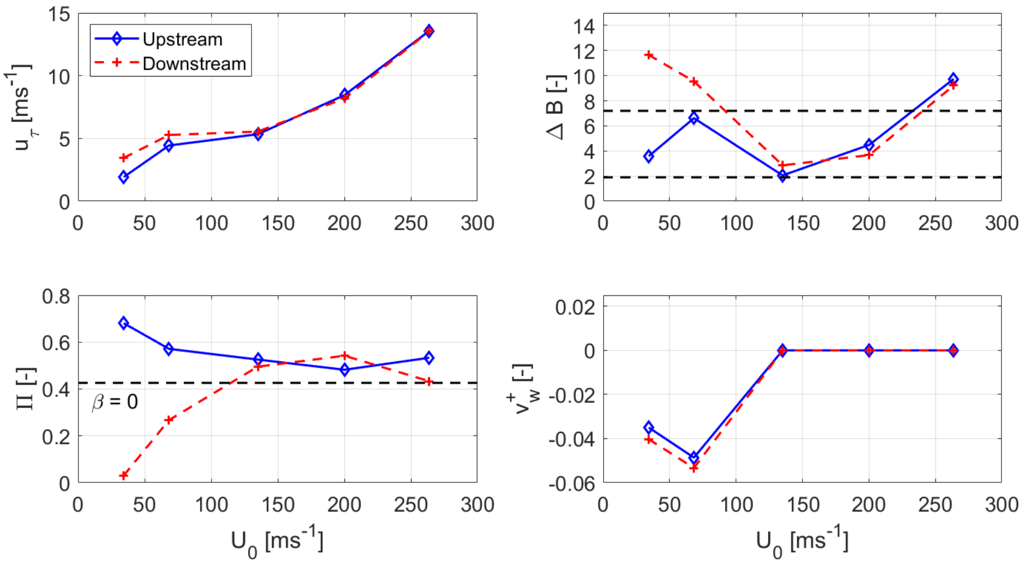

Figure 9.7: Log-law fitting parameters fort the high-SPL Mach sweep results. The dashed lines in the ΔB graph denote the transitional roughness regime. The dashed line in the Π graph shows the flat-plate value $\Pi_{\beta=0} \approx 0.426$. Suction/blowing is disabled for $U_0 \geq 135ms^{-1}$.

Next, two main trends are observed. For tunnel velocities $U_0 \geq 135ms^{-1}$, a monotonic increase of ΔB with the flow velocity is seen. This can be explained by looking at the behaviour of sand-grain roughness. Here, the roughness height in wall units is $k^+ = ku_\tau/\nu$, where $\Delta B \approx \frac{1}{\kappa} ln(1 + 0.3k^+)$. For a fixed physical roughness height k, an increase in k^+ and subsequently in ΔB is expected for an increasing friction velocity. This trend does not hold for the two low-velocity cases, which rise noticeable above it. This can be explained by the fact that in these low-R_I cases, vortex shedding is expected to become apparent. This translates to an increase in effective surface roughness. If no-sound measurements were to be performed, it could be evaluated if this is indeed the underlying cause. Finally, the downstream location shows a larger increase in roughness than upstream, showing that the effective roughness grows downstream over the liner.

Cole's wake parameter

Next, the wake parameter Π is considered. The up- and downstream curves can be seen to converge at high tunnel velocities to a value above the $\beta \approx 0$ line, indicating a slightly adverse pressure gradient $\partial p/\partial x > 0$. From earlier experiments, the FDF is known to generally show a weak adverse pressure gradient, although this is not explicitly confirmed for the configuration used here. The convergence indicates that in these high-R_I conditions, the grazing flow dominates the acoustically induced effects, resulting in a more typical turbulent boundary layer.

At lower velocities, the trends are again not maintained. This may be either physical, or an artefact of the fitting process. Recall from subsection 9.1.2 the observation that a log-law modelling error seems to be present in low-R_I cases, but that the agreement to the momentum-integral results seems to show a physical phenomenon. The increase in Π for the upstream location and decrease downstream may therefore be physical and be related to the stronger acoustic influence. No clear reasoning could be established for such a relation, however.

Wall transpiration

Wall transpiration is only applied to the two low-velocity cases. The results may be approached from different perspectives. First, an approach from the discussion on the incident acoustic velocity in subsection 8.4.1 is used. Here, it was seen that for strong acoustic forcing at low Mach numbers, the outflow on the top boundary is reduced: mass is contained in the vortices, and convected downstream. This would correspond to an inflow of mass, thus of momentum, into the boundary layer. Such an inflow would correspond to a wall velocity $v_w^+ > 0$. This is not observed: the low-Mach cases show a negative wall transpiration coefficient.

Alternatively, a hypothesis can be started from the outflow from the orifices, and associated vortex shedding. This injects low-velocity mass near the face sheet. In a log-law perspective, suction (i.e. $v_w^+ < 0$) results in a reduced velocity near the wall [54]. This could be associated the negative values seen for the high-R_I (low U_0) cases in Figure 9.7. From this perspective, the lowest tunnel velocity should show the strongest suction, as R_I is lowest here. The opposite is seen, for which no explanation can be found. Suction is also see on the upstream position. It is postulated that this is caused by its close proximity to the liner, and therefore not representing a real 'upstream' condition.

Finally, the overall fitting process is considered. The low-R_I cases visually still show an error between the measurement and the log-law fit. Neither the wake law nor transpiration provides an adequate S-shape which allows to perfectly fit such a profile. Furthermore, effects from wall transpiration are most pronounced near the wall, where sampling points are lacking. Therefore, as no sound physical reasoning can be established, the results for the wake and transpiration parameters Π and v_w^+ may be a result of performing a fit with an inadequate model. The surface roughness is expected to fall outside of this argument, as it provides merely a fixed offset to the profile, while the wake and transpiration effects modify the gradient and shape of the profile.

Next, these observations are taken into account when deciding on the best estimate for the friction velocity. Furthermore, suggestions for improvements on all methods are presented.

9.1.4. Conclusions and recommendations on friction results

Based on the advantages and shortcomings of both methods mentioned above, the drag measurements over the liner sample are deemed the most accurate, and are used in all subsequent analyses. Its limitation at low tunnel velocities is deemed less severe than the limitations and unknowns for the PIV measurements, especially for the intermediate and high tunnel velocities. This choice may result in an underestimation of the friction velocity at low tunnel velocities. In Figure 9.4, a linear dependency of the friction velocity on the freestream velocity is seen. Therefore, the friction velocity for the acoustically forced liner is estimated using the relation shown in Equation 9.4. This function is fitted to the 'liner with sound' curve of the drag measurements.

$$u_\tau \approx 0.044u_o + 0.013 \tag{9.4}$$

In the discussions above, several points of improvement are identified. These recommendation are quickly summarized below:

- Future measurements are recommended, where the same liner sample is evaluated using both PIV and drag measurements. This could help to better evaluate the accuracy accuracy of the PIV methods. This has been intended for the current test, but is not executed due to time limitations.
- Improving the test set-up to allow PIV data closer to the wall (i.e. reducing laser sheet reflections) is expected to strongly improve log-law fitting.
- A larger sample allows to evaluate developed boundary layers: boundary layer development is discussed in Section 9.4, where it is concluded that the boundary layer and liner response may not be fully developed in low-R_I cases. The sample and its orientation used in the PIV study here is only $30mm$ long, with 4 orifices.
- A log-law modification may be proposed that is better capable of providing the observed S-shape in the velocity profile in strongly forced cases. This parameter could complement or replace the wall transpiration modification, and would be solely dedicated to the disturbance over an acoustic liner.
- The current 'upstream' location evaluated in the PIV results is deemed too close to the liner to be truly upstream. A larger field of view, or an additional measurement with a more upstream FOV would present a better condition for the 'upstream' results.

Despite the choice to use the drag measurements, the friction velocity results from both PIV approaches are deemed adequate. Trends between the drag and PIV measurements are similar, correct orders of magnitude are seen for the friction coefficient, and a physical reasoning explaining the results is possible. Furthermore, the similarity in results from the downstream log-law fit and the momentum thickness-based evaluation provides confidence in the results. Future tests, as recommended above, may in fact show that these results are more accurate than the drag measurements, but this can not be concluded here.

9.2. In-orifice velocity modelling

Having established a method of evaluating u_τ, the next quantity to be resolved is the orifice velocity $|\tilde{v}_{or}|_{RMS}$. This velocity scale can be evaluated both from the PIV and impedance results. Additionally, the impedance results allow to estimate the orifice quality factor Q of Equation 2.11d. The next sections first present the methods of extracting the in-orifice velocity and quality factor Q from the experimental results. After this, measured and modelled values for $|\tilde{v}_{or}|_{RMS}$ can be directly compared to each other.

9.2.1. Experimental orifice velocity extraction

The velocity from impedance is found using the expression in Equation 2.3c from Guess [10]. $|\tilde{p}|_{RMS}$ is computed from the sound pressure level measured at the face sheet using Equation 2.11c. Note that Equation 2.3c takes the total pressure signal, i.e. incident and reflected, which is the same as measured by the face sheet microphone. The speed of sound c_0 is taken from the experimental fit in Equation 5.4. Note that Equation 2.3c and the models suggested by Léon et al. [27] (Equation 2.11b), with Q as defined Equation 9.5, look very similar. It has been confirmed that these two formulations are in fact different equations before drawing a comparison.

For the PIV results, $|\tilde{v}_{or}|_{RMS}$ is evaluated by evaluating $|\tilde{v}|_{RMS}$ at the lowest $y = 0.6mm$ available, with the RMS taken over the 12 phases. The reflections due to accumulated seeding at the face sheet and wind tunnel vibrations result in noisy results for $M_0 \geq 0.4$. Therefore, only results from lower Mach numbers are evaluated. A Gaussian-like distribution above the face sheet is seen, which is seen convected downstream for increasing grazing velocities. This effect is visible in Figure 9.8, comparing the velocity distributions for the no-flow and Mach 0.1 cases. For each orifice, the peak value is taken. $|\tilde{v}_{or}|_{RMS}$ is then taken as the RMS over the four orifices. In the four cases examined, the third orifice consequently shows the highest peak velocity RMS. It is unknown whether this is an effect from the downstream development of the liner response, or from the specific geometry of this sample.

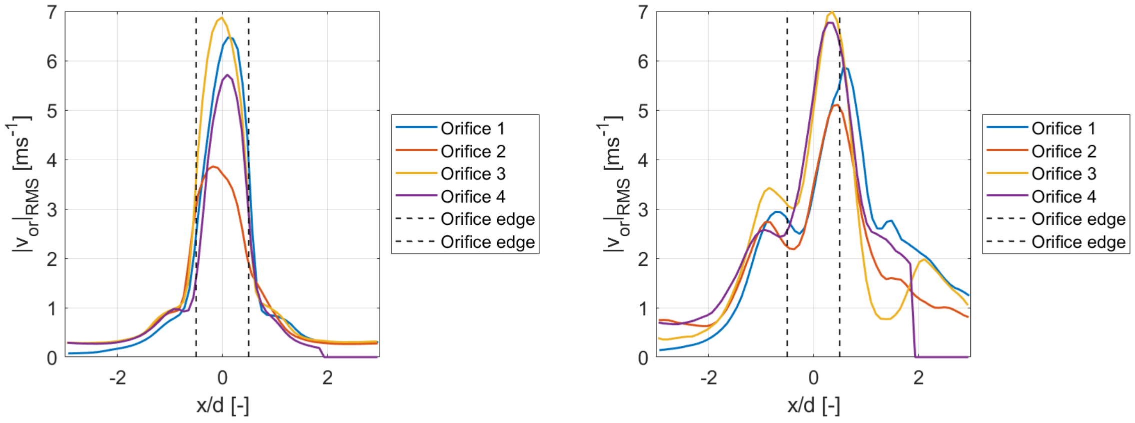

(a) Without grazing flow, $138.7dB$.

(b) $U_0 = 34ms^{-1}$, $u_\tau = 1.6ms^{-1}$, $144.3dB$, $R_I = 44$.

Figure 9.8: $|\tilde{v}|_{RMS}$ over the orifices.

An asymmetry due to the grazing flow can be seen between Figures 9.8a-9.8b. This seems to resemble the asymmetry seen in earlier results [27, 48, 60] in Figures 2.16, 2.14, 2.15 and 2.18. The downstream shift of the $|\tilde{v}|_{RMS}$ peak in Figure 9.8 is attributed to the convection of the grazing flow, and not directly to in-orifice effects. These velocity fluctuations are evaluated at $d = 0.6$ orifice diameters above the face sheet, where convection by the boundary layer is expected to be dominant over the in-orifice asymmetries.

9.2.2. Orifice quality factor

The orifice quality factor Q can be found from the resistance, as explained by Ingard [14]. This is shown in Equation 9.5, note that the definition given by Ingard [14] must be corrected for the liner porosity σ, as the original statement concerns the resistance of a single orifice. τ^* is the corrected face sheet thickness from subsection 1.2.1.

$$Q = \frac{\omega_0 \tau^*}{c_0 \sigma \theta} \tag{9.5}$$

Evaluating the quality factor from the current impedance results then yields Figure 9.9. Being related to the vena contracta effect from the grazing flow in Figure 2.26, Q is shown against the friction velocity. Note that only the Mach sweep results at high SPL are shown here. Q is seen to be inversely proportional to the friction velocity. The dependence of the quality factor on sound pressure level is further investigated using calibration measurements for the horn. These measurements constitute an SPL sweep without grazing flow. Figure 9.10 shows the quality factor results. The effect of the sound pressure level on the quality factor and the resistance is associated to the symmetrical vena contracta effect of Figure 2.26. Therefore Q is plotted against the in-orifice velocity RMS from the impedance values. It can be seen that Q approaches $Q \approx 6$ at low in-orifice velocities, and reduces to $Q \approx 0.9$ at strong in-orifice flows. As for the friction velocity, an inverse proportionality is seen.

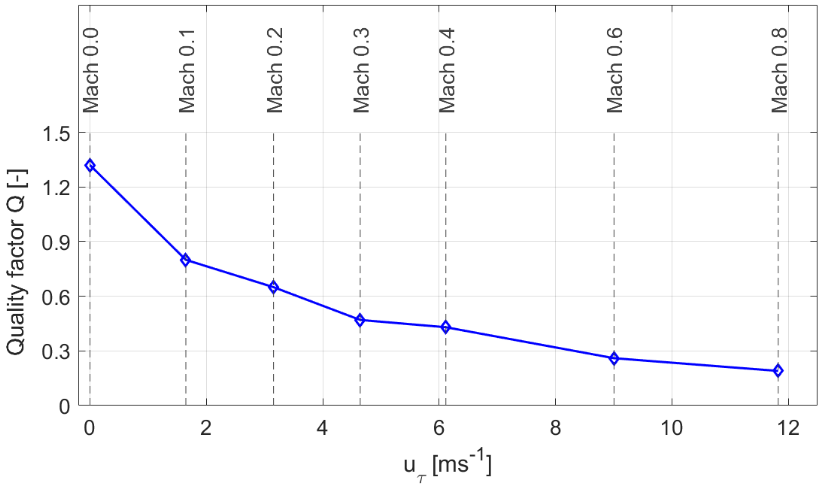

Figure 9.9: Variation of orifice quality factor with friction velocity. Results from the high-SPL Mach sweep.

All results for the quality factor confirm qualitatively the observations by Léon et al. [27] and Zhang and Bodony [60], discussed in length in subsection 2.2.3: the effective open orifice area reduces due to a high friction velocity and due to a high in-orifice velocity. This confirms the influence of both velocity scales on the resistance, as sketched in Figure 3.1. Note that Zhang and Bodony [60] use the discharge coefficient C_D of Equation 2.12. This is qualitatively similar, if not identical, to the quality factor. C_D can not be quantified here, as the in-orifice boundary layers are not resolved. Quantitatively, the results of Figures 9.9-9.10 match with statements made by Léon et al. [27]: it seems reasonable that the trend in Figure 9.10 yields $Q \approx 10$ in a no-flow, no-sound condition. At high SPL and with a weak (low u_τ) grazing flow, $Q \approx 1$ is indeed seen in Figure 9.9.

Léon et al. [27] show good agreement to PIV results using Equation 2.11b with a fixed $Q = 1$. This holds for their tested Mach numbers $0.05 \leq M_0 \leq 0.24$, and forcing at 11 pure tones with an $SPL = 132dB$ per tone. Based on the results shown here, a quality factor $Q \approx 1$ is seen as appropriate for the conditions tested by Léon et al. [27]. Differences start to become apparent at the higher Mach numbers, and at different sound pressure levels. It is concluded that a fixed value for Q can not be used when evaluating a large range of grazing velocities or sound pressure levels. Q is seen to be inversely proportional to u_τ and $|\tilde{v}_{or}|_{RMS}$. Not enough sampling points are available to determine a function form for a combined dependence on both velocity scales.

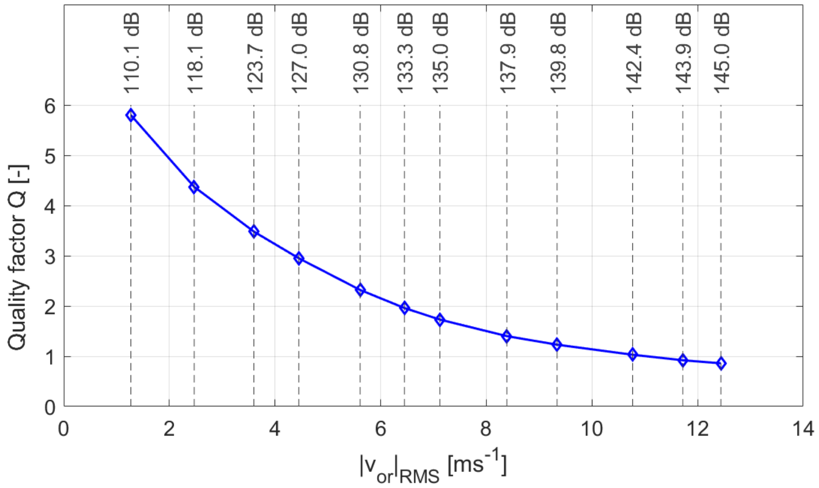

Figure 9.10: Variation of orifice quality factor with in-orifice velocity RMS. No-flow SPL sweep results.

9.2.3. Orifice velocity results

The orifice velocity can be evaluated next. In Table 9.2, results from impedance and PIV measurements are shown, as well as the model suggested by Léon et al. [27] (cf. Equation 2.11b). Only cases with a grazing flow are shown here. For the model, the fixed value $Q = 1$ and the values found from the resistance are both included. The first block includes all measurements from the high-SPL Mach sweep. A second block shows measurements conducted at lower sound pressure levels.

Table 9.2: Comparison of $|\tilde{v}_{or}|_{RMS}$, for high-SPL (top) and lower-SPL cases (bottom).

			Current results		Equation 2.11b	
$M_0[-]$	SPL $[dB]$	$Q[-]$	Impedance	PIV	$Q = 1$	$Q = Q(\theta)$
0.0	138.7	1.32	8.71	5.84	7.42	9.58
0.1	144.3	0.80	10.72	6.23	14.15	11.43
0.2	145.0	0.65	9.71	3.06	15.34	10.17
0.3	148.0	0.47	10.01	-	21.72	10.44
0.4	140.3	0.43	3.73	-	8.98	3.93
0.6	140.3	0.26	2.3	-	8.93	2.41
0.8	134.3	0.19	0.87	-	4.50	0.90
0.06	117.5	4.50	2.00	0.91	0.65	2.05
0.1	109.1	2.67	0.49	-	0.25	0.57
0.6	123.8	0.28	0.37	-	1.33	0.39
0.6	116.0	0.28	0.15	-	0.54	0.16

First, the current impedance and PIV results are compared. It can be quickly seen that the velocity found from PIV is lower than the impedance measurements. This can be attributed to the height at which both are evaluated. Equation 2.3c finds the in-orifice velocity from the in-situ measurements. The PIV results, on the other hand, can only be evaluated as low as $y/d = 0.6$, already more than one radius above the face sheet. The larger height is expected to reduce the peak velocity observed here, as the in-orifice velocity is diffused, convected and transferred into vorticity and turbulent kinetic energy. For comparison, Léon et al. [27] are able to evaluate the velocity at $y/d = 0.07$ above the face sheet. Here, it should be noted that Léon et al. [26] do not mention how they determine the face sheet in the PIV results. In the current work, it is seen that locating the face sheet using the velocity profile can be erroneous, as discussed in subsection 5.3.2.

The reduction in $|\tilde{v}_{or}|_{RMS}$ due to the height over the face sheet is confirmed using Figure 9.11: the ratio between the orifice velocities found from the PIV and impedance measurements decreases with increasing Mach number. The point at $u_\tau = 1.04ms^{-1}$ seems to provide a kink. This point corresponds to the test point at Mach 0.06 (cf. Table 8.1), with a low SPL and as a result a very high $R_I = 568$. This high value indicates that the boundary layer is relatively strong with respect to the acoustically-induced velocity. A stronger reduction in $|\tilde{v}_{or}|_{RMS}$ is therefore expected between $y/d = 0$ (at the orifice) and $y/d = 0.06$ (above the orifice). Based on this reasoning, the two measurements are argued to agree with each other, with the differences caused by effects from the grazing boundary layer and the separation in y-coordinate. In further analyses, the impedance-based velocity scale is used, as most models from literature concern the in-orifice scale.

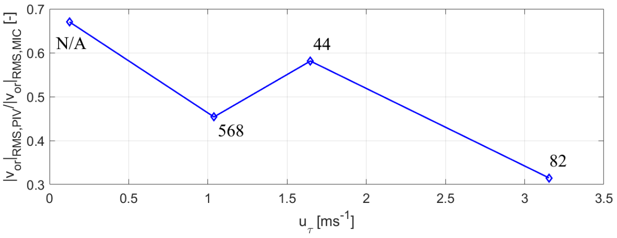

Figure 9.11: Difference between orifice velocity RMS found from PIV and impedance measurements. The labels indicate R_I values.

Finally, impedance results in Table 9.2 are compared to the model of Equation 2.11b. It can be seen that the model is far off from the impedance measurements, when using fixed value of $Q = 1$. The reason is quickly established to be the variation in the quality factor. When implementing the experimentally obtained values for Q, a good match to the impedance results is obtained. This shows that Equation 2.11b indeed is an appropriate model to estimate $|\tilde{v}_{or}|_{RMS}$. It requires an accurate estimation of the orifice quality factor Q, however. Figures 9.9 and 9.10 show Q being inversely proportional to the friction velocity u_τ and the in-orifice velocity scale $|\tilde{v}_{or}|_{RMS}$, due to the vena contracta effects from the grazing and in-orifice flows. Future studies are recommended to further quantify the orifice quality factor as a function of the friction- and in-orifice velocity.

9.3. Non-linear resistance

Having established the velocity scales u_τ and $|\tilde{v}_{or}|_{RMS}$, the onset and quantification of the non-linear resistance can be evaluated. This is to answer the main research question and first sub-question of Chapter 3. First, a method to quantify the intensity of vortex shedding of the liner is set up. This is then combined with the acoustic measurements to evaluate the resistance from the combined aero-acoustic perspective.

9.3.1. Intensity of vortex shedding

For the evaluation of vorticity, three grazed cases are available. These are the Mach 0.1, 0.2 and 0.06 cases for which $|\tilde{v}_{or}|_{RMS}$ is shown in Table 9.2. The reflections of the higher-Mach cases prevent a proper evaluation of vorticity near the wall. Vorticity fields are computed for all phases using the denoised acoustic velocity vector fields. Denoising is performed as explained in Section 7.4. To evaluate the intensity of vortex shedding, the standard deviation of the vorticity fields is computed over all phases. This field is then averaged in x-direction, yielding a y-profile of vortex shedding intensity. These profiles are shown in Figure 9.12a. It is observed that all three cases have converged to a nearly constant intensity around $y \approx 5mm$. The level to which a curve converges increases with Mach number. This is attributed to the measurement noise introduced at the higher tunnel velocities: vorticity is expected to reduce to zero in the outer part of the boundary layer. For this reason, vorticity intensity profiles are corrected to $stddev(\omega_z) = 0s^{-1}$ at $y = 5mm$. To avoid confusion with the measurement noise and liner porosity, standard deviation is simply denoted $stddev$ in stead of the more common σ.

The resulting profiles are shown in Figure 9.12b. $|\widetilde{v}_{or}|_{RMS}$ values in the legend are taken from the impedance measurements, with u_τ found from Equation 9.4. Mach 0.1, $144.3dB$ shows the strongest forcing at $|\widetilde{v}_{or}|_{RMS}/u_\tau = \Omega_V = 6.5$. It can be seen that this results in a large 'bulge' in the profile: vorticity is introduced in the boundary layer up to a height of $y \approx 3.5mm$, or $y/\delta_{99} \approx 0.25$. Next, the Mach 0.2, $145dB$ case with $\Omega_V = 3.1$ shows shedding to a much lower degree. Vorticity standard deviation is much lower, and reduces to near-zero around $y \approx 2mm$. Finally, the case with weakest acoustic forcing is the Mach 0.06 set at $\Omega_V = 1.9$. Only a minor, but still noticeable addition of vorticity is seen below $y = 2mm$.

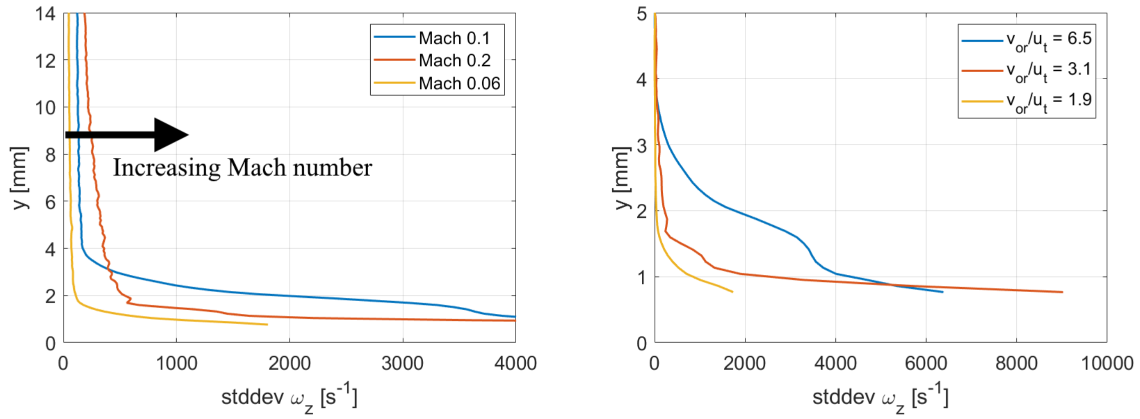

(a) Raw: the steady vorticity level increases with Mach number. Residual vorticity in the outer part of the boundary layer is deemed non-physical. Residual vorticity 'noise' can also be seen in Figure 8.18b.

(b) Corrected to $0s^{-1}$ at $y = 5mm$.

Figure 9.12: Vortex shedding intensity for the available grazed cases.

To quantify the total intensity of vortex shedding, the profiles in Figure 9.12b are integrated over y, from 0.7 to $5mm$. The lower limit is set at $0.7mm$, this effectively removes the lowest row of vorticity values, which is at the edge of the domain. This is done because vorticity is a derived quantity, and therefore defined less accurately at such an edge. Vorticity is units s^{-1}, thus integration yields a quantity with units ms^{-1}. This resembles a velocity scale, associated to the intensity of acoustically induced vortex shedding. This integrated vorticity is denoted v_ω and is shown in Equation 9.6 as it is implemented here. Next, vortex shedding intensity is compared to the impedance results.

$$v_\omega = \int_{0.7mm}^{5mm} stddev(\omega_z)dy \tag{9.6}$$

9.3.2. Acoustic resistance as a function of friction- and in-orifice velocity

In the high-SPL Mach sweep, a linear increase in θ with u_τ is seen. This is consistent with literature [18, 58]. To evaluate the onset of non-linearity, resistance is divided by the friction velocity and normalized with the porosity σ. The result is shown in the upper figure in Figure 9.13. To determine the onset of non-linearity, a composite function consisting of a constant level and a linear slope is fitted, shown as the dashed line. The kink indicating the onset of non-linear behaviour is fitted at $\Omega_V = 2.3$. Notice the great similarity between the impedance results in Figure 9.13, and the results by Kooi and Sarin [21] in Figure 2.17c. When comparing the two, note that Kooi and Sarin [21] use the orifice velocity amplitude in stead of the RMS value. Also, resistance values seem similar, but it should be remembered that in Figure 2.17c, $\sigma\theta$ is plotted, as opposed to $\sigma\theta/u_\tau$ in Figure 9.13. The liner geometry used by Kooi and Sarin [21] is similar to the current sample, and it is estimated that $u_\tau \approx 1$ in their case, leading to similar results for $\sigma\theta$ and $\sigma\theta/u_\tau$. However, as the friction velocity for [21] is not known, a full quantitative comparison between the two figures can not be made.

The bottom graph in Figure 9.13 shows the integrated vorticity v_ω of Equation 9.6, evaluated for the curves in Figure 9.12b. v_ω is seen to be just larger than zero at $\Omega_v = 1.9$. For larger values of Ω_V , a nearly linear increase in v_ω is seen. The similarity between the two graphs in Figure 9.13 confirms the onset of non-linear behaviour from both the acoustic and aerodynamic perspective at $\Omega_V \approx 2$.

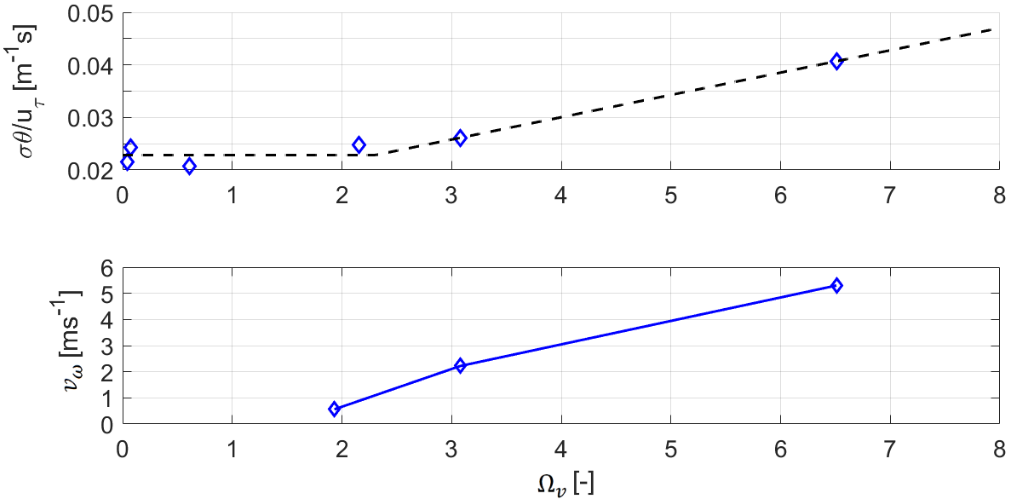

Figure 9.13: Acoustic resistance, normalized with the friction velocity (top) as a function of Ω_V . The dashed line indicates the fit from Equation 9.7. Also shown is the vorticity-related velocity scale v_ω from subsection 9.3.1 (bottom).

Table 9.3 compares the values found here to values suggested in literature. The results from Kooi and Sarin [21] and Goldman [9] have been converted from amplitude scales to RMS scales for comparison. It can be seen that all results indicate an onset of non-linear behaviour at $\Omega_V \approx 2$. Furthermore, it is demonstrated that v_ω as suggested is an appropriate method to quantify the intensity of vortex shedding. Values from both acoustic [9, 21] and aerodynamic [27] studies are confirmed in the current combined approach. One point of attention is that the impedance-based studies (including the current) seem to result in a slightly higher value for $\Omega_{v,NL}$ than the PIV-based ones. This is addressed in the discussion in subsection 9.3.3.

Table 9.3: Values of $\Omega_V = |\tilde{v}_{or}|_{RMS}/u_\tau$ at which the onset of non-linear resistance is observed.

Source	$\Omega_{V,NL}$	Method
Kooi and Sarin [21]	2.8	Impedance
Goldman [9]	2.1	Impedance
Léon et al. [27]	2	PIV
Current	2.4	Impedance
Current	1.9	PIV

Qualitative confirmation for Figure 9.13 and Table 9.3 is sought by visually inspecting phase dependent vorticity fields. Figure 9.14 shows an instantaneous vorticity field for each case. At $\Omega_v = 1.9$, barely any vorticity is seen. Very small counter-rotating regions are seen close to the face sheet. As the aerodynamic effects are nearly indistinguishable, $\Omega_v \approx 1.9$ indeed seems to mark the onset of non-linear behaviour from an aerodynamic point of view. At $\Omega_v = 3.1$, large regions of negative vorticity are seen, which remain attached to the wall. A half period apart from Figure 9.14b, similar regions of positive vorticity are seen, albeit much smaller. It is thought that the steady negative vorticity of the boundary layer (without the mean removed) promotes any negative vorticity and opposes positive values. The vertical structures in Figure 9.14b do not move in time, and are attributed to laser sheet reflections from the orifices. Finally, at $\Omega_v = 6.5$, free vortices are seen. Again, these are with a negative vorticity: the regions with positive vorticity are also large, but remain attached to the wall.

Finally, the dependence of the resistance on $|\tilde{v}_{or}|_{RMS}$, u_τ and their ratio Ω_V is evaluated. For this purpose, the fitted function in the top graph in Figure 9.13 is used. The resulting expression is shown in Equation 9.7. In this fit, the resistance increases linearly with the friction velocity up to $\Omega_V = 2.3$. For $\Omega_V \geq 2.3$, the slope $\mathrm{d}\theta/\mathrm{d}u_\tau$ is linearly increased by Ω_V .

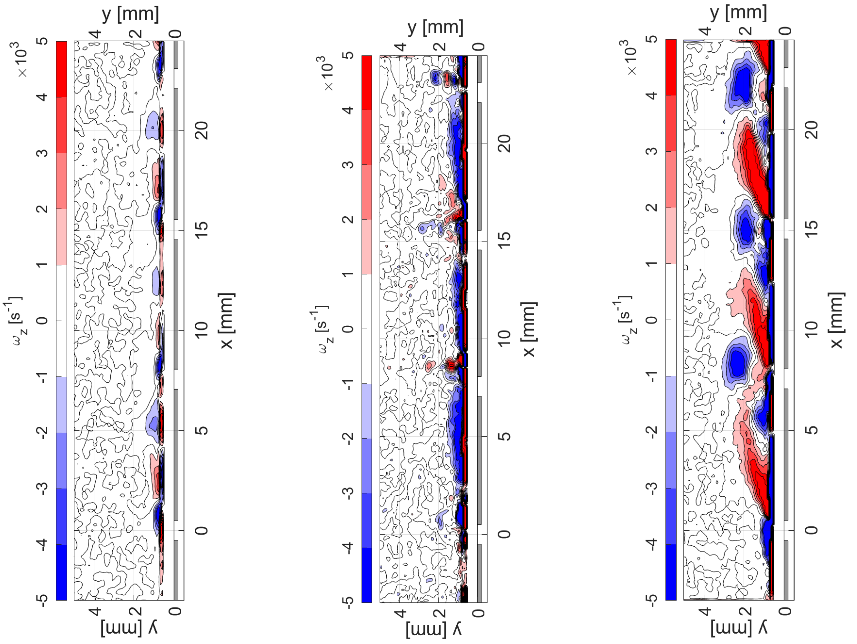

(a) Mach 0.06, phase $\phi = 120^0$, $\Omega_v = 1.9$, $v_\omega = 0.87$ (b) Mach 0.2, phase $\phi = 150^0$, $\Omega_v = 3.1$, $v_\omega = 3.56$ (c) Mach 0.1, phase $\phi = 360^0$, $\Omega_v = 6.5$, $v_\omega = 5.96$

Figure 9.14: Instantaneous vorticity fields, calculated using the acoustic velocity fields. Phases selected to best show the ejection of vortices. Images rotated for compact presentation.

$$\sigma\theta \approx \begin{cases} 0.023u_\tau & \text{for } \frac{|\tilde{v}_{or}|_{RMS}}{u_\tau} \leq 2.3 \\ u_\tau\left(0.023 + 0.004\left(\frac{|\tilde{v}_{or}|_{RMS}}{u_\tau} - 2.3\right)\right) & \text{for } \frac{|\tilde{v}_{or}|_{RMS}}{u_\tau} > 2.3 \end{cases} \tag{9.7}$$

If expressions are found for $Q = Q(u_\tau, |\tilde{v}_{or}|_{RMS})$, $u_\tau = u_\tau(u_0, v_\omega)$, and $v_\omega = v_\omega(u_\tau, |\tilde{v}_{or}|_{RMS})$, an iterative method may correctly estimate all velocity scales and the orifice quality factor. Furthermore, such a method also directly estimates the resistance, as it can be found from the quality factor using Equation 9.5. Alternatively, this method may also be reversed to evaluate the resistance from a PIV measurement: if $|\tilde{v}_{or}|_{RMS}$ is reliably found, the quality factor can by found by fitting Equation 2.11b to the measurement. Then, the resistance is obtained through Equation 9.5.

9.3.3. Discussion

Despite the good results obtained using the velocity scale v_ω from Equation 9.6 to express the intensity of vortex shedding, further work is suggested to confirm this velocity scale. In the current results, only three data-points are evaluated, and the missing $0.6mm$ at the wall can affect the values obtained, as vorticity is expected to be shedded in this region as well. Nevertheless, v_ω is still expected to provide a meaningful expression for the vortex shedding intensity, also in case values are increased by integrating closer towards the face sheet. The sharp increase in the vorticity near the face sheet in Figure 9.12b may be an artefact of the evaluation: with the denoising and vorticity both derived quantities, discontinuities at $0.6mm$ due to masking may protrude relatively far in y. It has been explained that the integrated vorticity is evaluated from $0.7mm$ upwards for this reason, but it has not been investigated whether this suffices. Resolving further towards the wall allows to more accurately evaluate this effect. Alternatively, the increase may be associated to measurement noise near the wall, creating strong gradients: the increase of vorticity near the wall resembles the local increase in noise seen in Figure 8.11. The recommendations of subsection 8.5.4 should be considered to prove or disprove this explanation.

Next, the difference in $\Omega_{v,NL}$ between impedance and PIV-based studies is addressed. Two possible explanations are postulated below, along with several suggestions for improvement:

- Measurement noise in the PIV velocity fields results in increased velocity gradients, which yield higher vorticity values. Recall from Chapter 8 that the Mach 0.06 case, shown here with $\Omega_v = 1.9$, is deemed just resolved in time. At this DVR limit, the increase in vorticity due to measurement noise may become noticeable. Denoising (cf. Section 7.4) reduces spatially uncorrelated noise, but is not expected to remove it fully. Vorticity due to residual noise artificially increases v_ω, which in turn leads to a lower onset of non-linearity from an aerodynamic view. An alternative interpretation of this argument is that v_ω can never be exactly 0, due to this residual noise. The value $v_\omega = 0.56$ at $\Omega_v = 1.9$ may be (near) the lower limit, or noise floor, of v_ω. Further test-points are required to see to which value v_ω converges for high values of R_I.
- The difference in $\Omega_{v,NL}$ may also be physical: it is deemed possible that the aerodynamic effects visualised in Figure 9.14a are still too weak to cause an increase in resistance. In other words: the onset of non-linear resistance could occur at a higher value for v_ω. With the current data, the onset can not be finely determined. Further test points with both impedance and PIV measurements are suggested in the region $1.5 \leq \Omega_v \leq 3$ to more accurately study the onset.

In the current study, the upper limit on the integral in Equation 9.6 is picked visually from the vorticity profiles, as is the correction to $stddev(\omega_z)(y = 5mm) = 0$ in Figure 9.12b. A more general statement may be formed, by changing $y = 5mm$ to $y/\delta_{99} = 0.35$. In future studies, the validity of v_ω and the log-law fitting could be further evaluated. This could complement the suggestions made in subsection 9.1.4. It is expected that v_ω would be directly related to a log-law modification which provides the S-shape deformation observed for the strongly forced cases.

9.4. Boundary layer development

This section addresses the third question, and associated fifth objective in Chapter 3, which concern the downstream development of the boundary layer and liner response. As the turbulence results are deemed unusable (cf. Section 8.1), the feedback mechanism through turbulence intensity can not be evaluated. Instead, an analysis is made by evaluating local log-law fit results. Section 9.1 discusses that the drag measurements are used for the estimation of the friction velocity, but also concludes that log-law fitting is deemed adequate.

A local evaluation is also attempted using the momentum-integral relation method, but this yields very noisy results. This can be explained by examining the definition of $C_f = 2\ \partial\theta/\partial x$. The momentum thickness θ itself is an integral quantity of the boundary layer. The friction velocity, however, is a derived quantity in x. The derivative $\partial\theta/\partial x$ is approximated using a simple forward finite difference, which introduces a truncation error. Using small steps in x amplifies any noise present in the values for θ itself. The method is shown to work over longer distances δx in Figure 9.4. A higher-order finite difference scheme may improve performance at small step sizes. Another improvement may be obtained by using the momentum-integral relation in its full form to account for local fluctuations. The results for the wake parameter Π in Figure 9.7 indicate that a weak adverse pressure gradient pressure may be present, violating the flat-plate assumption currently made in Equation 9.2. The full form is shown in Equation 9.8, with H the shape factor. This is seen to include effects from the local variation in u_0.

$$\frac{\mathrm{d}\theta}{\mathrm{d}x} + (2 + H)\frac{\theta}{u_0}\frac{\partial u_0}{\partial x} = \frac{C_f}{2} \tag{9.8}$$

As the log-law fitting procedure is not dependent on x-coordinate, it can be applied locally without problems. Instead of averaging over a larger downstream distance as performed in Section 9.1, profiles are now averaged in narrow regions. The boundary layer is averaged over bins $1mm$ wide, spaced $0.5mm$ apart, creating 50% overlap. The log-law is then fitted to each boundary layer. Two cases are selected for this analysis, to present an insight in the development at strong and weak forcing. The measurement at 0.1, $144.3dB$ with $\Omega_V = 6.5$ is used for the strongly forced case. For the weakly forced case, the Mach 0.06, $117.5dB$ with $\Omega_V = 1.9$ is used. Two low Mach number cases are used to reduce errors in the near-wall due to reflections. As prescribed in subsection 9.1.1, the Mach 0.06 case is examined with wall transpiration disabled, as $R_I = 568 > 282$.

9.4.1. Strong acoustic forcing: $\Omega_v = 6.5$

First, the case with strong forcing is considered. Figure 9.15 shows the fitting results for all parameters, locally over the liner. The face sheet and orifices are included for easier interpretation. Strong periodic behaviour can be seen. Firstly, the friction velocity, hence the wall shear stress, shows a sharp local increase at each orifice. Shear stress peaks just before halfway between two orifices, after which it reduces. A net growth is obtained for one full period, and peak friction increases per period as well. The surface roughness coefficient follows a nearly identical trend: roughness jumps at each orifice, peaks, and reduces towards the next. A net growth per orifice is also seen in ΔB.

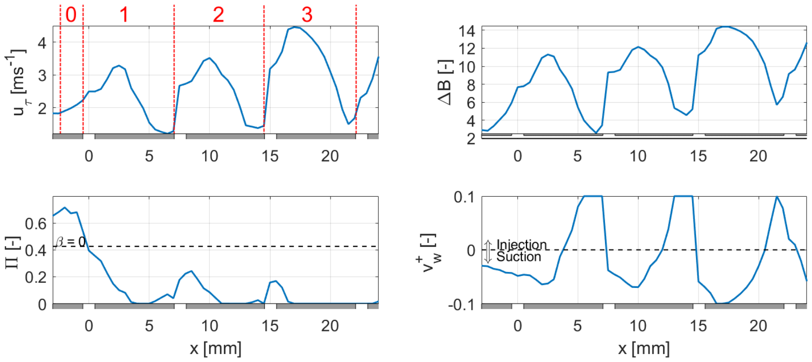

Figure 9.15: Downstream development of the boundary layer over the liner at $M_0 = 0.1$, SPL= $144.3 dB$. The dashed red lines indicate regions of averaging per orifice.

The third quantity to show strong periodic behaviour is the wall transpiration coefficient v_w^+. An effective suction is seen during each half period following an orifice. The other half periods show injection, which is limited by the upper limit imposed at $v_{w,max}^+ = 0.1$. It is argued that this shows the aerodynamic effect of the vortex shedding, as is discussed in subsection 9.1.3. During the outflow phase, low-velocity air is injected into the boundary. This reduces velocity in the near-wall region just aft of each orifice, an effect similar to wall suction. The injection before each orifice is then deemed to be associated to the inflow phase. As the orifices act as a temporary sink, air is drawn towards it, increasing the velocity. An increase in velocity at the wall corresponds to blowing [54]. Therefore, the trends in wall transpiration are associated to the injection of low-velocity pockets of air and sink-like behaviour at the orifices. Their time-dependent behaviour then averages out to the results seen here. The wall transpiration can not be directly interpreted as in- or outflow velocities at the orifices, due to the time-averaged nature of the profiles.

Finally, the wake parameter Π is seen to rapidly decrease over the liner. Small increases at the second and third orifice are seen. Outside of these locations, the wake parameters quickly reduces to its lower bound at $\Pi = 0$, effectively deactivating the wake law. As before, this is attributed to the inability of the method to fully fit the disturbed boundary layers; a zero wake parameter then simply provides the best fit through the S-shape of the boundary layer (cf. Figure 9.2).

The strong spatial dependence of the parameters in Figure 9.15 shows that the boundary layers used for log-law fitting or momentum-integral analysis can not be chosen arbitrarily. Instead, it is posed that quantities must be averaged over an integer number of spatial periods. In the top-left graph in Figure 9.15 the regions from Figure 9.1 are repeated: each region over the liner starts at the upstream edge of an orifice, and continues downstream up to the upstream edge of the next.

All properties are now averaged over these spatial domains, to evaluate net development per orifice. These results are shown in Figure 9.16. As expected from the local developments, a monotonic increase in friction velocity and effective surface roughness is seen. It is also clear that both parameters are still increasing rapidly, indicating that the boundary layer is not fully developed after 3 orifices. Π monotonically decreases towards 0. Finally, the wall friction coefficient shows non-trivial behaviour. Suction is strongest at the upstream (1) and downstream (3) domains. It is argued that this may be due to complex interactions between orifices, which require the phase-dependent turbulence results to observe qualitatively and quantitatively. As with earlier arguments, it must also still be taken into account that the parameters Π and v_w^+ together do not allow for a perfect fit through the velocity profile. Applying a more suitable modification than classic wall transpiration may yield clearer results.

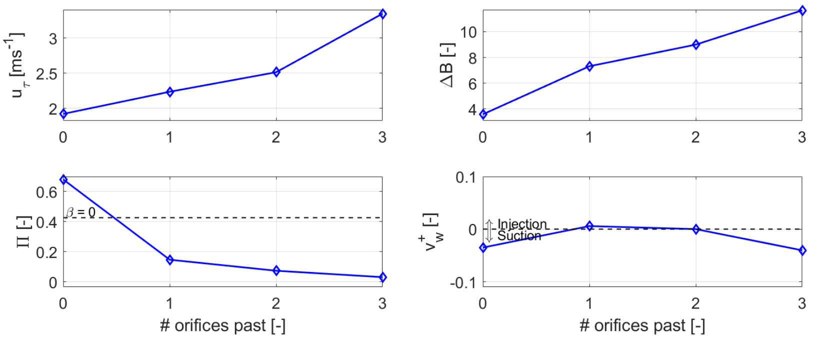

Figure 9.16: Downstream development of the boundary layer over the liner at $M_0 = 0.1$, SPL= $144.3dB$.

9.4.2. Weak acoustic forcing: $\Omega_v = 1.9$

Next, the above results are compared to a case where acoustic forcing is much weaker. In Figure 9.17a, no periodic behaviour is seen as opposed to the strongly forced case in Figure 9.15. Instead, a very noisy signal is found. Figure 9.17b shows that friction velocity and surface roughness are seen to grow over the liner sample. The growth rate is smaller than in Figure 9.16. The wake parameter Π seems to remain steady around $\Pi \approx 0.2$ initially, but drops to $\Pi \approx 0.1$ after the third orifice. While the growth in u_τ and ΔB seems reasonable, such a jump in Π is difficult to explain physically.

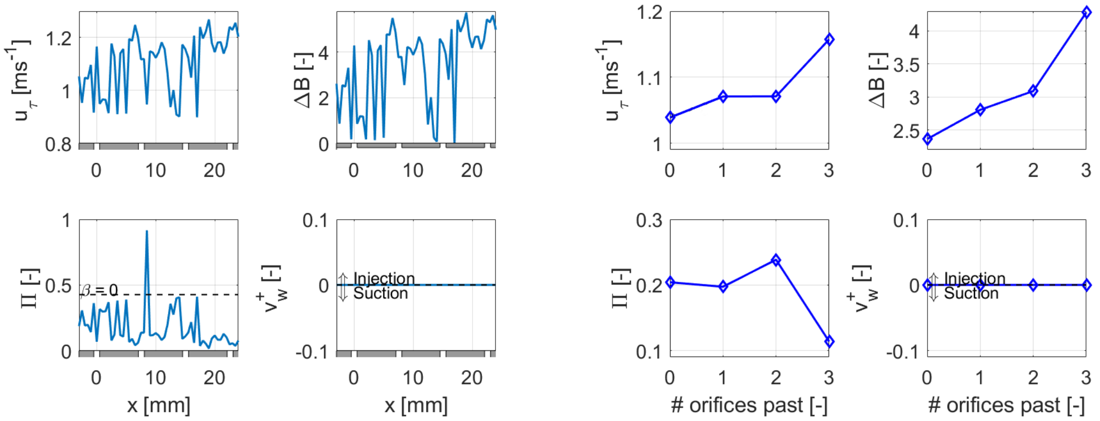

(a) Local development (b) Development per orifice

Figure 9.17: Downstream development of the boundary layer over the liner at $M_0 = 0.06$, SPL= $117.5dB$, fitting with wall transpiration disabled.

A second analysis is attempted, where wall transpiration is allowed in the weakly forced case. In Figure 9.18a, development is seen to be steady, but also much less noisy than without transpiration in Figure 9.17a. The friction velocity and surface roughness parameters seem to convergence. The wake parameter Π is seen to reduce quickly, as in the $M_0 = 0.1$ case. For this case, it decreases to a value $\Pi \approx 0.5 \pm 0.1$. Recall that Π is closely related to Clauser's equilibrium parameter β, where constant-β are in a turbulent equilibrium. As Π converges to a certain steady value, it can then be argued that the boundary layer is fully developed to a turbulent equilibrium. The convergence to $\Pi \approx 0.5$ agrees with the values seen for the higher-Mach cases in Figure 9.7. This could further indicate that for low acoustic forcing, i.e. low $|\tilde{v}_{or}|_{RMS}/u_\tau$, the boundary layer approaches a flat-plate flow in a weak adverse pressure gradient. Finally, the wall transpiration results in Figure 9.18 show a nearly constant value, associated to strong suction. This may correspond to observations made by Léon et al. [27] and in Figures 9.3.1 and 9.14a: for low acoustic forcing, acoustically induced vorticity remains close to the wall. It is argued that this provides a low-velocity, highly turbulent 'cushion' over the face sheet. A low wall velocity is again associated to wall suction. This explanation is not consistent with subsection 9.1.1, where it is stated that v_w^+ should go to zero for weak acoustic forcing.

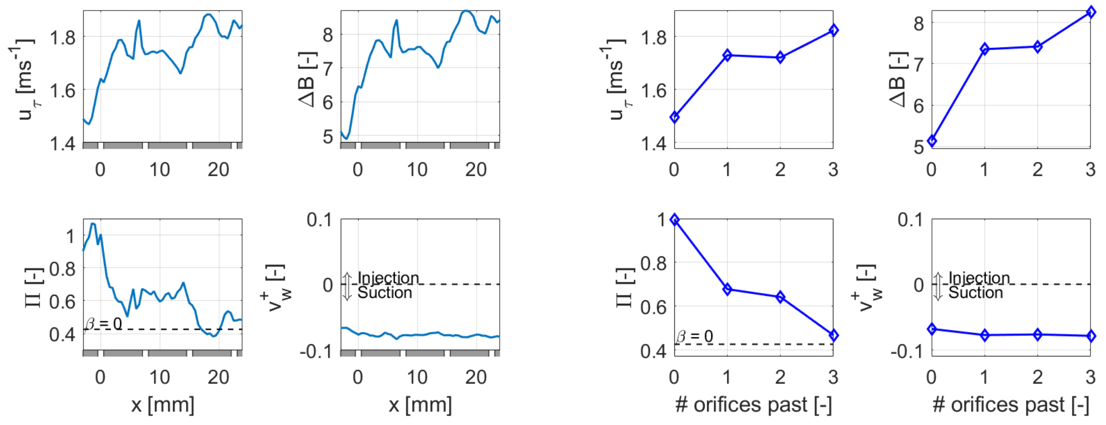

(a) Local development.

(b) Development per orifice

Figure 9.18: Downstream development of the boundary layer over the liner at $M_0 = 0.06$, SPL$= 117.5dB$, fitting with wall transpiration enabled.

The results with suction enabled are stable, and physical reasoning can be established. This is less so for the results without wall transpiration. Therefore, the results and interpretation of Figure 9.18 are maintained. It is stressed again that further insight into the log-law fits are required, and that a more appropriate modification than wall transpiration can be found that better represents the aerodynamic influence of the aero-acoustic interaction over the liner.

9.4.3. Evaluation of results

While the current liner sample is deemed too short for definitive conclusions on the boundary layer development, several statements may be formed. First, a clear influence of the aero-acoustic interaction on the boundary layer is seen, both locally and periodically per orifice. This agrees to the observations from Section 9.1, where the friction velocity of the entire liner sample is evaluated. Boundary layers must be evaluated over an integer amount of spatial periods due to the strong periodic behaviour at strong acoustic forcing. The boundary layer seems to converge to a steady state sooner in a weakly forced case than in strong forcing, but this must be confirmed using longer liner samples. Complex orifice interactions may occur, it is recommend to further study these using phase-dependent turbulence results. Nonetheless, the results show that effects from changes in (local) friction velocity and from orifice interactions can not be neglected in either numerical or experimental studies.

The recommendations made in subsection 9.1.4 also hold for the local evaluation presented here. Furthermore, future studies using larger liner samples are suggested to evaluate the downstream length required for boundary layer development over an acoustic liner. It can then be evaluated whether this downstream length can be expressed in terms of parameters associated to the geometrical, acoustic and aerodynamic conditions tested.

10

Conclusions

In this chapter, the findings of this thesis are summarized in three categories: first, the lessons regarding multi-δt PIV are stated, followed by the conclusions regarding the characterization of the aero-acoustic response of the liner. Finally, the answer to the main research question is formulated.

10.1. Multi-dt PIV

First, the following question regarding the methodology is addressed:

> *Can the PIV methodology be modified to provide the required DVR of* 900*?*

A multi-frame PIV method is chosen to provide a high DVR. Setting up the timing range for the multi-δt measurements is shown to be possible using simple log-law modelling. In the current work, a DVR up to 600 is reached far from the face sheet. This value is as predicted, and corresponds to a typical measurement noise of $\sigma_{\Delta x} \approx 0.1px$. It is also shown that the DVR decreases towards the face sheet. This decrease is attributed to an increase in measurement noise, resulting from laser sheet reflections, turbulence intensity and the timing range k_t. These effects affect all results, and must be further studied and quantified. Both multi-δt and grid refinement techniques suffer similarly from the variation in measurement noise. An improvement in DVR is obtained with respect to a comparable grid refinement approach, but the gain is small and reduces towards the face sheet. The variation in measurement noise with the timing range also makes the potential DVR difficult to predict. For the acoustic problem at hand, it is shown that the DVR must exceed the expected range of velocity scales by approximately 25% in order to accurately resolve phase-dependent quantities.

Combining phase-locking with multi-δt recordings allows to decompose velocity fields in four components: these are the time-averaged, the phase-dependent, the turbulent fluctuations and the measurement noise fields. The decomposition between fluctuations from turbulence and noise is not applicable to the current case, as the measurement noise is not independent of the pulse separation time. Correlation peak height and measurement noise are affected negatively by laser sheet reflections and turbulence intensity. A timing range or grid refinement factor amplify these effects.

10.2. Aero-acoustic liner response

Next, the research questions associated to the aero-acoustic interaction over the liner are re-stated and answered. Firs, the sub-questions are treated. After treating all sub-questions, the main research question can be answered.

> *What are the bounds for the orifice-to-friction velocity ratio* Ω_v *to classify the types of aerodynamic effects over the liner?*

A velocity scale indicating the intensity of vortex shedding is established by integrating the added vorticity RMS in the near-wall region. A clear link between this velocity scale and the non-linear resistance is seen. Both the aerodynamic and the acoustic perspectives confirm the onset of non-linear resistance occurs at a ratio of $\Omega_V \approx 2$. At this value, vortices are barely visible in the boundary layer.

Can a formulation be found to extract the friction velocity U_τ of the grazing boundary layer disturbed by strong acoustic forcing?

The friction velocity of the boundary layer, disturbed by the liner's aero-acoustic interaction, is found accurately from the PIV measurements. The momentum-integral allows to extract the friction velocity over a downstream length of several orifices. Alternatively, a logarithmic law with modifications for surface roughness, wall transpiration and inclusion of the outer layer can be fitted to the measurements. This allows to evaluate the friction velocity locally. The results agree with direct drag measurements.

Can the interaction between orifices be observed?

The boundary layer is seen to develop periodically per each orifice, with the wall friction and effective surface roughness growing downstream. Any bulk parameter associated to the boundary layer must be averaged over an integer number of orifices, which includes the space between two orifices. The boundary layer is not yet fully developed after 3 orifices, or $30mm$ for the case of strong acoustic forcing, at $\Omega_v = 6.5$. A weakly forced case at $\Omega_v = 1.9$, shows a faster and more steady boundary layer development. The boundary layer development and interaction between orifices could not be investigated further from the perspective of local, phase-dependent turbulence intensity. Also, the downstream length required for a fully developed boundary layer and aero-acoustic interaction could not be studied, and must be studied in future work using a longer liner sample. Nonetheless, the influence of the liner's aero-acoustic interaction on the friction velocity is shown to be non-negligible.

What is an appropriate scale for the in-orifice velocity amplitude $|\tilde{v}_{or}|$?

The results for the in-orifice velocity RMS are consistent between the in-situ impedance measurements and the PIV velocity fields. A weaker fluctuation is seen in the PIV results, which can be explained by the height above the face sheet at which it is evaluated. The lumped-element model suggested by Léon et al. [27] is shown to accurately predict the in-orifice velocity scale, provided that an accurate value for the orifice quality factor is used. A fixed quality factor is not applicable to a range of Mach numbers and sound pressure levels. The quality factor is associated to the reduction in effective open orifice area, known as a vena contracta. It is thereby inversely proportional to the friction velocity, and the in-orifice velocity scale. The current results on the quality factor agree qualitatively and quantitatively to statements and suggestions from literature.

10.3. Main research question

How is the non-linear resistance θ_{NL} of a single degree of freedom acoustic liner a function of the in-orifice velocity scale $|\tilde{v}_{or}|_{rms}$, the friction velocity U_τ, and the ratio $|\tilde{v}_{or}|_{rms}/U_\tau$, for grazing flow Mach numbers $M_0 \leq 0.8$ and sound pressure levels $\leq 155\ dB$?

From the literature study, the friction velocity is shown to be related to a reduction in the effective orifice open area, due to flow recirculation in the upstream part of the orifice. This effect is known as a vena contracta, and the associated driving velocity scale is the friction velocity u_τ. A second mechanism reducing the open area is seen at high in-orifice velocities, caused by flow separation from the entire orifice edge. This is characterised by the in-orifice velocity fluctuation, $|\tilde{v}_{or}|_{RMS}$. Within the current work, the expression below is found experimentally:

$$\sigma\theta \approx \begin{cases} 0.023 u_\tau & \text{for } \frac{|\tilde{v}_{or}|_{RMS}}{u_\tau} \leq 2.3 \\ u_\tau\left(0.023 + 0.004\left(\frac{|\tilde{v}_{or}|_{RMS}}{u_\tau} - 2.3\right)\right) & \text{for } \frac{|\tilde{v}_{or}|_{RMS}}{u_\tau} > 2.3 \end{cases}$$

If expressions are found for the orifice quality factor, the friction velocity and the vortex shedding velocity scale, an iterative method may be set up to solve all velocity scales and the orifice quality factor. This simultaneously estimates the acoustic resistance, due to its relation to the orifice quality factor.

Bibliography

[1] Fabien Anselmet and Pierre-Olivier Mattei. *Acoustics, Aeroacoustics and Vibrations*. Joch Wiley & Sons, first edition, 2016. ISBN 978-1-84821-861-1.

[2] R. Astley. Numerical methods for noise propagation in moving flows, with application to turbofan engines. *Acoustical Science and Technology*, 30:227–239, 2009.

[3] R.J. Astley and A. Cummings. A finite element scheme for attenuation in ducts lined with porous material: Comparison with experiment. *Journal of Sound and Vibration*, 116(2):239–263, 1987. doi: 10.1016/S0022-460X(87)81302-0.

[4] F. Bake and K. Knobloch. Novel liner concepts. *CEAS Aeronautical Journal*, 10(1):123–136, 3 2019. doi: 10.1007/s13272-019-00380-7.

[5] Martha Brown and Michael Jones. Effects of cavity diameter on acoustic impedance in a complex acoustic environment. 06 2018. doi: 10.2514/6.2018-3443.

[6] Christian Cierpka, Benjamin Lütke, and Christian J. Kähler. Higher order multi-frame particle tracking velocimetry. 54(5):1533, May 2013. doi: 10.1007/s00348-013-1533-3.

[7] P.D. Dean. An in situ method of wall acoustic impedance measurement in flow ducts. 34(1).

[8] Paolo L. Gatti and Vittorio Ferrari. *Applied Structural and Mechanical Vibrations : Theory, Methods and Measuring Instrumentation.* CRC Press, 1999. ISBN 9780419227106.

[9] A.L. Goldman. *The acoustic properties of an orifice under a turbulent boundary layer*. PhD thesis, University of Texas at Austin, 1975.

[10] A.W. Guess. Calculation of perforated plate liner parameters from specified acoustic resistance and reactance. *Journal of Sound and Vibration*, 40(1):119–137, 1975.

[11] R. Hain and C. J. Kähler. Fundamentals of multiframe particle image velocimetry (PIV). 42(4): 575–587. ISSN 0723-4864, 1432-1114. doi: 10.1007/s00348-007-0266-6. URL `http://link.springer.com/10.1007/s00348-007-0266-6`.

[12] George William Herbert and Diego Copiello. Acoustic liner composite sandwich. URL `https://commons.wikimedia.org/wiki/File:Acoustic_Liner_Composite_Sandwich.png`.

[13] Claus Heuwinkel, Estelle Piot, Francis Micheli, André Fischer, Lars Enghardt, Friedrich Bake, and Ingo Röhle. Characterization of a Perforated Liner by Acoustic and Optical Measurements. In *16th AIAA/CEAS Aeroacoustics Conference*, Stockholm, Sweden, June 2010. American Institute of Aeronautics and Astronautics. doi: 10.2514/6.2010-3765.

[14] Uno Ingard. On the theory and design of acoustic resonators. *The Journal of the Acoustical Society of America*, 25(6):1037–1061, 1953. doi: 10.1121/1.1907235.

[15] U. Ingård and S. Labate. Acoustic circulation effects and the nonlinear impedance of orifices. *The Journal of the Acoustical Society of America*, 22(2):211–218, 1950. doi: 10.1121/1.1906591.

[16] Young Jin Jeon, Ludovic Chatellier, and Laurent David. Fluid trajectory evaluation based on an ensemble-averaged cross-correlation in time-resolved PIV. 55(7):1766. ISSN 0723-4864, 1432-1114. doi: 10.1007/s00348-014-1766-9. URL `http://link.springer.com/10.1007/s00348-014-1766-9`.

[17] Xiaodong Jing and Xiaofeng Sun. Experimental investigations of perforated liners with bias flow. *The Journal of the Acoustical Society of America*, 106(5):2436–2441, November 1999. doi: 10.1121/1.428128.

[18] Xiaodong Jing, Xiaofeng Sun, Jingshu Wu, and Kun Meng. Effect of Grazing Flow on the Acoustic Impedance of an Orifice. *AIAA Journal*, 39(8), August 2001. doi: 10.2514/2.1498.

[19] Michael Jones and W Watson. On the use of experimental methods to improve confidence in educed impedance. *17th AIAA/CEAS Aeroacoustics Conference 2011 (32nd AIAA Aeroacoustics Conference)*, 06 2011. doi: 10.2514/6.2011-2865.

[20] Michael Jones, Maureen Tracy, Willie Watson, and Tony Parrott. Effects of liner geometry on acoustic impedance. 02 2002. doi: 10.2514/6.2002-2446.

[21] J. Kooi and S. Sarin. An experimental study of the acoustic impedance of Helmholtz resonator arrays under a turbulent boundary layer. In *7th Aeroacoustics Conference*, Palo Alto,CA,U.S.A., October 1981. American Institute of Aeronautics and Astronautics. doi: 10.2514/6.1981-1998.

[22] *Aerosol generator for tracer particle generation*. LaVision, September 2010.

[23] *Davis 10.1 Software, product manual*. LaVision, July 2020.

[24] *LaVision Imagager sCMOS CLHS*. LaVision, August 2020.

[25] L. E. M. Lignarolo, D. Ragni, F. Scarano, C. J. Simão Ferreira, and G. J. W. van Bussel. Tip-vortex instability and turbulent mixing in wind-turbine wakes. *J. Fluid Mech.*, 781, October 2015. doi: 10.1017/jfm.2015.470.

[26] Olivier Léon, Estelle Piot, Delphine Sebbane, and Frank Simon. Measurement of acoustic velocity components in a turbulent flow using LDV and high□repetition rate PIV. *Experiments in Fluids*, 58, 2017. doi: 10.1007/s00348-017-2348-4.

[27] Olivier Léon, Fabien Méry, Estelle Piot, and Claudia Conte. Near-wall aerodynamic response of an acoustic liner to harmonic excitation with grazing flow. *Exp Fluids*, 60(9), September 2019. doi: 10.1007/s00348-019-2791-5.

[28] Tabor Electronics Ltd. *User manual, Models 5064/1074/2074*, March 2007. Publication No. 070307.

[29] Kyle Lynch and Fulvio Scarano. A high-order time-accurate interrogation method for time-resolved piv. *Measurement Science and Technology*, 24, 02 2013. doi: 10.1088/0957-0233/24/3/035305.

[30] B. J. McKeon, M. V. Zagarola, and A. J. Smits. A new friction factor relationship for fully developed pipe flow. 538:429, 2005. doi: 10.1017/S0022112005005501.

[31] T.H. Melling. The acoustic impendance of perforates at medium and high sound pressure levels. *Journal of Sound and Vibration*, 29(1):1–65, July 1973. doi: 10.1016/S0022-460X(73)80125-7.

[32] P. Morse and K. Ingard. *Theoretical Acoustics*. International Series in Pure and Applied Physics. Princeton University Press, Princeton, 1968.

[33] R.E. Motsinger and R.E. Kraft. Design and performance of duct acoustic treatment. In *NASA. Langley Research Center, Aeroacoustics of Flight Vehicles: Theory and Practice*, volume 2, August 1991.

[34] Prateek Mustafi. Improved turbofan intake liner design and optimization, February 2013.

[35] Tim Persoons. High Dynamic Range Particle Image Velocimetry Applied to Heat Convection Studies. *EPJ Web of Conferences*, 67, 2014. doi: 10.1051/epjconf/20146701001.

[36] Tim Persoons and Tadhg S. O'Donovan. High Dynamic Velocity Range Particle Image Velocimetry Using Multiple Pulse Separation Imaging. *Sensors*, 11(1):1–18, December 2010. doi: 10.3390/s110100001.

[37] Stephen B. Pope. *Turbulent Flows*. Cambridge University Press, 2000. doi: 10.1017/CBO9780511840531.

[38] *Evergreen*. Quantel laser, March 2020.

[39] Markus Raffel, Christian E. Willert, Fulvio Scarano, Christian J. Kähler, Steve T. Wereley, and Jürgen Kompenhans. *Particle Image Velocimetry*. Springer International Publishing, Cham, 2018. doi: 10.1007/978-3-319-68852-7.

[40] Sven Scharnowski. Accurate turbulence level estimations using PIV/PTV. page 12.

[41] A. Sciacchitano and F. Scarano. Ae4180 - flow measurement techniques lecture slides, 2018.

[42] Andrea Sciacchitano, Fulvio Scarano, and Bernhard Wieneke. Multi-frame pyramid correlation for time-resolved PIV. page 19.

[43] André Spillere, Danillo Reis, and Julio A Cordioli. A systematic review of semi-empirical acoustic liner models under grazing flow and high SPL. In *Acoustics for the 21st century*, page 10, Buenos Aires, September 2016.

[44] André Mateus Netto Spillere, Lucas Araujo Bonomo, Júlio Apolinário Cordioli, and Edward James Brambley. Experimentally testing impedance boundary conditions for acoustic liners with flow: Beyond upstream and downstream. page 115676. doi: 10.1016/j.jsv.2020.115676.

[45] Rie Sugimoto, Paul Murray, and R. Jeremy Astley. *Folded Cavity Liners for Turbofan Engine Intakes*. doi: 10.2514/6.2012-2291.

[46] Christopher K. W. Tam and Konstantin A. Kurbatskii. Microfluid Dynamics and Acoustics of Resonant Liners. *AIAA Journal*, 38(8):1331–1339, August 2000. doi: 10.2514/2.1132.

[47] Christopher K.W. Tam, Hongbin Ju, and Bruce E. Walker. Numerical simulation of a slit resonator in a grazing flow under acoustic excitation. *Journal of Sound and Vibration*, 313(3-5), June 2008. doi: 10.1016/j.jsv.2007.12.018.

[48] Christopher K.W. Tam, Nikolai N. Pastouchenko, Michael G. Jones, and Willie R. Watson. Experimental validation of numerical simulations for an acoustic liner in grazing flow: Self-noise and added drag. *Journal of Sound and Vibration*, 333(13), June 2014. doi: 10.1016/j.jsv.2014.02.019.

[49] C.K.W. Tam, K.A. Kurbatskii, K.K. Ahuja, and R.J. Gaeta. A numerical and experimental investigation of the dissipation mechanisms of resonant acoustic liners. *Journal of Sound and Vibration*, 245(3):545–557, August 2001. doi: 10.1006/jsvi.2001.3571.

[50] Aaron C. True and John P. Crimaldi. High dynamic range particle image velocimetry analysis of viscous inhalant flows. *Physics of Fluids*, 31(10):103605, October 2019. doi: 10.1063/1.5125813.

[51] Mark-Jan Van der Meulen. Piv test of a grazed liner at low speed. Unpublished test results, internal communication, 2019.

[52] Mark-Jan Van der Meulen. Drag measurements over a grazed liner sample. Unpublished test results, internal communication, 2021.

[53] Willie R. Watson and Michael G. Jones. A Comparative Study of Four Impedance Eduction Methodologies Using Several Test Liners. In *19th AIAA/CEAS Aeroacoustics Conference*, Berlin, Germany, May 2013. American Institute of Aeronautics and Astronautics. doi: 10.2514/6.2013-2274.

[54] F.M. White. *Viscous Fluid Flow*. McGraw-Hill international edition. McGraw-Hill, 2006. ISBN 9780071244930.

[55] Bernhard Wieneke. PIV uncertainty quantification and beyond. URL `https://doi.org/10.4233/uuid:4ca8c0b8-0835-47c3-8523-12fc356768f3`.

[56] W.J. Worraker and N.A. Halliwell. Jet engine liner impedance: An experimental investigation of cavity neck flow/acoustics in the presence of a mach 0·5 tangential shear flow. 103(4):573–592. doi: 10.1016/S0022-460X(85)80025-0.

[57] T. Zandbergen. On the practical use of a three-microphone technique for in-situ acoustic impedance measurements on double layer flow duct liners. In *7th Aeroacoustics Conference*. American Institute of Aeronautics and Astronautics, 1981. doi: 10.2514/6.1981-2000.

[58] Qi Zhang and Daniel J. Bodony. Numerical Simulation of Two-Dimensional Acoustic Liners with High-Speed Grazing Flow. *AIAA Journal*, 49(2):365–382, February 2011. doi: 10.2514/1.J050597.

[59] Qi Zhang and Daniel J. Bodony. Numerical investigation and modelling of acoustically excited flow through a circular orifice backed by a hexagonal cavity. *J. Fluid Mech.*, 693:367–401, February 2012. doi: 10.1017/jfm.2011.537.

[60] Qi Zhang and Daniel J. Bodony. Numerical investigation of a honeycomb liner grazed by laminar and turbulent boundary layers. *J. Fluid Mech.*, 792:936–980, April 2016. doi: 10.1017/jfm.2016.79.

[61] Dan Zhao and X.Y. Li. A review of acoustic dampers applied to combustion chambers in aerospace industry. *Progress in Aerospace Sciences*, 74:114–130, April 2015. doi: 10.1016/j.paerosci.2014.12.003.

IV

Appendices

A

Results summary

This appendix presents a quick overview of the most important experimental results. Only fully processed data-sets are included, which are 2021, multi-δt sets from Table 8.1. Table A.1 shows the test conditions. The speed of sound c_0 and freestream velocity U_0 are found from the Mach number M_0 using Equation 5.4. The sound pressure level is taken from the face sheet microphone, and is the level at $2kHz$. The timing range shows the exact settings as used in the recording: pulse separation times are rounded to two decimals in Davis. Finally, the range of velocity scales of interest R_I from subsection 3.2.1 is listed.

Table A.1: Recording parameters

Test conditions								
				Timing range				
M_0	c_0	U_0	SPL	δt_0	δt_1	δt_2	δt_3	R_I
$-$	ms^{-1}	ms^{-1}	dB	μs	μs	μs	μs	$-$
0.0	343.0	0.0	138.7	5	12.5			0
0.06	343.0	20.6	117.5	2.29	4.01	10.3	12.37	568
0.1	343.0	34.3	144.3	1.37	2.75	9.89	12.37	44
0.2	341.5	68.3	145.0	0.69	1.72	8.59	10.99	82
0.4	337.6	135.0	140.3	0.34	0.86	4.29	5.5	282
0.6	333.6	200.2	140.3	0.23	0.57	2.86	3.66	420
0.8	329.7	263.8	134.3	0.17	0.43	2.15	2.75	1168

Results from Chapter 8 are summarized in Table A.2. The measurement noise $\sigma_{\Delta x}$ and DVR results from Section 8.3 are shown, as well as the relative velocity error $|\varepsilon_{v,inc}|_{RMS}$ and ratio between required and achieved DVR R_I/DVR from Sections 8.4-8.5.

Table A.2: DVR and assessment

Test conditions		DVR		Assessment	
M_0	SPL	$\sigma_{\Delta x}$	DVR	R_I/DVR	$|\varepsilon_{v,inc}|_{RMS}$
$-$	dB	px	$-$	$-$	$-$
0	138.7	0.070	143	0.00	0.05
0.06	117.5	0.041	532	1.07	0.18
0.1	144.3	0.065	559	0.08	0.08
0.2	145.0	0.123	516	0.16	0.04
0.4	140.3	0.090	718	0.39	0.04
0.6	140.3	0.121	526	0.80	0.34
0.8	134.3	0.130	497	2.35	0.44

The impedance results are displayed in Table A.3. This is comprised by the acoustic resistance θ, the reactance χ, and for completeness the absorption coefficient α from Equation 1.7. The orifice quality factor Q from Equation 2.11d is also included, as it is computed directly from the resistance.

Table A.3: Impedance and quality factor results

Test conditions		Impedance			
M_0	SPL	θ	χ	α	Q
$-$	dB	$-$	$-$	$-$	$-$
0	138.7	0.81	-0.47	0.93	1.32
0.06	117.5	0.24	-0.26	0.59	4.50
0.1	144.3	1.34	-0.56	0.93	0.80
0.2	145.0	1.65	-0.58	0.90	0.65
0.4	140.3	2.54	-0.88	0.76	0.43
0.6	140.3	4.19	-1.28	0.59	0.26
0.8	134.3	5.73	-1.41	0.48	0.19

Finally, the relevant velocity scales and ratios are listed in Table A.4. Friction velocity results from Section 9.1 are shown four-fold: the 'fit' column lists the values from the linear fit through the drag measurement results, shown in Equation 9.4. The column indicated 'mom.' relate to the momentum-integral PIV results. The $\log_{\mathbf{0}}$ and $\log_{\mathbf{3}}$ columns are the values found from the log-law fits in the up- and downstream domains indicated as **0** and **3** in Figure 9.1. The in-orifice velocity $|\widetilde{v}_{or}|_{RMS}$ are the results from the impedance measurements, which are used throughout Chapter 9 as discussed in Section 9.2. The values from the PIV measurements and model of Equation 2.11b can be found in Table 9.2. Finally, the last two columns show the ratio between in-orifice and friction velocity Ω_v, and the integrated vorticity v_ω, both discussed in Section 9.3.

Table A.4: Velocity scales

Test conditions		Velocity scales						
				u_τ				
M_0	SPL	fit	mom.	$\log_{\mathbf{0}}$	$\log_{\mathbf{3}}$	$\lvert\widetilde{v}_{or}\rvert_{RMS}$	Ω_v	v_ω
$-$	dB	ms^{-1}	ms^{-1}	ms^{-1}	ms^{-1}	ms^{-1}	$-$	ms^{-1}
0	138.7	-	-	-	-	8.71	-	-
0.06	117.5	1.04	1.34	1.49	1.82	2.00	1.9	0.56
0.1	144.3	1.65	2.49	1.92	3.45	10.72	6.5	5.3
0.2	145.0	3.15	4.34	4.44	5.27	9.71	3.1	2.22
0.4	140.3	6.11	5.91	5.34	5.55	3.73	0.6	-
0.6	140.3	9.00	7.91	8.45	8.19	2.30	0.3	-
0.8	134.3	11.82	-	13.57	13.53	0.87	0.1	-

B

Multi-dt code

In this appendix, the most important sections of code are displayed. These are the scripts that perform the multi-δt vector evaluation. The code *decomposeMultiDt2.m* in Section B.1 is run within a high-level script that handles file specification, which will not be discussed. This script provides the *dirName* input. The *options* variable is a Matlab struct which handles all global options. The relevant fields and the default values used here are displayed in Table B.1.

Table B.1: Relevant fields in the 'options' struct needed for decomposeMultiDt2.m. The 'Options' column lists possible values; default values are indicated in **bold**. For integer and float types, only the default value is displayed.

Field name	Type	Options	Description
sampleSize	Integer	**1000**	Number of PIV samples
dI	Integer	**32**	Interrogation window size in pixels
shiftMode	String	integer, ceil, floor, **subpixel**, none	Implementation of window shift, options used to reverse engineer Davis 8.4.
normalisationMode	String	minmax, maxnz, pdfmm, pdfnz, **normalizedSOC**, none	How to normalize correlation maps.
weighingMode	String	circ, **none**	Weighing of correlation maps, which is usually implemented in Davis.
combinationMode	String	**sum**, mean, product	How to combine multiple correlation maps into a scatter maps.
peakFittingMode	String	poly, **gauss**, (centroid), abs	Correlation peak fitting method.
readNew	Boolean	**true**, false	Whether to read new data.
dtMode	Float	**0**	0 makes the code read the δt's from the files. Otherwise, specify a vector with values to override.
excludeDt	Integer	**0**	How many δt's to ignore, starting at the longest.
runMode	String	**SOC**, STD, Corr	Specify which processing to execute, can take a list of multiple.
detectReflections	String	**peakRatio**, none	Whether to detect reflections at the orifice.
peakRatioLimit	Float	**0.35**	Named wrong: correlation peak value below which it is assumed the data is in a reflection.
useParallel	Boolean	true, **false**	Whether to use parallelization.

decomposeMultiDt2.m itself is another shell whose main function is to collect and store processed multi-δt velocity fields and associated metadata. The main work is executed by several subroutines, the following are deemed relevant to show here:

- *shiftCorrelationMap.m*: this script is called within *readSOCMaps2* (line 20 in *decomposeMultiDt2*), and shifts and scales higher-δt correlation maps to to δt_0. This is the numerical implementation of Equation 7.1a. The reflection clean-up of subsection 7.3.5 is also implemented here.
- *combinedScatterMap.m*: this code sets up the scattered multi-δt correlation map, as visualized in Figure 7.12.
- *fitScatteredPeak.m*: this is the correlation peak fitting and velocity evaluation of Equation 7.2.
- *turbNoisefit.m*: as the name suggests, this performs the decomposition between turbulence intensity and measurement noise, shown in Equation 7.3

The scripts are cleaned up for conciseness: lines associated to debugging and diagnostics have been exluced. Other functions such as data import are deemed trivial and are also not shown. Similarly, the numerical implementation of all analyses on the velocity fields are straightforward, and are not discussed.

B.1. Main: decomposeMultiDt2.m

```
1  function [X,Y,U,V,peakHeight,numUsed,roundness,TI,sigma,corrMap_coll,coord_I,coord_J,dt_comb,options] =
       decomposeMultiDt2(dirName,options)
2
3  % Set temporary dummy outputs: all parameters must be defined for output
4  X = nan;
5  Y = nan;
6  U = nan;
7  V = nan;
8  peakHeight = nan;
9  roundness = nan;
10 numUsed = nan;
11 dt_comb = nan;
12 TI = nan;
13 sigma = nan;
14 corrMap_coll = nan;
15 coord_I = nan;
16 coord_J = nan;
17
18 % read SOC maps, pixel coordinates, vector with dt's, mask, and dimensions of the vector field
19 if contains(options.runMode,'SOC') || contains(options.runMode,'Corr')
20     [corrMap_coll,coord_I,coord_J,X,Y,~,~,dt_comb,options.mask,vecDim] = readSOCMaps2(dirName,options.
       dtMode,options);
21 end
22
23 %% SOC
24
25 if contains(options.runMode,'SOC')
26
27     % Pre-allocate
28     U = zeros(vecDim);
29     V = zeros(vecDim);
30     peakHeight = zeros(vecDim);
31     roundness = zeros(vecDim);
32     numUsed = zeros(vecDim);
33     dt = dt_comb(1); % Everything is scaled down in time to dt0, this is set as the global dt
34
35     % Print status update, for impatient people such as myself
36     time = fix(clock);
37     fprintf('\n[%02i:%02i:%02i]□Finding□displacement...□000.0%%\n',time(4),time(5),time(6));
38
39     for I = 1:vecDim(1)*vecDim(2) % Nested (2D) for-loop converted to single loop for parallel
        distribution over all vectors
40
41         % Convert back to two seperate indices (legacy)
42         if mod(I,vecDim(2)) == 0
43             i = (I - mod(I,vecDim(2)))/(vecDim(2));
44             j = vecDim(2);
45         else
46             i = 1 + (I - mod(I,vecDim(2)))/(vecDim(2));
47             j = mod(I,vecDim(2));
48         end
49
50         if options.mask(i,j) == 1 % Only loop through subroutines if it is in a valid region (where mask =
     1)
51             % Extract single multi-dt correlation map, combine and fit peak
52             [smallMap,smallMap_I,smallMap_J] = extractSingleMap(corrMap_coll,coord_I,coord_J,i,j,options.
       dI);
```

```
            [scatterMap,numUsed(i,j)] = combinedScatterMap2(smallMap,smallMap_I,smallMap_J,options);
            [U(i,j),V(i,j),~,~,peakHeight(i,j),roundness(i,j)] = fitScatteredPeak(scatterMap,dt,options.peakFittingMode,1);
        end

    end

    [X,Y] = calibrateCoordinates(X,Y,'first'); % Calibarate (0,0) to be in the centre of the first orifice

    % In some odd cases, complex results are found, usually with a zero imaginary component. These give errors, so must be corrected to real values
    U = real(U);
    V = real(V);
    peakHeight = real(peakHeight);
    roundness = real(roundness);

    options.numUsed = numUsed; % write to options (keep global)

    Vmag = sqrt(U.^2 + V.^2); % Velocity magnitude
    Vscale = ceil(median(maxk(Vmag(:),8000))/10)*10; % Scale for velocity magnitude plots
    peakHeight = peakHeight./numUsed; % Average peak height

    % Save important variables into .m files and a struct
    if options.storeDir ~= ”none”
        mask = options.mask;
        SOCinfo.dt = dt_comb;
        SOCinfo.vecDim = vecDim;
        U0 = nanmean(Vmag(X >= options.farField(1) & Y >= options.farField(2) & X <= options.farField(3) & Y <= options.farField(4)));
        SOCinfo.U0 = U0;

        % SOCresults.mat contains the multi-dt velocity fields and most important metadata. These are used when evaluating the results.
        save(fullfile(options.storeDir,'SOCresults.mat'),”X”,”Y”,”U”,”V”,”dt_comb”,”peakHeight”,”numUsed”,”mask”,'-v7');

        % SOCinfo contains only basic information
        save(fullfile(options.storeDir,'SOCinfo.mat'),”dt_comb”,”vecDim”,”U0”,'-v7');
        writestruct(SOCinfo,fullfile(options.storeDir,'info.xml'));
    end
end

%% Turbulence/noise fit

if contains(options.runMode,'STD')

    % Read data from multi-dt SOC processing, must be included in the process or run seperately before.
    SOCresults = load(fullfile(options.storeDir,'SOCresults.mat')); % SOCresults .mat
    SOCinfo = load(fullfile(options.storeDir,'SOCinfo.mat')); % info struct
    options.mask = SOCresults.mask;
    options.numUsed = SOCresults.numUsed;
    options.vecDim = SOCinfo.vecDim;

    % Read velocity stddev fields
    [U_stddev,V_stddev,dt] = readSTD2(dirName,'auto',options);

    if dt ~= SOCinfo.dt_comb % Check if dt's match to SOC results
        error(”SOC and STD dt's do not match”);
    end

    U0 = nanmean(U(X > -10 & X < 6 & Y > 15 & Y < 16),'all'); % Find freestream velocity

    [TI,sigma] = turbNoiseFit(SOCresults.U,U_stddev,SOCresults.V,V_stddev,dt',U0,'local',options); % Perform decomposition

    if options.storeDir ~= ”none”
        writestruct(SOCinfo,fullfile(options.storeDir,'info.xml'));
        save(fullfile(options.storeDir,'STDresults.mat'),”TI”,”sigma”,'-v7');
    end

end
```

B.2. shiftCorrelationMap.m

```
function [coord_I,coord_J] = shiftCorrelationMap(corrDim,Vx,Vy,dI,dt0,dti_1,dti,shiftMode)

params = getParameters3;
pixelSize = params.pixelSize/1e3;
vecDim = corrDim/(dI+1);
[I_raw,J_raw] = meshgrid(1:corrDim(2),1:corrDim(1));

coord_I = zeros(size(I_raw));
coord_J = zeros(size(J_raw));

% Part 1: Shift around the window centre due to dt scaling. Varies within
% the window, but each window throughout the field is identical.
[scaleShiftX,scaleShiftY] = meshgrid(-(dI-2)/2:1:(dI)/2,-(dI-2)/2:1:(dI)/2);
scaleShiftX = scaleShiftX*(1 - dt0/dti);
scaleShiftY = scaleShiftY*(1 - dt0/dti);

% Part 2: shift due to window displacement. Constant within window, varying
% throughout field
if shiftMode == "subpixel"
    velocityShiftX = squeeze(Vx)*dti*1e-6/pixelSize;
    velocityShiftY = -squeeze(Vy)*dti*1e-6/pixelSize;
elseif shiftMode == "integer"
    velocityShiftX = round(squeeze(Vx)*dti*1e-6/pixelSize);
    velocityShiftY = round(squeeze(Vy)*dti*1e-6/pixelSize);
elseif shiftMode == "ceil"
    velocityShiftX = ceil(squeeze(Vx)*dti*1e-6/pixelSize);
    velocityShiftY = ceil(squeeze(Vy)*dti*1e-6/pixelSize);
elseif shiftMode == "floor"
    velocityShiftX = floor(squeeze(Vx)*dti*1e-6/pixelSize);
    velocityShiftY = floor(squeeze(Vy)*dti*1e-6/pixelSize);
elseif shiftMode == "none"
    velocityShiftX = zeros(size(squeeze(Vx)));
    velocityShiftY = zeros(size(squeeze(Vy)));
end


for i = 1:vecDim(1)
    for j = 1:vecDim(2)

        ind_I = i + (i-1)*dI:1:i + i*dI - 1;
        ind_J = j + (j-1)*dI:1:j + j*dI - 1;

        coord_I(ind_I,ind_J) = I_raw(ind_I,ind_J) + velocityShiftX(i,j)*dt0/dti - scaleShiftX;
        coord_J(ind_I,ind_J) = J_raw(ind_I,ind_J) + velocityShiftY(i,j)*dt0/dti - scaleShiftY;
    end
end
```

B.3. combinedScatterMap.m

```
function [scatterMap,numUsed] = combinedScatterMap2(smallMaps,coords_I,coords_J,options)

mode = options.combinationMode; % Legacy

if options.detectReflections == "peakRatio"
    maxima = max(smallMaps,[],[2 3]); % Absolute peak per map (vector result)
    numUsed = size(smallMaps,1) - sum(maxima < options.peakRatioLimit); % numUsed = #dt's - #removed
    numOriginal = size(smallMaps,1); % Extract original number of dt's
    if numUsed  == 0 % Keep the shortest dt in case all peaks are below the threshold
        numUsed = 1;
    elseif numUsed == size(smallMaps,1) - 1 % Switch directly from 4 dt's to 2: estimator for 3rd map wrong in reflections
        numUsed = 2;
    end

    % Remove maps of higher dt's
    smallMaps = smallMaps(1:numUsed,:,:);
    coords_I = coords_I(1:numUsed,:,:);
    coords_J = coords_J(1:numUsed,:,:);

    % Perform reflection clean-up on remaining maps
    if numUsed ~= numOriginal
        range = floor(options.dI/4); % Find quarter of the window size
        yMean = repmat((mean(smallMaps(:,1:range,:),2) + mean(smallMaps(:,end-range:end,:),2))/2,1,options.dI); % Find average profile
        smallMaps = smallMaps - yMean; % Subtract profile
    end
else % All dt's used
    numUsed = size(smallMaps,1);
end
```

```

for i = 2:size(smallMaps,1)

    % Interpolate the results of one level lower to the current level
    interpolatedMap = interp2(squeeze(coords_I(i-1,:,:)),squeeze(coords_J(i-1,:,:)),squeeze(smallMaps(i-1,:,:)),squeeze(coords_I(i,:,:)),squeeze(coords_J(i,:,:)));

    if mode == ”sum” % Add interpolated lower map to current level
        smallMaps(i,:,:) = squeeze(smallMaps(i,:,:)) + interpolatedMap;
    elseif mode == ”mean” % Take mean of current level and interpolated lower map
        smallMaps(i,:,:) = mean(cat(3,squeeze(smallMaps(i,:,:)), interpolatedMap),3);
    elseif mode == ”product” % Multiply current level with interpolated lower map
        smallMaps(i,:,:) = squeeze(smallMaps(i,:,:)).*interpolatedMap;
    end

    % Remove overlapping results from lower map (information now included in current level)
    overlap = coords_I(i-1,:,:) >= min(coords_I(i,:,:),[],’all’) & coords_I(i-1,:,:) <= max(coords_I(i,:,:),[],’all’) & coords_J(i-1,:,:) >= min(coords_J(i,:,:),[],’all’) & coords_J(i-1,:,:) <= max(coords_J(i,:,:),[],’all’);
    smallMaps(i-1,squeeze(overlap)) = nan;
    coords_I(i-1,squeeze(overlap)) = nan;
    coords_J(i-1,squeeze(overlap)) = nan;
end

scatterMap = [coords_I(:) coords_J(:) smallMaps(:)]; % Reorganise into [dI^2]x[3] double
scatterMap(any(isnan(scatterMap),2),:) = []; % Remove rows that have a NaN in it (overlapping results, other weird stuff)
```

B.4. fitScatteredPeak.m

```
function [Vx,Vy,dx,dy,peakHeight,peakRoundness] = fitScatteredPeak(scatterMap,dt,mode,steps)

% ’steps’ was intended to allow for larger kernels (for example 5-point
% peak fitting), but was never fully implemented
if steps ~= 1
    warning(’Only␣3-point␣estimator␣implemented’);
    steps = 1;
end

% Obtain pixel size
params = getParameters3;
pixelSize = params.pixelSize/1e3;

% In case an empty or flat map is provided (happens in masked regions),
% return nan values
if isempty(scatterMap) || max(scatterMap(:,3)) == min(scatterMap(:,3))
    Vx = nan;
    Vy = nan;
    dx = nan;
    dy = nan;
    peakHeight = nan;
    peakRoundness = nan;
else

    % Interrogation window center
    x0 = (max(scatterMap(:,1)) + min(scatterMap(:,1)) - 1)/2;
    y0 = (max(scatterMap(:,2)) + min(scatterMap(:,2)) - 1)/2;

    % Find maximum location
    xm = scatterMap(scatterMap(:,3) == max(scatterMap(:,3)),1);
    ym = scatterMap(scatterMap(:,3) == max(scatterMap(:,3)),2);

    % Catch identical maxima (expected to be next to each other). Was added
    % when setting up the script, but does not seem needed
    if length(xm) > 1
        xm = mean(xm);
        ym = mean(ym);
    end

    if mode ~= ”abs”
        % Sorted distances to maximum location
        dist = sqrt((scatterMap(:,1) - xm).^2 + (scatterMap(:,2)-ym).^2);
        sorted = sortrows([scatterMap dist],4);

        % Create linear interpolator, recovers neighbours exactly if they are present
        linInterpolator = scatteredInterpolant(sorted(1:32*steps,1),sorted(1:32*steps,2),sorted(1:32*steps,3));

        % Pre-allocate and set coordinates
        fitData = zeros(4*steps+1,3);
        gridDistance = sorted(2,4);

        % Set xdata
        fitData(2:1+steps,1) = (-steps*gridDistance:gridDistance:-gridDistance) + xm; % x < xm points
        fitData(2+steps:1+2*steps,1) = (gridDistance:gridDistance:steps*gridDistance) + xm; % x > xm points
        fitData(2:1+2*steps,2) = ym; % Fixed y points

        % Set ydata
        fitData(2+2*steps:1+3*steps,2) = (-steps*gridDistance:gridDistance:-gridDistance) + ym; % y < ym points
        fitData(2+3*steps:end,2) = (gridDistance:gridDistance:steps*gridDistance) + ym; % y > ym points
        fitData(2+2*steps:end,1) = xm; % Fixed y points

        % Set correlation data
        fitData(1,:) = sorted(1,1:3); % First entry: peak
        fitData(2:end,3) = linInterpolator(fitData(2:end,1),fitData(2:end,2)); % Rest: interpolate (pick) from interpolant

        % Set up vectors of monotonically increasing coordinates with corresponding (interpolated) correlation values
        xdata = [fitData(2:1+steps,1);fitData(1,1);fitData(2+steps:1+2*steps,1)] - x0;
        xfitdata = [fitData(2:1+steps,3);fitData(1,3);fitData(2+steps:1+2*steps,3)];
        ydata = [fitData(2+2*steps:1+3*steps,2);fitData(1,2);fitData(2+3*steps:end,2)] - y0;
        yfitdata = [fitData(2+2*steps:1+3*steps,3);fitData(1,3);fitData(2+3*steps:end,3)];

    end

    % Fit peak location
    if mode == ”poly” % Fit 2nd order polynomial peak

        % Set up linear system and solve
        Ax = [xdata.^2 xdata ones(size(xdata))]; % Array with coordinates
        fitx = Ax\xfitdata; % Result vector
        dx = fitx(2)/(-2*fitx(1)); % x-displacement
        xh = fitx(3)-fitx(1)*dx^2; % peak height of x-peak

        % Same steps, but in y-direction
        Ay = [ydata.^2 ydata ones(size(ydata))];
        fity = Ay\yfitdata;
        dy = fity(2)/(-2*fity(1));
        yh = fity(3)-fity(1)*dy^2;

        % Evaluate metadata
        peakRoundness = fitx(1)/fity(1);
        peakHeight = mean([xh yh]);

    elseif mode == ”gauss” % Fit Gaussian peak

        % Set up linear system and solve
        Ax = [xdata.^2 xdata ones(size(xdata))]; % Array with coordinates
        fitx = Ax\log(xfitdata); % Results vector
        xc = sqrt(-1/(2*fitx(1))); % Associated to denominator of exponent
        dx = xc^2*fitx(2); % x-displacement
        xh = exp(fitx(3) + 0.5*(dx/xc)^2); % peak height of x-peak

        % Same steps, but in y-direction
        Ay = [ydata.^2 ydata ones(size(ydata))];
        fity = Ay\log(yfitdata);
        yc = sqrt(-1/(2*fity(1)));
        dy = yc^2*fity(2);
        yh = exp(fity(3) + 0.5*(dy/yc)^2);

        % Evaluate metadata
        peakRoundness = fitx(1)/fity(1);
        peakHeight = mean([xh yh]);

    elseif mode == ”centroid” % Centroid method
    elseif mode == ”abs” % Directly take peak, only used in early stages when setting up the code
        dx = xm - x0;
        dy = ym - y0;
        peakRoundness = 1;
        peakHeight = max(scatterMap(:,3));
    end

    if isempty(dx) || isempty(dy) % Catch nan's (can occur in masked regions)
        Vx = nan;
        Vy = nan;
    else % Convert particle image displacement to velocity. Note the inverted y-axis
        Vx = dx*pixelSize/(dt*1e-6);
        Vy = -dy*pixelSize/(dt*1e-6);
    end
end
```

B.5. turbNoisefit.m

```
function [TI,noise] = turbNoiseFit(U,Ustddev,V,Vstddev,dt,U0,dxoption,options)

[~,~,pixelSize,~,~] = getParameters2;

U_mag = sqrt(U.^2 + V.^2);  % Velocity magnitude in m/s
U_mag(U_mag == 0) = 1e-6; % Set small value to avoid divisions by 0 later on

% Permute in case a (constant) 2D velocity field is used
if size(U_mag,3) == 1
    U_mag = permute(U_mag,[3 1 2]);
end

if dxoption == "local"
    TI_raw = sqrt(0.5*(Ustddev.^2 + Vstddev.^2))./U_mag; % Measured turbulence intensity
    dx = dt.*U_mag/(pixelSize*1e3); % Displacement magnitude in px
elseif dxoption == "global"
    TI_raw = sqrt(0.5*(Ustddev.^2 + Vstddev.^2))/U0; % Measured turbulence intensity
    dx = dt.*ones(size(U_mag))*U0/(pixelSize*1e3); % Uniform field with displacement based on freestream
end

% Reshape all fields into vectors (intended for parallelisation)
[dtdim,xdim,ydim] = size(TI_raw); % Get dimensions for reshaping
TI_raw = reshape(TI_raw,dtdim,[]); % Reshape into [N_dt x N_vectors]
dx = reshape(dx,dtdim,[]); % Reshape into [N_dt x N_vectors]
mask = reshape(options.mask,1,[]);
numUsed = reshape(options.numUsed,1,[]);

% Set initial condition and bounds
x0 = 0.1^2*ones(2,xdim*ydim); % IC for noise is 0.1px
x0(1,:) = (0.9*squeeze(min(TI_raw))).^2; % IC for TI is the minimum observed over the dt's
lb = zeros(size(x0)); % zero lower bounds :)
ub = (4*ones(size(x0))).^2; % ub for noise is 4px
ub(1,:) = squeeze(nanmin(TI_raw)).^2; %min(TI_raw,[],'all')*ones(size(lb(1,:))); % ub for TI is 5 times the global maximum TI observed

% Catch nan's
ub(isnan(ub)) = 1;
x0(isnan(x0)) = 0.1;

fitField = zeros(2,xdim*ydim); % pre-allocate
lsqlinoptions = optimoptions('lsqlin','algorithm','interior-point','display','off'); % Optimization (regression) parameters

% Solve linear system Ax=b, where x = [TI_real^2; sigma^2]
% TI_meas^2 = TI_real^2 + sigma^2/dx^2 = [1 1/dx^2][TI_real^2; sigma^2]

% Progress tracker
time = fix(clock);
fprintf('[%02i:%02i:%02i]␣Decomposing␣noise/turbulence...␣000.0\n%%',time(4),time(5),time(6));

for i = 1:xdim*ydim % Loop over vectors, can be made parfor but is quite fast anyways
    fprintf('\b\b\b\b\b\b\b%05.1f%%\n',i/(xdim*ydim)*100); % Update progress field

    if mask(i) == 1 && numUsed(i) >= 2 && max(isnan(TI_raw(1:numUsed(i),i))) == 0
        A = [ones(numUsed(i),1) 1./dx(1:numUsed(i),i).^2]; % A matrix: first column 1's, 2nd column is 1/dt^2 [N_dt x 2]
        b = TI_raw(1:numUsed(i),i).^2; % b matrix: column vector with corresponding measured TI's
        [fitField(:,i),~,] = lsqlin(A,b,[],[],[],[],lb(:,i),ub(:,i),x0(:,i),lsqlinoptions); % Solve linear system (LS regression)
    end
end

% Extract, reshape and return turbulence and noise components
TI = sqrt(reshape(fitField(1,:),xdim,ydim)); % [-]
noise = sqrt(reshape(fitField(2,:),xdim,ydim)); % [px]
TI = TI.*squeeze(U_mag)/U0; % Re-define turbulence intensity to the freestream velocity
```